# Main Chamber and Preburner Injector Technology

**Final Report**
**for**
**NASA Cooperative Agreement Grant No. NCC 8-46**

**Robert J. Santoro and Charles L. Merkle**

***Propulsion Engineering Research Center***
***and***
***Department of Mechanical and Nuclear Engineering***
***The Pennsylvania State University***
***University Park, Pennsylvania***

**March, 1999**

PENNSTATE
1855

# TABLE OF CONTENTS

# ABSTRACT

This document reports the experimental and analytical research carried out at the Penn State Propulsion Engineering Research Center in support of NASA's plan to develop advanced technologies for future single stage to orbit (SSTO) propulsion systems. The focus of the work is on understanding specific technical issues related to bi-propellant and tri-propellant thrusters. The experiments concentrate on both cold flow demonstrations and hot-fire uni-element tests to demonstrate concepts that can be incorporated into hardware design and development. The analysis is CFD-based and is intended to support the design and interpretation of the experiments and to extrapolate findings to full-scale designs. The research is divided into five main categories that impact various SSTO development scenarios. The first category focuses on RP-1/gaseous hydrogen ($GH_2$)/gaseous oxygen ($GO_2$) tri-propellant combustion with specific emphasis on understanding the benefits of hydrogen addition to RP-1/oxygen combustion and in developing innovative injector technology. The second category investigates liquid oxygen (LOX)/$GH_2$ combustion at main chamber near stoichiometric conditions to improve understanding of existing LOX/$GH_2$ rocket systems. The third and fourth categories investigate the technical issues related with oxidizer-rich and fuel-rich propulsive concepts, issues that are necessary for developing the full-flow engine cycle. Here, injector technology issues for both LOX/$GH_2$ and LOX/RP-1 propellants are examined. The last category, also related to the full-flow engine cycle, examines injector technology needs for $GO_2$/$GH_2$ propellant combustion at near-stoichiometric conditions for main chamber application.

# I. OVERALL PROGRAM STRUCTURE

This document reports all the research work carried out at the Penn State (PSU) Propulsion Engineering Research Center (PERC) for the NASA Marshall Space Flight Center (MSFC) funded activity titled Main Chamber and Preburner Injector Technology under NASA Cooperative Grant No. NCC 8-46. The experimental and analytical research for various facets of the Reusable Launch Vehicle Program (RLV) documented here were conducted between the time frame from June, 1994 to May, 1998. During the course of the program, the goals of the program were continually realigned by NASA MSFC to conform to the evolving goals of the overall RLV program. Consequently, it is necessary to provide a history of the program genesis to aid the reader in fully understanding the scope of the program reported here.

In 1994, Penn State was awarded two separate projects under NRA8-11, Advanced Propulsion Technologies. These two projects, Advanced Propulsion Technologies for Tri-propellant Combustion and Oxygen-Rich Rocket Combustor Technology, were awarded to

**Table 1.1. Advanced Propulsion Technologies for Tri-propellant Combustion**

| **Program Element (Status 11/95)**<br>**TA-2 Tri-Propellant Combustion** | **Current Status** | **Future Plans** |
|---|---|---|
| 1.1.1 Experimental Studies of Tri-Propellants | in progress | refer to sub-elements |
| 1.1.1.1 Experimental Studies of Tri-Propellants Effects of $GH_2$ Addition to $GO_2$/RP-1 and LOX/RP-1 (Coaxial-Type Tri-propellant Injector) | in progress | defer studies of $GH_2$ addition to LOX/RP-1 |
| 1.1.1.2 Experimental Studies of Tri-Propellants Cold Flow Studies (Coaxial-Type Tri-propellant Injector) | in progress | continue |
| 1.1.1.3 Experimental Studies of Tri-Propellants Effervescent Atomization Studies for $GO_2$/RP-1/$GH_2$ (Hot-Fire and Cold Flow Studies) | in progress | continue on limited basis |
| 1.1.2 Experimental Studies of Mode Transition from $GO_2$/RP-1/$GH_2$ to $GO_2$/$GH_2$ Combustion | in design phase | defer |
| 1.1.3 Experimental Studies of RP-1 Drop Combustion in $GO_2$ and $GO_2$/$GH_2$ | complete | N/A |
| 1.1.4 Common Cold Flow Manifold Experiments to Understand Effects of $LH_2$ on RP-1 During Fuel Transition | in progress | defer |
| 2.1.1 Analytical Studies of Tri-Propellants - Hydrocarbon Combustion Processes | in progress | continue |
| 2.1.2 Analytical Studies of Tri-Propellants - Hydrogen/RP-1 Manifold Analysis | in progress | defer |

**Table 1.2. Oxygen-Rich Rocket Combustor Technology**

| Program Element (Status 11/95)<br>TA-3 Oxygen Rich Combustor Technology | Current Status | Future Plans |
|---|---|---|
| 1.1.1. High O/F Experimental Studies ($LOX/GH_2$; Swirl Coaxial Injector) | in progress | continue |
| 1.1.2. High O/F Experimental Studies (LOX/RP-1; Pintle\Impinging Injector) | in progress | continue |
| 1.1.3 Determine flame stability, ignition characteristics, combustion efficiency and wall heating effects | in progress | continue |
| 2.1.1. High O/F Direct Injection Analytical Studies | in progress | continue |
| 2.1.2. Near-stoichiometric Core/Dilution Analysis | in progress | continue |
| 2.1.3. Assess validity and utility of analysis for CFD hardware applications | in progress | continue |

understand the issues with RP-1/Hydrogen/Oxygen tri-propellant combustion for main chamber RLV application, and oxidizer-rich combustion for full-flow engine cycle preburner application.

The Advanced Propulsion Technologies for Tri-propellant Combustion project addressed NASA's plans to develop advanced technologies for future single stage to orbit (SSTO) propulsion systems and specifically responded to Technical Area 2 (Modular Bipropellant and Tri-propellant Thrusters and Thrust Cells) of NRA NRA8-11. The focus of the work was on understanding specific technical issues that needed to be resolved for minimizing risk and cost associated with developing tri-propellant propulsive concepts. The experiments concentrated on both cold flow demonstrations and hot-fire uni-element tests to demonstrate concepts that could be rapidly incorporated into hardware design and development. The analysis was CFD-based and was intended to support the design and interpretation of the experiments and to extrapolate findings to full-scale designs. The proposed effort emphasized innovative injector concepts and issues related to performance enhancement resulting from gaseous hydrogen ($GH_2$) addition to RP-1/Oxygen propellants.

The Oxygen-Rich Rocket Combustor Technology project was oriented to supporting NASA's plan to develop advanced technologies for future single stage to orbit (SSTO) propulsion systems and specifically responded to Technical Area 3 (Oxygen Rich Turbine Drive) of NRA NRA8-11. The research work in this area was both experimental and analytical. The focus of the work was on understanding specific technical issues that needed to be resolved for developing oxygen-rich rocket preburners. The experiments concentrated on hot-fire uni-element tests to

**Table 1.3. Main Chamber and Preburner Injector Technology**

| **Program Element (After program realignment 11/95)** **TA-2 Bi-propellant, tri-propellant and gas/gas combustion** | **Current Status** | **Future Plans** |
|---|---|---|
| 1.1.1 Experimental Studies of Tri-Propellants | in progress | refer to sub-elements |
| 1.1.1.1 Experimental Studies of Tri-Propellants Effects of $GH_2$ Addition to $GO_2$/RP-1 and LOX/RP-1 (Coaxial-Type Tri-propellant Injector) | in progress | **Defer studies of $GH_2$ addition to LOX/RP-1** |
| 1.1.1.2 Experimental Studies of Tri-Propellants Cold Flow Studies (Coaxial-Type Tri-propellant Injector) | in progress | continue |
| 1.1.1.3 Experimental Studies of Tri-Propellants Effervescent Atomization Studies for $GO_2$/RP-1/$GH_2$ (Hot-Fire and Cold Flow Studies) | in progress | continue on limited basis |
| 1.1.2 Experimental Studies of Mode Transition from $GO_2$/RP-1/$GH_2$ to $GO_2$/$GH_2$ Combustion | in design phase | **Defer** |
| 1.1.3 Experimental Studies of RP-1 Drop Combustion in $GO_2$ and $GO_2$/$GH_2$ | complete | N/A |
| 1.1.4 Common Cold Flow Manifold Experiments to Understand Effects of $LH_2$ on RP-1 During Fuel Transition | in progress | **Defer** |
| 1.1.5 Bi-propellant studies of LOX/$GH_2$ at sub-critical and super-critical conditions | **New task** | |
| 1.1.6 Fuel rich preburner combustion and injector technology | **New Task** | |
| 1.1.7 Advanced gas/gas injector technology | **New Task** | |
| 2.1.1 Analytical Studies of Tri-Propellants - Hydrocarbon Combustion Processes | in progress | continue |
| 2.1.2 Analytical Studies of Tri-Propellants - Hydrogen/RP-1 Manifold Analysis | in progress | **Defer** |
| 2.1.3 Analytical studies of gas/gas injectors | **New Task** | |
| **Program Element (After program realignment 11/95)** **TA-3 Oxygen Rich Combustor Technology** | | |
| 1.1.1. High O/F Experimental Studies (LOX/$GH_2$; Swirl Coaxial Injector) | in progress | continue |
| 1.1.2. High O/F Experimental Studies (LOX/RP-1; Pintle\Impinging Injector) | in progress | continue |
| 1.1.3 Determine flame stability, ignition characteristics, combustion efficiency and wall heating effects | in progress | continue |
| 2.1.1. High O/F Direct Injection Analytical Studies | in progress | continue |
| 2.1.2. Near-stoichiometric Core/Dilution Analysis | in progress | continue |
| 2.1.3. Assess validity and utility of analysis for CFD hardware applications | in progress | continue |

demonstrate concepts that could be rapidly incorporated into hardware design and development. The analysis was CFD-based and supported the design and interpretation of the experiments.

In response to NASA MSFC's request in late 1995, these two independent programs were consolidated and realigned under a unified title of Main Chamber and Preburner Injector Technology to focus more specifically on the goals of the Reusable Launch Vehicle (RLV) Long Term/High Payoff Technology Program. Specifically, this realignment incorporated the need for research advancements in the following three areas:

**A.** main chamber technology for bi-propellant propulsion systems.

**B.** fuel-rich preburner combustion and injector technology.

**C.** gas/gas injector technology in support of engine development by industry.

This realignment procedure involved deferring certain task items in favor of new task items. To align the reader with this realignment, the original tasks for Advanced Propulsion Technologies for Tri-propellant Combustion and Oxygen-Rich Rocket Combustor Technology are summarized in Tables 1.1 and 1.2, respectively, whereas the tasks for the realigned and unified Main Chamber and Preburner Injector Technology are presented in Table 3. Note that in each table the status and future plans (i.e. after realignment) are also included.

With this brief description of the programmatic evolution for this project, this report presents the results of the experimental and analytical efforts in Chapters II and III, respectively for the multitude of tasks investigated under this program.

# II. EXPERIMENTAL STUDIES

## 2.1. INTRODUCTION

The experimental phase of the Main Chamber and Preburner Injector Technology program is discussed in this chapter. This chapter is sub-divided into eight distinct sections that address the various tasks listed in Table 1.3. This lead section provides an introduction to the organization of this chapter. Section 2.2 provides a description of the Cryogenic Combustion Laboratory (CCL) where the majority of the experiments described in this chapter were conducted, and an introduction to the workhorse modular uni-element optically-accessible rocket chamber that was utilized for a significant portion of the experiments. Sections 2.3 and 2.4 discuss the single RP-1 drop combustion and RP-1/$GH_2$/$GO_2$ tri-propellant experiments, respectively. For the tri-propellant experiments discussed in Section 2.4, cold flow characterization and hot-fire results are presented for two injector concepts. These two sections address tasks 1.1.1 and 1.1.3 of program element TA-2 Bi-propellant, tri-propellant and gas/gas combustion as indicated in Table 1.3. Note that tasks 1.1.2 and 1.1.4 of the same program element were deferred during the reorganization of the project. Experiments for bi-propellant studies of LOX/$GH_2$ at near-stoichiometric conditions are discussed in Section 2.5 and address task 1.1.5 of program element TA-2. Experiments in support of advancing oxidizer-rich combustion for preburner application are discussed in Section 2.6 and tasks 1.1.1-1.1.3 of program element TA-3 Oxygen Rich Combustor Technology. This section includes oxidizer-rich experimental research for both $GO_2$/RP-1 and $GO_2$/$GH_2$ propellant combinations. Results for both direct injection and stoichiometric core/downstream dilution approaches are presented. Complementary to this effort, Section 2.7 presents results and discussion for fuel-rich preburner applications in support of Task 1.1.6 of program element TA-2. Finally, experimental research for Task 1.1.7 of program element TA-2 in the area of advanced gas/gas injector technology for main chamber application is discussed in Section 2.8.

## 2.2. EXPERIMENTAL FACILITY

All rocket chamber combustion experiments were carried out at Penn State's Cryogenic Combustion Laboratory (CCL). This laboratory was established in 1989 to be the flagship facility for Penn State's Propulsion Engineering Research Center (PERC). In this section, the capabilities of the CCL are discussed first. This is followed by a description of the optically-accessible rocket chamber that was used for the uni-element rocket flowfield characterization experiments.

### 2.2.1. CRYOGENIC COMBUSTION LABORATORY

The CCL is a unique university facility where researchers conduct work on representative rocket engine flowfields. The laboratory is designed based on a similar test cell at NASA Lewis Research Center. The CCL, a remotely controlled laboratory, features a control room, diagnostic room and the test cell. The test cell, where the combustion experiment is housed, is isolated from the control and diagnostic rooms with reinforced concrete walls. For experimentation, the test cell's garage door is fully opened and the ventilation turned on to prevent the possible buildup of combustible materials. The diagnostic room located adjacent to the test cell is utilized for situating all the laser-based diagnostics. Optical ports between the diagnostics room and the test cell provide access into the test cell. The control room houses the computer control system that is used for timing the rocket firing. Video cameras with pan features enable remote visualizations of the test room. The operation of the entire system is designed with two levels of safety.

The CCL was initially operable for gaseous oxygen/hydrogen propellants. Liquid oxygen capability was initiated within a year of the laboratory's operation. Liquid hydrocarbon capability was brought on-line three years later. Finally airflow capability was brought on-line in early 1997. The propellant flowrate capabilities are tabulated Table 2.2.1.

### 2.2.2. OPTICALLY-ACCESSIBLE ROCKET CHAMBER

The injector flowfield characterization experiments reported here were conducted using the optically accessible rocket chamber at Penn State's Cryogenic Combustion Laboratory. The rocket chamber was designed in a modular fashion to easily provide optical access along the chamber length. A cross-sectional view of the rocket assembly is shown Fig. 2.2.1. The rocket chamber is comprised of several sections that include an injector assembly, igniter, window and blank

**Table 2.2.1. Flowrate Capabilities of Cryogenic Combustion Laboratory**

| Propellant | Maximum Flowrate (lbm/s) |
|---|---|
| Gaseous Oxygen ($GO_2$) | 1 |
| Gaseous Hydrogen ($GH_2$) | 0.25 |
| Liquid Oxygen (LOX) | 1 |
| Liquid Hydrocarbon | 0.5 |
| Air | 4 (can be upgraded to 16) |

sections, and a nozzle assembly. These sections are held together by a hydraulic jack which allows for ease of assembly and arrangement of the various sections. The chamber length is varied by inserting or removing blank sections.

The modular design of the rocket chamber allows the testing of various injector geometries/propellant combinations up to a maximum chamber pressure of approximately 1000 psia. The injector assembly shown in Fig. 2.2.1 is for the shear coaxial element. However, the injector assembly can be easily configured to test various injector geometries. To date, shear coaxial, swirl coaxial, impinging jet, pintle, effervescent and triaxial injector elements have been tested in this chamber.

The igniter section of the rocket chamber consists of an ignition chamber (assembly shown on top of rocket chamber in Fig. 2.2.1) which utilizes a spark-ignited gaseous hydrogen/oxygen mixture to provide an ignition torch in the main combustion chamber. The window-section allows optical access into the combustion chamber for laser-based diagnostic techniques. As illustrated in Fig. 2.2.1, this section can be placed anywhere along the chamber length by interchanging it with other sections. Two diametrically opposed windows, 2 in. in diameter and 1 in. thick, provide optical access into the 2 in. square rocket chamber. Two slot windows measuring 0.25 x 2 in. on the remaining two sides provide additional optical access into the rocket chamber for laser sheet diagnostics. All windows are protected from the hot combustion gases by a gaseous nitrogen ($GN_2$) curtain purge which flows across each of the interior window surfaces. Lastly, the water-cooled nozzle assembly is also modular in design. Nozzles of different throat diameters can be interchanged, thus providing the capability for varying the chamber pressure for the same propellant flow rate.

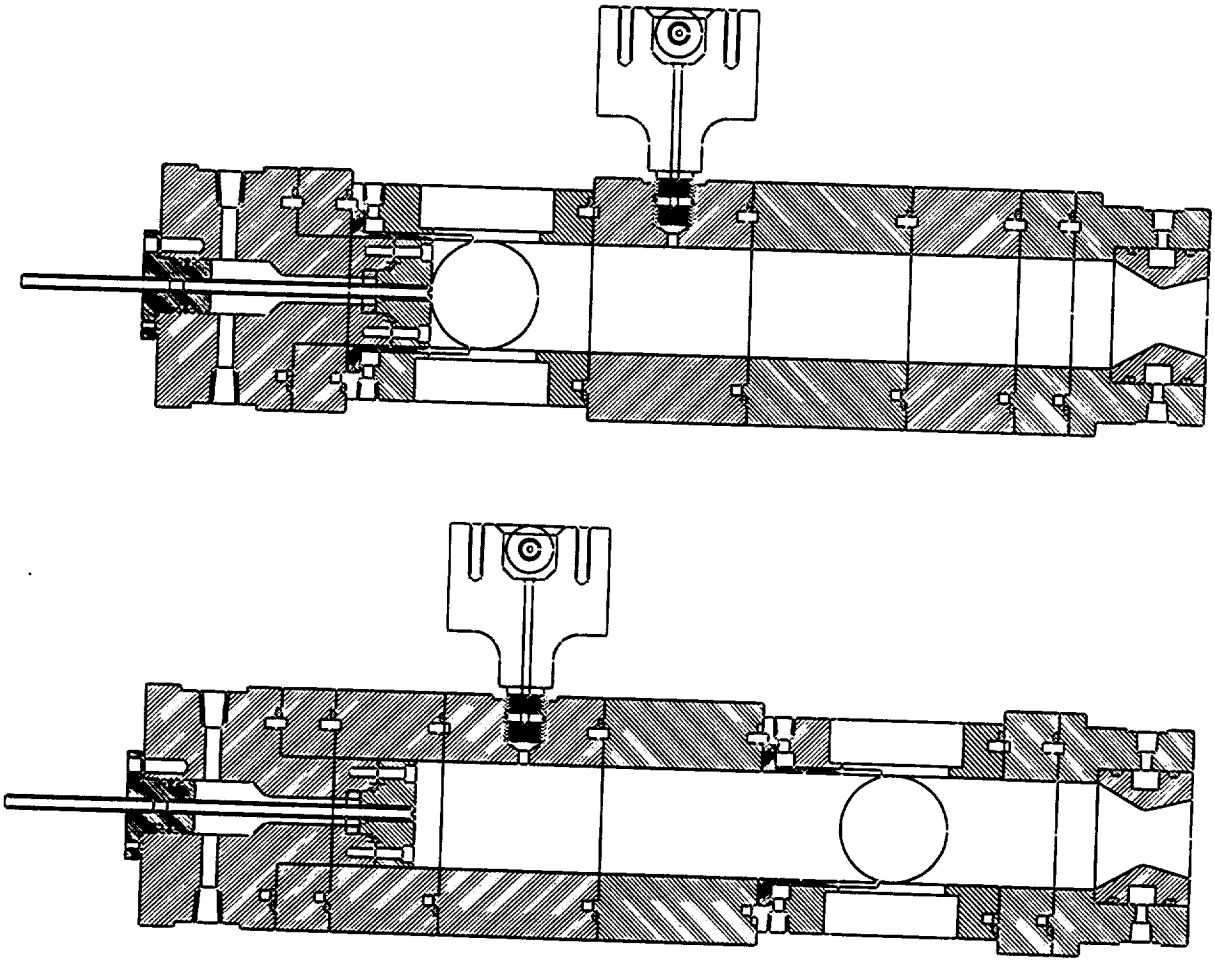

**Fig. 2.2.1. Schematic of the optically-accessible rocket chamber. The chamber is designed such that optical access can be gained for any axial location by interchanging sections. Two configurations illustrating this feature are shown in the figure.**

The time duration of a rocket test firing is typically set between two to four seconds depending on the target propellant flowrate, mixture ratio and chamber pressure. This run time represents a compromise between quartz window/chamber wall survivability and the time required for steady-state chamber pressure to be reached.

## 2.3. RP-1 DROP COMBUSTION STUDIES

The RP-1/$O_2$ propellant combination has historically been considered for rocket propulsion due to the vehicle weight benefits derived from the use of high density RP-1 fuel. An inspection of the twenty-two U.S. engine designs summarized in NASA's Liquid Rocket Engine Injectors handbook [1] indicates that eight of these employed the RP-1/$O_2$ propellant combination. However, the design of RP-1/$O_2$ rocket engines has been plagued with combustion instability and heat transfer issues [2], and hence the choice of $H_2/O_2$ propellants for the SSME. The combustion characteristics of RP-1/$O_2$ propellants can be significantly improved by the addition of a small amount of $H_2$ [3-7]. Hydrogen addition to RP-1/$O_2$ combustion has been experimentally observed to increase combustion efficiency and improve combustion stability, and also provides the possibility of alleviating chamber heat transfer issues through regenerative $H_2$ cooling [3-7]. Although these researchers have reported improved combustion efficiencies with the addition of $H_2$ to RP-1/$O_2$ combustion, the physical mechanism(s) for the increase in combustion efficiency is/are not understood.

The increased efficiency noted for some experimental configurations using tripropellant combustion [3-7] can not be easily attributed to a single effect because of the inter-related processes of RP-1 atomization, inter-propellant mixing, RP-1 vaporization and/or chemical kinetics, and combustion. In fact, earlier work [3-7] showed that for some injector geometric configurations, efficiency was noted to decrease with addition of $H_2$. To isolate the various mechanisms, two sets of experiments were conducted under this contract. The first set of experiments involved characterizing single RP-1 drop combustion in a pure oxygen environment and in a $H_2/O_2$ flame. For these controlled experiments, the RP-1 drop regression rates in both environments were measured and contrasted. In this section, the results of these single drop experiments are presented and discussed. These initial single drop combustion experiments were followed by uni-element combustion experiments in an optically-accessible rocket chamber. Two injector configurations, a coaxial-type tripropellant element and an effervescent injector, were chosen for injecting the tripropellants into the rocket chamber. For both these elements, the gaseous hydrogen ($GH_2$) is injected "intimately" with the RP-1/gaseous oxygen ($GO_2$) propellants. These experiments are results are discussed in the next section.

### 2.3.1. SINGLE DROP EXPERIMENTAL SETUP

The atmospheric pressure single drop experiments were conducted using four setups as shown in Figs. 2.3.1-2.3.4. The various setups were necessitated to circumvent problems associated with increasing the complexity of the experiment. In Experimental Setup #1 (Fig. 2.3.1), a piezoelectric generator (which was fed liquid fuel from a plastic syringe) formed the single fuel drops, whereas a small methane flame was used to ignite the drops. This setup was used with dodecane ($C_{12}H_{26}$) fuel with a boiling point similar to that of RP-1, to test the drop generator and to provide a basis for comparison with RP-1 drop results. For this setup, the environment surrounding the drop was pure oxygen kept at room temperature. When RP-1 was utilized using this setup, the measurements were not consistently reproducible. The problem was attributed to the piezo-electric drop generator. To eliminate this problem, an aerodynamic drop generator, as shown in Fig. 2.3.2 was used in place of the piezoelectric device. For this configuration, the aerodynamic generator used oxygen flowing through an outer quartz tube to strip an incompletely formed suspended drop from the tip of a small exposed wire. The oxygen flowing through the outer tube cooled the fuel enough to prevent early evaporation of the lighter components. This improved setup allowed the study of RP-1 drops burning in pure oxygen at room temperature. But in order to determine the effect of hydrogen on the drop burning rate, the setup was again altered to allow safe addition of hydrogen to the system. The result was Experimental Setup #3, Fig. 2.3.3, in which a co-flowing hydrogen/oxygen flame was used to ignite the RP-1 drop. In addition to acting as an ignition stimulus for the RP-1 fuel, the $H_2/O_2$ flame created a hot post-combustion zone surrounding the drop. Experimental Setup #3 proved to be a good way to add hydrogen safely to the system. Unfortunately, once hydrogen and oxygen burned, there was little control over the environment surrounding the drop. Therefore, the setup was again altered to using a flashback-resistant burner, Fig. 2.3.4, to form the post-combustion zone in which the drop burned. In this case, a methane/oxygen/nitrogen flame was used to create an ambient environment that consisted of a mixture of oxygen, nitrogen, carbon dioxide, and water vapor. Experiments were performed with excess oxygen concentrations between 24 and 52% by volume. Note that for Experimental Setup #4, hydrogen was not used as the gaseous fuel for the flame because the large amounts of water formed with this reaction blocked the holes of the burner. Brief descriptions of all four setups are presented next.

### 2.3.1.1. Experimental Setup #1

A schematic of the burner configuration for Experimental Setup #1 is shown in Fig. 2.3.1. The setup included a piezoelectric drop generator, a burner (consisting of a methane ignitor and oxygen injection plate), a glass chimney, and two translation stages which were used to position the experimental setup relative to a camera and data acquisition system to be discussed later.

The piezoelectric generator was used to form the single fuel drops. It consisted of a fuel reservoir, a piezoelectric transducer, and a plastic fuel feed line connected to a 20 ml syringe (not shown in the figure). This generator was placed on top of a mount incorporating translating stages for adjusting the position of the device during operation without disrupting other components of the setup.

Once the drop size, velocity, and spacing appeared steady, the drop generator and mount were fixed to the top of the burner. The burner consisted of two aluminum plates, each with a diameter and thickness of 5 in. and 1 in., respectively. Oxygen was introduced into the system

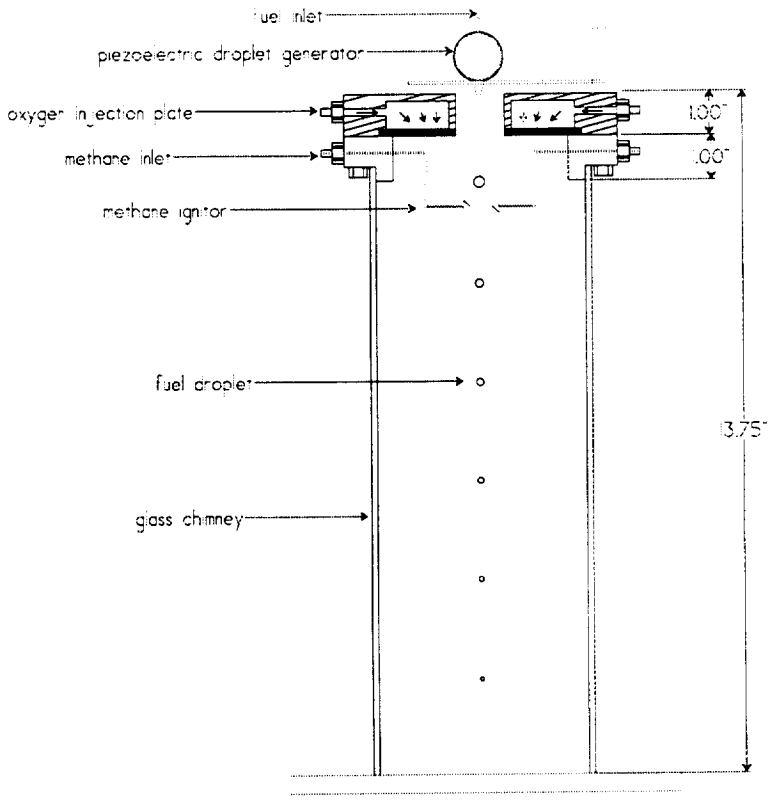


**Fig. 2.3.1. Schematic of experimental setup #1.**

through the top plate. Two inlet holes, located on opposite sides of the plate, led to a small cavity closed off with a square porous brass plate (with dimensions $2.7 \times 2.7 \times 0.25$ in.). This brass plate straightened the oxygen flow prior to its entrance into the chimney. Both the oxygen and brass plates were equipped with 2.54 cm (1 in) center holes to provide ample room for the drop to pass from the generator to the chimney. The burner's second plate held the small methane ignitor. Similar to the oxygen plate, methane was introduced into the system through two inlet holes located on opposite sides of the plate.

### 2.3.1.2. Experimental Setup #2

The second experimental setup was very similar to the first. The only difference was that an aerodynamic drop generator was used instead of a piezoelectric device. The reason for this change was discussed earlier. A schematic of the aerodynamic drop generator [8] is shown in Fig. 2.3.2. This device consisted of a series of telescoped tubing whose final capillary had an outer diameter of 0.01 in. and an inner diameter of 0.005 in. A 0.0035 in. wire was inserted into

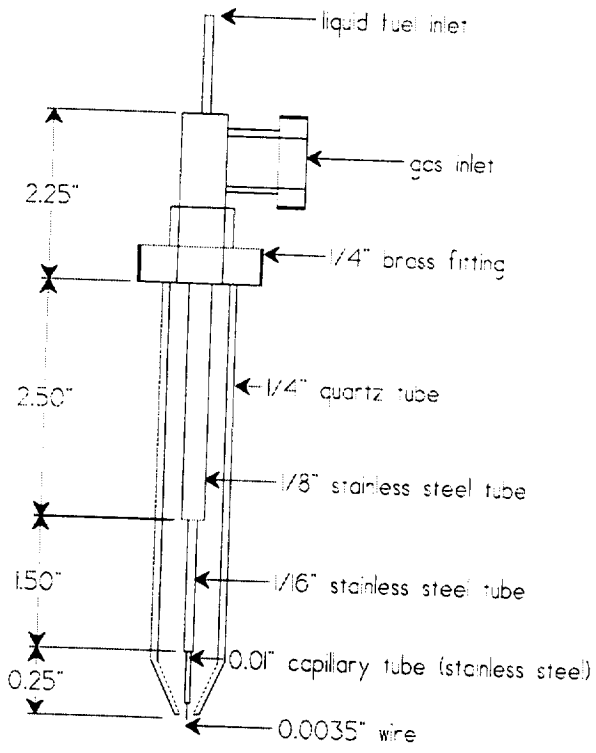


**Fig. 2.3.2. Schematic of the aerodynamic drop generator.**

the final tube. Between 1/16 in. and 1/32 in. of this wire was left exposed from the capillary tube. A 1/4 in. quartz tube was then placed over the telescoped tubing such that the tip of the wire was exposed. A small hole, 0.03 in. in diameter, was bored into the tip of the quartz tube to allow room for the 0.0035 in. wire. This drop generator used gas flowing through the outer quartz tube (which in this experimental setup was oxygen) to strip an incompletely formed drop from the tip of the small exposed wire. With this setup, drops of about 250 μm were generated.

### 2.3.1.3. Experimental Setup #3

The third experimental setup, Fig. 2.3.3, used a co-flowing hydrogen/oxygen flame to ignite the drop. In this case, the aerodynamic generator was mounted to the bottom support plate such that the drop trajectory was upwards instead of downwards (as in the previous two setups). The oxygen plate was also inverted and attached to the bottom support plate with four small aluminum posts. The glass chimney was then placed on top of the oxygen plate. A copper screen was placed on the glass chimney to help stabilize the $H_2/O_2$ flame. Since this flame was

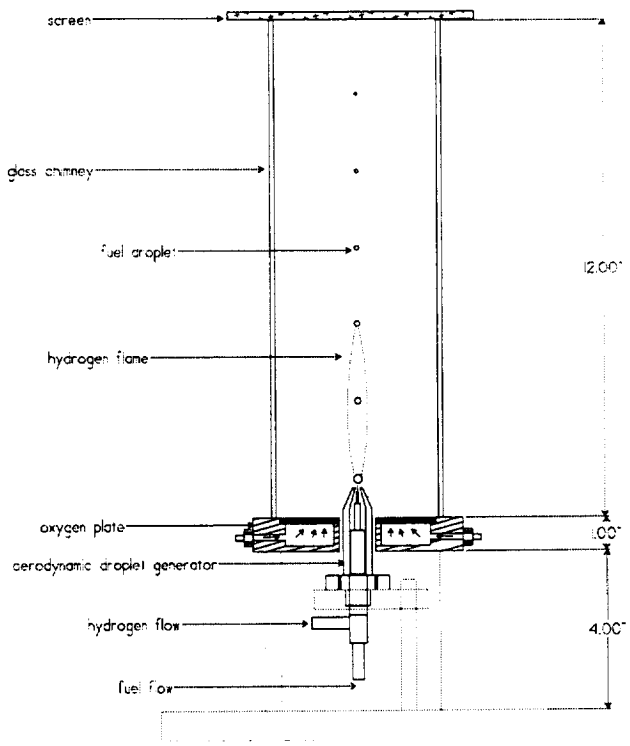


**Fig. 2.3.3. Schematic of experimental setup #3 with co-flowing hydrogen/oxygen flame.**

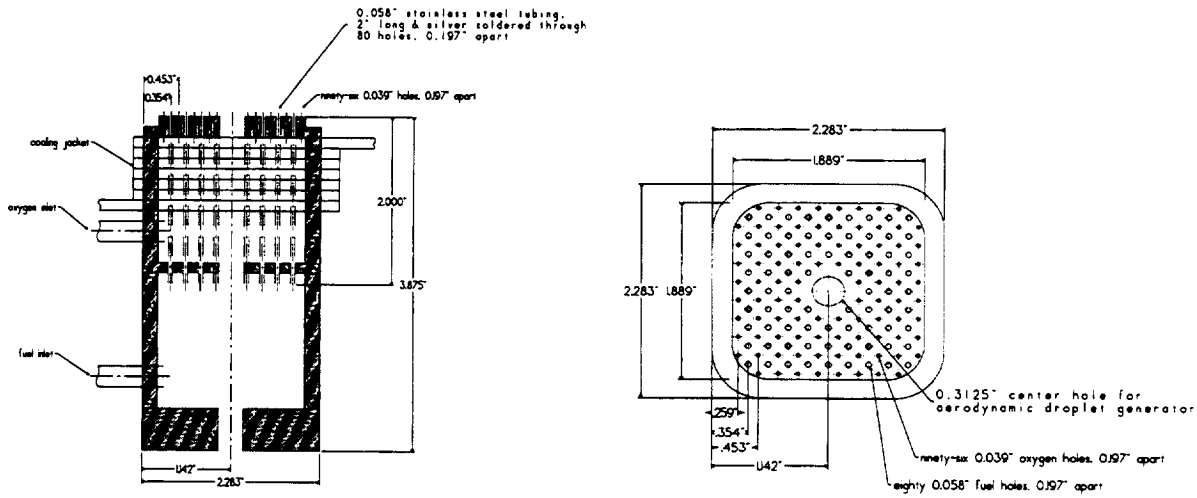


(a) (b)

**Fig. 2.3.4. (a) Cutaway view of the flashback-resistant burner used in Experimental Setup #4 and (b) top view showing the fuel and oxidizer grid pattern.**

used to ignite the drop, the second stage of the burner, which introduced methane into the system for Setups #1 and #2, was not necessary.

### 2.3.1.4. Experimental Setup #4

The fourth experimental setup used a flashback-resistant burner to create the post combustion zone in which the drop burned. The burner used was modeled after a Krupa style burner for analytical spectrometry purposes. A cross section of the burner can be seen in Fig. 2.3.4.

This brass burner consisted of two stages. The oxidizer entered the burner through the top stage via a ¼ in. port. The oxidizer then exited the burner through ninety-six 0.039 in. diameter holes 0.197 in. apart. The gaseous fuel entered the burner through the bottom stage. It exited the top surface through eighty stainless steel capillary tubes. Each had an outer diameter of 0.058 in., an inner diameter of 0.042 in., and a length of 2 in. The tubes were silver soldered between the top and bottom stages to prevent mixing of the gaseous oxidizer and fuel prior to burning. A 0.3125 in. brass tube was silver soldered through the center of the burner (from the top to the bottom surfaces) to allow access for the aerodynamic drop generator.

### 2.3.1.5. Drop Size/Velocity Measurement Technique

For all four experimental setups, the same photographic technique was utilized for measuring the drop size and velocity as a function of axial distance from the drop generator. The employed technique used a CID camera and a strobe light (delayed for double pulsing) to image a given drop at a fixed time separation. The size of the drop was measured from the image and the spacing/time provided the drop velocity.

In Experimental Setup #1, a pulse Generator was used to trigger the entire data acquisition system. The pulse generator also controlled the piezoelectric drop generator. By adjusting the pulse delay and width, the spacing between consecutive drops was established. The size and velocity of the drops were established by adjusting the amplitude settings on the generator. A second pulse generator controlled the delay of the strobe light. The CID camera was equipped with a 2X Macro Focusing Teleconverter, bellows and a 70 mm lens. The lenses and bellows magnified the size of the drop by about 100X. Since there were no electrical connections to the aerodynamic generator used in Setups #2 through #4, it was impossible to synchronize the generator with the strobe light, computer, and camera. To remedy this problem, a laser pointer and a photodiode were added to the triggering system. These two devices were mounted on top of the burner in Experimental Setup #2 (on opposite sides of the glass chimney in Experimental Setups #3 and #4) across from one another such that as the drop was stripped from the small wire, it crossed the laser pointer's beam path. This interference was then picked up by the photodiode and a signal was sent through a pre-amplifier. This pre-amp was connected to the pulse generator which then triggered the remaining components of the data acquisition system (the computer, camera, and strobe light).

Images of the drops were taken at every 0.25 in. along the drop's trajectory until 1) the trajectory become too unsteady to take clear images, or 2) the drop become too small to take clear images without adjusting the camera lens. The velocity of each drop was found at 0.25 in. intervals along the glass chimney. The double pulsing of the strobe light yielded two images of the same drop. The measured separation distance was then used to evaluate the local drop velocity.

## 2.3.2. RP-1 DROP COMBUSTION RESULTS

The results obtained for each experimental setup are first described individually and then discussed globally in terms of conclusions.

### 2.3.2.1. Single Drop Measurements From Experimental Setup#1

For experimental setup #1, a piezoelectric generator was used to form individual dodecane ($C_{12}H_{26}$) drops. A small methane flame was used to ignite the drops that subsequently burned in a pure oxygen environment as described earlier. Using the photographic technique described earlier, the burning rate for individual dodecane drops was measured. The $D^2$ versus time plot for dodecane burning in a 100% oxygen environment is shown in Fig. 2.3.5 (a). In the figure, the flat portion of the curve represents the transient drop heating process. This period takes up about 20% of the drop's lifetime. Once the drop reaches a steady temperature (slightly lower than its boiling point of 880 R), it burns at a steady rate. The burning rate found by first order linear regression of the curve after the drop heat up period, is found to be $2.852\times10^{-3}$ in.$^2$/s (1.84 mm$^2$/s). The corresponding velocity profile for dodecane drops burning in pure oxygen is shown in Fig. 2.3.5 (b). The results show that as the drop is heated, its velocity increases to the terminal velocity. At further times, both the drop diameter and velocity decrease.

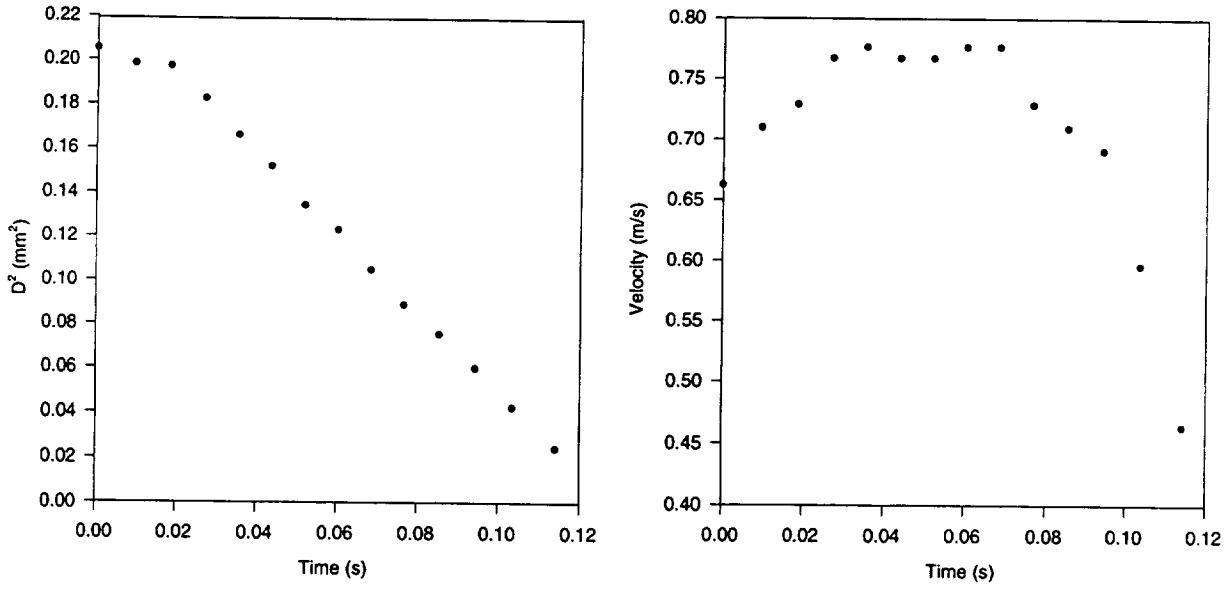


(a) (b)

**Fig. 2.3.5. (a) $D^2$ versus time plot and (b) evolution of drop velocity for dodecane burning in pure oxygen. $D_o$ = 0.0178 in. (453 μm), $V_o$ = 2.17 ft/s (0.66 m/s), and $\lambda_b = 2.852\times10^{-3}$ in.$^2$/s (1.84 mm$^2$/s). Please note that the graphs are in S.I. units.**

For these experiments involving dodecane drops, the initial drop diameter, $D_o$, and drop velocity, $V_o$, ranged from 0.0157 to 0.0197 in. (400 to 500 μm) and between 2.13 and 2.95 ft/s (0.65 and 0.90 m/s), respectively. For these experimental conditions, the measured burning rates ranged from a minimum of $2.852\times10^{-3}$ in.$^2$/s (1.84 mm$^2$/s) to a maximum of $3.023\times10^{-3}$ in.$^2$/s (1.95 mm$^2$/s).

### 2.3.2.2. Single Drop Measurements From Experimental Setup#2

When the fuel was switched from dodecane to RP-1 in the first experimental setup, the drop size, velocity and spacing were not consistently reproducible. There was also a 30% difference between the highest and lowest burning rate values for each run. To eliminate this problem, the piezoelectric drop generator was replaced by an aerodynamic drop generator. Experimental Setup #2 with the aforementioned change allowed the study of RP-1 drops burning in pure oxygen at room temperature. The $D^2$ versus time and velocity evolution plots for RP-1 drop burning are shown in Fig. 2.3.6 (a) and (b), respectively. The initial RP-1 drop diameter for these experiments was around 500 μm, whereas the average velocity was 4.27 ft/s (1.3 m/s). The burning rates, similar to those calculated from the dodecane results, varied less than 10%

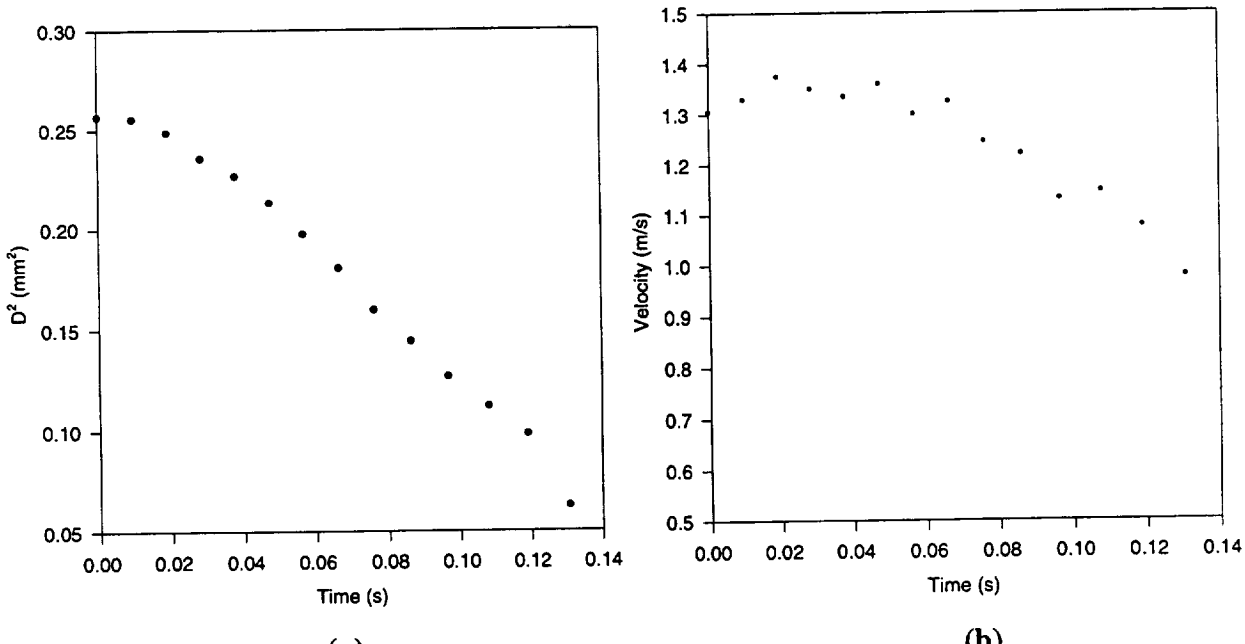


(a) (b)

**Fig. 2.3.6. (a) $D^2$ versus time plot and (b) evolution of drop velocity for RP-1 burning in pure oxygen. $D_o$ = 0.0199 in. (506 μm), $V_o$ = 4.30 ft/s (1.31 m/s), and $\lambda_b = 2.542\times10^{-3}$ in.$^2$/s (1.64 mm$^2$/s). Please note that the graphs are in S.I. units.**

and ranged from $2.387\times10^{-3}$ in.$^2$/s (1.54 mm$^2$/s) to $2.542\times10^{-3}$ in.$^2$/s (1.64 mm$^2$/s). These results were judged to be of sufficient reproducibility to serve as a baseline for RP-1 drop combustion.

The time history of an RP-1 drop as it combusts is shown in the series of images shown in Fig. 2.3.7. The dark circle is the image of the drop while the bright spot in the center of each image is a reflection from the strobe light.

Once the burning rate of RP-1 in a 100% oxygen environment was determined, inert gases were added to the system. The goal here were to determine the effects of adding a gas (helium) with a thermal conductivity similar to that of hydrogen on the burning rate of RP-1 drops. A secondary goal was to ascertain the effects of adding a gas with a different thermal conductivity than hydrogen or helium on the RP-1 burning rate. For these experiments, argon was chosen as the inert gas. These additions were made to the system in Experimental Setup #2.

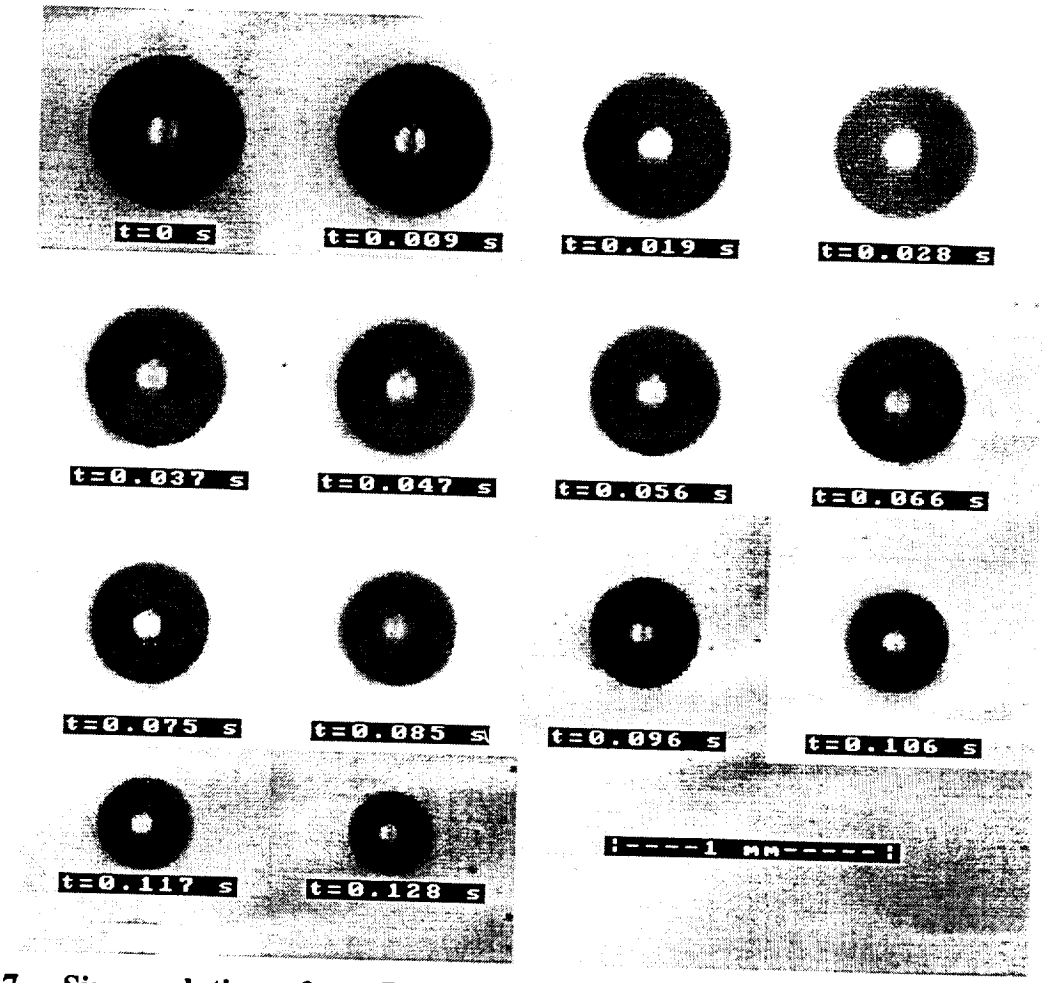


**Fig. 2.3.7. Size evolution of an RP-1 drop burning in 100% oxygen; $D_o$ = 0.0209 in. (530 μm), $V_o$ = 4.27 ft/s (1.3 m/s), and $\lambda_b = 2.433\times10^{-3}$ in.$^2$/s (1.57 mm$^2$/s).**

Helium was added to the system such that the environment surrounding the drop was 20% He/80% $O_2$ by volume. Results for this case are shown in Fig. 2.3.8. Although the second point of the $D^2$ versus time plot in Fig. 2.3.8 (a) does not fall directly on the curve, there is still a slight heat up period followed by steady state burning. A first order linear regression of the linear portion of this curve indicates a burning rate of $2.728\times10^{-3}$ in.$^2$/s (1.76 mm$^2$/s), which is higher than that for RP-1 burning in pure oxygen. This result was expected since helium increases the thermal diffusivity that in turn increases the heat transfer to the drop. When the helium volume percentage was increased to 40%, the RP-1 drop ceased to burn shortly after its ignition by the methane flame. The drop burning did not reach steady state before extinction of the flame, so no burning rate was measured for this case.

When the inert gas was argon instead of helium, (making the environment surrounding the drop 20% Ar/ 80% $O_2$ by volume), the burning rate decreased to 1.48 mm$^2$/s. The corresponding $D^2$ versus time and drop velocity profiles are shown in the two inset graphs of Fig. 2.3.9, respectively. For this case, the thermal diffusivity of the Ar/$O_2$ mixture was comparable to that in the 100% oxygen case. Thus, the effect of decreasing the oxygen concentration while maintaining the thermal diffusivity decreased the burning rate of the drop.

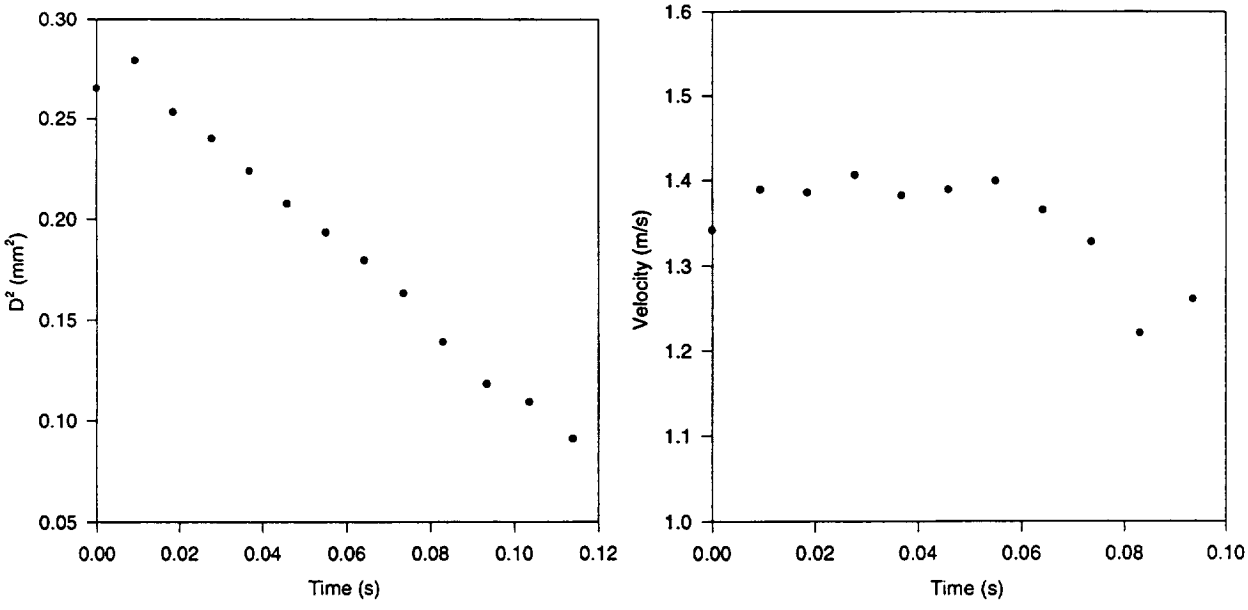


(a) (b)

**Fig. 2.3.8. (a) $D^2$ versus time plot and (b) evolution of drop velocity for RP-1 burning in 80% $O_2$/20% He environment. $D_o$ = 0.0203 in. (515 μm), $V_o$ = 4.40 ft/s (1.34 m/s), and $\lambda_b = 2.681\times10^{-3}$ in.$^2$/s (1.73 mm$^2$/s). Please note that the graphs are in S.I. units.**

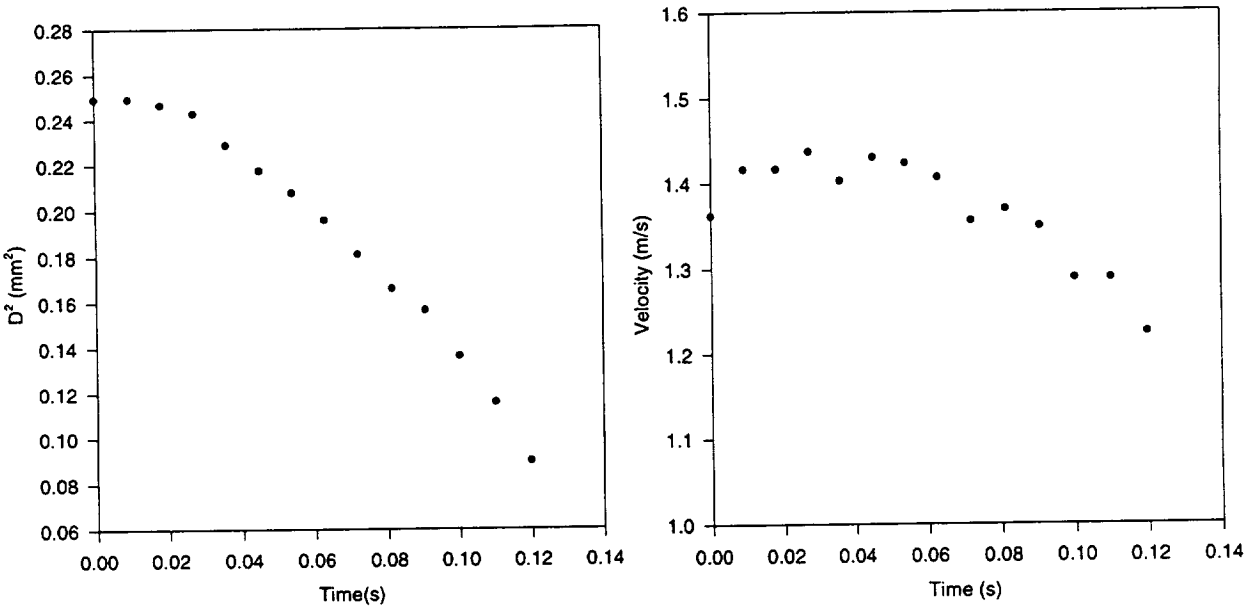


(a) (b)

**Fig. 2.3.9. (a) $D^2$ versus time plot and (b) evolution of drop velocity for RP-1 burning in 80% $O_2$/20% Ar environment. $D_o$ = 0.0196 in. (499 μm), $V_o$ = 4.46 ft/s (1.36 m/s), and $\lambda_b = 2.294 \times 10^{-3}$ in.$^2$/s (1.48 mm$^2$/s). Please note that the graphs are in S.I. units.**

As with helium, when the argon percentage was increased to 40%, it was not possible to keep the drop ignited before it reached steady state conditions. Thus, no burning rate was measured for this case.

### 2.3.2.3. Single Drop Measurements From Experimental Setup#3

Following the work done using Experimental Setup #2, the configuration was again modified to allow the safe addition of hydrogen to the system. This resulted in Experimental Setup #3 in which a co-flowing hydrogen/oxygen flame acted as an ignition source for the aerodynamic injector produced RP-1 drops. The $D^2$ versus time plot and velocity profile of RP-1 drops burning in the post combustion zone of this co-flowing flame are shown in the two graphs of Fig. 2.3.10. As can be seen from the figure, the initial drop velocity of 19.2 ft/s (5.85 m/s) was much higher than those described for the earlier studies. This was a due to the high volumetric flowrate of hydrogen used to strip the drop from the thin wire of the aerodynamic generator. This high flowrate led to high initial drop velocities, which in turn caused smaller drops to form. The initial drop diameters for this configuration were around 0.0096 in. (245 μm).

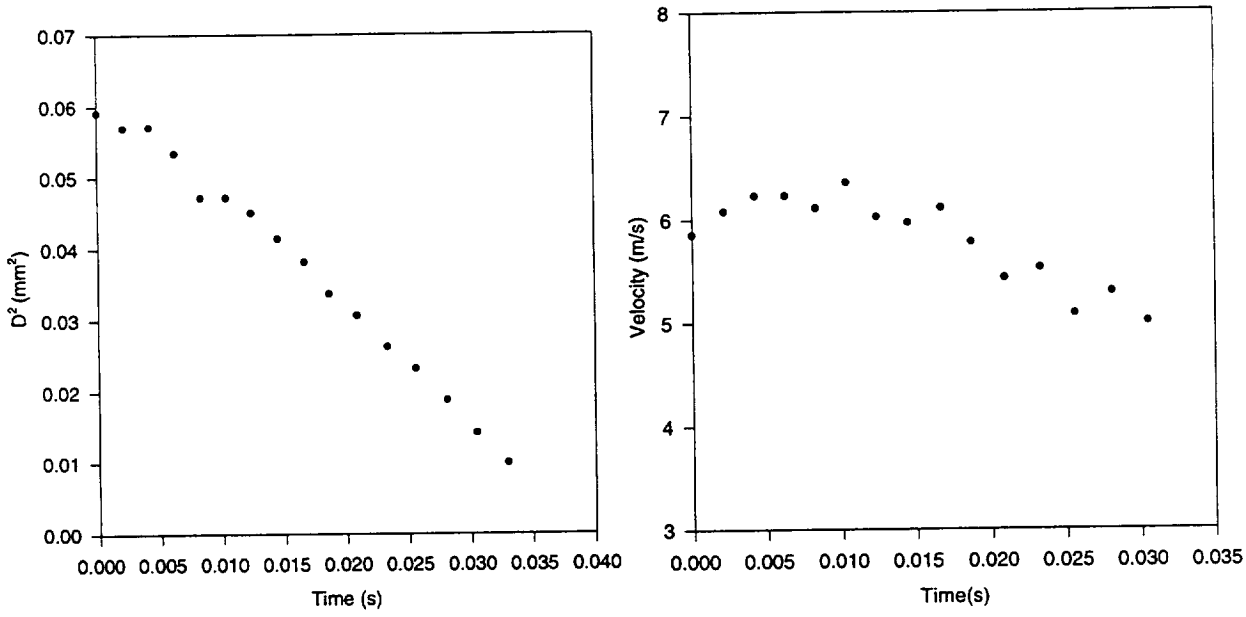


**Fig. 2.3.10. (a) $D^2$ versus time plot and (b) evolution of drop velocity for RP-1 burning in 83% $O_2$/17% $H_2O$ environment. $D_o$ = 0.0096 in. (245 μm), $V_o$ = 19.2 ft/s (5.85 m/s), and $\lambda_b = 2.573\times10^{-3}$ in.$^2$/s (1.66 mm$^2$/s). Please note that the graphs are in S.I. units.**

The flat portion of the curve in Fig. 2.3.10 (a) represents the drop heat up period. The unsteady behavior in the first portion of the plot can be attributed to the high initial drop velocities. The first images taken of the RP-1 drops showed that they were slightly elliptical when injected into the oxygen environment. This was caused by the large difference between the initial velocity of the drops and that of the surrounding gas. By taking the mean diameter of the drop in both the horizontal and vertical directions and averaging the two, a correction for the drop size was made. Note that this correction is crude and consequently could be the cause of the discrepancy in the initial portion of the curve. After the drop traveled about 1.5 in. (38 mm) away from the tip of the aerodynamic drop generator, the relative velocity between the drop and the hot surrounding environment became small. As a result, no correction was necessary after this axial (and therefore time) location. The curve in Fig. 2.3.10 (a) is relatively linear after this point. The corresponding drop velocity profile is not very smooth indicating small measurement errors at these high drop velocities. A first order linear regression of the latter portion of this curve was performed to obtain the burning rate of the RP-1 drop in this hydrogen/oxygen combustion region. The burning rate was found to be $2.573\times10^{-3}$ in.$^2$/s (1.66 mm$^2$/s), which is close to the values obtained for RP-1 drops burning in a pure oxygen environment.

### 2.3.2.4. Single Drop Measurements From Experimental Setup#4

Although Experimental Setup #3 was a good way to add hydrogen safely to the system, there was little control over the environment surrounding the drop once hydrogen and oxygen burned. Thus, the setup was again altered resulting in Experimental Setup #4. This setup used a flashback resistant burner to form the hot post-combustion zone in which the drops burned. For this case, a methane/oxygen/nitrogen flame was used to create the environment surrounding the drop. The post-combustion zone was a mixture of oxygen, nitrogen, carbon dioxide, and water vapor. The experimental conditions were such that the excess oxygen concentrations were between 24 and 52% by volume. The motivation behind these experiments was to complement the studies done on RP-1 drop burning in the co-flowing hydrogen/oxygen flame.

The $D^2$ versus time plots and velocity profiles from the experiments conducted with Experimental Setup #4 for a range of oxygen concentrations is shown in Figs. 2.3.11-2.3.14. The results show that the burning rate of RP-1 increased as the oxygen concentration increased. Complementary video images showed that as more oxygen was added to the system, the flame moved closer to the surface of the liquid fuel drops. This led to an increase in the thermal

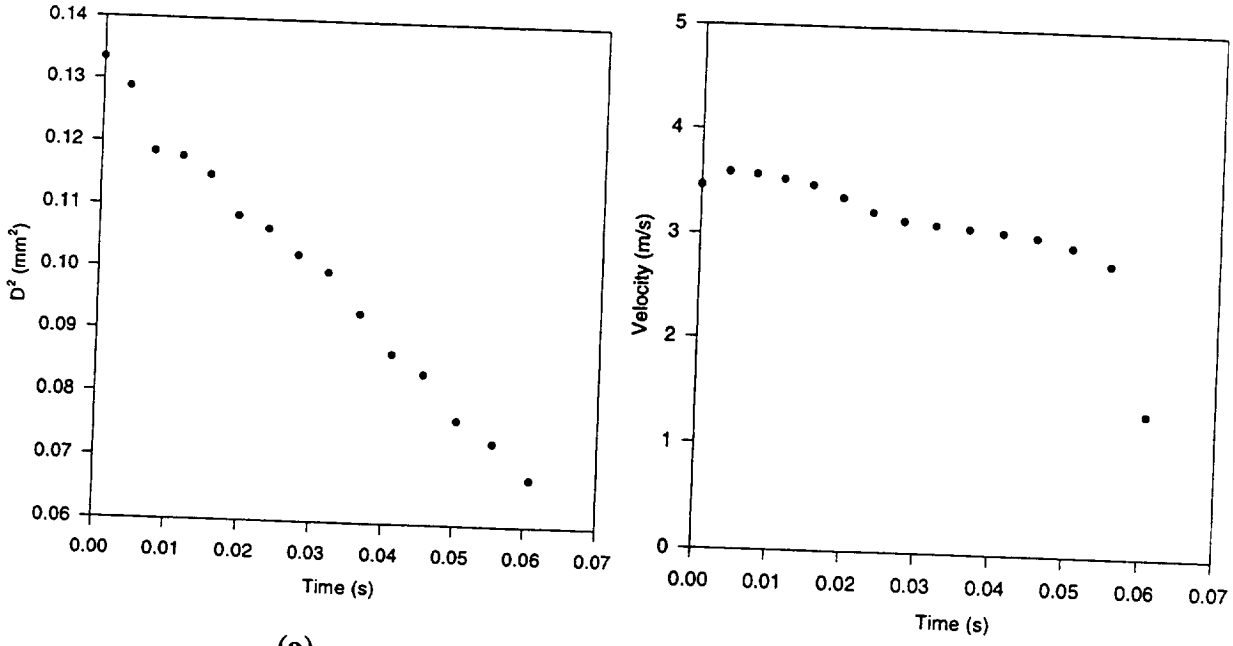


**Fig. 2.3.11. (a) $D^2$ versus time plot and (b) evolution of drop velocity for RP-1 burning in 24% $O_2$/ environment. $D_o$ = 0.0144 in. (365 μm), $V_o$ = 11.4 ft/s (3.46 m/s), and $\lambda_b = 1.628 \times 10^{-3}$ in.$^2$/s (1.05 mm$^2$/s). Please note that the graphs are in S.I. units.**

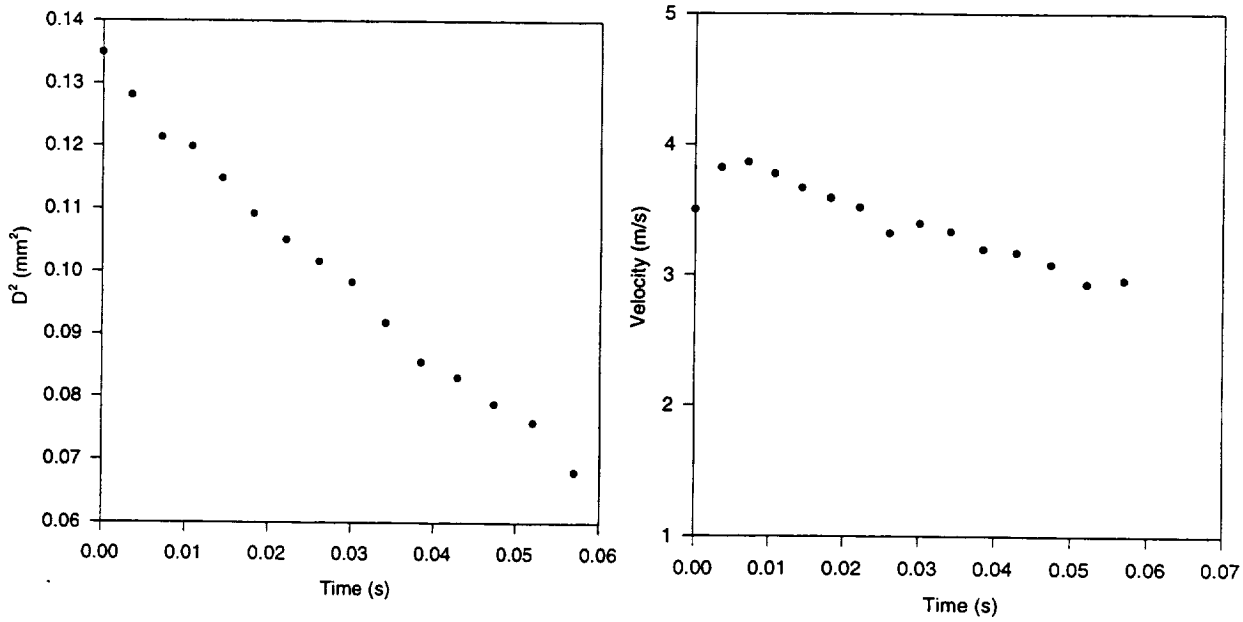


(a) (b)

**Fig. 2.3.12. (a) $D^2$ versus time plot and (b) evolution of drop velocity for RP-1 burning in 33% $O_2$/ environment. $D_o$ = 0.0144 in. (367 μm), $V_o$ = 11.7 ft/s (3.58 m/s), and $\lambda_b = 1.736 \times 10^{-3}$ in.$^2$/s (1.12 mm$^2$/s). Please note that the graphs are in S.I. units.**

conduction between the flame sheet and the drop surface, which in turn increased the RP-1 drop burning rate. Note that at low oxygen concentrations, the drop $D^2$ versus time plots appear more linear. In the 24 and 33% $O_2$ cases (see Figs. 2.3.11 and 2.3.12), there are several points on the curves that do not follow a linear profile (as if the burning rate of the drop changes during its lifetime or the drop has difficulty sustaining a flame). In initial tests using Experimental Setup #4, if the excess $O_2$ concentration was slightly less than 24%, extinction of the flame was visibly noted at different points along the drop's trajectory with subsequent re-light. In short, the environment surrounding the liquid fuel drop was hot enough to ignite the drop, but there was not enough oxygen surrounding it to ensure that combustion continued. A similar situation could have occurred in the 24 and 33 % oxygen cases. Even though flame extinction was not captured by the camera or seen with the naked eye, the drop could have had difficulty sustaining the flame. When the oxygen concentration was increased to 41%, the $D^2$ versus time curve shown in Fig. 2.3.13 (a) is relatively smooth. The same is true for the $D^2$ versus time plot for 52% oxygen case shown in Fig. 2.3.14 (a). Thus, in the final two sets of experiments, there was sufficient oxygen to sustain a stable flame surrounding the drop.

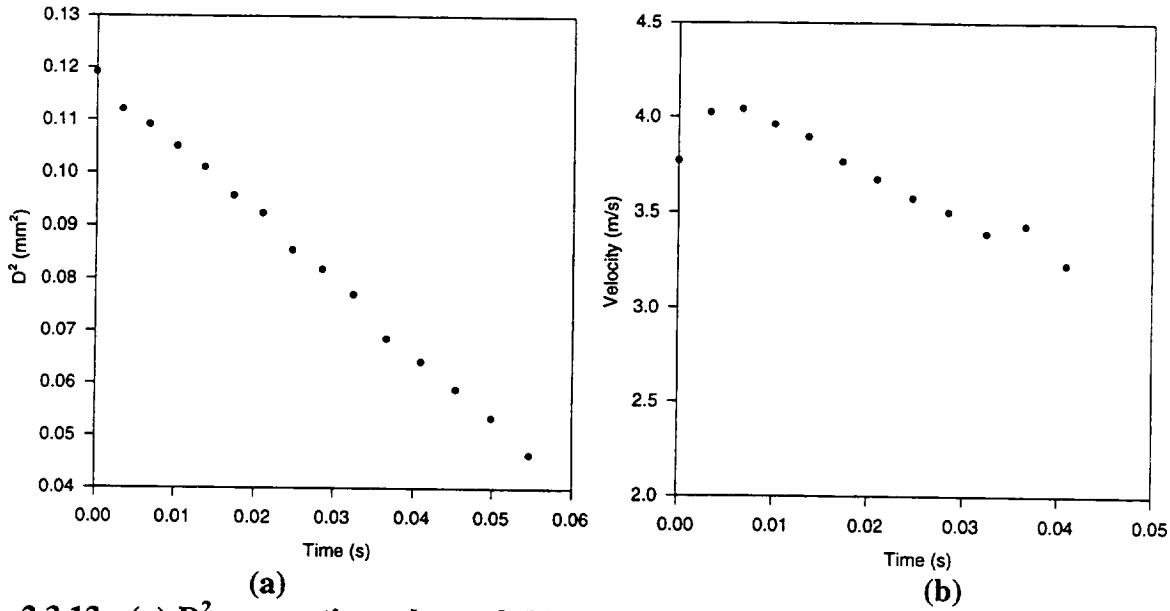


**Fig. 2.3.13. (a) $D^2$ versus time plot and (b) evolution of drop velocity for RP-1 burning in 41% $O_2$/ environment. $D_o$ = 0.0136 in. (345 μm), $V_o$ = 12.4 ft/s (3.78 m/s), and $\lambda_b = 2.062 \times 10^{-3}$ in.$^2$/s (1.33 mm$^2$/s). Please note that the graphs are in S.I. units.**

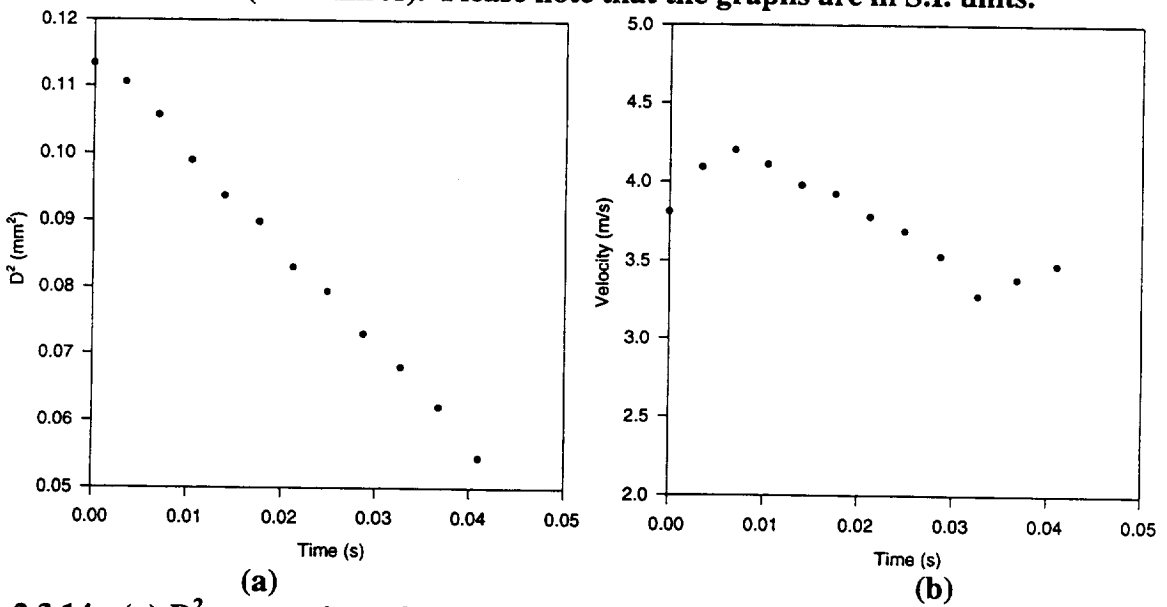


**Fig. 2.3.14. (a) $D^2$ versus time plot and (b) evolution of drop velocity for RP-1 burning in 52% $O_2$/ environment. $D_o$ = 0.0133 in. (337 μm), $V_o$ = 12.5 ft/s (3.81 m/s), and $\lambda_b = 2.232 \times 10^{-3}$ in.$^2$/s (1.44 mm$^2$/s). Please note that the graphs are in S.I. units.**

The drop velocity profiles, however, show an opposite trend. When the oxygen concentration was low (24 and 33% excess $O_2$), the velocity profile was smooth. When the concentration was increased (41 and 52% excess $O_2$), the profile becomes skewed. This observation could be due to changes in the buoyancy effects that the post-combustion zone gases have on the drop.

**Table 2.3.1. Summary of Single Drop Combustion Results.**

| Experimental Setup | Fuel | $D_o$, μm ($\times 10^{-3}$in.) | $V_o$, ft/s | $V_{gas}$, ft/s | $\lambda_b$, $mm^2/s$ ($\times 10^{-3}in.^2/s$) | Re | $\rho_{amb}$, $lbm/ft^3$ | $T_{amb}$, R |
|---|---|---|---|---|---|---|---|---|
| #1 100% $O_2$ | ($C_{12}H_{26}$) | 400 – 500 (15.8-19.7) | 2.13 – 3.12 | ≈0 | 1.84 - 1.95 (2.85 – 3.02) | 31 | 0.0892 | 535 |
| #2a 100% $O_2$ | RP-1 | 500 (19.7) | 4.27 | ≈0 | 1.54 - 1.64 (2.39 – 2.54) | 49 | 0.0892 | 535 |
| #2b 20% Ar/80% $O_2$ | RP-1 | 500 (19.7) | 4.43 | ≈0 | 1.48 (2.29) | 49 | 0.0936 | 535 |
| #2c 20% He/80% $O_2$ | RP-1 | 510 (20.1) | 4.43 | ≈0 | 1.73 (2.68) | 43 | 0.0736 | 535 |
| #3 17% $H_2$/83% $O_2$ | RP-1 | 245 (9.65) | 19.2 | 19.7 | 1.66 (2.57) | 3.10 | 0.0159 | 2700 |
| #4 a 24% $O_2$ 45% $N_2$ 10% $CO_2$ 21% $H_2O$ | RP-1 | 365 (14.4) | 11.1 | 10.7 | 1.03 (1.60) | 0.45 | 0.020 | 1990 |
| #4b 33% $O_2$ 36% $N_2$ 10% $CO_2$ 21% $H_2O$ | RP-1 | 367 (14.4) | 11.8 | 11.2 | 1.14 (1.77) | 0.70 | 0.0212 | 1975 |
| #4c 41% $O_2$ 26% $N_2$ 11% $CO_2$ 22% $H_2O$ | RP-1 | 345 (13.6) | 12.4 | 12.1 | 1.33 (2.06) | 1.30 | 0.020 | 1980 |
| #4d 52% $O_2$ 15% $N_2$ 11% $CO_2$ 22% $H_2O$ d | RP-1 | 336 (13.2) | 12.0 | 17.2 | 1.47 (2.28) | 3.00 | 0.0225 | 1825 |

As the oxygen concentration is increased, the adiabatic flame temperature of the methane/oxygen/nitrogen reaction increases. This temperature increase may adversely affect the velocity of the gases surrounding the drop leading to a non-uniform velocity profile at higher oxygen concentrations. In any case, neither the difficulty in sustaining the flame surrounding the drop nor the changes in the velocity profile had any effect on the burning rate of the RP-1 drop in this environment.

### 2.3.2.5. Summary for Single RP-1 Drop Measurements

The results presented in the preceeding three sections are summarized in Table 2.3.1. This work shows that a decrease in ambient oxygen concentration leads to a decrease in the burning rate of RP-1 drops if the thermal diffusivity is unaffected (as was the case with the 20% argon addition). But if the thermal diffusivity is increased throughout the system then RP-1 drop

burning is enhanced and the burning rate increases (as was seen when helium was added to the surrounding environment).

Unfortunately, the explosive nature of premixed hydrogen and oxygen did not allow a quantitative study of a burning RP-1 drop in such an environment. However, the work done with a co-flowing hydrogen/oxygen flame does show that increasing the ambient temperature surrounding the drop has little effect on the burning rate of RP-1. The final experiments, which involved changing the oxygen concentration surrounding the droplet, show that an increase in $O_2$ concentration in the ambient environment causes the flame to move closer to the liquid fuel drop surface. This, in turn, increases the thermal conduction between the drop and the flame, causing the burning rate to increase as well.

Based on the results of the current single drop combustion studies, improvements in combustion performance and stability observed with the addition of hydrogen are not due to the effects related to altercation of the individual drop combustion process.

## 2.4. EXPERIMENTAL STUDIES OF TRI-PROPELLANTS

The RP-1/$O_2$ propellant combination has historically been considered for rocket propulsion due to the vehicle weight benefits derived from the use of high density RP-1 fuel. However, the design of RP-1/$O_2$ rocket engines has been plagued with combustion instability and heat transfer issues [2]. The combustion characteristics of RP-1/$O_2$ propellants can be significantly improved by the addition of a small amount of hydrogen [3-7]. Hydrogen addition to RP-1/$O_2$ combustion has been experimentally observed to increase combustion efficiency, and also provides the possibility of alleviating chamber heat transfer issues through regenerative $H_2$ cooling [3-7]. In the United States, tri-propellant combustion (RP-1/$O_2$/$H_2$) for rocket propulsion has been proposed from the early eighties [9] and continues to receive attention as a viable propulsive concept [10-11].

Although both Russian and Japanese researchers [3-6] have reported improved combustion efficiencies with the addition of $H_2$ to RP-1/$O_2$ combustion, the physical mechanism(s) for the increase in combustion efficiency is/are not understood. Furthermore, before tri-propellant combustion can be considered for application, a mature data base is necessary. The goal of the work reported in this section was to provide a tri-propellant combustion data base for understanding the physical mechanism(s) responsible for improvements in performance and stability due to the addition of $H_2$.

The increased efficiency noted for some experimental configurations using tri-propellant combustion [3-7] can not be easilt attributed to a single effect because of the inter-related processes of RP-1 atomization, inter-propellant mixing, RP-1 vaporization and/or chemical kinetics, and combustion. In fact, earlier work [3-6] showed that for some injector geometric configurations, efficiency was noted to decrease with addition of $H_2$. To isolate the various mechanisms, the first set of experiments involved characterizing single RP-1 drop combustion in a pure oxygen environment and in a $H_2/O_2$ flame. The results for these controlled experiments (described in detail in Section 2.3) showed that the presence of hydrogen did not significantly affect the RP-1 drop regression rate in both environments were measured and contrasted. These initial single drop combustion experiments were followed by uni-element combustion experiments in an optically-accessible rocket chamber. Two injector configurations, a coaxial-type tri-propellant element and an effervescent injector, were chosen for injecting the tri-propellants into the rocket chamber. For both these elements, the gaseous hydrogen ($GH_2$) was injected "intimately" with the

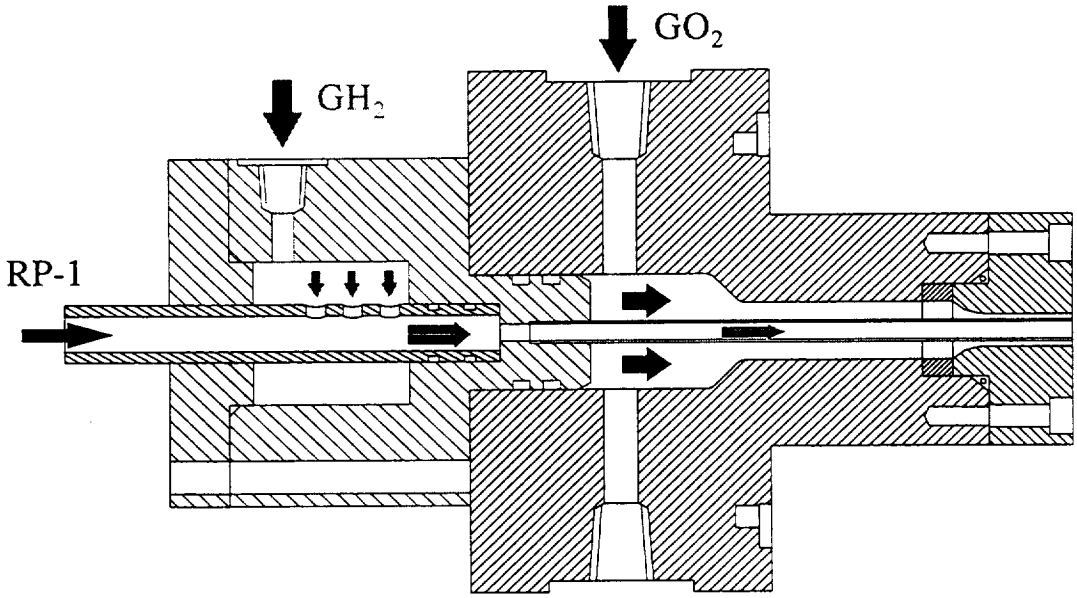


**Fig. 2.4.1. Schematic of the uni-element effervescent injector used for RP-1/$GH_2$/$GO_2$ combustion studies.**

RP-1/gaseous oxygen ($GO_2$) propellants. In this section, the rocket experiments involving uni-element injectors are described.

## 2.4.1. COMBUSTION STUDIES FOR RP-1/$GH_2$/$GO_2$ EFFERVESCENT INJECTOR

The effervescent injector element was chosen for tri-propellant application because of its design simplicity and high liquid atomization efficiency. Also, during the design phase of this program, the need for injector elements that "intimately" injected the hydrogen with the RP-1/Oxygen was recognized. The effervescent injector element satisfies these criteria and consequently, this design was chosen for investigation.

### 2.4.1.1. Experimental Scope

In this section, the effervescent injector geometry, experimental flow conditions and experimental scope are presented.

#### 2.4.1.1.1. Injector Geometry

The effervescent injector is a two-phase mixing device that has been documented to be an extremely efficient atomizer for various spray applications [12-13]. However, for bipropellant rocket injection, it has clearly not been considered as an injector design because it requires fuel/oxidizer pre-mixing. However, for tri-propellant applications, flow of the gaseous fuel ($GH_2$)

in the liquid (RP-1) passage does not compromise any safety aspects and can be used beneficially to atomize the RP-1. Capitalizing on the aforementioned atomizing feature, the effervescent injector for RP-1/$GH_2$/$GO_2$ propellants shown in Fig. 2.4.1 was designed. The effervescent injector design is similar to a shear coaxial element, with the major difference being that both the fuels (RP-1 and $GH_2$ here) flow through the central post. The $GH_2$ flow enters the central RP-1 flow through the three holes shown on the upstream end of the central post. The inner diameter of the central post is 0.15 in., whereas the inner and outer diameters of the annulus are 0.18 in. and 0.5 in., respectively. The lower density $GH_2$ "mixes" with the higher density RP-1 and the two-phase fuel flow that exits the central post is a dense drop cloud. Photographic visualizations of the flowfield for cold flow (water/$GN_2$/$GN_2$ simulants) conditions indicated that for high gas to liquid volumetric flow ratios, the flow exiting the injector is an extremely dense cloud of small liquid drops.

2.4.1.1.2. Scope of Cold Flow Experiments

Cold flow experiments were conducted for the effervescent injector to improve understanding of the two-phase flow emanating from the central part of the injector. Water/nitrogen fluids were used to simulate the RP-1/$GH_2$ propellants. Since the motivation was to understand the two-phase fluid dynamic characteristics, a larger version of the injector employing a glass tube was fabricated as shown in Fig. 2.4.2. The inner diameter of the glass tube was 0.15 in.

Inspection of the literature for two-phase flow in a tube [14-16] indicates that various flow regimes are possible depending on the injector geometry and flowrates, properties and

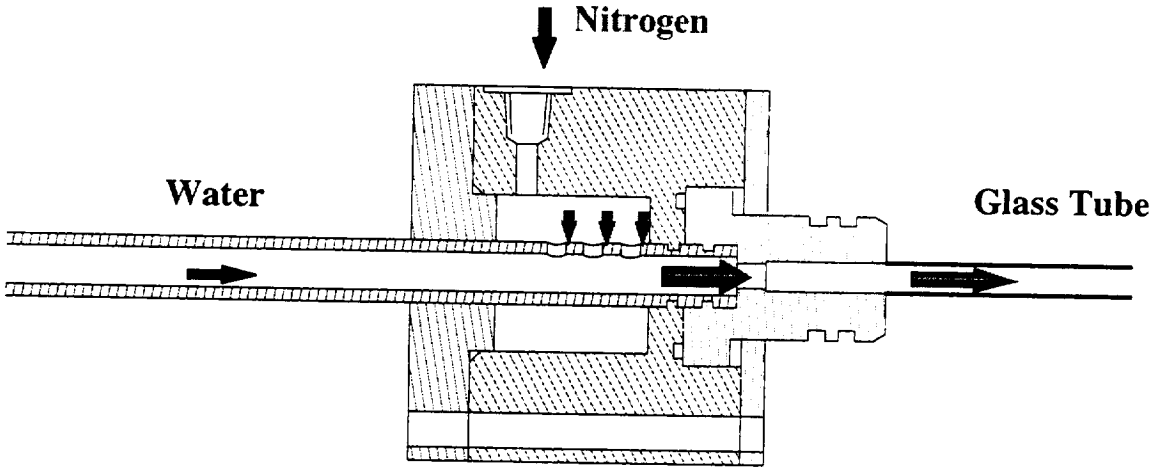


**Fig. 2.4.2. Effervescent injector with glass tube for cold flow water/nitrogen simulants.**

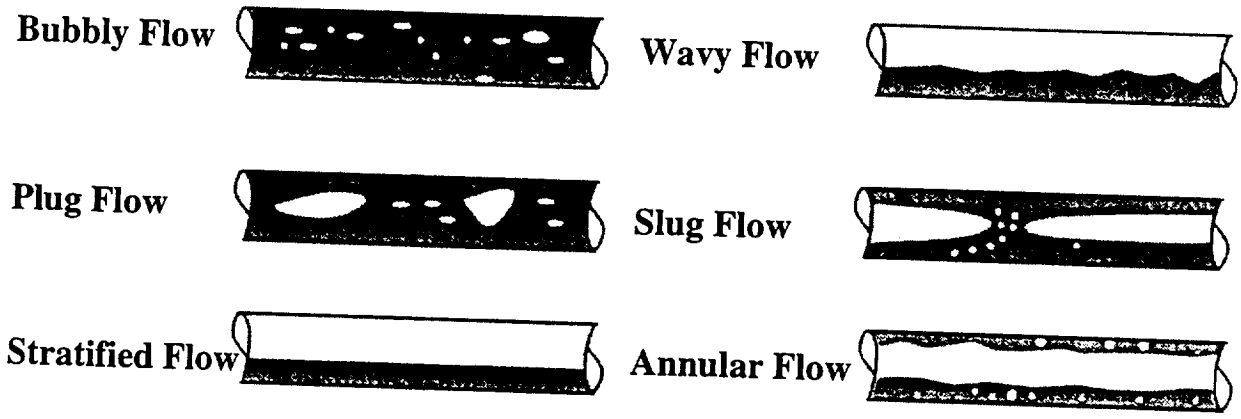


**Fig. 2.4.3. Schematic showing various two-phase flows in a tube.**

pressure conditions of the liquid and gas phases. The possible two-phase flow conditions and the demarcation map for these possible flow conditions are shown in Figs. 2.4.3 and 2.4.4, respectively. As is evident from Fig. 2.4.4, the two parameters necessary for defining the type of two-phase flow are the J-numbers (units of velocity) corresponding to the liquid and gas phases.

These cold flow experiments were conducted to verify these two-phase flow regimes and to establish the regime(s) of operation for the rocket hot-fire experiments. Note that in Fig. 2.4.4, the two-phase flow regime for the current set of hot-fire experiments to be discussed later is demarcated.

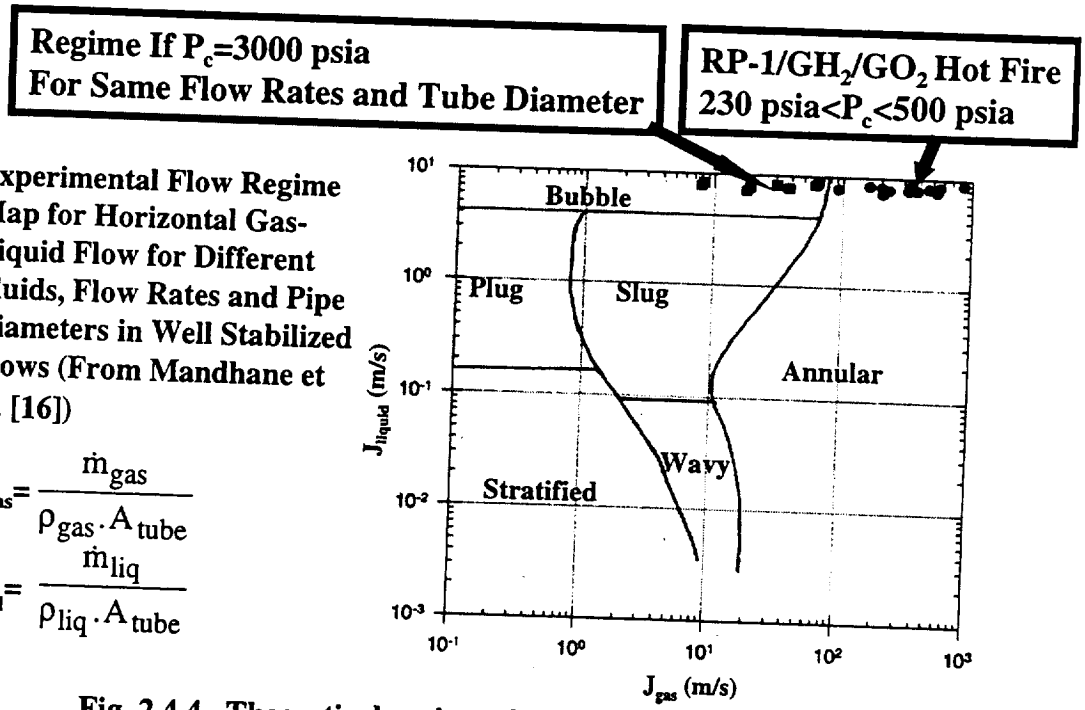


- **Experimental Flow Regime Map for Horizontal Gas-Liquid Flow for Different Fluids, Flow Rates and Pipe Diameters in Well Stabilized Flows (From Mandhane et al. [16])**
- $J_{gas} = \dfrac{\dot{m}_{gas}}{\rho_{gas} \cdot A_{tube}}$
- $J_{liq} = \dfrac{\dot{m}_{liq}}{\rho_{liq} \cdot A_{tube}}$

**Fig. 2.4.4. Theoretical regimes for two-phase flow in tubes.**

2.4.1.1.3. Scope of Hot Fire Experiments

The tri-propellant RP-1/$GH_2$/$GO_2$ uni-element hot fire experiments were conducted over a range of hydrogen addition conditions at overall near-stoichiometric conditions. The chamber utilized for the experiments is described in Section 2.2. The first goal of these experiments was to verify the effects of hydrogen addition on the performance. Supporting measurements included wall heat flux measurements for a select set of flow conditions. The tri-propellant flowfield was qualitatively characterized using a laser sheet imaging approach for RP-1 liquid region identification over a range of flow conditions. Additionally, RP-1 drop size and velocity measurements were also made using phase Doppler interferometry for select flow conditions spanning chamber pressures from RP-1 sub-critical to super-critical pressures.

The measurement of transient heating within a rocket chamber was possible with a heat flux gauge developed by Liebert [17] at the NASA Lewis Research Center. As demonstrated by Liebert, the time-histories of multiple in-depth thermocouples may be used to deduce the wall heat flux provided that the heat flow near those thermocouples is one-dimensional. Two such gauges were employed in this study. These gauges were designed to replace a window of the rocket test section. Consequently, by moving the rocket window section, heat transfer measurements at various axial locations were made. As shown in Fig. 2.4.5, the gauge consists of four Type K thermocouples soldered to a copper rod (designated T1--T4). Since an air gap exists between the rod and the remainder of its housing, the heat flow from the hot wall approximates one-dimensional heat flow with an adiabatic backface condition. The entire gauge is constructed of Oxygen-Free High-Conductivity Copper. The thermocouple positions ranged from 0.063 in. to 0.875 in. in-depth (nominally) with equal spacing between them.

Surface heat flux $q_w(t)$ is estimated by integrating the one-dimensional heat conduction equation with respect to the spatial dimension $x$ as shown below: ($\rho$, $c$, $k$ are the copper density, heat capacity, and conductivity, respectively)

$$\int_0^L \left(\rho c \frac{\partial T}{\partial t}\right) dx = \int_0^L \frac{\partial}{\partial x}\left(k \frac{\partial T}{\partial x}\right) dx$$

$$\int_0^L \left(\rho c \frac{\partial T}{\partial t}\right) dx = \left(k \frac{\partial T}{\partial x}\right)\Bigg|_0^L = q(0) - q(L) \qquad (2.4.1)$$

where $q \equiv -k\,\partial T / \partial x$. Since the backface is insulated (i.e. $q(L) = 0$), this results in

$$q_w \equiv q(0) = \int_0^L \left( \rho c \frac{\partial T}{\partial t} \right) dx \qquad (2.4.2)$$

In practice, the measured time-histories *T1(t), T2(t), T3(t), T4(t),* are curve-fitted by fifth-order polynomial functions. The time-history of wall temperature, which is needed for the above integration, is estimated by linear extrapolation of the near-wall temperatures *T1(t)* and *T2(t).* All temperatures are then differentiated numerically to obtain *dT1/dt, dT2/dt, dT3/dt, dT4/dt.* A trapezoidal rule integration in space is finally performed, accounting for temperature dependent properties, to get the desired wall heat flux. The above computations were restricted to the steady-state combustion portion of each rocket firing.

The RP-1/$GH_2$/$GO_2$ combusting flowfield was first visually characterized using a laser sheet technique. These experiments provided global information on the fluid dynamics of the RP-1 atomization process and also helped in guiding the approach for measuring RP-1 drop size and velocity using phase Doppler interferometry. A laser sheet formed from the continuous wave beam of an argon-ion laser ($\lambda$=514.5 nm) was introduced through one of the slot windows. A 35 mm camera equipped with a 10 nm bandpass filter centered around 514.5 nm was used to record the scattered light from the RP-1 drop cloud through one of the circular windows. The bandpass filter was used to reject light from the luminous flame.

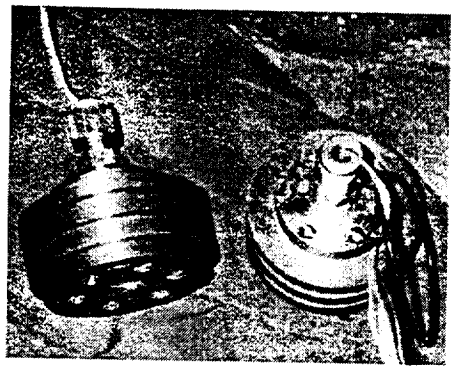

- **2 Heat Flux Gauges Used**
  - **On Opposing Sidewalls of Rocket**
  - **Heat Xfer. Computed from Temps. T1, T2, T3, T4**
  - **Technique by NASA LeRC,**
  - **Ref: Liebert '88, NASA-TP-2840**
- **Transient Heat Flux Obtained**

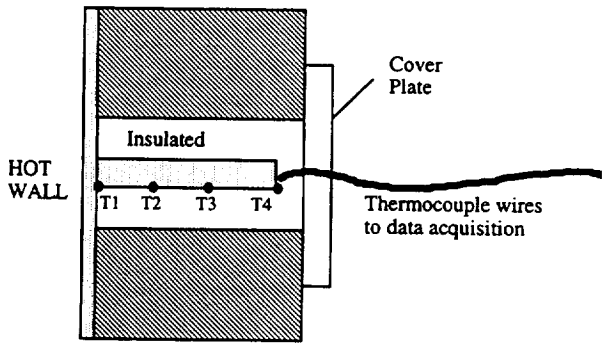


Thermocouple Locations (in-depth)

| Gauge A | | Gauge B | |
|---|---|---|---|
| T1 | 0.062 in. | T1 | 0.100 in. |
| T2 | 0.322 in. | T2 | 0.335 in. |
| T3 | 0.583 in. | T3 | 0.600 in. |
| T4 | 0.875 in. | T4 | 0.875 in. |

**Fig. 2.4.5. Heat transfer gauge.**

Phase Doppler interferometry was used to measure RP-1 drop size and velocity in the rocket chamber under combusting conditions. The technique is a point measurement technique that has been used extensively over the last decade by several researchers (for example, Refs. 18-22). The technique extends the basic principles of the conventional dual beam laser Doppler velocimeter to obtain particle size in addition to velocity. An argon-ion laser beam is split into two equal intensity beams and focused to an intersection to form a probe volume as shown in Fig. 2.4.6. For the present experiments, the receiver system was located at a 30° off axis angle from the forward propagation vector of the laser beam to best exploit the characteristics of the interference pattern of the refractive RP-1 drops. This was achieved by inclining both the transmitting and receiving optics at a 15° angle, thus resulting in a net 30° off-axis angle. A 10 nm bandpass filter centered around 514.5 nm was placed in front of the collection optics to reject light from the luminous flame. Note that the collection optics of the receiving system coupled with the transmitting optics define the probe volume characteristics. In addition to the collection optics, the receiving system consists of three detectors at appropriate separations that independently measure the burst signal generated by drops traversing the probe volume, albeit with a phase shift. The velocity of the particle is then extracted from the temporal frequency of the burst signal, whereas the particle size is calculated from the measured phase shift between any two detectors and the *a priori* calculated linearity between the detector separation and the phase angle.

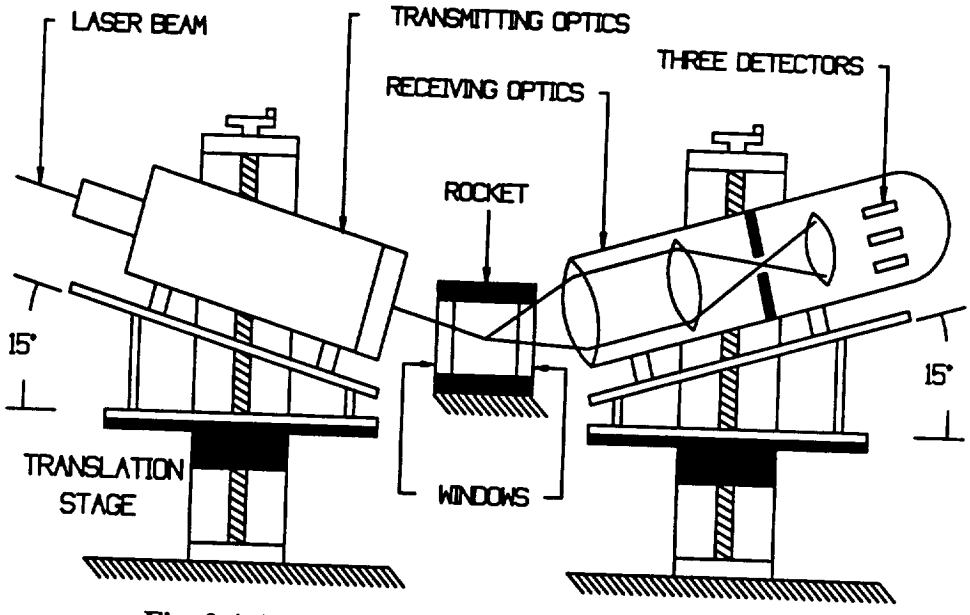


**Fig. 2.4.6. Phase Doppler interferometry setup.**

### 2.4.1.2. Results and Discussion

#### 2.4.1.2.1. Cold Flow Results

The cold flow experiments were conducted with a glass tube version of the effervescent injector to verify the different two-phase flow regimes possible in tubes. As mentioned earlier, the flow regime is defined by the geometry and flow conditions. Near tube exit close-up photographs for five of the possible two-phase flow regimes are shown in Figs. 2.4.7-2.4.11. The calculated J-numbers for both cases as well as the flow regime are also indicated in the figures. These visualizations indicate that the demarcations identified in the literature are realistic.

Clearly, for a tri-propellant effervescent injector design, the atomization characteristics would be similar to a shear coaxial design if the two-phase flow were either in the "plug" or "slug" modes. For the "stratified" or "wavy" regimes, the effects of gravity are important and consequently, operation in these two modes is not recommended. For the "annular" region, the flowfield emanating from the tube consists of annular flow of liquid with mainly gas flow

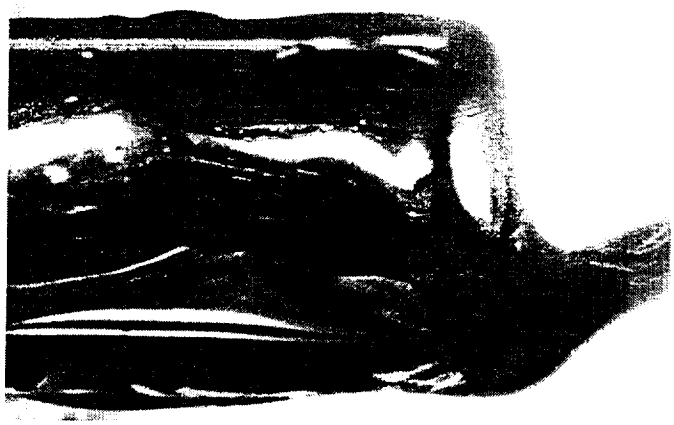

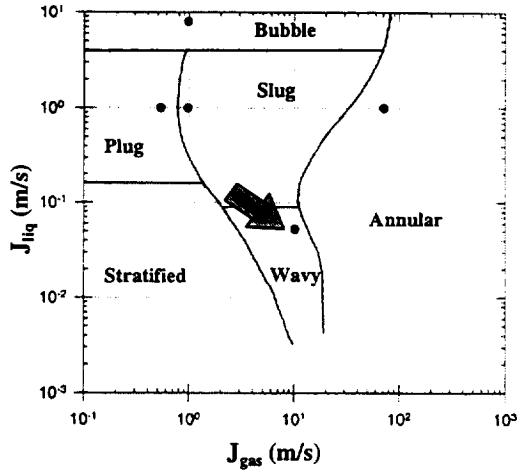


**Fig. 2.4.7. Image of Wavy flow in tube. Tube length = 9 in.; tube diameter = 0.15 in.; J ($H_2O$) = 0.16 ft/s; J ($N_2$) = 33.5 ft/s.**

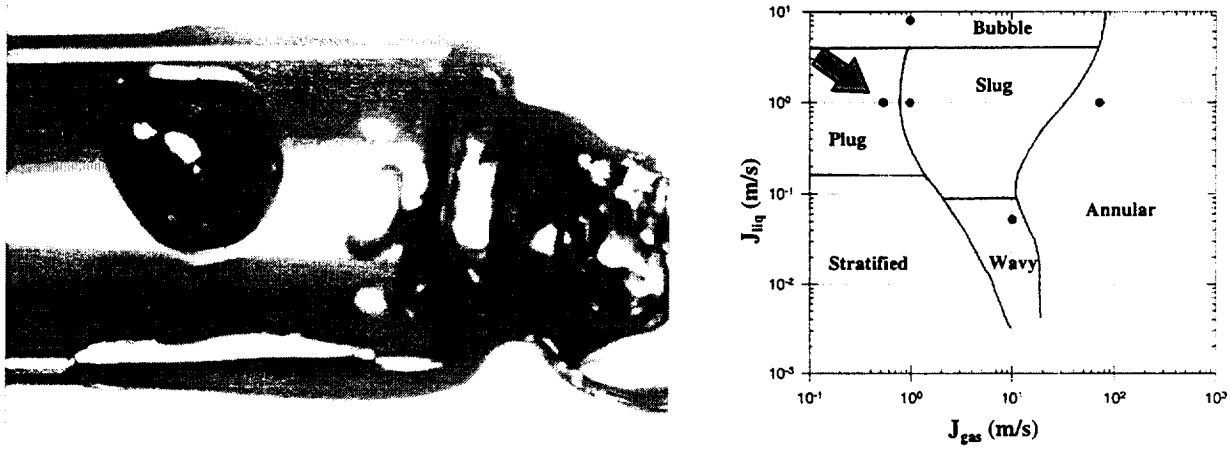


**Fig. 2.4.8. Image of Plug flow in tube. Tube length = 9 in.; tube diameter = 0.15 in.; J ($H_2O$) = 3.3 ft/s; J ($N_2$) = 1.6 ft/s.**

constituting the central core. The "bubbly" flow regime is characterized by a more homogeneous two-phase flow emanating from the tube. The "annular" and "bubbly" modes would provide improved atomization in comparison to the "slug" or "plug modes. For the combustion experiments over the 230 to 500 psia pressure range discussed next, based on the calculated J-numbers, the two-phase RP-1/$GH_2$ flow emanating from the central tube would be in the "annular" regime. However, if these experiments had been conducted at a chamber pressure of 3000 psia (estimated main chamber pressure for a full scale combustor) for the same geometry and flowrate conditions, the two-phase flow would have been in the "bubbly" flow regime. The actual hot-fire experimental data points (and extrapolated to 3000 psia operation) are plotted

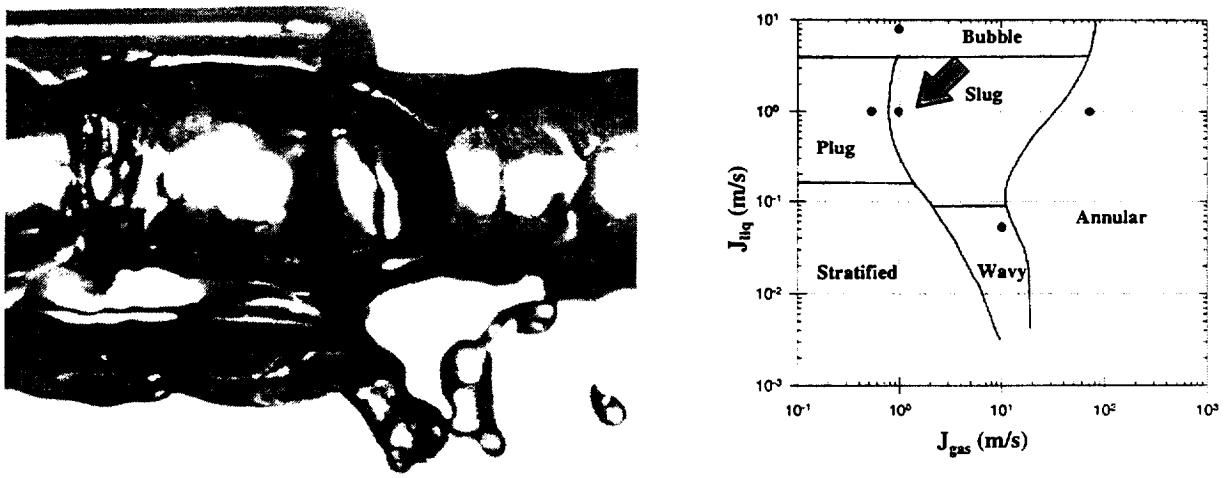


**Fig. 2.4.9. Image of Slug flow in tube. Tube length = 9 in.; tube diameter = 0.15 in.; J ($H_2O$) = 3.3 ft/s; J ($N_2$) = 3.3 ft/s.**

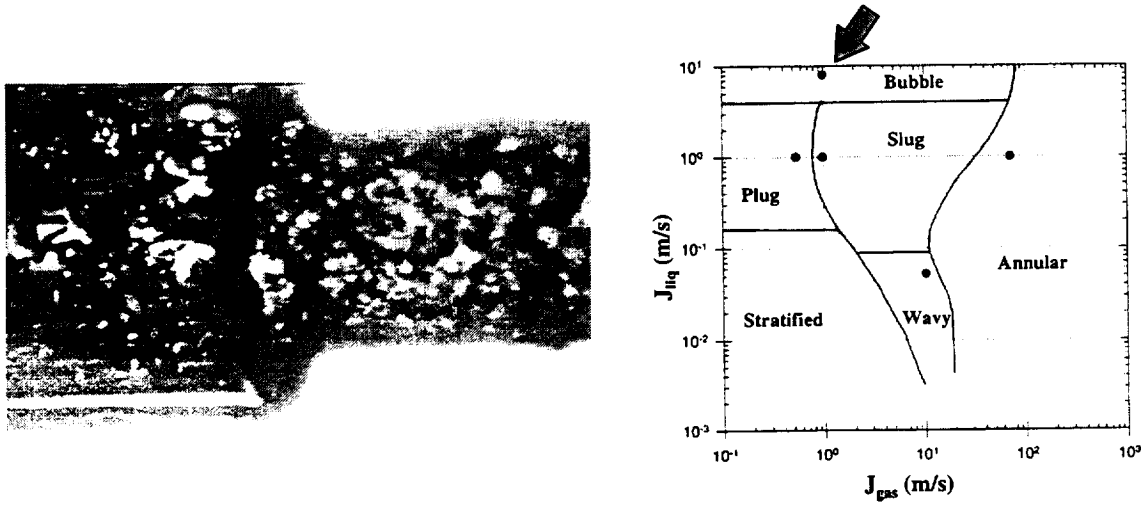


**Fig. 2.4.10. Image of Bubbly flow in tube. Tube length = 9 in.; tube diameter = 0.15 in.; J ($H_2O$) = 26.2 ft/s; J ($N_2$) = 3.3 ft/s.**

in the flow regime map shown in Fig. 2.4.4. With this brief introduction on two-phase flow characteristics, the results of the combustion experiments are presented next.

2.4.1.2.2. Hot-Fire Results

The discussions below address the combustion performance and wall heat transfer characteristics if RP-1/$GH_2$/$GO_2$ propellants for the effervescent injector. In addition, visualizations of the RP-1 liquid region in the combustion zone and RP-1 drop size and velocity measurements made for one flow condition are also presented for this injector.

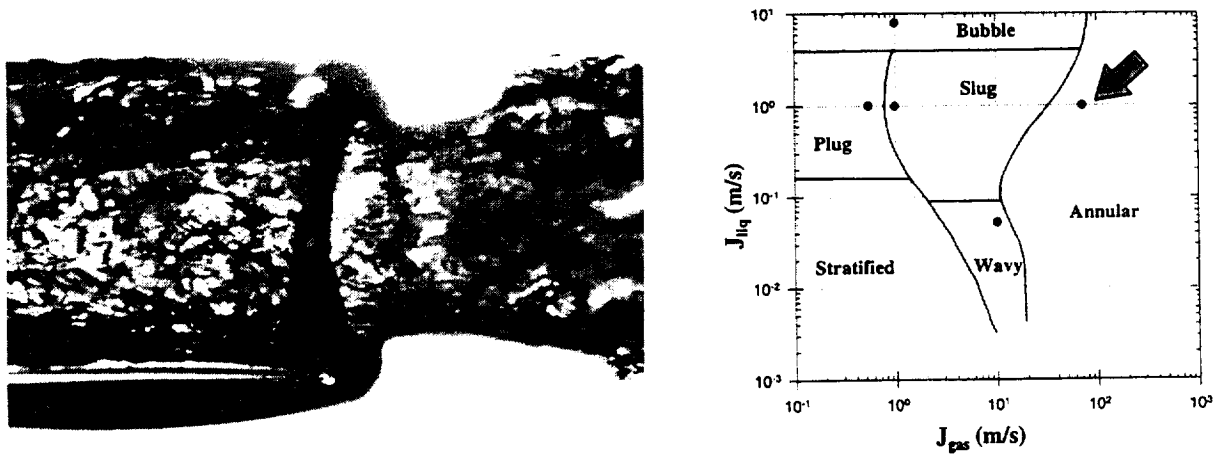


**Fig. 2.4.11. Image of Annular flow in tube. Tube length = 9 in.; tube diameter = 0.15 in.; J ($H_2O$) = 3.3 ft/s; J ($N_2$) = 234.9 ft/s.**

*2.4.1.2.2.1. Performance*

The experiments with the effervescent injector involved performance measurements in terms of c* efficiency for $GH_2$ mass flowrate additions from 2 to 10% (of RP-1 flowrate) for target chamber pressures from 230 to 500 psia. This pressure range covers the sub-, trans- and super-critical regimes for RP-1. For reference, the critical pressure and temperature of RP-1 are 340 psia and 676 K, respectively. The target RP-1, $GH_2$ and $GO_2$ flowrates were adjusted for different $GH_2$ flow additions such the $GO_2$ mass flowrate was always 8 times the $GH_2$ mass flowrate plus 2.4 times the RP-1 flowrate. In this manner, the effects of $GH_2$ mass addition from 2 to 10% (of RP-1 mass flowrate) on c* efficiency could be studied for the same target pressure condition. The chamber pressure was then varied from 230 to 500 psia by changing the nozzle.

The effects of $GH_2$ mass addition on RP-1/$GO_2$ combustion c* efficiency for the effervescent injector is presented in Fig. 2.4.12 for three target chamber pressure cases. Note that

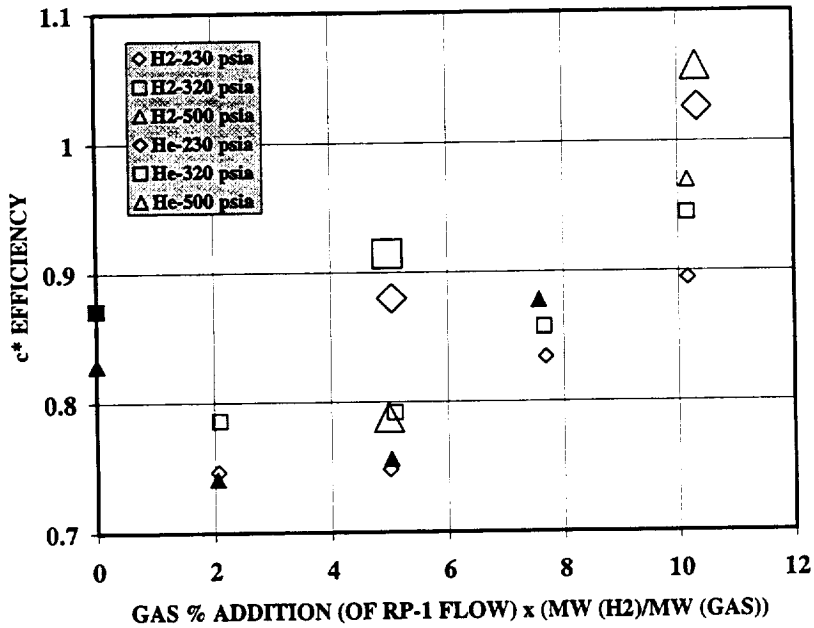


**Fig. 2.4.12. c* efficiency vs. % mass (of RP-1) gas addition ($GH_2$ or He; normalized with respect to molecular weight of $GH_2$) for RP-1/$GH_2$/$GO_2$ effervescent injector. Gas addition percentage is in terms of RP-1 flow. Indicated pressures are nominal target values. Dark symbols are for experiments where a small amount of window nitrogen purge was introduced. For these tests, the GN2 flow was included in the c* efficiency calculations. Small symbols are for $GH_2$ addition; large symbols are for He addition. Additional details are summarized in Table 2.4.1.**

**Table 2.4.1. Flow Conditions for Effervescent Injector.**

| Nominal % $GH_2$ or He (of RP-1) | Avg. of # Runs | $\dot{m}_{RP\text{-}1}$ (lbm/s) | $\dot{m}_{GO_2}$ (lbm/s) | $\dot{m}_{GH_2}$ ($\times 10^{-3}$ lbm/s) | $\dot{m}_{He}$ ($\times 10^{-3}$ lbm/s) | $\dot{m}_{GN_2}$ (lbm/s) | Measured $P_c$ (psia) | c* Efficiency |
|---|---|---|---|---|---|---|---|---|
| ***RP-1/$GH_2$/$GO_2$ Combustion*** | | | | | | | | |
| 2 | 6 | 0.170 | 0.448 | 3.50 | 0 | 0 | 154.2 | 0.747 |
| 5 | 7 | 0.158 | 0.454 | 7.94 | 0 | 0 | 175.9 | 0.749 |
| 7.5 | 6 | 0.166 | 0.516 | 12.75 | 0 | 0 | 197.5 | 0.834 |
| 10 | 37 | 0.155 | 0.514 | 15.77 | 0 | 0 | 210.8 | 0.894 |
| 0 | 1 | 0.182 | 0.474 | 0 | 0 | 0.028 | 262.6 | 0.871 |
| 2 | 6 | 0.158 | 0.426 | 3.33 | 0 | 0 | 258.1 | 0.786 |
| 5 | 6 | 0.145 | 0.424 | 7.40 | 0 | 0 | 258.5 | 0.792 |
| 7.5 | 8 | 0.168 | 0.519 | 12.85 | 0 | 0 | 278.9 | 0.858 |
| 10 | 24 | 0.158 | 0.522 | 16.04 | 0 | 0 | 308.5 | 0.945 |
| 0 | 1 | 0.182 | 0.475 | 0 | 0 | 0.028 | 453.7 | 0.829 |
| 2 | 1 | 0.169 | 0.448 | 3.50 | 0 | 0.029 | 390.7 | 0.741 |
| 5 | 2 | 0.155 | 0.431 | 7.80 | 0 | 0.029 | 391.0 | 0.756 |
| 7.5 | 3 | 0.167 | 0.489 | 12.67 | 0 | 0.029 | 449.6 | 0.878 |
| 10 | 19 | 0.158 | 0.519 | 16.03 | 0 | 0 | 499.8 | 0.970 |
| ***RP-1/He/$GO_2$ Combustion*** | | | | | | | | |
| 10 | 2 | 0.158 | 0.392 | 0 | 15.75 | 0 | 298.1 | 0.914 |
| 20 | 3 | 0.181 | 0.449 | 0 | 37.43 | 0 | 540.6 | 1.058 |
| 10 | 2 | 0.169 | 0.425 | 0 | 17.15 | 0 | 206.6 | 0.880 |
| 20 | 1 | 0.181 | 0.492 | 0 | 37.50 | 0.375 | 256.6 | 1.026 |
| 10 | 2 | 0.170 | 0.414 | 0 | 16.95 | 0 | 400.0 | 0.788 |

the graph also presents results for helium addition (instead of $GH_2$) which are discussed later in this section. The abscissa for the graph is percent by mass of gas ($GH_2$ here) relative to RP-1 flowrate multiplied by the ratio of the molecular weights of $GH_2$ and the gas in question ($GH_2$ here). Consequently, when the added gas is $GH_2$, the ratio is one. This manner of normalization allows the comparison of results for different gases on an equal gas volumetric flow basis. More detailed information in terms of mass flowrates, chamber pressure, etc. is summarized in Table 2.4.1. The results clearly show that in general, as $GH_2$ mass flowrate increases, the c* efficiency increases. However, the zero $GH_2$ mass addition case has a higher efficiency than that of the 2% addition case. The reason for this difference is not understood. The results are consistent for the target chamber pressures tested here, i.e. from 230, 320 and 500 psia. The improved $c^*$ efficiency with $GH_2$ addition to RP-1/$GO_2$ combustion noted here for the effervescent injector complement the experimental results obtained by the Japanese researchers [3-6]. In their experiments on

RP-1/$O_2$/$H_2$ tri-propellant combustion, they used two injector configurations, 12 F-O-F triplet elements for RP-1/LOX propellants with $GH_2$ as faceplate coolant, and 12 O-F-O triplets for RP-1/LOX propellants with $GH_2$ as faceplate coolant. Their results showed improvements in $c^*$ efficiency with $GH_2$ addition for the O-F-O triplet arrangement and not for the F-O-F case. They correctly reasoned that for both their geometries, the low velocity $GH_2$ flow would not affect the atomization and mixing characteristics of the main injector flows of RP-1 and LOX. In explaining the differing trends of $c^*$ efficiency with $GH_2$ addition for the two geometries, they argued that for triplet geometries, the flow from the outer holes envelop the flow from the inside hole. Consequently, for the O-F-O arrangement, the surrounding low velocity $GH_2$ flow would react readily with the oxygen from the main elements promoting liquid drop vaporization, whereas for the F-O-F arrangement, the injected $GH_2$ flow would reduce the temperature of the fuel-rich recirculation zone around the main elements, thus decreasing the vaporization rates of the liquid drops. In capitalizing on their experimental results, the effervescent injector element investigated here was designed for integral $GH_2$ addition to the RP-1/$GO_2$ flows. Unlike the injector configuration experimented by the Japanese researchers, for the injector element investigated here, the additional $GH_2$ flow significantly affects the liquid RP-1 atomization characteristics. To explain the increase in $c^*$ efficiency of RP-1/$GO_2$ combustion with $GH_2$ addition, the following qualitative arguments are presented. To achieve a $c^*$ efficiency of one for liquid propellant rocket combustion, the liquid propellant(s) must atomize to a certain liquid surface area threshold such that the processes of vaporization, mixing and combustion are completed before the entry of the nozzle. For the effervescent injector, atomization is clearly enhanced with the addition of $GH_2$. The fast reaction rate of $GH_2$ compared to that of RP-1 translates to a high temperature oxidizer rich environment in the near-injector region. Clearly, fast $GH_2$/$GO_2$ combustion would enhance RP-1 drop heatup and vaporization process; however, based on the single RP-1 drop combustion results reported earlier, the degree of enhancement may not be significant. Additionally, the effects of $GH_2$ on the chemical kinetics of RP-1/$GO_2$ combustion as suggested by Rhys and Hawk [23] may also play a role. Based on these arguments, the measured improvement in $c^*$ efficiency with $GH_2$ addition reported here is therefore viewed as being mainly due to improved RP-1 atomization and partially due to higher RP-1 drop vaporization rates resulting from the presence of a high temperature oxidizer-rich zone (products of fast reacting $GH_2$/$GO_2$ combustion) surrounding the RP-1 drop cloud.

Additional experiments were conducted to verify/refute the improved atomization argument described previously for explaining the increase in c* efficiency with hydrogen addition. Experiments were conducted with nominally 10% and 20% by mass of helium (instead of $GH_2$) to independently assess improved RP-1 atomization for the injector. These experiments were conducted for the same three target pressure conditions as those of the RP-1/$GH_2$/$GO_2$ experiments. Since helium is an inert gas with a density twice as large as that of hydrogen, a one-to-one comparison needs to be made on a volumetric flow basis. As an example, a 10% by mass of helium case should be compared with a 5% by mass of $GH_2$ to equate the volumetric flowrates. The results of these experiments are also plotted in Fig. 2.4.12 and detailed in Table 2.4.1. The volumetric flow basis of comparison for different gases explains the choice of the molecular weight ratio normalization utilized for the abscissa in Fig. 2.4.12.

The experiments with inert helium addition instead of combustible $GH_2$ also showed improved c* efficiency with helium addition. In fact, the c* efficiencies for helium addition were slightly greater than that of $GH_2$ addition when compared on a volumetric flow basis. This indicates that the improved c* efficiencies noted with $GH_2$ of helium addition for the effervescent injector is mainly due to improved atomization. When compared on an equal volumetric flow basis, the momentum ratio between gas flow to RP-1 flow for the two-phase flow emanating from the injector tube exit is twice as large for helium as that of $GH_2$, and may explain the higher c* efficiencies noted for helium addition.

*2.4.1.2.2.2. Wall Heat Flux*

Concurrent measurements of wall heat flux for three axial locations were obtained at the two lower target chamber pressure cases, viz. 230 and 320 psia, for the RP-1/$GH_2$/$GO_2$ effervescent injector rocket firings. Two heat flux gauges (designated as Gauge A and Gauge B) were placed diametrically opposite to each other (instead of windows) in the window section of the rocket. Consequently, for a rocket firing, wall heat flux at two walls was measured at one axial station. For these experiments, nitrogen purge was not introduced. The rocket window section was moved progressively downstream. In this manner, the wall heat transfer characteristics of the injector element were gauged for various flow conditions. In this copper heat-sink chamber, heat flux to the wall varies with time during the firing. Initially, the heating level is high owing to the lower wall temperatures. As wall temperature rises, the wall heat flux

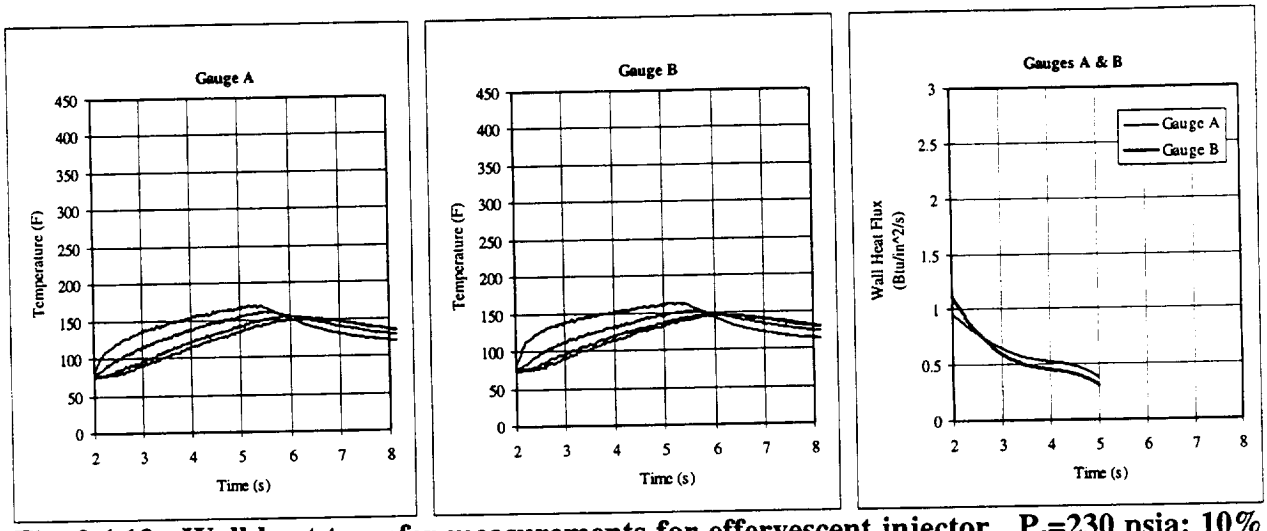


**Fig. 2.4.13. Wall heat transfer measurements for effervescent injector. $P_c$=230 psia; 10% $GH_2$ Addition; x = 1 in.**

decreases steadily during the firing. In most cases, the heat flux diminishes by a factor of two during the steady combustion period.

The measurements corresponding to a target chamber pressure of 230 psia for 10% $GH_2$ addition (by mass of RP-1) at an axial distance of 1 in. from the injector face are shown in Fig. 2.4.13. In the figure, the first two plots show the temperature versus time traces of the four progressively recessed thermocouples for gauges A and B. Obviously, the higher temperature traces correspond to thermocouples closer to the hot wall surface. The time dependent heat flux

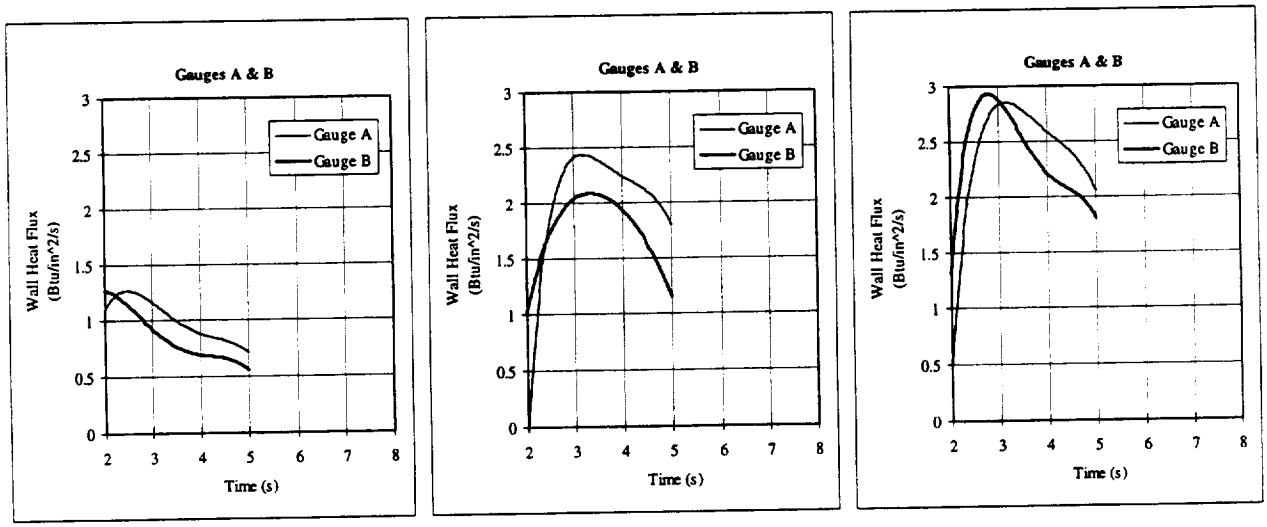


**x = 1 in.** **x = 3 in.** **x = 6 in.**

**Fig. 2.4.14. Wall heat transfer measurements for effervescent injector. $P_c$=230 psia; 2% $GH_2$ Addition.**

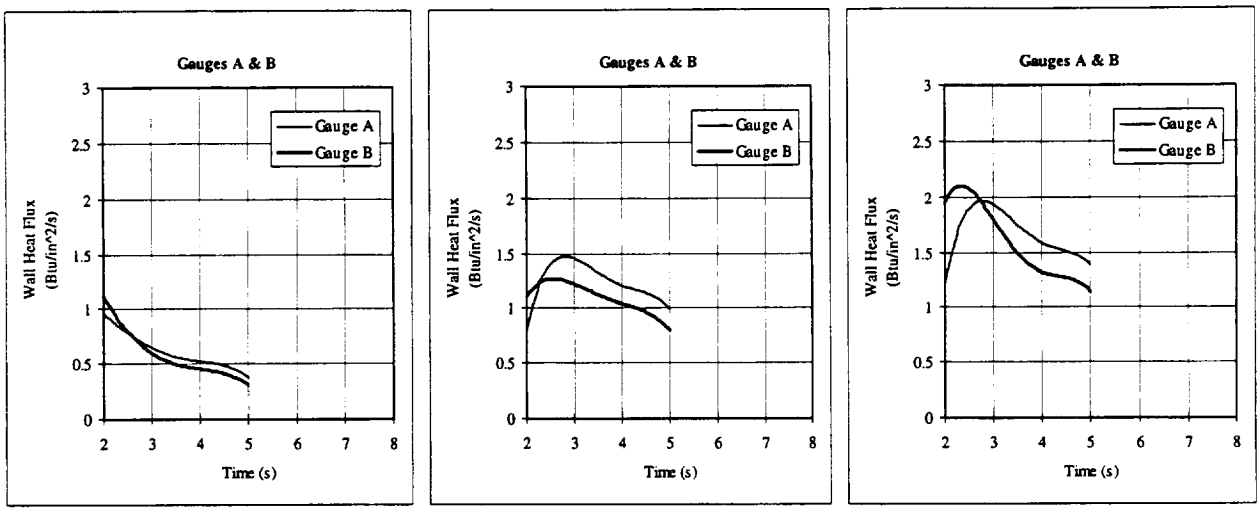


**x = 1 in.** **x = 3 in.** **x = 6 in.**

**Fig. 2.4.15. Wall heat transfer measurements for effervescent injector. $P_c$=230 psia; 10% $GH_2$ Addition.**

for both gauges is shown in the last plot of the figure. Note that the results for the two gauges show good agreement indicating that the flowfield in the rocket chamber is symmetric.

The effect of $GH_2$ addition to the wall heat flux can be gauged by comparing the time dependent wall heat flux profiles for 2% $GH_2$ addition (by mass of RP-1) shown in Fig. 2.4.14 with the corresponding profiles for 10% $GH_2$ addition depicted in Fig. 2.4.15. Additional performance details for these conditions are provided in Table 2.4.1. Measurements for three axial locations from the injector face, viz. 1, 3 and 6 in., for a target chamber pressure of 230 psia, are shown in each of these figures. Note that all traces indicate reasonable agreement between measurements from the two gauges indicating that the flowfield is nominally axisymmetric. For both of these flow conditions, the wall heat flux increases with downstream distance. This observation is consistent with the flowfield visualizations presented in the next section that indicate that the combustion zone increases radially with downstream distance. Comparison of these two sets of measurements show that the heat flux is higher for the 2% $GH_2$ heat addition case than the 10% $GH_2$ heat addition case.

The final set of heat flux measurements presented in Fig. 2.4.16 is for the 10% $GH_2$ addition case for a target chamber pressure of 320 psia. Contrasting Figs. 2.4.15 and 2.4.16 for the same 10% $GH_2$ addition but different chamber pressures indicates little if any difference.

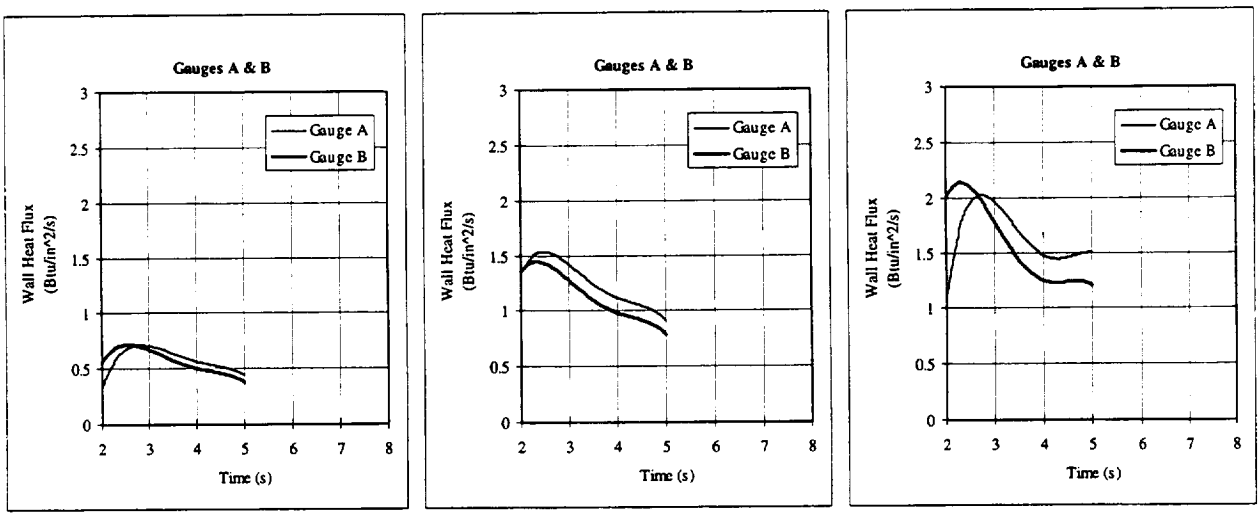


**x = 1 in.** **x = 3 in.** **x = 6 in.**

**Fig. 2.4.16. Wall heat transfer measurements for effervescent injector. $P_c$=320 psia; 10% $GH_2$ Addition.**

Heat transfer coefficients can not be obtained from these sets of measurements because of the lack of detailed understanding of the recirculation zones that exist in the near-injector face region. Nevertheless, the results can be used for supporting design and CFD efforts.

*2.4.1.2.2.3. Flowfield Visualizations*

The RP-1/$GH_2$/$GO_2$ combusting flowfield was characterized by flame photography and RP-1 region visualizations. Visualizations for the two target chamber pressure conditions, viz. 230 and 320 psia, are shown in Figs. 2.4.17 and 2.4.18, respectively for the nominally 10% $GH_2$ addition case. In both figures, flame photographs at three axial locations are shown in the top half. The bottom images for both figures were taken at the same flow conditions by first illuminating the combusting spray field with a 514.5 nm laser sheet (from an Argon-ion laser) and then recording only the Mie scattered light from the flowfield. The "green" areas therefore indicate the RP-1 regions. Since the camera time duration was 1 ms, the images represent time averages of the flowfield. These images show that with axial distance from the injector face, the combusting flowfield increases radially. The images also show that liquid RP-1 is present throughout the viewing region (0-7 in. from injector face).

The RP-1 regions in the combusting flowfield as indicated by Mie scattered light are compared for three chamber pressure conditions (230, 320 and 500 psia) in Fig. 2.4.19. The 0-2 in. location photographs for the three chamber pressure conditions do not differ significantly. However, at the 5-7 in. axial location, liquid RP-1 is present at greater radial

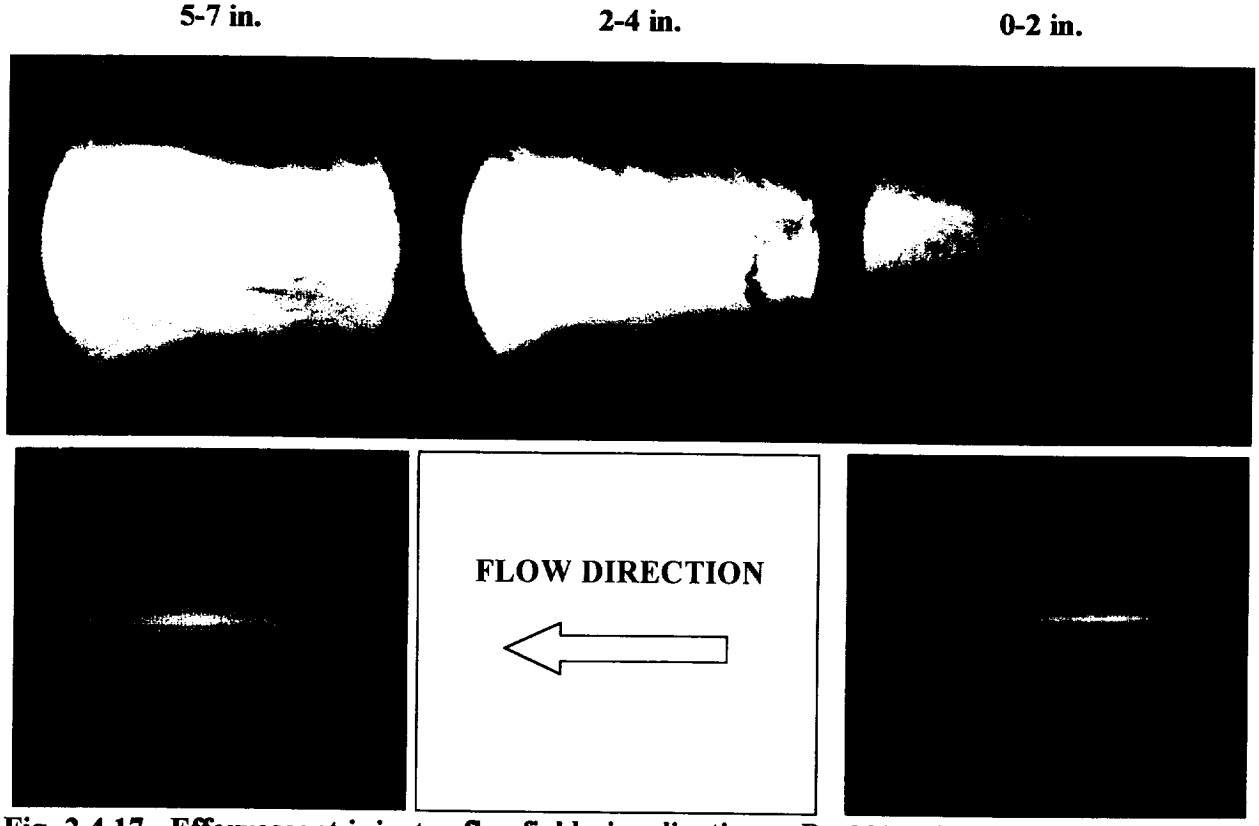


**Fig. 2.4.17. Effervescent injector flowfield visualizations. $P_c$=230 psia; 10% $GH_2$ Addition. Flame photographs shown on top. Mie scattered light images (1/1000 s) shown on bottom.**

locations for increasing chamber pressure. Note that the three pressures correspond to sub-, trans- and super-critical conditions. The reason for this difference is not clear, but might be due to the shift from sub- to super-critical conditions.

*2.4.1.2.2.4. RP-1 Drop Size and Velocity*

The RP-1 drop sizes in the combusting flowfield were measured using phase Doppler interferometry. The measured drop size and velocity probability density functions are shown in the two inset graphs of Fig. 2.4.20. In these two graphs, the measurements at one fixed point, x=6 in. and r= 0.2 in., are compared for the three chamber pressure conditions. These results are for the 10% $GH_2$ addition case. The results are very interesting because drop sizes could be measured at both trans- (320 psia case) and super-critical conditions (500 psia case). Since phase Doppler interferometry only works for sizing spherical drops, effective measurements at trans- and super- critical conditions indicate that under conditions where "liquid" RP-1 is not surrounded by a pure RP-1 "vapor", RP-1 can exist as liquid at pressures exceeding the critical pressure. Clearly, these interesting results need to be pursued in greater detail.

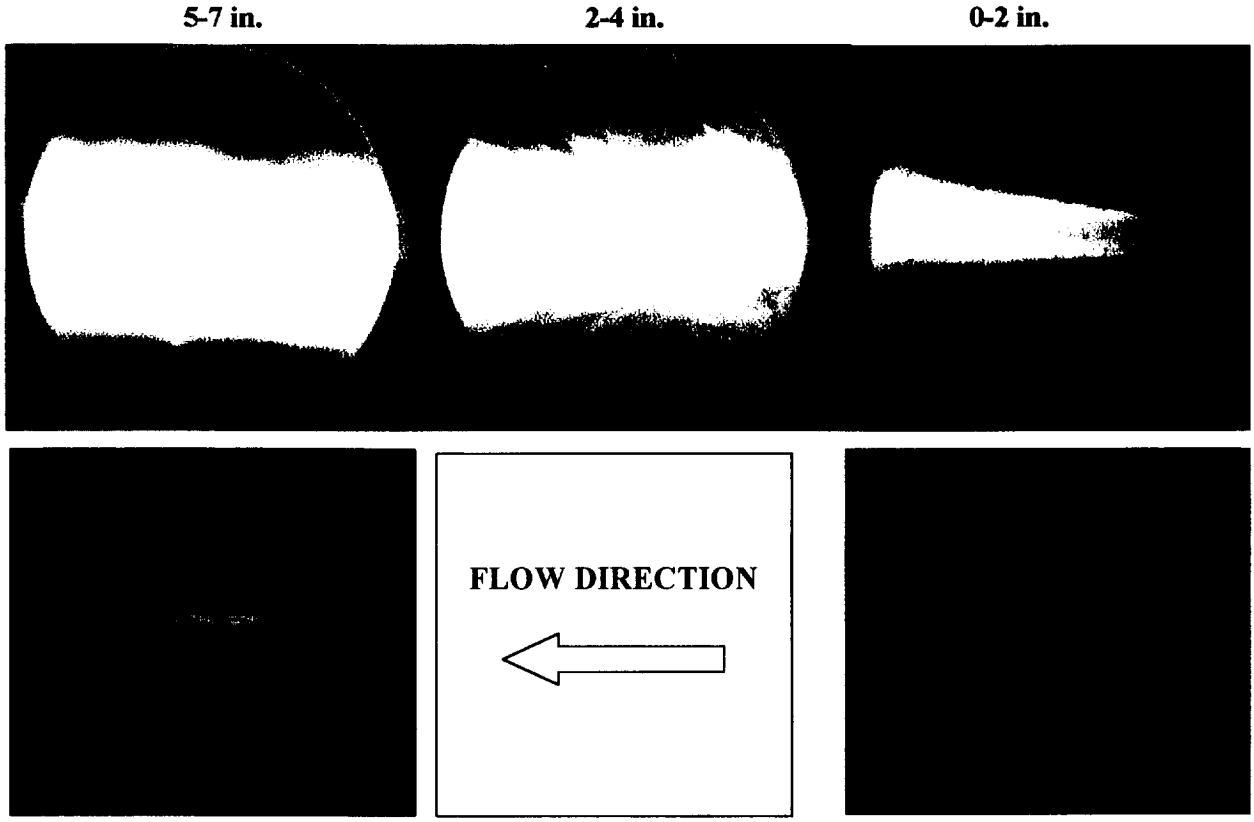


**Fig. 2.4.18. Effervescent injector flowfield visualizations. $P_c$=320 psia; 10% $GH_2$ Addition. Flame photographs shown on top. Mie scattered light images (1/1000 s) shown on bottom.**

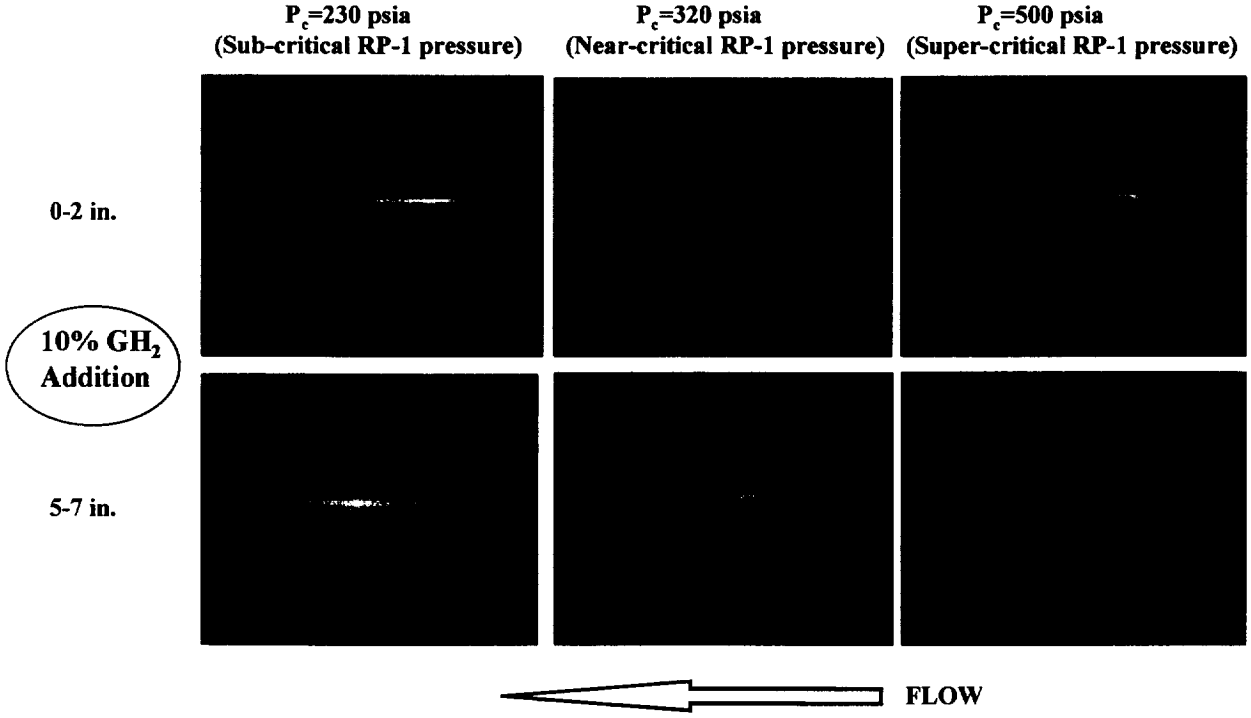


**Fig. 2.4.19. Mie scattering from RP-1 in combustion zone.**

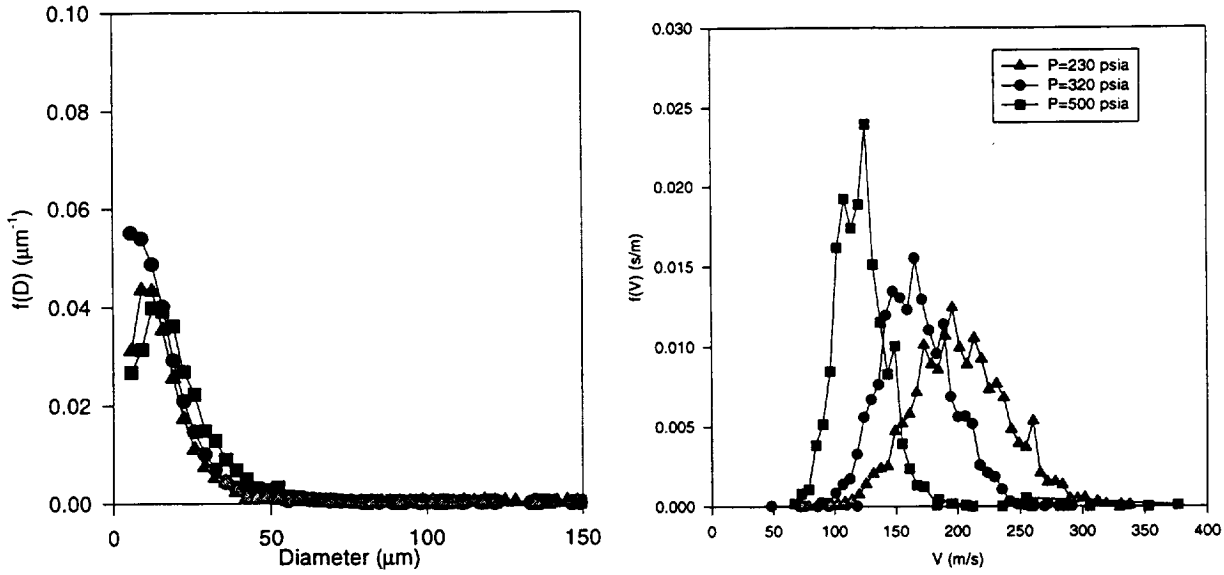


**a) Drop size pdfs** **(b) Drop Velocity pdfs**

**Fig. 2.4.20. RP-1 drop size and velocity probability density functions (pdf) for three chamber pressure conditions. x=6 in., r=0.2 in. @230 psia >13900 Drops, @320 psia > 6900 Drops; @500 psia > 1950 Drops; 2 s firing.**

## 2.4.2. COMBUSTION STUDIES FOR RP-1/$GH_2$/$GO_2$ COAXIAL-TYPE INJECTOR

The coaxial-type injector element was chosen as the second injector for tri-propellant application because of its design simplicity and high liquid atomization efficiency. Also, during the design phase of this program, the need for injector elements that "intimately" injected the hydrogen with the RP-1/Oxygen was recognized. The coaxial-type injector with swirled RP-1 flow satisfies these criteria and consequently, this design was also chosen for investigation.

### 2.4.2.1. Experimental Scope

In this section, the coaxial-type injector geometry, experimental flow conditions and experimental scope are presented.

#### 2.4.2.1.1. Injector Geometry

For designing a tri-propellant injector, previous work [3-7] indicated that benefits in combustion efficiency and stability required that $GH_2$ addition be integral to RP-1/$GO_2$ injection. In satisfying this integral $GH_2$ addition concept, the coaxial-type geometry was devised as an alternate to the earlier discussed effervescent injector. This injector is similar to a swirl coaxial

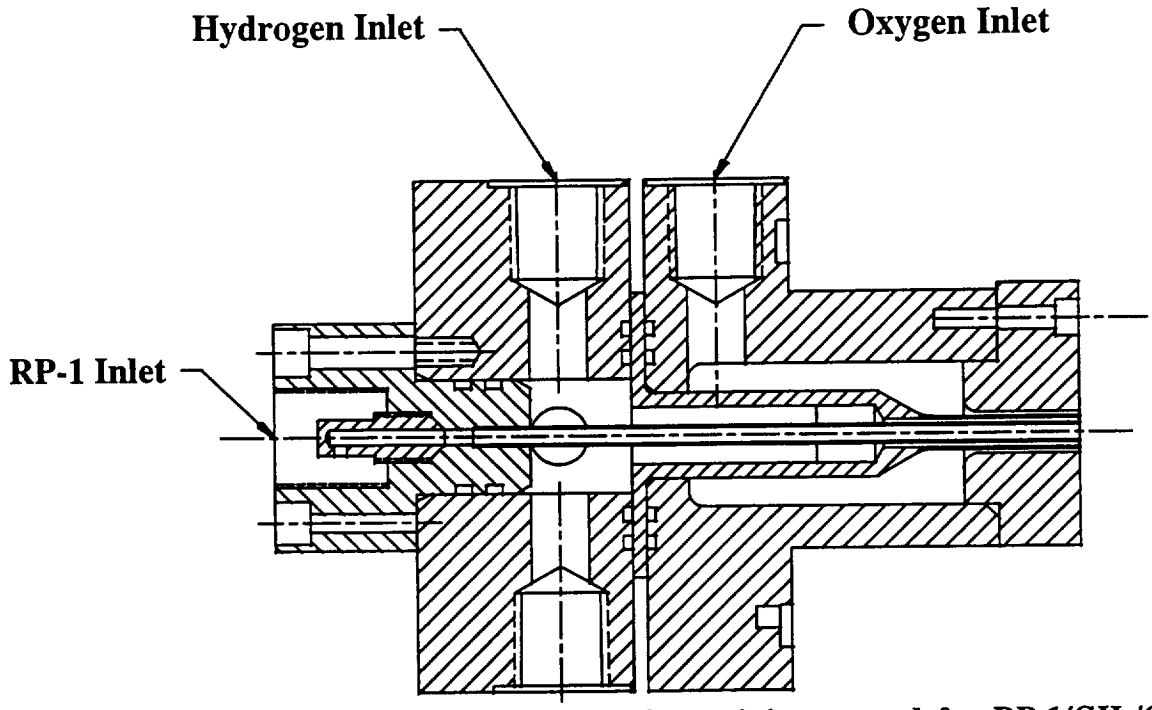


**Fig. 2.4.21. Schematic of the uni-element coaxial-type injector used for RP-1/$GH_2$/$GO_2$ combustion studies.**

element but with an additional annular passageway. A schematic of the coaxial-type tri-propellant injector for RP-1/$GH_2$/$GO_2$ propellants is shown in Fig. 2.4.21. For the injector, RP-1 is introduced through the central post and swirled using a tangential swirl nut. The design of the swirl nut is shown in Fig. 2.4.22. Initial cold flow experiments showed that the swirl cone angle for this post is 35°. $GH_2$ and $GO_2$ are injected through the first and second annular flow passages, respectively. The inner diameter of the central post is 0.135 in., the inner and outer diameters of the $GH_2$ annulus are 0.165 in. and 0.305 in., and the inner and outer diameters of the $GO_2$ annulus are 0.345 in. and 0.46 in., respectively.

2.4.2.1.2. Scope of Cold Flow Experiments

Cold flow experiments were conducted for the coaxial-type injector, Fig. 2.4.21, to improve understanding of the atomization characteristics of the injector. Water/helium/nitrogen fluids were used to simulate the RP-1/$GH_2$/$GO_2$ propellants. The mass flowrates of water, helium and nitrogen were 0.267 lbm/s, $1.7 \times 10^{-3}$ lbm/s and $2.05 \times 10^{-2}$ lbm/s, respectively. Since the water flow was swirled, the flow exited the inner post of the injector as a hollow cone sheet. The water flow velocity was calculated to be about 45 ft/s. The helium and nitrogen injection velocities were 455 ft/s and 558 ft/s, respectively. Cold flow experiments were

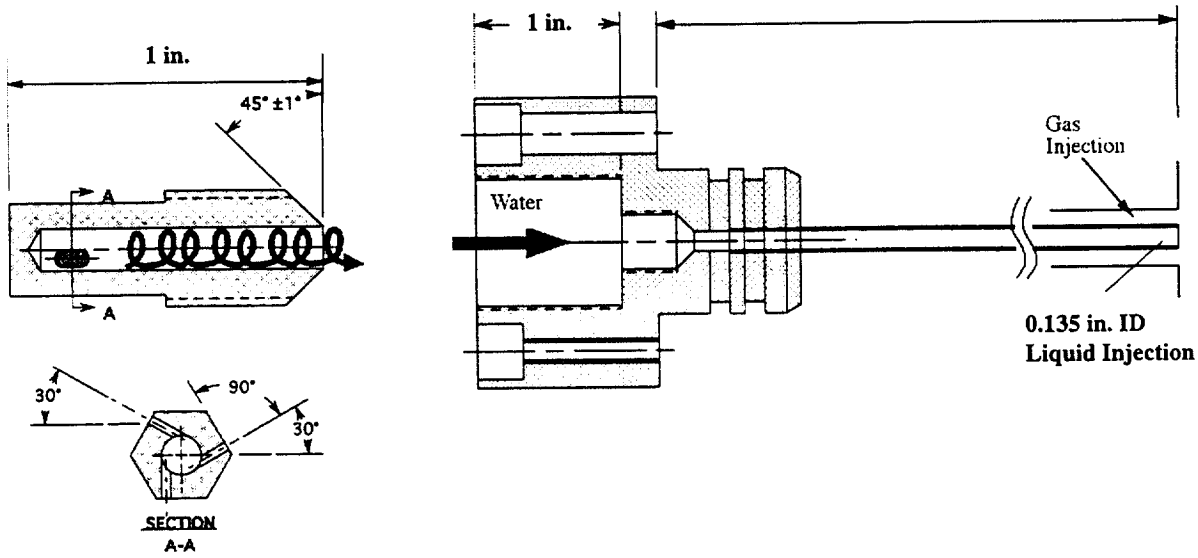


**Fig. 2.4.22. Schematic of swirler design for coaxial-type tri-propellant injector.**

conducted with water only through the swirl post, water through the swirler, no flow through the first annulus and nitrogen through the second annulus, and finally, water through the swirler, helium through the first annulus and nitrogen through the second annulus. In this manner, the effects of each annulus flow on the overall atomization of the swirling liquid flow could be gauged.

The drop size and velocity measurements were made using phase Doppler interferometry. The implementation of the technique was described earlier in the section, however, for completeness is briefly discussed here. The technique extends the basic principles of the conventional dual beam laser Doppler velocimeter to obtain particle size in addition to velocity. An argon-ion laser beam is split into two equal intensity beams and focused to an intersection to form a probe volume. The receiver system was located at a 30° off axis angle to best exploit the characteristics of the interference pattern of the refractive water drops. The receiving system consists of three detectors at appropriate separations that independently measure the burst signal generated by drops traversing the probe volume, albeit with a phase shift. The velocity of the particle is then extracted from the temporal frequency of the burst signal, whereas the particle size is calculated from the measured phase shift between any two detectors and the *a priori* calculated linearity between the detector separation and the phase angle.

2.4.2.1.3. Scope of Hot Fire Experiments

The tri-propellant RP-1/$GH_2$/$GO_2$ uni-element hot fire experiments were conducted over a range of hydrogen addition conditions at overall near-stoichiometric conditions. The chamber utilized for the experiments is described in Section 2.2. The scope of these experiments involving the coaxial-type injector was to verify the effects of hydrogen addition on the performance. The base case for the experiments was $GO_2$/RP-1 combustion at an O/F mass flow ratio of 2.4. For $GH_2$ mass addition of 5 and 10% of RP-1 flowrate, the RP-1 and $GO_2$ flowrates were adjusted such that the O/F ratios between $GO_2$/RP-1 and $GO_2$/$GH_2$ were 2.4 and 8, respectively.

### 2.4.2.2. Results and Discussion

2.4.2.2.1. Cold Flow Results

For the cold flow experiments, drop size and velocity measurements were made using phase Doppler interferometry for the coaxial-type tri-propellant injector shown in Fig. 2.4.21 under cold flow (simulants) atmospheric pressure conditions. For hot-fire experiments described later, the RP-1 is introduced through the central post and swirled using a tangential swirl nut. Photographs of the flowfield under cold flow conditions indicated that the full swirl cone angle for this post is 35°. $GH_2$ and $GO_2$ are injected through the first and second annular flow passages, respectively. The water/helium/nitrogen flow conditions for these cold flow experiments were described earlier. To document the effect of added gas flows on the atomization of the swirling water flow, measurements of the drop size and velocity field were made for injector flows of water only, water and nitrogen, and water, helium and nitrogen. The radial variations of the arithmetic mean drop size ($D_{10}$) and mean drop velocity are shown in Figs. 2.4.23 and 2.4.24, respectively, for three axial measurement locations. The corresponding radial profiles of percent validation for the measurements are shown in Fig. 2.4.25.

Inspection of the drop size measurements shown in Fig. 2.4.23 shows that the added high speed gas flows enhance the atomization characteristics of the injector. The results for the pure water case indicate that the spray is hollow cone, i.e. at a given axial location, the drop size is smallest at the centerline, increases to a peak value with radial distance, and then decreases. Note that for the water flow case, drop size and velocity measurements could not be made at the

2 in. axial location because at this location, the spray field is dominated by sheet vestiges and ligaments from the fragmenting conical liquid sheet. Comparison of the drop size measurements between the 5 and 8 in. measurement locations shows that the spray size is uniform. In contrast to these results, the drop size field significantly changes with co-flow of gas. The radial profiles of drop size for the water/nitrogen and water/helium/nitrogen flows peak at the centerline and decrease with radial distance. For the flow conditions of these experiments, the drop size field is similar for the water/nitrogen and water/helium/nitrogen flows.

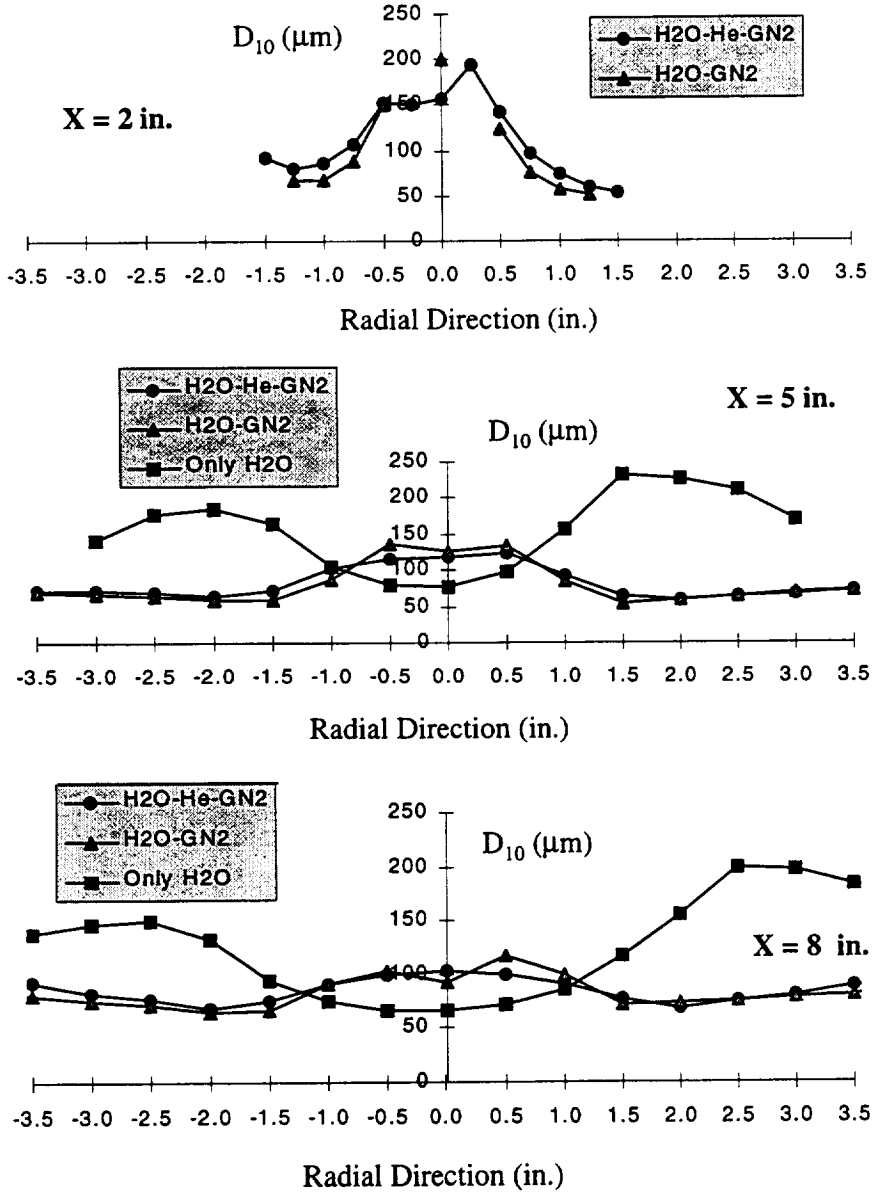


**Fig. 2.4.23. Radial variation of arithmetic mean diameter, $D_{10}$ for three (2, 5 and 8 in.) axial locations. Note S.I. units in graphs.**

The corresponding drop mean velocity results depicted in Fig. 2.4.24 also differ between the pure water, and water/nitrogen and water/helium/nitrogen flows. For the water flow case, the mean drop velocities at the 5 and 8 in. axial locations do not change with radial location. In contrast to these results, the addition of the high speed gas flows accelerates the drop field in the central part of the spray. Again, no significant mean drop velocity differences are noted between the water/nitrogen and water/helium/nitrogen flowfields.

The percent validation rates for the PDPA measurements shown in a similar manner in Fig. 2.4.25 indicate that except for the 2 in. axial location, the rates are between 65 and 90%.

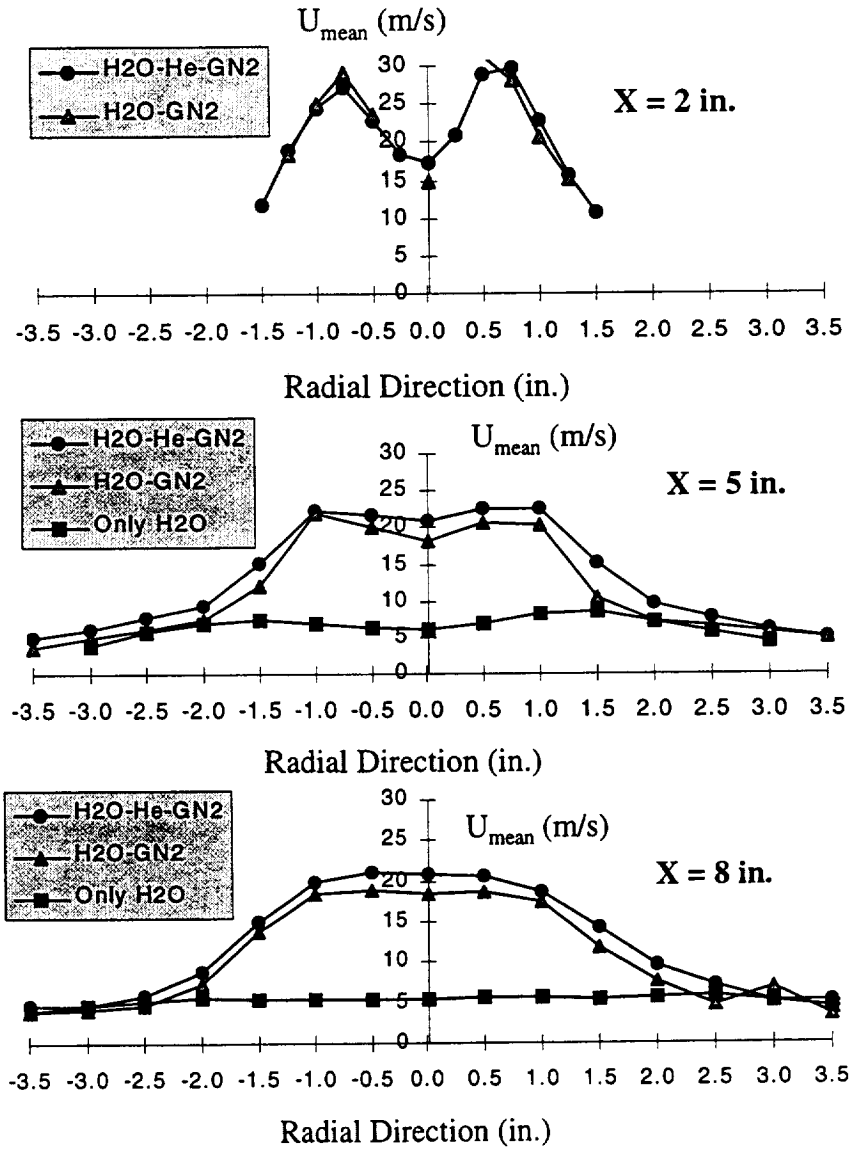


**Fig. 2.4.24. Radial variation of mean drop velocity for three (2, 5 and 8 in.) axial locations. Note S.I. units in graphs.**

Since the phase Doppler interferometric technique rejects measurements based on drop asphericity and signal to noise criteria, the validation rates provide an indication of drop sphericity and drop cloud local number density. For the results shown here, the low validation rates (40%) at the central part of the flowfield for the 2 in. axial location indicates the presence of a dense drop cloud with aspherical liquid structures. Since with axial distance from the injector, the spray consists of mainly spherical drops, the validation rates increase with downstream distance.

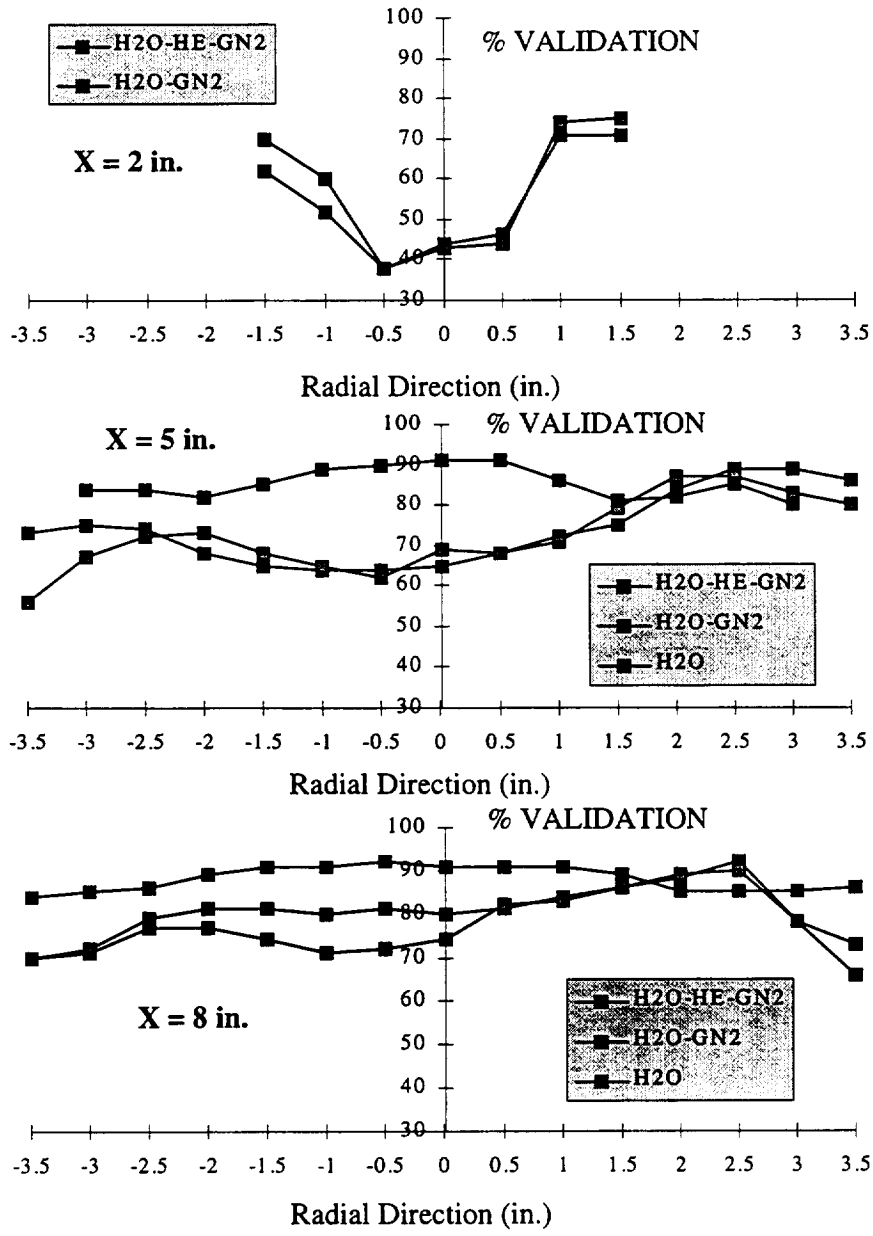


**Fig. 2.4.25. Radial variation of % validation for phase Doppler interferometric measurements of drop size for three (2, 5 and 8 in.) axial locations.**

These cold flow measurements provide a qualitative understanding of the atomization characteristics and overall fluid dynamics of the coaxial-type tri-propellant injector. Combustion experiments involving this injector are discussed next.

2.4.2.2.2. Hot Fire Results

Hot fire experiments were conducted for three different flow cases for the coaxial-type tri-propellant injector. These results summarized in Table 2.4.2 clearly indicate that $c^*$ efficiency increases with $GH_2$ addition. The first case corresponding to RP-1/$GO_2$ combustion at an O/F mass flow ratio of 2.43 indicates low $c^*$ efficiency. Note that the $c^*$ efficiency was calculated with, and without, the $GN_2$ flow used for cooling the rocket windows. For cases 2 and 3 of Table 2.4.2 corresponding to $GH_2$ mass addition of 5 and 10%, the $c^*$ efficiencies are 0.96 and 0.98.

Both visible and ultraviolet (UV) images of the near-injector flowfield for the test conditions corresponding to case 3 of Table 2.4.2 are shown in Fig. 2.4.26. The image on the left shows that the $GO_2/GH_2$ flame is anchored to the $GH_2$ post tip and that the RP-1 flow crosses the $GO_2/GH_2$ flame downstream of the injector. Inspection of the UV photograph on the right shows

**Table 2.4.2. Flow Conditions for Coaxial-Type Injector.**

| | **Case 1 RP-1/$GO_2$** | **Case 2 RP-1/$GH_2$/$GO_2$ (5% $GH_2$ Addition)** | **Case 3 RP-1/$GH_2$/$GO_2$ (10% $GH_2$ Addition)** |
|---|---|---|---|
| $\dot{m}_{GO_2}$ (lbm/s) | 0.823 | 0.789 | 0.785 |
| $\dot{m}_{RP\text{-}1}$ (lbm/s) | 0.339 | 0.289 | 0.251 |
| $\dot{m}_{GH_2}$ (lbm/s) | N/A | 0.015 | 0.025 |
| $\dot{m}_{GN_2}$ (lbm/s) | 0.031 | 0.029 | 0.029 |
| O/F ($GO_2/GH_2$) | N/A | 8 | 8 |
| O/F ($GO_2$/RP-1) | 2.43 | 2.33 | 2.33 |
| $P_C$ (theoretical) (psia) (without $GN_2$ in calculations) | 525 | 508 | 504 |
| $P_C$ (theoretical) (psia) (with $GN_2$ in calculations) | 535 | 518 | 514 |
| $P_C$ (measured) (psia) | 440 | 499 | 503 |
| $c^*$ efficiency (without $GN_2$ in calculations) | 0.84 | 0.98 | 0.999 |
| $c^*$ efficiency (with $GN_2$ in calculations) | 0.82 | 0.96 | 0.98 |

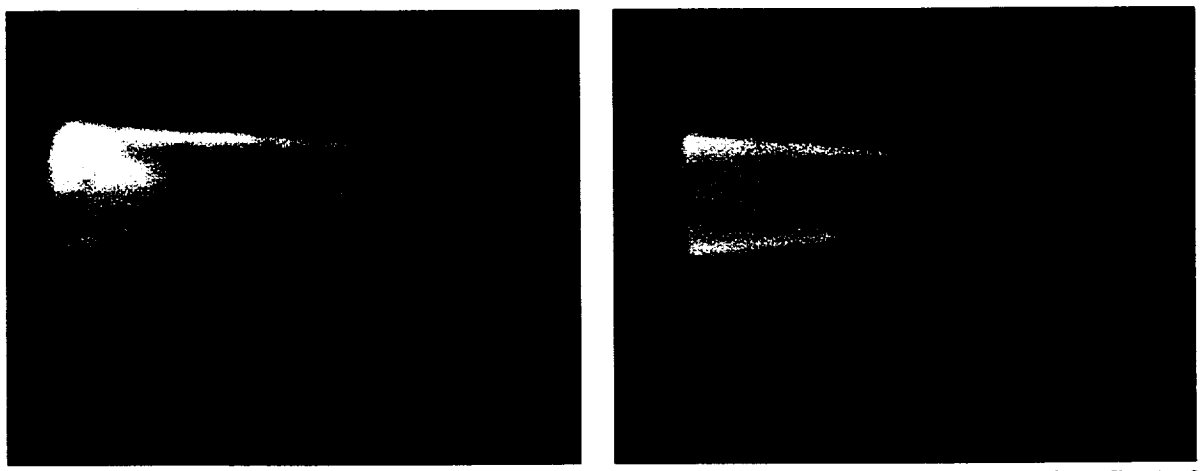

**Fig. 2.4.26. Photographs of the near-injector (0 to 2 in.) combusting flowfield for RP-1/$GH_2$/$GO_2$ propellants. Left and right photographs are for visible light and ultraviolet (UV) only. Flow is from right to left. Flow conditions correspond to (case 3 in Table 2.4.2) 10% $GH_2$ addition and had a measured c* efficiency of 98%.**

that the intensity of UV light increases at the point where the RP-1 fuel crosses the $GO_2$/$GH_2$ flame indicating $GO_2$/RP-1 combustion.

The improved $c^*$ efficiency with $GH_2$ addition to RP-1/$GO_2$ combustion noted here for the coaxial-type injector complements the experimental results obtained by the Japanese researchers [3-6] and the effervescent injector research reported here. Similar to the effervescent injector, the coaxial-type injector was designed for integral $GH_2$ addition to the RP-1/$GO_2$ flows. For this injector, the additional $GH_2$ flow significantly affects the liquid RP-1 atomization characteristics as attested by visualizations of the spray field and drop size measurements made under cold flow conditions. The same qualitative arguments presented earlier for the effervescent injector again hold true in explaining the increase in $c^*$ efficiency of RP-1/$GO_2$ combustion with $GH_2$ addition for this injector. The fast reaction rate of $GH_2$ compared to that of RP-1 translates to a high temperature oxidizer rich environment in the near-injector region. Clearly, fast $GH_2$/$GO_2$ combustion would enhance RP-1 drop heatup and vaporization process; however, based on the single RP-1 drop combustion results reported earlier, the degree of enhancement may not be significant. Additionally, the effects of $GH_2$ on the chemical kinetics of RP-1/$GO_2$ combustion as suggested by Rhys and Hawk [23] may also play a role. The measured improvement in $c^*$ efficiency with $GH_2$ addition is viewed as being mainly due to improved RP-1 atomization and partially due to higher RP-1 drop vaporization rates resulting from the presence of a high temperature oxidizer-rich zone (products of fast reacting $GH_2$/$GO_2$ combustion) surrounding the RP-1 drop cloud.

## 2.5. BI-PROPELLANT LOX/$GH_2$ STUDIES AT NEAR-STOICHIOMETRIC CONDITIONS

In this section, studies for LOX/$GH_2$ shear coaxial elements for sub- and super-critical conditions (of LOX) are reported. A two-element geometry was considered to assess element to element interactions. The shear coaxial element was chosen for these studies because historically, for the LOX/$GH_2$ propellant combination, the element of choice has been the shear coaxial injector. The shear coaxial injector has been successfully used in the J-2, RL10A-1 and Space Shuttle Main Engine (SSME).

The current studies of the two-element LOX/$GH_2$ shear coaxial injector extends earlier work at Penn State conducted for a uni-element version of the injector at sub-critical conditions [22, 24-25]. Since the current studies build on the earlier work, a brief summary of the earlier work is provided. Experiments for mapping the LOX atomization characteristics in a LOX/$GH_2$ combusting flowfield for a uni-element shear coaxial injector (LOX post inner diameter, LOX post outer diameter and $GH_2$ annulus outer diameter of 0.135, 0.165 and 0.28 in., respectively) were conducted at chamber pressures of 270 and 405 psia. The flowrates of LOX and $GH_2$ were 0.37 and 0.075 lbm/s, respectively, for a mixture ratio of 5. The experiments involved laser sheet imaging of the LOX region and phase Doppler interferometry measurements of LOX drops. Mie scattered light images from LOX for the 270 psia case at three axial locations are shown in Fig. 2.5.1. The first image corresponding to 0-2 in. from the injector face clearly shows that the LOX region is confined to a narrow circumferential region. From the image, it is not quite clear whether the LOX core is intact or not; however distinct sinusoidal structures are evident. Further downstream at 2-4 in., the LOX region is grainier in structure, possibly attesting to the presence of small LOX drops surrounding a core region. Finally, at the furthest measurement location, 5-7 in., the image shows the presence of disconnected drop/ligament

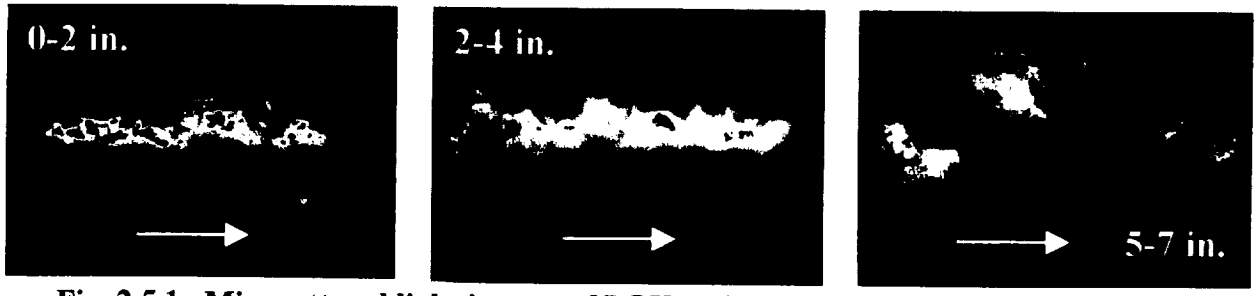


**Fig. 2.5.1. Mie scattered light images of LOX region for LOX/$GH_2$ combustion [24].**

clouds that travel in the axial direction in a sinusoidal manner. These images show the presence of LOX far from the injector face. The complementary LOX drop size and velocity measurements indicated that for the interrogation region (up to 7 in. from injector face), the LOX jet was largely un-atomized.

The experiments described in this section were based on the results of the earlier study. A two-element injector configuration was chosen as the test geometry to gauge the effects of inter-element flowfield interactions. In addition, the chamber pressure range of the experiments was increased to a maximum of about 900 psia to include measurement points in the super-critical pressure range for LOX. Schlieren photography instead of laser sheet imaging was attempted as the visualization technique to support flame imaging.

### 2.5.1. EXPERIMENTAL SCOPE

In this section, the two-element shear coaxial injector geometry, target experimental flow conditions and scope for both cold flow and hot fire experiments are presented.

#### 2.5.1.1. Two-Element Shear Coaxial Injector Geometry

A schematic of the two-element shear coaxial injector design is shown in Fig. 2.5.2. The element size for the two-element shear coaxial injector was based on the earlier uni-element

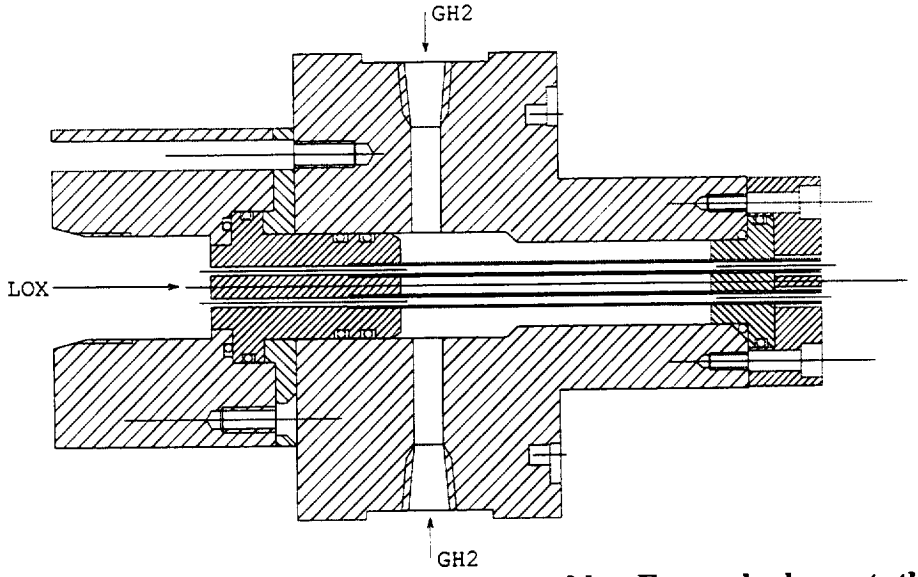


**Fig. 2.5.2. Two-element shear coaxial injector assembly. For each element, the LOX post inner and outer diameters are 0.085 and 0.125 in., respectively. The outer diameter of the $GH_2$ annulus is 0.2 in. Two injectors were fabricated; one with center to center distance between the two elements of 0.3 in and the other of 0.5 in.**

**Table 2.5.1. Target Flow Conditions for Two-Element Injector Experiments.**

| | LOX | | $GH_2$ | | CHAMBER | | | | |
|---|---|---|---|---|---|---|---|---|---|
| Case | Flowrate per Element (lbm/s) | U (ft/s) | Flowrate per Element (lbm/s) | U (ft/s) | Total Flowrate for Two-Elements (lbm/s) | Pressure (psia) | O/F | Velocity Ratio (F/O) | Momentum Flux Ratio (F/O) |
| A | 0.161 | 65.6 | 0.0324 | 2434 | 0.388 | 287 | 5.0 | 38.1 | 7.6 |
| B | 0.161 | 65.6 | 0.0324 | 1667 | 0.388 | 421 | 5.0 | 26.0 | 5.2 |
| C | 0.161 | 65.6 | 0.0324 | 1443 | 0.388 | 486 | 5.0 | 22.6 | 4.5 |
| D | 0.232 | 91.9 | 0.0465 | 1125 | 0.556 | 892 | 5.0 | 12.2 | 2.5 |
| E | 0.146 | 59 | 0.0260 | 630 | 0.344 | 889 | 5.6 | 10.9 | 1.9 |

$LOX/GH_2$ shear coaxial experiments conducted at Penn State [22, 24-25]. For each element, the LOX post inner and outer diameters are 0.085 and 0.125 in., respectively. The outer diameter of the $GH_2$ annulus is 0.2 in. The LOX post is not recessed with respect to the injector face.

The element to element centerline distance was scaled with respect to the SSME shear coaxial elements in terms of the $GH_2$ annulus outer diameter [26]. This scaling indicated that an element to element centerline distance of 0.3 in. would provide a basis for comparison between the designed and SSME shear coaxial injector. A second injector with an element to element distance of 0.5 in. was also fabricated for comparison purposes.

The target hot fire experimental conditions for the two-element injector are presented in Table 2.5.1. The first three target conditions correspond to sub-critical operation, whereas the last two conditions target super-critical conditions. The calculated $GH_2$ to LOX velocity and momentum ratios are also tabulated. Note that for target cases D and E, these two ratios are close to J-2 engine operation [2].

### 2.5.1.2. Scope of Cold Flow Experiments

Cold flow experiments were conducted for the two-element shear coaxial injector using water/$GN_2$ simulants. The experiments involved flowfield visualizations for a matrix of water/$GN_2$ flows. Based on these visualizations and the hot fire target flow conditions, one flow conditions was chosen for drop size and velocity measurements. The flow conditions for the cold flow experiment are compared to the hot fire experiments (actual results for Case B) in Table 2.5.2. Note that in terms of scaled variables, the velocity and momentum ratios are

**Table 2.5.2. Comparison of Cold Flow/Hot Fire Experiments.**

| | Cold Flow Water/$GN_2$ | Hot Fire (Test B) LOX/$GH_2$ | Ratio Hot Fire/Cold Flow |
|---|---|---|---|
| Liquid Flowrate (lbm/s) | 0.0774 | 0.320 | 4.1 |
| Liquid Velocity (ft/s) | 15.7 | 65.6 | 4.2 |
| Liquid Density ($lbm/ft^3$) | 62.4 | 63.0 | 1.0 |
| Liquid Surface Tension (lbf/ft) | $5.07\times10^{-3}$ | $4.65\times10^{-4}$ | 0.1 |
| | | | |
| Gas Flowrate (lbm/s) | 0.0108 | 0.063 | 5.8 |
| Gas Velocity (ft/s) | 571 | 1640 | 2.9 |
| Gas Density ($lbm/ft^3$) | 0.071 | 0.144 | 2.0 |
| | | | |
| Chamber Pressure (psia) | 14.7 | 420 | 29.0 |
| O/F | 7.2 | 5.1 | 0.7 |
| Velocity Ratio | 36.3 | 25.0 | 0.7 |
| Momentum Ratio | 5.06 | 4.83 | 1.0 |
| Reynolds Number | $7.53\times10^3$ | $3.79\times10^5$ | 50.3 |
| Weber Number | $9.50\times10^2$ | $1.69\times10^5$ | 177.9 |

comparable, whereas the liquid Reynolds number and Weber numbers are orders of magnitude different due to the differences in liquid viscosity and surface tension between the hot fire and cold flow experiments. The phase Doppler interferometry technique was used for these measurements.

The implementation of the phase Doppler interferometric technique was described in the last section, however, for completeness is briefly discussed here. The technique, see Fig. 2.5.3, extends the basic principles of the conventional dual beam laser Doppler velocimeter to obtain particle size in addition to velocity. An argon-ion laser beam is split into two equal intensity beams and focused to an intersection to form a probe volume. The receiver system was located at a 30° off axis angle to best exploit the characteristics of the interference pattern of the refractive water drops. The receiving system consists of three detectors at appropriate separations that independently measure the burst signal generated by drops traversing the probe volume, albeit with a phase shift. The velocity of the particle is then extracted from the temporal frequency of the burst signal, whereas the particle size is calculated from the measured phase

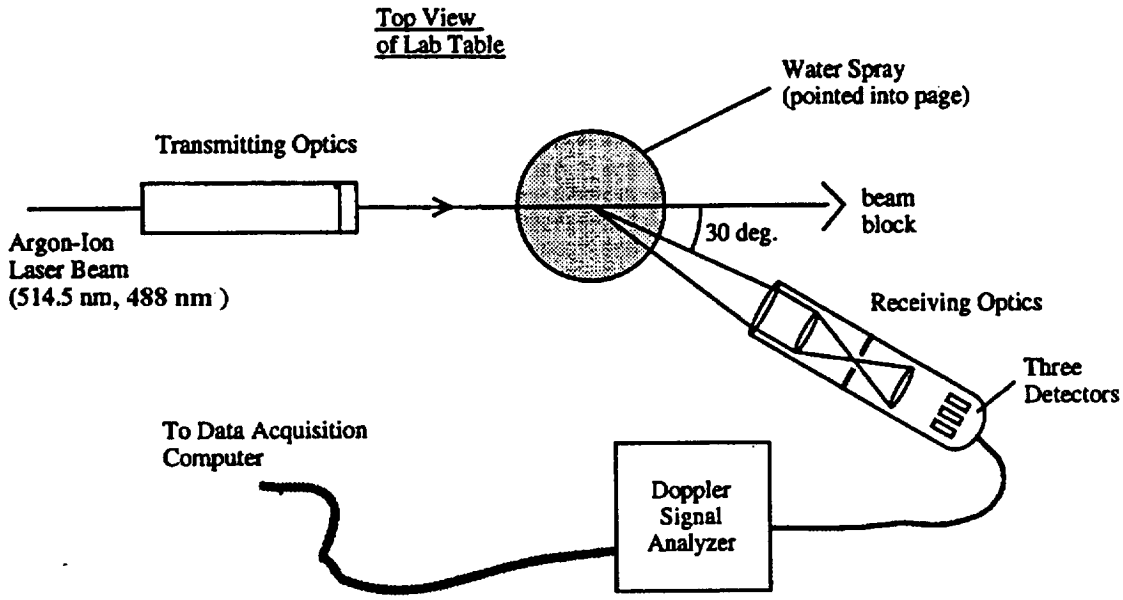


**Fig. 2.5.3. Phase Doppler interferometry setup for drop size and velocity measurements.**

shift between any two detectors and the *a priori* calculated linearity between the detector separation and the phase angle.

### 2.5.1.3. Scope of Hot Fire Experiments

The $LOX/GH_2$ two-element hot fire experiments were conducted for a nominal O/F ratio of 5 for chamber pressures ranging from 300 to over 850 psia as detailed in Table 2.5.1. The chamber utilized for the experiments is described in Section 2.2. Note that the chamber pressure was varied by replacing nozzles with different throat areas. Flame photography and Schlieren imaging were used to qualitatively assess the near-injector face combustion zone.

Schlieren photography was utilized as the technique for qualitative visualizations of the $LOX/GH_2$ flowfield. The technique highlights regions of density gradients within flows and is therefore well suited for $LOX/GH_2$ combustion environments [27-28]. A schematic of the Schlieren optical setup is shown in Fig. 2.5.4. The system consists of a point light source, two parabolic mirrors, a knife edge and a 35 mm camera. The point light source was obtained by directing the beam from a Nd:Yag laser (532 nm wavelength) on to a stainless steel plate. The camera and the laser were both triggered at 2 Hz. Synchronization was provided by the camera controller (four channel digital delay/pulse generator) used to record the diffracted light in phase with the laser. The filters used between the knife edge and the camera were a WG-320 filter, a BG-3 filter and a 532 nm NOTCH filter.

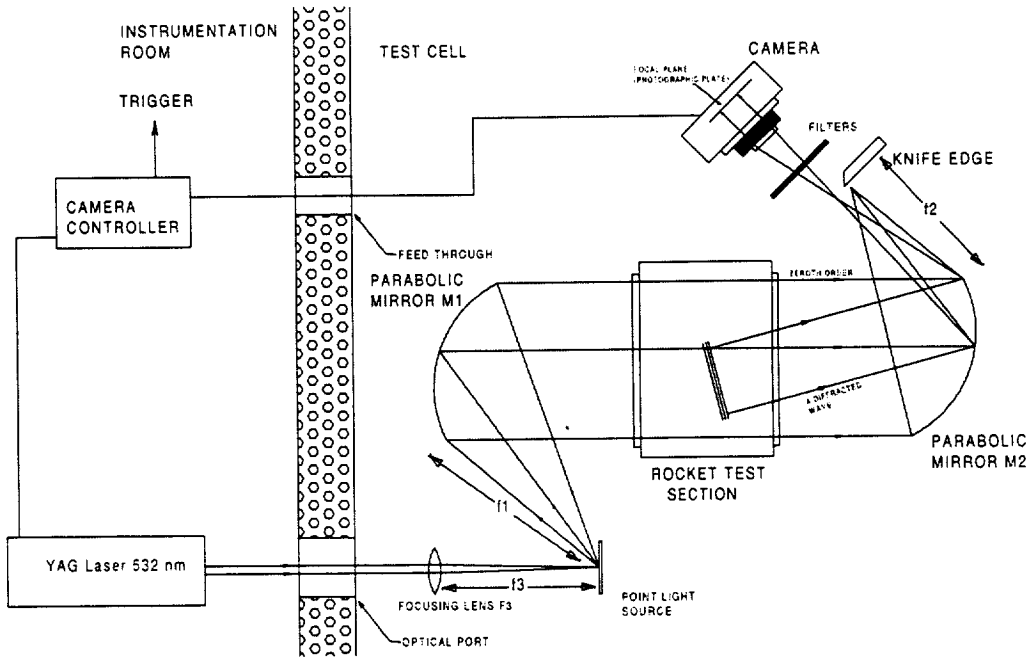


**Fig. 2.5.4. Optical setup for Schlieren photography.**

## 2.5.2. RESULTS AND DISCUSSION

### 2.5.2.1. Cold Flow Results

Visualizations of the water/$GN_2$ flows from the two-element injector are shown in Fig. 2.5.5 at atmospheric pressure conditions for a matrix of operating conditions. A total of 12 images are shown in the figure. For the inset images, the visualizations show the effect of increasing liquid velocity (left to right) and gas velocity (top to bottom) on the resulting spray field. Inspection of the images show that for a fixed gas velocity, increasing the liquid velocity results in less atomized sprays. In contrast, for a fixed liquid velocity, increasing the gas velocity improves atomization. These observations are consistent with the notion that for the shear coaxial injector, atomization increases with increasing gas to liquid velocity and momentum ratios.

Based on these visualizations and the target hot fire experiments, one cold flow condition was chosen for further characterization in terms of quantitative drop size and velocity measurements. The flow conditions of the experiment were devised to equate the geometry, and velocity and momentum ratios as closely as possible. Since the same injector was used, geometric similitude was achieved. The cold flow conditions for the experiment are compared to the flow conditions of the hot fire experiments (Case B; actual hot-fire conditions) in Table 2.5.2.

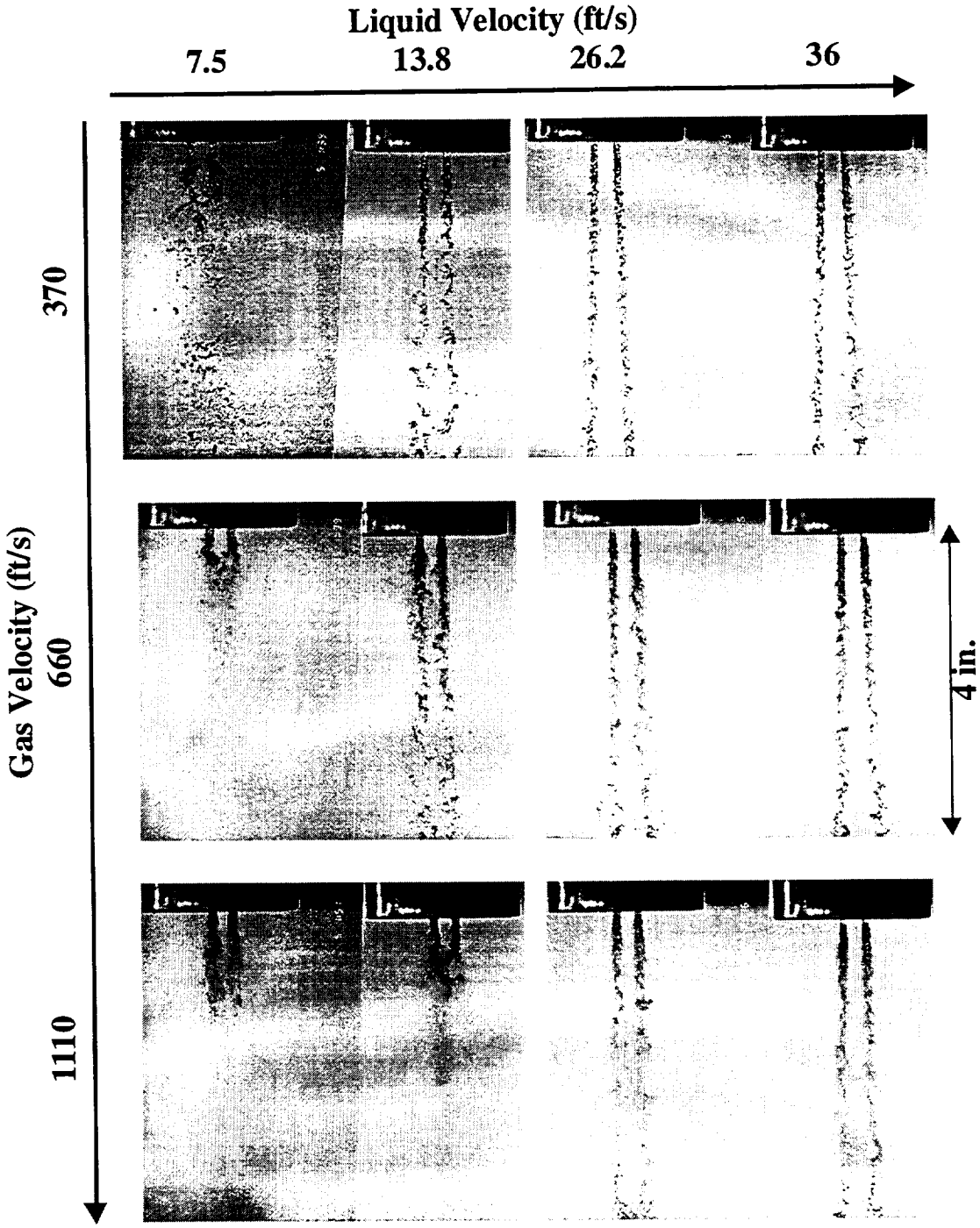


**Fig. 2.5.5. Cold flow visualizations of the two-element shear coaxial injector flowfield for a matrix of water/nitrogen flow conditions.**

Note that water and LOX have nearly the same density but different surface tension and dynamic viscosities. On the other hand, gaseous nitrogen has a density 14 times that of gaseous hydrogen and therefore, a cold flow experiment with $GN_2$ at atmospheric pressure has the same gas density as a hot fire experiment with $GH_2$ at 206 psia. With these differences in fluid properties,

relatively close matching of the velocity and momentum ratios are possible but simultaneous matching of the liquid Reynolds number and liquid/gas Weber number is not possible. The hot fire/cold flow ratios between the two experiments are also provided in Table 2.5.2 for reference.

Radial profile measurements of drop size and velocity were made for the two-element injector at an axial location 10.25 in. from the injector face. In terms of the inner diameter of a post, this translates to 120 L/d. At this axial location, drop size/velocity measurements were made at 0.1 in. intervals in the radial location. For some radial locations, measurements at finer intervals (0.05 in.) were also made. In scaled units, the center to center distance between the two elements is 3.5. The radial axis is defined to be centered at the center point between the two elements. For each measurement point, in excess of 10000 drop measurements were used to calculate statistics.

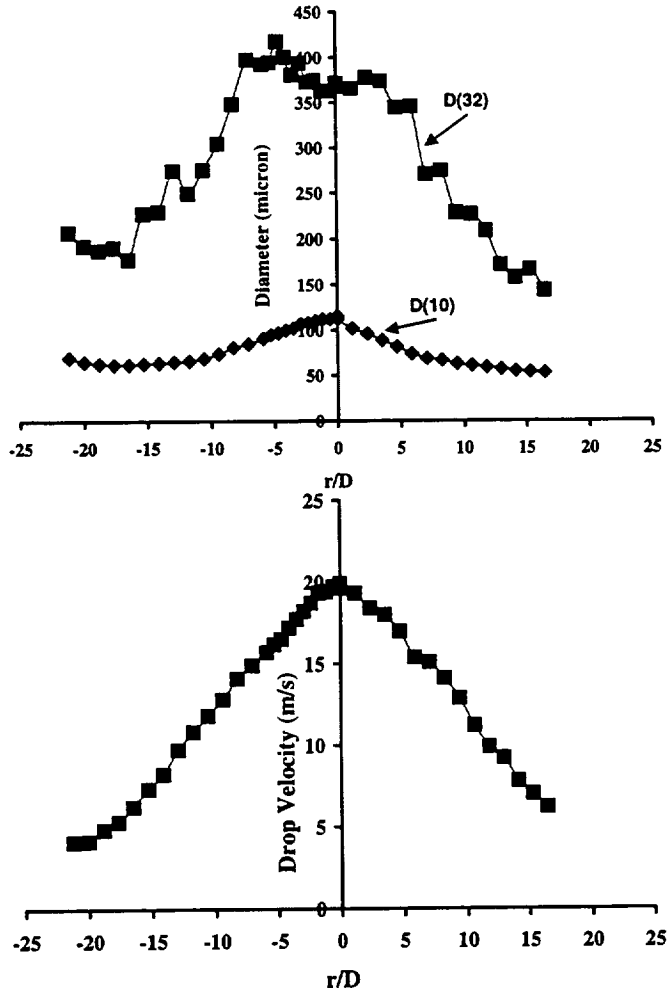


**Fig. 2.5.6. Phase Doppler interferometry measurements of drop size and velocity for an axial distance of 10.2 in. (z/D = 260). The radial axis is non-dimensionalized with the inner diameter of the post (D=0.085 in.). Flow conditions are detailed in Table 2.5.2.**

The measured arithmetic mean diameter, $D_{10}$, and Sauter mean diameter, $D_{32}$, are plotted versus non dimensional radial distance, *R/d* (*d* is the inner diameter of the post) in the top inset graph of Fig. 2.5.6. The bottom inset graph shows the corresponding mean drop velocity versus scaled radial distance. At this axial measurement location far from the injector face, the mean drop mean size measurements do not show much evidence in terms of injector element origin. The Sauter mean diameter radial profile shows a slight decrease in the center region between the two elements but this is not evident in the corresponding profile for the arithmetic mean diameter. Away from the center region, both profiles show a decrease in the drop size. The mean drop velocity profile also shows no indication in terms of injector element origin. Both these sets of measurements indicate that the flowfields from the two injector elements are mixed at this far axial measurement location. The corresponding drop validation profile (not shown here) shows a minimum of about 60% validation in the center region that increases to about 90% with radial distance. The phase Doppler interferometric technique rejects measurements based on drop asphericity, signal to noise limits and both velocity and size dynamic range limits. The relatively low percent validation (60%) in the region between the two elements indicates that within this region the liquid jets from the two elements have not completely atomized into spherical drops.

### 2.5.2.2. Hot Fire Results

The results of the LOX/$GH_2$ hot fire experiments for the two-element shear coaxial injector are presented in this section. Results include injector performance characteristics and flowfield visualizations.

#### 2.5.2.2.1. Performance

Over thirty rocket firing tests were conducted for the two geometric variations (0.3 and 0.5 in. separation) of the two-element shear coaxial injector for the target flow conditions presented in Table 2.5.1. Sample pressure versus time traces for both sub- and super-critical operation are presented in Fig. 2.5.7, whereas tabulated performance numbers are summarized in Table 2.5.3. Note that for the calculation of the c* efficiencies, the small amount of $GN_2$ utilized for window cooling was included in the calculations.

The performance numbers indicate c* efficiencies from 0.93 to 0.99 for the sub-critical operating points. For the high pressure points (Case D and E), the c* efficiencies are lower.

**Table 2.5.3. Performance of Two-Element Injector Experiments.**

| Case | Total LOX Flowrate (lbm/s) | Total $GH_2$ Flowrate (lbm/s) | $GN_2$ Flowrate (lbm/s) | O/F | $P_c$ (psia) | c* Efficiency | Velocity Ratio (F/O) | Momentum Ratio (F/O) |
|---|---|---|---|---|---|---|---|---|
| ***Injector with 0.3 in. Separation Between Elements*** | | | | | | | | |
| A | 0.333 | 0.063 | 0.040 | 5.3 | 305 | 0.993 | 34.6 | 6.52 |
| B | 0.320 | 0.063 | 0.040 | 5.1 | 420 | 0.957 | 25.4 | 4.96 |
| C | 0.333 | 0.063 | 0.040 | 5.3 | 510 | 0.983 | 20.5 | 3.87 |
| E | 0.294 | 0.069 | 0.055 | 4.3 | 878 | 0.825 | 14.8 | 3.47 |
| ***Injector with 0.5 in. Separation Between Elements*** | | | | | | | | |
| A | 0.322 | 0.064 | 0.039 | 5.0 | 304 | 1.003 | 35.5 | 7.09 |
| B | 0.317 | 0.063 | 0.041 | 5.0 | 408 | 0.934 | 26.4 | 5.26 |
| C | 0.309 | 0.063 | 0.040 | 4.9 | 493 | 0.994 | 21.9 | 4.47 |
| D | 0.436 | 0.090 | 0.048 | 4.8 | 851 | 0.952 | 12.7 | 2.62 |

The cause for this is partially due to the correspondingly lower momentum ratios for these cases. Inspection of the pressure versus time plots shown in Fig. 2.5.7 shows that for the high chamber pressure case, steady state pressure was not achieved. Since the c* efficiency for this case was calculated based on the highest achieved chamber pressure, the c* efficiency was lower. Longer time duration experiments were not attempted since this could have compromised the window section of the rocket. In any case, the achieved chamber pressures for these cases exceeded the super-critical pressure of LOX.

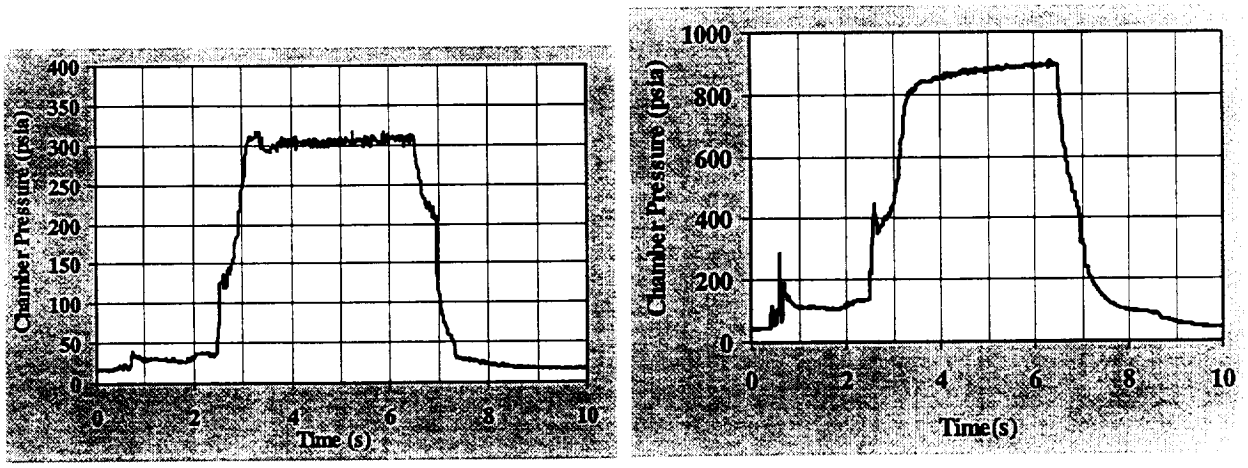


(a) (b)

**Fig. 2.5.7. Chamber pressure versus time traces for Cases A and E (Table 2.5.3). The traces are for rocket firings with the 0.3 in. separation two-element shear coaxial injector.**

2.5.2.2.2. Flowfield Visualizations

Photographs of the near-injector region were taken to provide information on the flame front and flame anchoring. The two images shown in Fig. 2.5.8 contrast the visible flame between sub-critical and super-critical pressure conditions. These images were taken for the two-element injector configuration with 0.3 in. element to element center separation distance. For both pressure conditions, the images show that the individual flames have not interacted within the axial extent of the image. In terms of scaled variables, the 2 in. axial extent of the image corresponds to 23.5 LOX post inner diameters. Similar images for the 0.5 in. separation injector (not shown here) also show similar flame spread with radial distance. For all images taken for the various flow conditions, the flame is always seen to attach to the LOX post tip. This observation is consistent with uni-element LOX/$GH_2$ shear [24-25] and swirl coaxial (next section) injector results.

The growth of flame width with axial distance was measured from all the images taken for the various flow conditions (similar to the images shown in Fig. 2.5.8). The results of these measurements are presented in scaled variables (with respect to the LOX post inner diameter) in Fig. 2.5.9. The results show very small differences between the flow conditions. The results

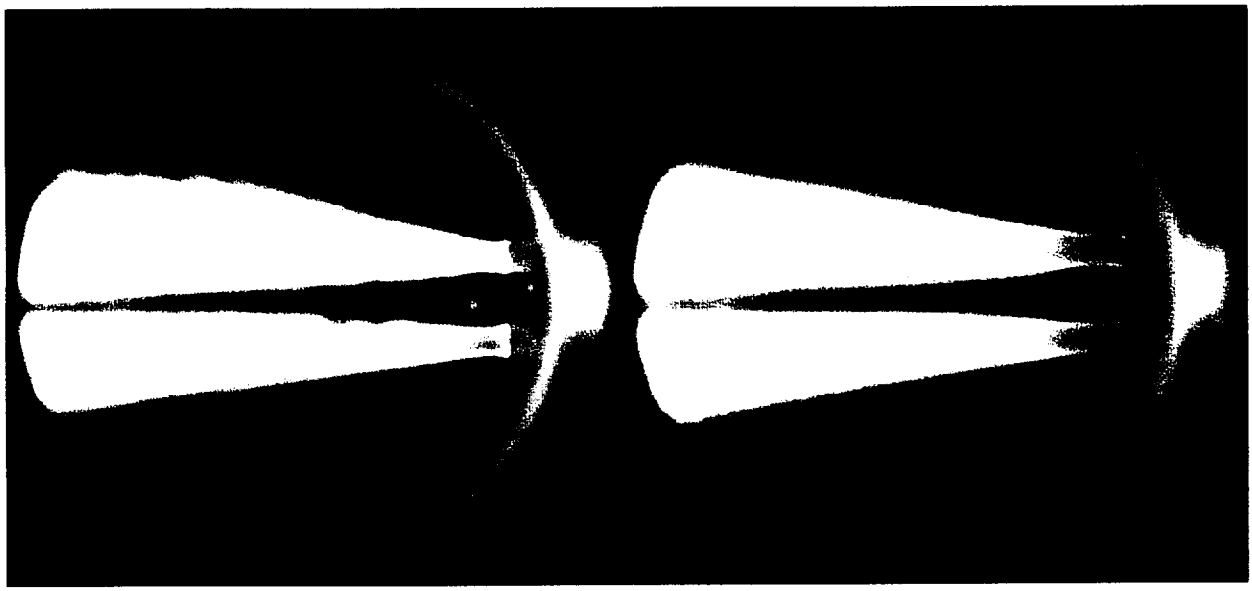

(a) (b)

**Fig. 2.5.8. Near-injector flame photographs for (a) Case B (420 psia) and (b) Case E (878 psia) of Table 2.5.3. Photographs are for injector with element center to center distance of 0.3 in. Flow is from right to left.**

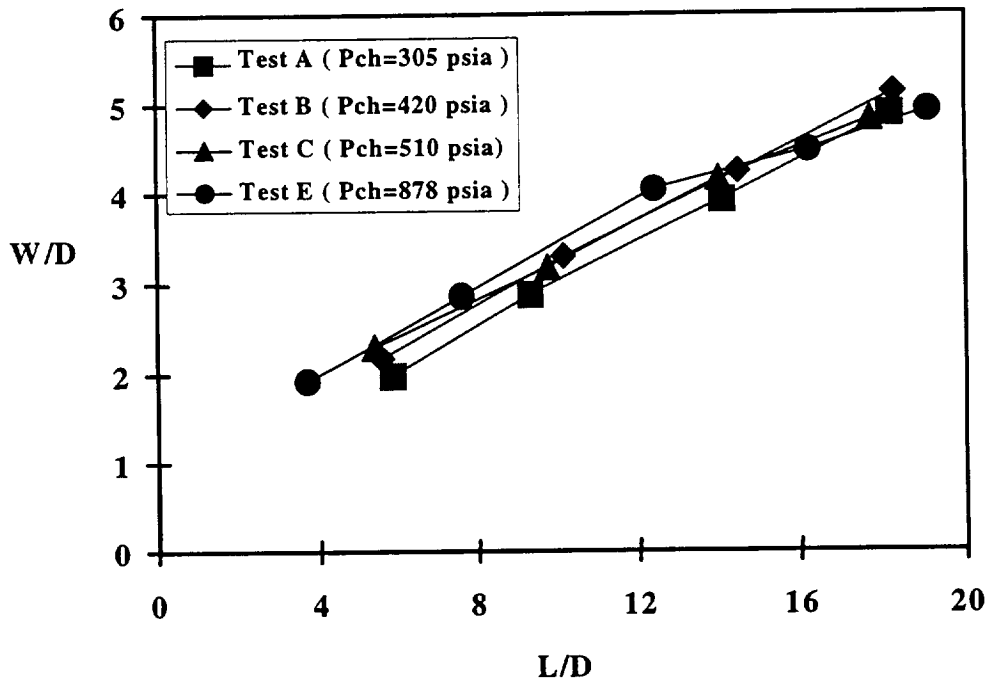


**Fig. 2.5.9. Flame width versus axial distance measured from images. Flow conditions for test cases are summarized in Table 2.5.3. Both axes are scaled with the LOX post inner diameter.**

also indicate that the included total angle of flame growth is about 10°. This indicates that in full scale engines, the near injector face region is characterized by the presence of long re-circulation flows.

Schlieren images for sub- and super-critical chamber pressure conditions are shown in Fig. 2.5.10. The quality of the images is not very good because of the highly luminous nature of the LOX/$GH_2$ flame. The image for the sub-critical chamber pressure condition is clearer than the image for the super-critical flow condition. The LOX, flame and gaseous hydrogen regions for each element can be construed for the sub-critical image, whereas for the super-critical image, the luminous flame overwhelms the Schlieren image.

The results presented in this section on near stoichiometric LOX/$GH_2$ combustion show that good performance can be achieved for the shear coaxial injector provided that the chamber is long compared to the dimensions of the element. The flames from the individual elements extended radially at about 10° for all the tested flow conditions, and consequently, flowfield interactions between elements depend on the element to element separation distance and this radial flame growth rate.

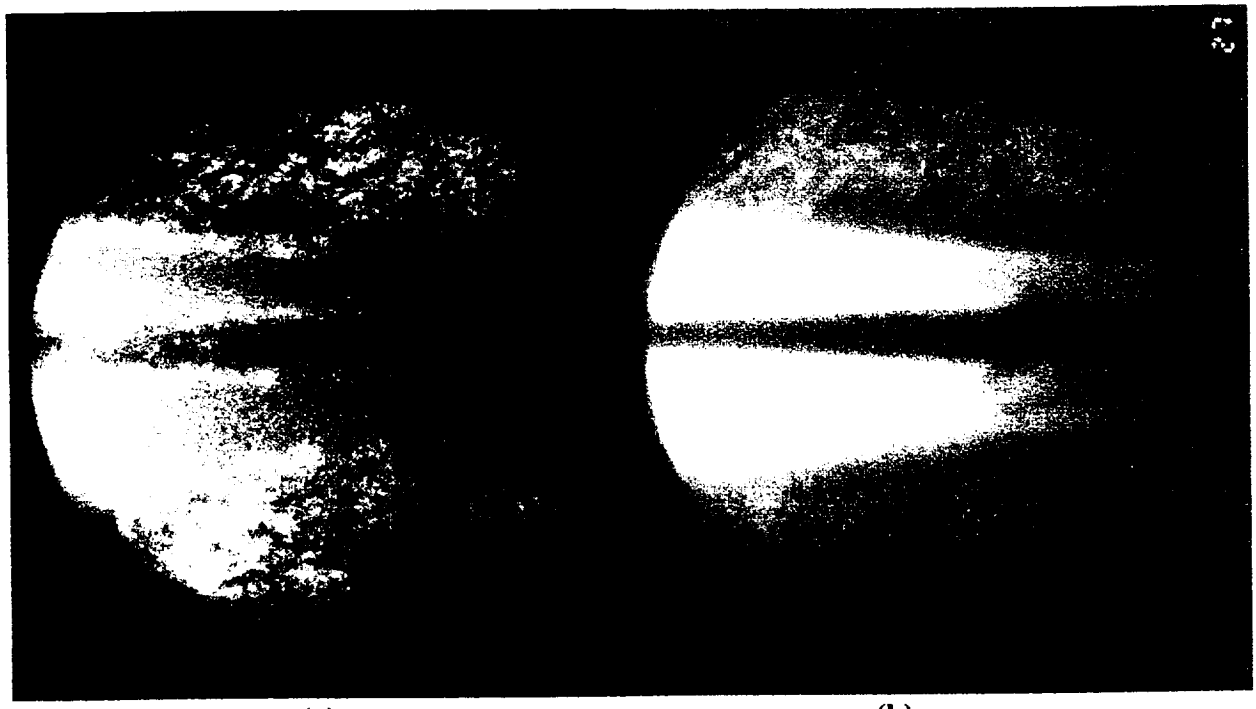

(a) (b)

**Fig. 2.5.10. Schlieren images of the near-injector flowfield for (a) Case B (420 psia) and (b) Case E (878 psia) of Table 2.5.3. Photographs are for injector with element center to center distance of 0.3 in. Flow is from right to left.**

## 2.6. OXIDIZER-RICH PREBURNER COMBUSTION AND INJECTOR TECHNOLOGY

In this section, research work carried out for oxidizer-rich combustion for both $LOX/GH_2$ and LOX/RP-1 propellant combinations are presented and discussed. The motivation for the current work is driven by the need to advance injector development technologies for oxidizer-rich preburner applications. For the $LOX/GH_2$ propellant combination, both direct injection and downstream dilution methods were investigated. However, for LOX/RP-1 propellants, only the direct injection method was investigated. The direct injection method involves the injection of all the propellants from the main injector, whereas downstream dilution involves near-stoichiometric combustion for the main injector with downstream injection of addition oxidizer. For the direct injection method, the swirl coaxial injector element was employed for $LOX/GH_2$ propellants and both the pentad and pintle injectors for LOX/RP-1 propellants. The stoichiometric core/downstream dilution approach for $LOX/GH_2$ propellants utilized a swirl coaxial element for the stoichiometric core combustion and a matrix of LOX impinging jet injectors for downstream dilution. The injector design philosophy for the propellant combinations along with results obtained for cold flow and rocket firing experiments are presented and discussed in the following three sections.

### 2.6.1. $LOX/GH_2$ DIRECT INJECTION STUDIES

In this section, the studies related to oxidizer-rich $LOX/GH_2$ combustion for a swirl coaxial injector element are presented and discussed. The research impacts future technology development goals. One of the preburners of the conceptual full-flow staged combustion engine cycle operates under oxidizer-rich conditions. The swirl coaxial injector element was chosen in favor of the shear coaxial injector element in the present study because earlier efforts indicated that mixing and combustion zone lengths are significantly reduced for the swirl element [25,29].

#### 2.6.1.1. Experimental Setup

In this section the swirl coaxial injector geometry design is discussed. Two injectors were fabricated. The first injector was specifically designed for combustion experiments. Cold flow experiments were conducted for both this injector as well as a larger scale injector designed specifically for the purpose of ascertaining scaling relationships for the swirl coaxial injector.

The scope of the cold flow and hot-fire experiments as well as the diagnostic techniques employed are also discussed in the following sub-sections.

2.6.1.1.1. Swirl Coaxial Injector Geometry

The swirl coaxial rocket propellant injector is a variant of the well-known and widely used pressure-swirl injector (or atomizer) employed in many industrial applications [30]. Although a large body of data is available for industrial pressure-swirl injectors, there has been relatively little work done on the rocket injector version of the swirl atomizer. Rocket-type swirl injectors are distinguished by their larger size and higher mass flowrate, which result in large drop sizes. They also feature large length-to-diameter ratios ($L/d$ up to 20) of the exit tube, owing to propellant supply manifolding considerations. A non-swirled coaxial gas flow, surrounding the injected liquid, is also used to allow for oxidizer/fuel mixing similar to the case of air-assist swirl atomizers. For the present work, two such units were designed and fabricated: a smaller unit, and a larger unit of twice the size. The smaller version of the injector was used mainly for the hot-fire uni-element rocket experiments, whereas both injectors were used for cold flow studies. The hydrodynamic design of the two units is identical resulting in similar discharge coefficients, spray distributions, swirl strength, etc., but the difference in scale results in significantly different drop sizes.

A schematic illustrating the injector design is depicted in Fig. 2.6.1, where the smaller geometry is shown. Liquid swirl is imparted by means of three tangential-entry slots. Without coaxial gas flow, the mechanics of operation of this type of injector are similar to standard pressure-swirl atomizers [30]. The two injectors employed in the present study are compared in Table 2.6.1. Note that the gas gap width numbers shown in the table are only for the cold flow experiments. The smaller unit delivers 0.20 lbm/s at a pressure drop of nominally 70 psia, i.e. discharge coefficient of 0.32 according to the calculation methodology of Yule and

**Table 2.6.1. Swirl Injector Characteristics**

| | *Small Injector* | *Large Injector* |
|---|---|---|
| Tube Inner Diam., $d$ | **0.135 in.** | **0.27 in.** |
| Tube Length, $L$ | 2.76 in. | 5.5 in. |
| Tube Wall thick, $t$ | 0.03 in. | 0.06 in. |
| Gas Gap Width, $D_h/2$ | 0.06 in. | 0.115 in. |
| Exit Film Thick., $\delta$ | **0.0134 in.** | **0.0268 in.** |
| Discharge Coeff., $C_d$ | 0.32 | 0.32 |
| Length/diameter, $L/d$ | 20 | 20 |
| Swirl Cone Angle | 52° | 52° |

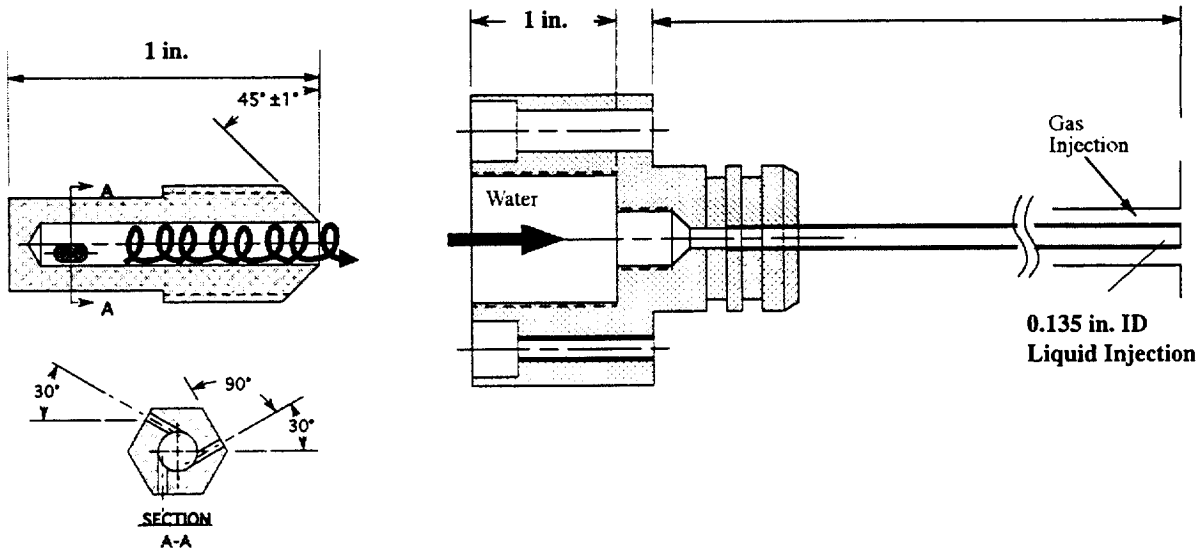


**Fig. 2.6.1 Schematic of swirl coaxial injector element.**

Chinn [31]. The liquid film thickness, $\delta$, within the tube is estimated to be 10% of the injector tube diameter. The larger element delivers liquid at the same discharge coefficient of 0.32, but provides four times the flowrate for the same pressure drop.

2.6.1.1.2. Cold Flow Experiments

Cold flow experiments with the swirl coaxial element injector were conducted to evaluate the atomization characteristics of the injector as well as to quantify possible scaling relationships. Instantaneous flowfield visualizations and drop size and velocity measurements were made using phase Doppler interferometry for both liquid only (i.e. no gas flow through annulus) and liquid/gas operations.

For liquid only swirl coaxial injector sprays, a dimensional analysis can be found in Giffen and Muraszew [32]. The analysis suggests that the spray may be described by the following functional relationship:

$$\overline{D}/d = fcn\left(\rho_l/\rho_g, \mu_l/\mu_g, We_d, Re_d, \theta\right) \qquad (2.6.1)$$

The relationship states that the globally averaged spray drop size $\overline{D}$, non-dimensionalized by injector diameter $d$, depends upon the liquid to gas density ratio ($\rho_l / \rho_g$), and viscosity ratio ($\mu_l / \mu_g$), Weber number ($We_d = \rho_l u_l^2 d/\sigma$), Reynolds number ($Re_d = \rho_l u_l d/\mu_l$), and swirl strength (in terms of cone angle). An equivalent form of this expression may be used where the

film thickness $\delta$ is substituted for $d$ as the length scale. With the hypothesis that local spray statistics may be scaled by $\delta$ as well, the following relationship could hold ($\overline{D}$ is now a local temporal average drop size)

$$\frac{\overline{D}}{\delta}\left(\frac{r}{\delta}\right) = fcn\left(\frac{\rho_l}{\rho_g}, \frac{\mu_l}{\mu_g}, We_\delta, Re_\delta, \theta\right) \tag{2.6.2}$$

This implies that local information (drop size and velocity) from one spray field can be scaled by $\delta$, and also mapped to a corresponding location in the spray field from a different size injector.

Similar arguments can be made to include the effects of annular gas flow for the swirl coaxial injector. Equation 2.6.2 can be extended to account for coaxial gas injection. Additional variables entering are the injection gas density, viscosity, and velocity ($\rho_g, \mu_g, U_g$), as well as two additional length scales, gas annulus gap size (hydraulic diameter $D_h$) and tube wall thickness ($t_w$). These can be recast into dimensionless lengths ($t_w/\delta, D_h/\delta$), transport property ratios ($\rho_g/\rho_\infty, \mu_g/\mu_\infty$), gas Reynolds number $Re_g = \rho_g U_g D_h/\mu_g$, and finally the liquid-to-gas momentum ratio $\dot{m}_l U_l/\dot{m}_g U_g$ (here $\dot{m}$ denotes flowrate).

Experiments with the small and large injectors were performed with water/nitrogen sprays at ambient pressure to validate/refute the aforementioned hypotheses. The flow conditions were chosen to equate the Weber number for the two sprays, as well as the liquid/gas momentum ratio. Hence, all parameters in Equation 2.6.2 remained unchanged, except for some difference in liquid and gas Reynolds number, but the effect of this on the spray is viewed to be secondary.

The visualization technique employed to obtain instantaneous images of the swirl coaxial liquid spray with and without coaxial flow of gas involved image acquisition using a CID (charge injection device) solid state camera under microsecond strobe flash illumination (backlit) conditions. The cold-flow tests were for water/nitrogen spray injection into an unconfined, ambient pressure and temperature environment.

The drop size and velocity measurements were made using phase Doppler interferometry. Phase Doppler interferometry is a point measurement technique that has been used extensively over the last decade by several researchers [18-22]. The technique extends the basic principles of the conventional dual beam laser Doppler velocimeter to obtain particle size in addition to velocity.

An argon-ion laser beam is split into two equal intensity beams and focused to an intersection to form a probe volume. For the experiments described here, the receiver system was located at a 30° off axis angle to best exploit the characteristics of the interference pattern of the refractive liquid drops. Note that the collection optics of the receiving system coupled with the transmitting optics define the probe volume characteristics. In addition to the collection optics, the receiving system consists of three detectors at appropriate separations that independently measure the burst signal generated by drops traversing the probe volume, albeit with a phase shift. The velocity of the particle is then extracted from the temporal frequency of the burst signal, whereas the particle size is calculated from the measured phase shift between any two detectors and the *a priori* calculated linearity between the detector separation and the phase angle.

2.6.1.1.3. Hot-Fire Experiments

The LOX/$GH_2$ uni-element hot fire experiments were conducted over a range of mixture ratios from near-stoichiometric to nominally 170. The chamber utilized for the experiments is described in Section 2.2. The first goal of these experiments was to verify that sustainable high performance combustion could be achieved at these high mixture ratios. Supporting measurements included high frequency pressure and wall heat flux measurements for a select set of flow conditions. Additionally, LOX drop size and velocity measurements were also made using phase Doppler interferometry for one down-selected flow condition.

An overall view of the instrumentation layout for the study is shown in Fig. 2.6.2. The illustration indicates the four axial positions that were surveyed with the high frequency pressure transducers, 1, 3, 9 and 12 in., and the three axial positions where wall heat transfer measurements were made, 1, 3 and 9 in. Two PCB pressure gauges (50 kHz sampling) supplied by PCB Piezotronics Inc., and two heat flux gauges built in-house were employed. One PCB transducer and two heat flux gauges were positioned at either the 1, 3 or 9 in. axial position for any given run, whereas the other PCB transducer was permanently located at the 12 in. near-nozzle position. Two upstream positions near the flame zone were chosen (1 and 3 in.), as well as one downstream location (9 in.) where more uniform flow conditions were expected. Heat transfer gauges and a PCB gauge were mounted into the window section. Standard chamber pressure measurements (Setra 204 transducers at 200 Hz sampling) were also made simultaneously for each combustion run at both upstream and downstream positions within the

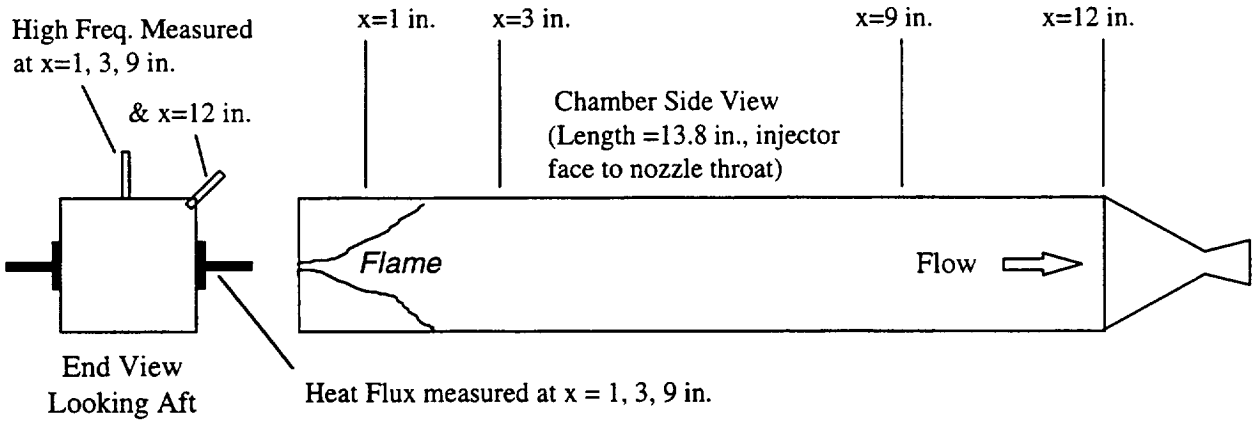


**Fig. 2.6.2 Illustration summarizing chamber locations surveyed with high frequency pressure gauges and heat flux gauges. The rocket chamber is shown to scale.**

rocket chamber. These were utilized for estimating rocket c*-efficiency. Relevant details regarding the instruments and measurement technique are summarized next.

The high frequency pressure transducers were PCB gauge Model 113A24 featuring 1 μs response with a 500 kHz natural frequency, well beyond any expected chamber frequencies. The gauge itself was mounted as close as possible to the inner wall of the rocket chamber. The mounting port was drilled to within 0.4 in. of the chamber side wall. A 0.04 in. hole was then drilled through to the chamber. Thus, direct impingement of combustion gases onto the sensing element was minimized whereas local pressure was measured through the small hole. For this combustion application, the gauge was encased in a water-cooling jacket (supplied by the manufacturer) for thermal isolation from the hot chamber walls. Transducer signals (voltage output) were recorded by a LeCroy high speed data acquisition system in digital form. The PCB gauge was employed in an AC-coupled mode so that only the fluctuating component of pressure was recorded. For these experiments the data acquisition allowed for a full-scale range of ±40 psi with a bit resolution of ~0.02 psi. The typical time-history of the pressure oscillation consists of 10 s of data recorded at 50 kHz sampling rate by the PCB gauge. The conversion of this time domain signal into a frequency domain power spectrum provided the desired combustion stability information.

The frequency content and energy spectrum of the time-domain pressure oscillation was determined by standard methods of Fourier analysis by Discrete Fourier Transform, as described for instance by Oppenheim and Schafer [33] and Press et al. [34]. In practice, the number of

samples used in the analyses were $2^{14}$, or 16384. This results in a 0.328 s period of (steady state) combustion at 50 kHz sampling. After conversion of the data into the frequency-domain, a frequency bandwidth (resolution) for the power spectrum of 3 Hz was achieved. This provides sufficient accuracy to ascertain the frequency content of the pressure oscillations.

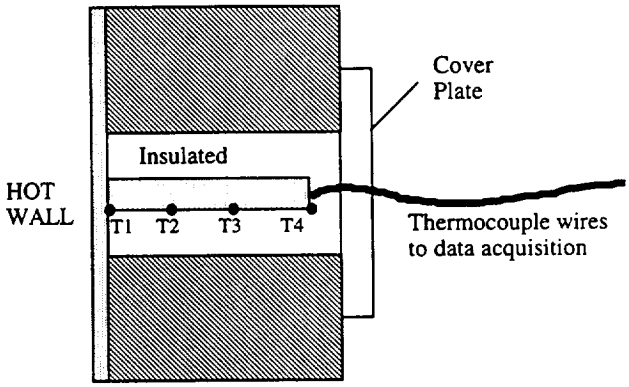


**Fig. 2.6.3 Schematic of heat flux gauges. Four in-depth thermocouples (Chromel-Alumel Type K) record the transient temperatures which are subsequently processed to obtain transient heat flux for the combustion run.**

The measurement of transient heating within a rocket chamber was possible with a heat flux gauge developed by Liebert [17] at the NASA Lewis Research Center. These heat flux gauges were also utilized for the tripropellant experiments discussed in Section 2.4. The principle of operation is repeated here for the sake of completenesss. As demonstrated by Liebert, the time-histories of multiple in-depth thermocouples may be used to deduce the wall heat flux provided that the heat flow near those thermocouples is one-dimensional. Two such gauges were employed in this study. As shown in Fig. 2.6.3, the gauge consists of four Type K thermocouples soldered to a copper rod (designated T1--T4). Since an air gap exists between the rod and the remainder of its housing, the heat flow from the hot wall approximates one-dimensional heat flow with an adiabatic backface condition. The entire gauge is constructed of Oxygen-Free High-Conductivity Copper. The thermocouple positions ranged up to 0.875 in. in-depth (nominally) with equal spacing between them.

Surface heat flux $q_w(t)$ is estimated by integrating the one-dimensional heat conduction equation with respect to the spatial dimension $x$ as shown below: ($\rho$, $c$, $k$ are the copper density, heat capacity, and conductivity, respectively)

$$\int_0^L \left(\rho c \frac{\partial T}{\partial t}\right) dx = \int_0^L \frac{\partial}{\partial x}\left(k \frac{\partial T}{\partial x}\right) dx$$

$$\int_0^L \left(\rho c \frac{\partial T}{\partial t}\right) dx = \left(k \frac{\partial T}{\partial x}\right)\Big|_0^L = q(0) - q(L) \qquad (2.6.3)$$

where $q \equiv -k\,\partial T / \partial x$. Since the backface is insulated (i.e. $q(L) = 0$), this results in

$$q_w \equiv q(0) = \int_0^L \left( \rho c \frac{\partial T}{\partial t} \right) dx \qquad (2.6.4)$$

In practice, the measured time-histories *T1(t)*, *T2(t)*, *T3(t)*, *T4(t)*, are curve-fitted by fifth-order polynomial functions. The time-history of wall temperature, which is needed for the above integration, is estimated by linear extrapolation of the near-wall temperatures *T1(t)* and *T2(t)*. All temperatures are then differentiated numerically to obtain *dT1/dt*, *dT2/dt*, *dT3/dt*, *dT4/dt*. A trapezoidal rule integration in space is finally performed, accounting for temperature dependent properties, to get the desired wall heat flux. The above computations were restricted to the steady-state combustion portion of each rocket firing.

The implementation of phase Doppler interferometry for measuring LOX drop size and velocity mimicked the description provided in the earlier sub-section on cold flow experiments, and is therefore not repeated here.

### 2.6.1.2. Results and Discussion

In this section, the results of the cold flow and hot-fire experiments are presented and discussed. For the cold flow experiments, spray visualizations and phase Doppler interferometry measurements of drop size are presented. For the combustion experiments, performance, wall heat transfer and stability results over a range of mixture ratios, and LOX drop size measurements at a chosen mixture ratio are presented and discussed.

#### 2.6.1.2.1. Cold Flow Results

The essential features of a swirl coaxial injector flowfield are revealed in the images shown in Fig. 2.6.4. Initially, a swirling liquid film of thickness $\delta$ emerges axially from the atomizer exit-orifice and turns away from the centerline owing to the azimuthal component of velocity. Small-scale structure is visible on the film, however, larger-scale structure quickly dominates the film as it expands into a swirling hollow cone sheet. Downstream from the exit-orifice the sheet begins to "tear" and lose its contiguity. As the "tear" propagates completely around the azimuth, the conical sheet becomes a series of circular ligaments or distorted ligament-like structures. Ligaments disintegrate into drops that are on the scale of the ligaments widths. Drops of various sizes are produced by other processes as well. For instance, shear between the phases is responsible for the production of small drops, whereas highly distorted ligaments yield many of the larger drops and globules. Further breakup of the larger drops into

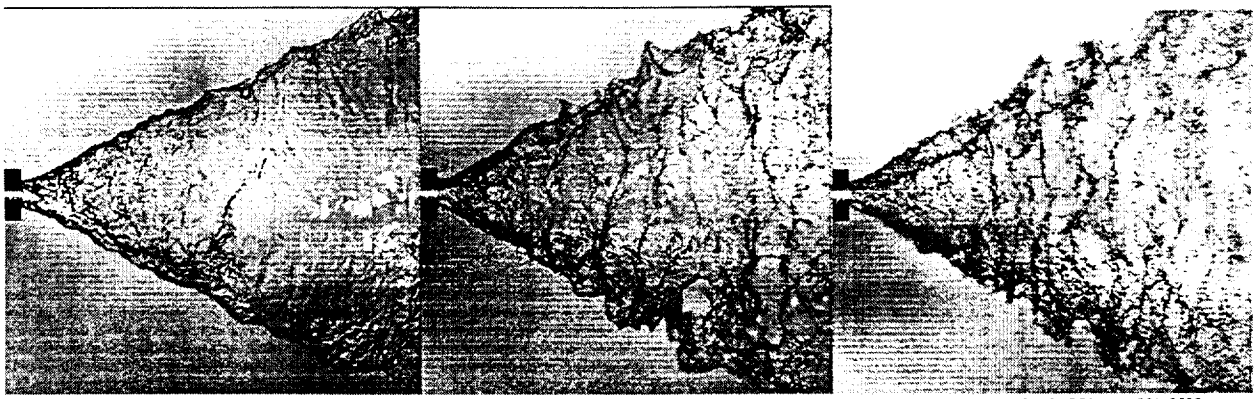

(a) $We_\delta$ =1060, ($\dot{m}_{H_2O}$ =0.099 lbm/s) (b) $We_\delta$=4250, ($\dot{m}_{H_2O}$ =0.200 lbm/s) (c) $We_\delta$=9500, ($\dot{m}_{H_2O}$ =0.298 lbm/s)

**Fig. 2.6.4. Effect of Weber number on swirled liquid flow.**

smaller ones can occur due to aerodynamic forces deforming the liquid spheres and also from collisions.

The mechanism of atomization is shown in Fig. 2.6.4 (a-c) for increasing values of Weber number. In this case, higher $We_\delta$ is achieved by increasing the flowrate. A 2 in. region downstream of the injector exit is visualized. In normalized terms, the sprays are imaged up to the location $z/\delta$ = 150, or 15 exit-orifice diameters. At $We_\delta$ of 1060, a wavy and contiguous hollow-cone sheet is observed with breakup occurring downstream of the field of view. For a higher Weber number of 4250, the disintegration of the sheet into ligaments is visualized in the image, but the ligaments break up further downstream. At the highest Weber number of 9500, both sheet and ligament disintegration takes place within the 2 in. field of view of the image. Thus, increasing Weber number tends to accelerate the breakup process as surface tension forces give way to the aerodynamic and inertia forces disrupting the sheet. Spray cone angle, the total angle subtended by the diverging sheet, is invariant with respect to Weber number in these experiments. This is consistent with the inviscid theory, which dictates that this angle depends only on the atomizer geometry, and not on the injection velocity or flowrate. At much lower Weber numbers (not shown), when the swirl momentum is insufficient for prefilming within the atomizer, the theory would not apply and experiments will show cone angle variations.

The effect of length-to-diameter ratio, $L/d$, of the exit-orifice is significant. For the present injector, the $L/d$ is 20. Wall friction effects for large $L/d$ orifices retard both components of film velocity, axial and azimuthal. Experiments conducted for varying $L/d$

*(a)* $L/d$=20, $\theta$ = 53° (b) $L/d$=30, $\theta$ = 46°, (c) $L/d$=40, $\theta$ = 37°,

**Fig. 2.6.5 Effect of $L/d$ on swirled liquid flow. $We_\delta$=4250, $\dot{m}_{H_2O}$ =0.200 lbm/s.**

ratios show that the spray cone angle diminishes with increasing $L/d$, suggesting that the azimuthal component is affected more than the axial (see Fig. 2.6.5). This has also been reported by Dombrowski and Hasson [35], whose experiments examined $L/d$ up to 5. From the continuity relation applied across the exit-orifice tube, it can be deduced that a decrease in velocity is associated with an increase in film thickness. This is verified experimentally and analytically by Hutt et al. [36] employing a transparent Plexiglas atomizer of a similar rocket-type design. The phenomenology for long exit-orifice tubes is important for several reasons: (1) a reduction in spray cone angle with $L/d$ implies a reduction in the spatial distribution of the spray, i.e. reduced "coverage," (2) the associated reduction in film velocity directly results in lower film injection velocity, and therefore lower drop velocity, and, (3) the increased film thickness at the injector exit manifests itself in larger drop sizes.

This overview of the salient features of swirl atomization applies over the range of injection conditions of this study and serves as the basis for interpreting both the visualizations and drop size and velocity measurements. Subsequent discussions now focus on injectors with an $L/d$ of 20, operating at flowrates corresponding to a fixed Weber number ($We_\delta$ = 4250)

Two pressure-swirl atomizers, different only in size by a factor of two, are compared in a series of visualizations at equivalent Weber number. From internal flow theory, the liquid film is estimated to be twice as thick for the large injector. The large unit thus delivers four times more flowrate for the same supply pressure. In order to operate both injectors flowing water at the same injection Weber number, the size difference is compensated by changing the injection velocity. The flowrates are given in Table 2.6.2 and the sprays are compared in Fig. 2.6.6.

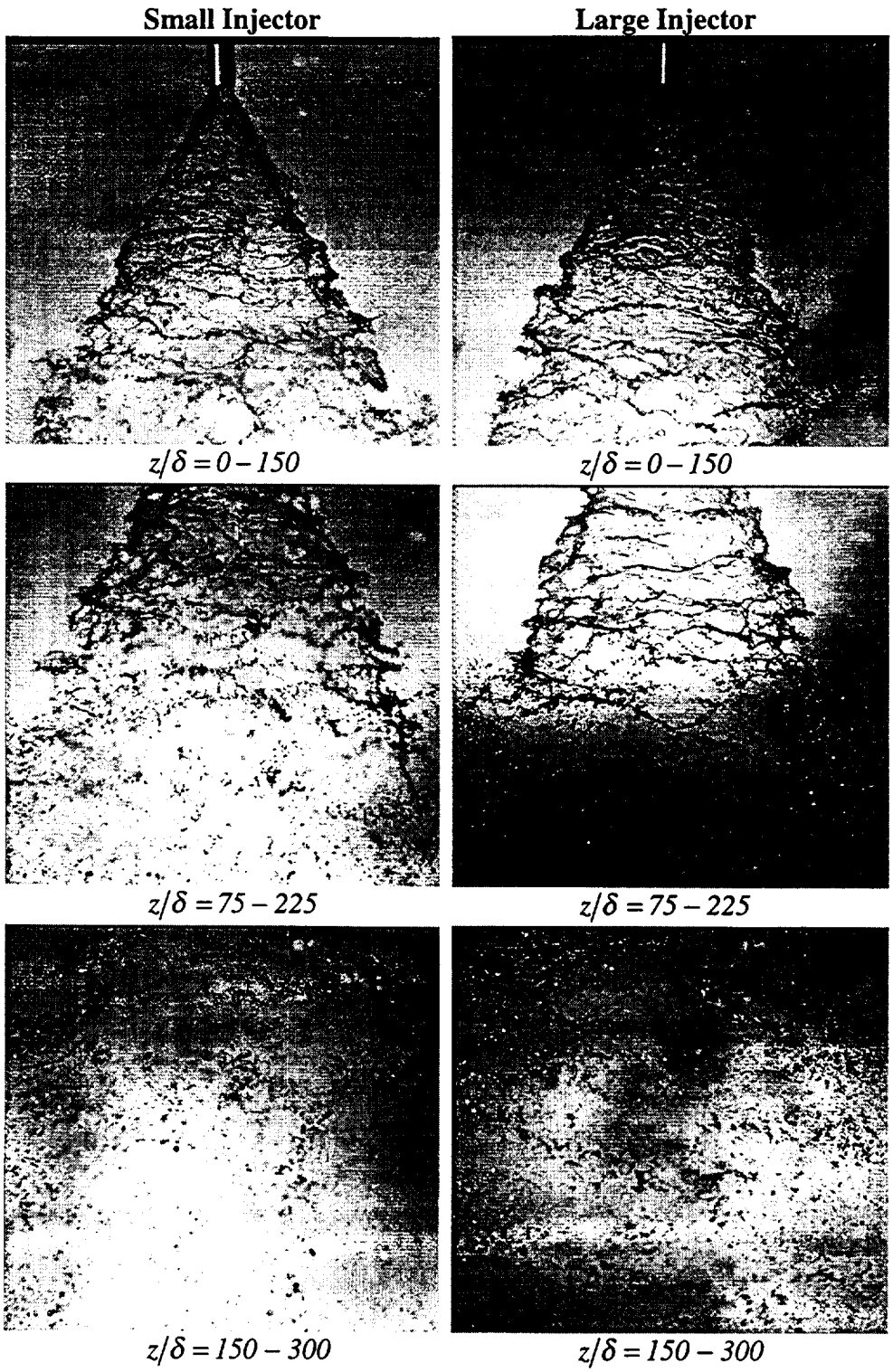


**Fig. 2.6.6. Visualizations of small and large swirl injector flowfields in scaled coordinates.**

In the figure, for each injector, the flowfields are visualized for $z/\delta = 0-150$, $z/\delta = 75-225$ and $z/\delta = 150-300$ non-dimensionalized regions. As is readily evident, the

**Table 2.6.2. Comparison of Injectors and Flow Conditions at Weber Number of 4250.**

| | Small Injector | Large Injector |
|---|---|---|
| *PHYSICAL* | | |
| $\delta$ | 0.0134 in. | 0.0268 in. |
| $d$ | 0.135 in. | 0.272 in. |
| $U_l$ | 98.4 ft/s | 68.9 ft/s |
| $\dot{m}_{H_2O}$ | 0.20 lbm/s | 0.57 lbm/s |
| *NON-DIMENSIONAL* | | |
| $C_d$ | 0.32 | 0.32 |
| $L/d$ | 20 | 20 |
| $\theta$ | 52° | 52° |
| $\rho_l/\rho_\infty$ | 850 | 850 |
| $\mu_l/\mu_\infty$ | 55 | 55 |
| $We_\delta$ | 4250 | 4250 |
| $Re_\delta$ | 10000 | 14000 |

two sprays are remarkably similar when viewed in scaled coordinates. In particular, breakup of the conical sheet occurs at the same dimensionless position for both, approximately $L_b/\delta = 110$ at an injection Weber number of 4250. Further dowstream, at $z/\delta = 75-225$ and $z/\delta = 150-300$, it may be seen that ligamentation and drop formation occur at approximately the same locations, and in the same manner for both injectors. In both cases, sheet breakup is followed by ligamentation, and then by disintegration of ligaments into rows of mostly spherical drops. The correspondence in the visualizations of the two sprays alludes to a deterministic mechanism for swirl coaxial injectors. Quantitative measurements of drop-size and velocity in these two sprays are presented next.

The complementary phase/Doppler interferometry measurements illustrate similitude in drop-size and velocity statistics at $We_\delta = 4250$. As seen in Fig. 2.6.6, breakup of the ligaments into drops is complete at the downstream position of $z/\delta = 300$, therefore, this axial station was suitable for conducting drop measurements. Specifically, the location $z/\delta$ of 300 corresponds to a distance of 4 in. and 8 in. downstream of the injector exit for the small and large units, respectively. The two sprays are interrogated at corresponding locations in terms of the normalized coordinates $(z/\delta, r/\delta)$ by traversing radially in equal increments along $r/\delta$.

Flow conditions, chosen to equate the Weber number, were previously summarized in Table 2.6.2. Recalling the hypothesis presented earlier, the following two cases were examined:

Case 1: $\overline{D}_1/\delta_1\left(300, r/\delta_1\right)$ = fcn.(850, 55, 4250, $10^5$, 52°); (small atomizer)

Case 2: $\overline{D}_2/\delta_2\left(300, r/\delta_2\right)$ = fcn.(850, 55, 4250, 1.4 x $10^5$, 52°); (large atomizer)

Since all parameters on the right-hand-side are equivalent for the two cases, except for $Re_\delta$ which cannot be matched simultaneously here. The motivation here was to see whether the scaled drop sizes and velocities at all non-dimensional positions were equivalent.

Results of the experiments comparing the two cases are given in Fig. 2.6.7. Variation of mean drop velocity $\overline{u}(r)$ and $\overline{v}(r)$, Sauter mean diameter $D_{32}(r)$, and mass flux $m''(r)$, with respect to radial position $r$ is shown in both physical and normalized variables. Data points represent 15000 drop realizations each, except at the centerline and outer periphery where the spray is very dilute. For both injector sprays, size and velocity minima are at the centerline whereas the maximum values occur away from the spray axis. As indicated earlier, size and velocity measurements are normalized using theoretical estimates of film thickness $\delta$, and liquid injection velocity $U_l$. Although actual values may be somewhat different, due to exit-orifice *L/d* effects, it is convenient to use the theory estimates as reference points. Flux is normalized by an "average" mass-flux, obtained by dividing the total atomizer flowrate by a circular cross-sectional area of radius $r/\delta$ = 300. After normalization of the data, the results show that drop size, velocity, and mass flux profiles from the two injectors are indeed similar in both trend and magnitude as hypothesized. In particular, the velocity results exhibit good correspondence between the two sprays for the entire traverse. Drop size results show good trendwise correspondence, but a difference in the size parameter $D_{32}/\delta$ is observed for $r/\delta$ greater than 100. The disparity is believed to be artificial, arising in large part from sizing range limitations of the phase Doppler interferometry system. The instrument does not measure drop diameters larger than 1350 μm, therefore an upper-end truncation of the drop distribution occurs for the large injector spray leading to lower than actual values of $D_{32}$. Flow visualizations of the large injector spray show the existence of drops which are larger than the upper limit for sizing. The profiles of mass flux indicate that the spray distribution is equivalent for the two injectors as

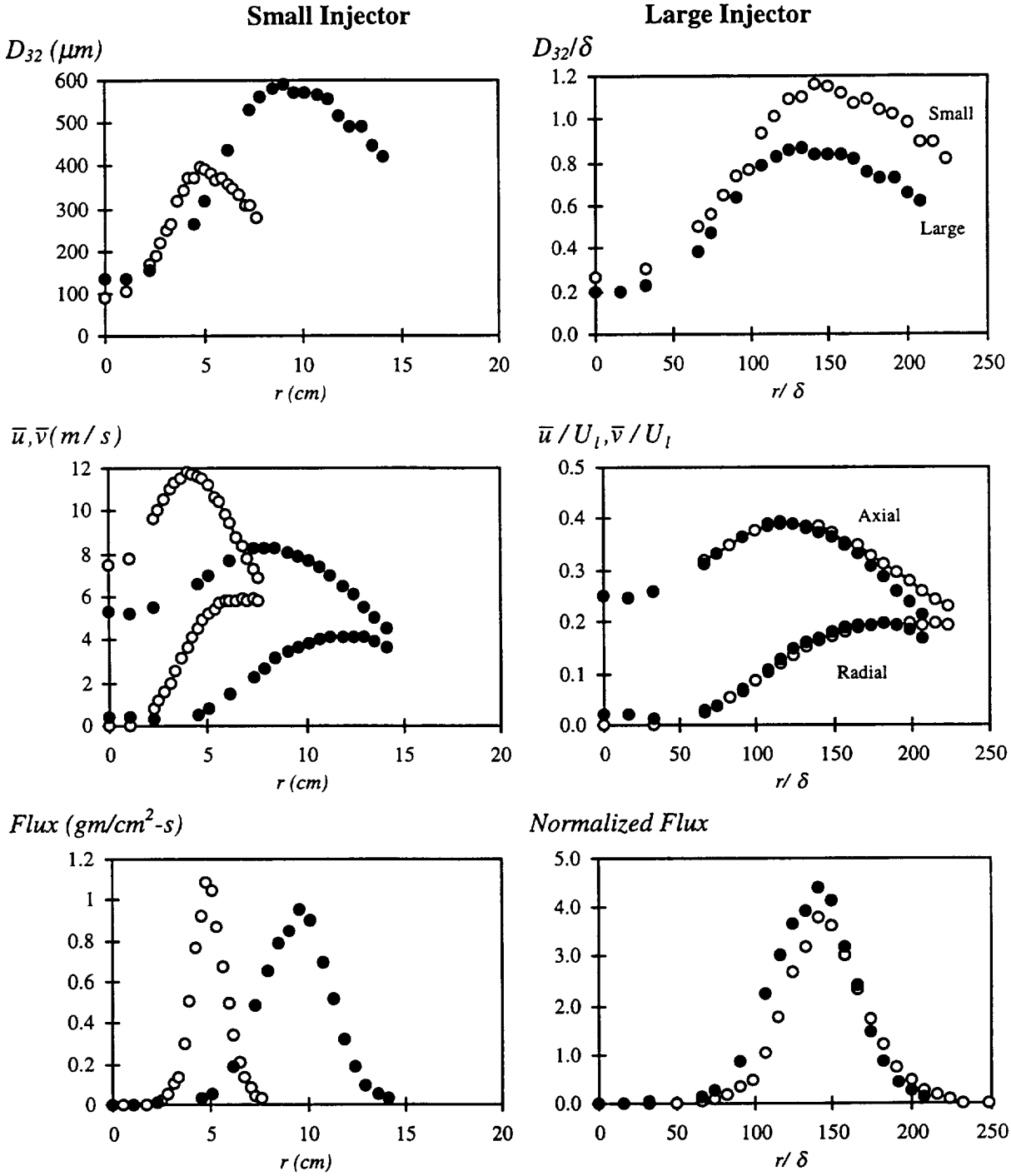


**Fig. 2.6.7. Characteristic drop size, mean drop velocity and mass flux of small and large injectors compared in physical and scaled variables. Note S.I. units in figures.**

well. Mass flux is a derived quantity based upon the size and velocity data, and upon estimates of the size of the measurement volume. The bulk of the spray is distributed in a Gaussian manner around the radial position $r/\delta$ of 140. This is also the location of size and velocity maxima. The location is consistent with the divergence angle of the spray cone. It is reasonable

to expect the mass flux to peak at a radius where the spray cone intersects the measurement plane. In this case, the predicted location according to $r/\delta = z/\delta \tan(\theta/2) = 300 \tan 26^\circ = 146$, which compares well with the measured value of 140. Upon radial integration, assuming spray symmetry, the flux profiles yield values of flowrate that compare favorably to the metered flowrate of water. The drop measurements integrated to 75% of the actual flow through the small atomizer, and 92% of the actual flow through the large atomizer. This serves as a consistency check for the mass flow estimates. Approximations incorporated into the flux calculations, in vendor-supplied software, allow for this level of disagreement, particularly in cases such as this where relatively high flowrate and large drop sizes are involved.

In order to test the scaling hypothesis for coaxial liquid/gas injection, experiments with the small and large injectors were performed with water/nitrogen sprays at ambient pressure. The flow conditions were chosen to equate the Weber number for the two sprays, as well as the liquid-to-gas momentum ratio. Hence, for the comparison, all parameters remained unchanged, except for some difference in liquid and gas Reynolds number, but the effect of this on the spray was believed to be secondary.

Drop measurements were made downstream in the spray where breakup into drops was complete, i.e. at $z = 4$ in. for the small injector and at $z = 8$ in. for the large injector, (normalized coordinate $z/\delta = 300$). The results of a radial survey of the axisymmetric spray at this location using Phase Doppler interferometry, is presented in Fig. 2.6.8. Results are given in both physical and dimensionless coordinates. Drop size and radius are non-dimensionalized by film thickness $\delta$, and velocity components are non-dimensionalized by the total liquid injection velocity $U_l$. Although the results are markedly different in physical space, normalization reveals that the sprays are near equivalent with similarity observed in the radial profiles of drop size, drop velocity, and mass flux.

Swirl injector spray atomization thus appears to be governed by the competing forces of liquid inertia and surface tension at the liquid/gas boundaries. The Weber number, as defined here with respect to the appropriate liquid injection length and velocity scales, represents the balance of forces. In the presence of the coaxial gas flow for the swirl coaxial injector, the liquid-

| | $\dot{m}_l$ (lbm/s) | $\dot{m}_g$ (lbm/s) | $U_l$ (ft/s) | $U_g$ (m/s) | $We_\delta$ | Mom. ratio |
|---|---|---|---|---|---|---|
| small injector: | 0.200 | 0.0066 | 98.4 | 328 | 4250 | 9 |
| large injector: | 0.573 | 0.0196 | 68.9 | 233 | 4250 | 9 |

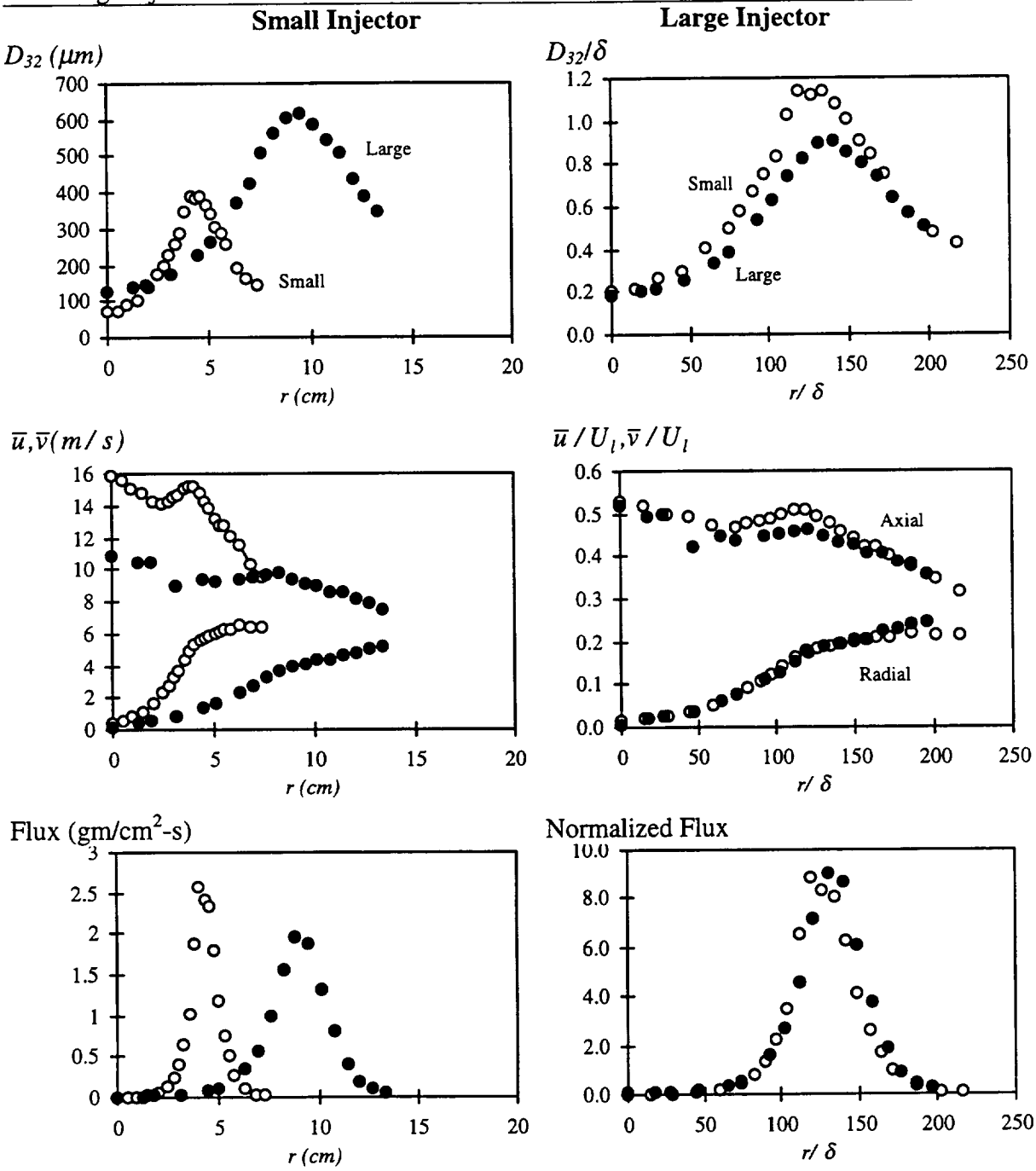


**Fig. 2.6.8. Characteristic drop size, mean drop velocity and mass flux of small and large injectors compared in physical and scaled variables for water/$N_2$ flows. Note S.I. units in figures.**

to-gas momentum ratio is found to be the important parameter. The collapsing of experimental data with respect to these two non-dimensional parameters, regardless of injector size, or fluid, promises to be a useful tool for estimating atomization results for swirl injectors.

2.6.1.2.2. Hot-Fire Results

The discussions below address the combustion performance, stability, and wall heat transfer characteristics for oxidizer-rich combustion of LOX/$GH_2$. In addition, LOX drop size and velocity measurements made for one flow condition are also presented. For the stability and wall heat transfer measurements, three axial locations within the combustion chamber were surveyed with the instrumentation, and each location at four O/F ratios ranging from 5 to 170. For the studies of the small swirl coaxial injector, the LOX flowrate was maintained for all combustion runs at a nominal value of 0.25 lbm/s with a nominal chamber pressure of 300 psia. This value of chamber pressure was chosen to be significantly above the local vapor pressure at the injector so that LOX inlet quality was assured. The LOX injection temperature (typically 216 R) was monitored to verify this. For the studies of the larger injector, the LOX flowrate was maintained at nominally 0.46 lbm/s with a nominal chamber pressure of 700 psia. In terms of the critical pressure of LOX, which is 730 psia, the pressures given above correspond to reduced pressure $P_r$ of 0.42 and 0.96. O/F ratio variation for these oxidizer-rich combustion studies was achieved by reducing the hydrogen flowrate. It is noteworthy that in this manner total flowrate was also approximately constant for the oxidizer-rich O/F ratios since hydrogen constituted a relatively small fraction of the injected mass.

*2.6.1.2.2.1. Performance*

A visualization of the near-injector combustion zone as seen through 2 in. round viewing windows is provided in Fig. 2.6.9. For this injector, the spray flame attaches to the LOX post for this injector/rocket flowfield, and rapidly expands to fill the chamber cross-section (cone angle is 38 degrees). This flame behavior is observed at near-stoichiometric conditions as well as oxidizer-rich conditions for this injector. The second image shown in Fig. 2.6.9 was taken by illumination with a laser light sheet and normal imaging with a bandpass filter. The green area of the image indicates the region of LOX presence within the combustion zone.

Chamber pressure was monitored and recorded by a pair of transducers, one at each end of the rocket. The chamber pressure time-histories for four typical combustion runs are shown in

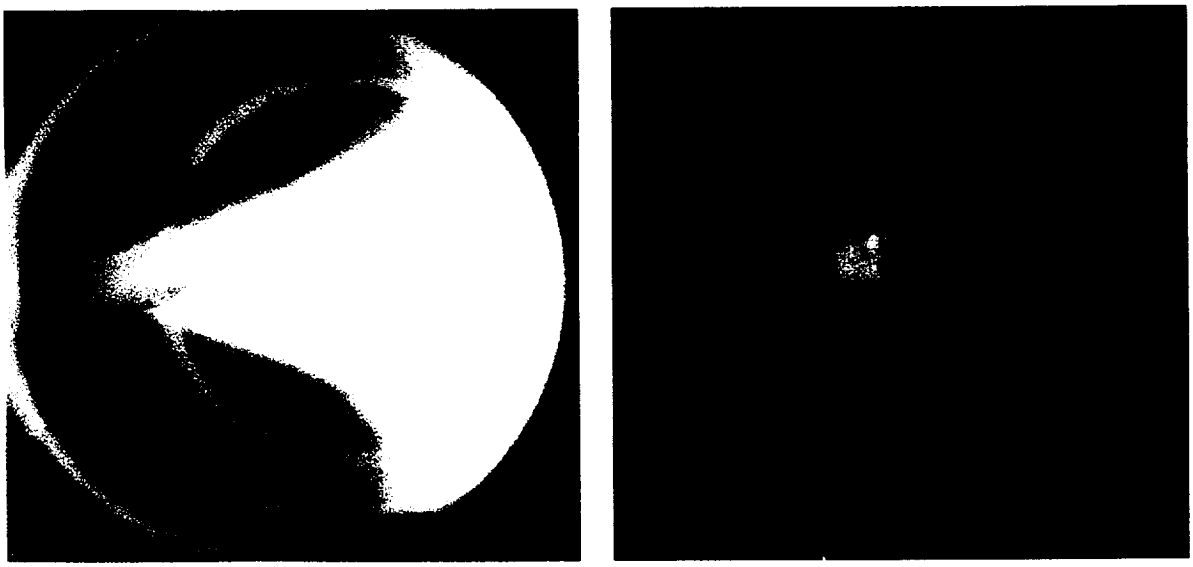

**(a) LOX/Hydrogen Spray Flame** **(b) Laser Light Scattered from LOX**

**Fig. 2.6.9. Visualizations of the LOX/$H_2$ near-injector flame region.**

Fig. 2.6.10. Ignition and shutdown transients are also included in the plots. The firing duration was limited by thermal constraints at the near-stoichiometric O/F ratio of 5.4 (flame temperature of 3350 K), but this was not a problem for oxidizer-rich cases where longer durations were employed to maximize the data collected.

A tabular summary of the performance results is shown in Table 2.6.3. The actual values of flowrates, chamber pressures, c*-efficiencies (characteristic exhaust velocity $\eta_{C^*}$) and

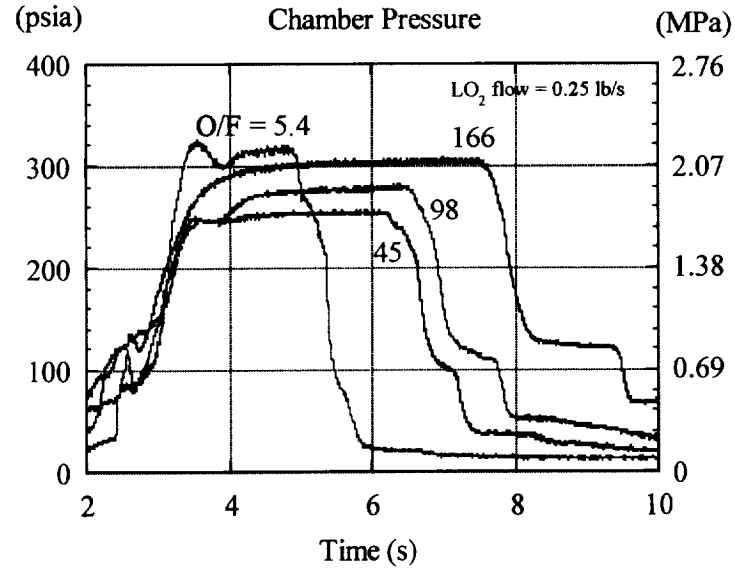


**Fig. 2.6.10. Chamber pressure time-history is shown for four typical combustion runs with the single-element swirl coaxial injector in the uni-element rocket.**

## Table 2.6.3. List of Run Conditions for Oxidizer-Rich Combustion Studies

| †LOX Flow kg/s | O/F Ratio | Chamber Pressure, $P_c$ psia | Est. Flame Temp., $T_{af}$ R | C*-Eff. (%) | Instrument Locations: Heat Flux Gauges A&B x = 1 in. | x = 3 in. | x = 9 in. | High Frequency Pressure Xdcrs. x = 1 in. | x = 3 in. | x = 9 in. | x= 12 in. |
|---|---|---|---|---|---|---|---|---|---|---|---|
| 0.256 | **6.1** | 295 | 6156 | 95.6 | × | | | × | | | × |
| 0.256 | **46.4** | 262 | 3429 | 94.9 | × | | | × | | | |
| 0.260 | **103** | 249 | 1764 | 84.3 | × | | | × | | | |
| 0.260 | **166** | 301 | 1098 | 90.3 | × | | | × | | | |
| 0.258 | **5.31** | 336 | 6012 | 100 | | × | | | × | | × |
| 0.258 | **46.6** | 258 | 3429 | 93.2 | | × | | | × | | |
| 0.258 | **96.5** | 277 | 1881 | 91.5 | | × | | | × | | |
| 0.258 | **168** | 302 | 1089 | 92.7 | | × | | | × | | |
| 0.258 | **5.32** | 315 | 6012 | 95.7 | | | × | | | × | × |
| 0.247 | **44.2** | 254 | 3555 | 93.5 | | | × | | | × | |
| 0.258 | **94.8** | 264 | 1908 | 86.5 | | | × | | | × | |
| 0.265 | **171** | 308 | 1062 | 92.7 | | | × | | | × | |
| 0.245 | **48.1** | 327 | 3348 | 80.2 | | | ** | | | × | × |
| 0.247 | **49.3** | 338 | 3285 | 81.8 | | | ** | | | × | × |
| 0.254 | **50.2** | 628 | 3240 | 80.9 | | | ** | | | × | × |
| ‡ 0.258 | **53.7** | 634 | 3078 | 83.2 | | | × | | | × | × |
| 0.474 | **50** | 434 | 3258 | 87.4 | | | × | | | × | × |
| 0.470 | **59.3** | 603 | 2853 | 84.7 | | | × | | | × | × |
| 0.474 | **49.9** | 658 | 3258 | 84.2 | | | × | | | × | × |
| 0.454 | **96.6** | 655 | 1818 | 81.7 | | | × | | | × | × |
| 0.465 | **146** | 708 | 1098 | 84.2 | | | × | | | × | × |
| 0.459 | **142** | 724 | 1296 | 86 | | | × | | | × | × |
| 0.468 | **144** | 721 | 1188 | 84.6 | × | | | | | * | * |
| 0.461 | **97.8** | 691 | 1836 | 85.6 | × | | | | | * | * |

* High frequency pressure data not available.

** Heat transfer data not available.

† Note that the two halves of the table represent studies at low chamber pressures and high chamber pressures respectively. Smaller injector is employed where the LOX flowrate is approximately 0.265 lbm/s, and larger injector where flow is 0.46 lbm/s.

‡ In this combustion run a smaller annulus was used to increase hydrogen injection velocity (OD of 0.0086 in.).

instrumentation are also given. c*-efficiencies of 95% and greater are achieved at the near-stoichiometric O/F ratio condition. For oxidizer-rich conditions, $\eta_{c^*}$ is 90-95% at the lower chamber pressures, and 80-87% at the higher pressures. The present research injector is not optimized to maximize c*-efficiency. Higher values can be achieved by tailoring the injector annulus to increase the gas injection velocities for instance. The purpose here is to report the specific c*-efficiencies for this oxidizer-rich series of combustion runs, and show that

performance is *not* significantly degraded at high O/F ratio for the swirl coaxial injector. It should be noted that the length of the rocket chamber for these experiments was 13.75 in. The chamber volume allowed for a propellant residence time of approximately 7 ms at near-stoichiometric mixture ratios, and approximately 100 ms at the highest mixture ratios for either injector.

Performance at oxidizer-rich conditions has also been previously reported by Bailey [37] ($\eta_{C^*} \sim 80\%$), and more recently by Farhangi et al. [38] ($\eta_{C^*} \sim 100\%$). These studies are complementary to the present results. For these studies, the chamber pressures were higher (800 to 3000 psia). Also, multi-element rocket injectors were employed in somewhat larger size chambers (shear coaxial element by Bailey [37] and impinging elements by Farhangi et al. [38]). Nevertheless, LOX/$GH_2$ was the propellant combination for each of these sets of experiments, and taken together the studies demonstrate ignition/combustion over a wide range of O/F ratios and chamber pressures for this propellant combination.

*2.6.1.2.2.2. Stability*

The stability of rocket combustion at very high O/F ratio has not been addressed in previous work. Although the combustion performance and chamber pressures suggest smooth and stable combustion, this is specifically verified through the use of high frequency pressure measurements (PCB gauges described earlier). The magnitude of the pressure oscillation levels for all combustion runs is summarized in Fig. 2.6.11. The root-mean-square of the fluctuation $P'_{rms}$ is shown as a percentage of the chamber pressure $P_c$. In most cases, the root-mean-square fluctuations are less than 2% of $P_c$, whereas the peak-to-peak fluctuations are below 6% of $P_c$. Oscillations which are lower than 5% of $P_c$ are generally associated with stable combustion.

The frequency content of the pressure fluctuations is also shown in Fig. 2.6.11 and listed in Table 2.6.4. In most of the combustion runs, it appears that the fluctuation energy is concentrated in a single longitudinal mode of the combustion chamber. Agreement between both PCB gauges as to the excited frequencies is also excellent. The sampling and data reduction methods allow for a frequency resolution of 3 Hz; therefore the frequencies reported in the table should be interpreted to be accurate to 3 Hz.

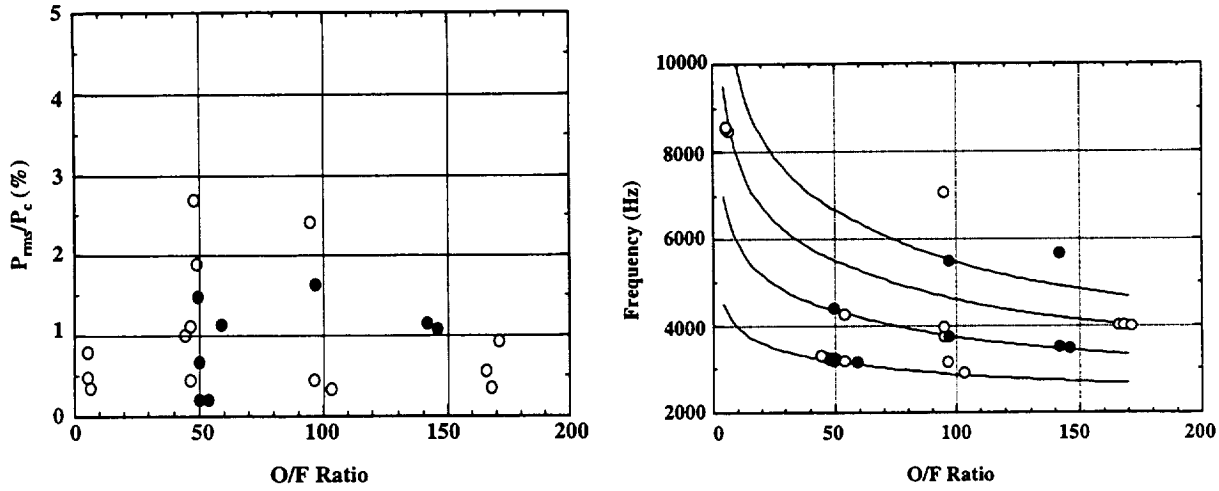


**Fig. 2.6.11. Root-mean-square of the high frequency pressure oscillations are shown normalized by chamber pressure for all the combustion runs (left graph), along with the associated frequency content (right graph): o – 300 psia combustion with small injector, and ● -- 700 psia combustion with large injector. Predicted frequencies 1L, 2L, 3L, 4L, are indicated by the curves.**

A prediction of chamber resonant frequencies $f_{res}$ (during combustion at a particular O/F ratio) is possible based upon the speed of sound, $a$, through the equation $f_{res} = (a/2)\sqrt{(n_x/l_x)^2 + (n_y/l_y)^2 + (n_z/l_z)^2}$. Predictions of the longitudinal mode frequencies are given in Fig. 2.6.11 along with the results. In the above formula for the resonant frequencies, the chamber dimensions are given by $l_x, l_y, l_z$ while the mode numbers (1st, 2nd, 3rd etc.) are indicated by $n_x, n_y, n_z$ in the respective coordinate $x$, $y$, $z$. The analysis shows that either the 1L or the 2L mode is the most strongly excited at O/F ratios of 50 and 100, with a small amount of resonant energy being found in higher order longitudinal mode subharmonics. At O/F ratios of 5 and 165, it is the 3L mode that is the most energetic. At high O/F ratios (45, 100, 165 nominal), agreement between measured and predicted frequencies is within 5%. For the near-stoichiometric case there is a 10% discrepancy, which is not unlikely considering the complexities of the actual combustor flowfield acoustics. Transverse mode pressure oscillations, which would occur at much higher frequencies, are not observed in the present study.

In one instance, O/F of 94.8, a number of unexpected frequencies were excited. This combustion run was repeated several times with similar results. Even longitudinal modes of the chamber (2L, 4L, 6L, 8L) were excited to levels which resulted in the largest pressure oscillations observed in this study. Coupling with the injection and feedline characteristics is

**Table 2.6.4. Results of High Frequency Pressure Studies.**

| O/F Ratio | $P'_{rms}/P_c$ (%) | Dominant Resonant Frequency Observed (Hz) for Various Positions in Chamber | | | |
|---|---|---|---|---|---|
| | | x = 1 in. | x = 3 in. | x = 9 in. | x = 12 in. |
| **6.1** | 0.35 | 6476 | | | * |
| **5.31** | 0.49 | | 6534 | | |
| **5.32** | 0.80 | | | 6580 | |
| **46.4** | 0.44 | 1279 | | | 1279 |
| **46.6** | 1.12 | | 1291 | | |
| **44.2** | 1.00 | | | 1309 | |
| **103** | 0.33 | 931 | | | 931 |
| **96.5** | 0.44 | | 1154 | | |
| **94.8** | 2.42 | | | 1740, 1975, 5081 | |
| **166** | 0.55 | 2032 | | | 2032 |
| **168** | 0.36 | | 2029 | | |
| **171** | 0.93 | | | 1987 | |
| **48.1** | ** 2.70 | | | 1224 | 1224 |
| **49.3** | 1.90 | | | 1245 | 1245 |
| **50.2** | 0.21 | | | 1251, 1236 | 1251, 1236 |
| **53.7** | 0.21 | | | 1196, 2258 | 1196, 2258 |
| † **50** | 0.67 | | | 1239 | 1239 |
| **59.3** | 1.14 | | | 1147 | 1147 |
| **49.9** | 1.48 | | | 1200, 2400 | 1200, 2400 |
| **96.6** | 1.63 | | | 1758, 3516 | 1758, 3516 |
| **146** | 1.07 | | | 1489 | 1489 |
| **142** | 1.16 | | | 1526 | 1526, 3693 |

* Data not available.

** Pressure data given for runs in bottom half of table are for the PCB gauge located at 305 mm.

† Larger injector used for run cases from this point on.

‡ Multiple frequencies are listed when the energy contained is those frequencies is comparable.

believed to be the source of the oscillations. It is noted that c*-efficiency dropped to 86.5% for this run as compared to 91.5% for a previous run at a very similar O/F ratio of 96.5

The present results are unique since they address the stability of a *single* injector element over a wide range of mixture ratios from 5 to 170. It is noteworthy that a previous stability characterization of swirl coaxial injectors with LOX/$GH_2$ propellants was performed by Hulka et al. [39] over a mixture ratio range of 3 to 9. In that study of dynamic stability of a multi-element, cylindrical chamber (70 to 250 lbm/s total flowrate), Hulka et al. noted stable engine response to pressure perturbations (induced by non-directional bombs) without the use of

stability aids for fuel-rich combustion. A comparison cannot be made, however, between the present oxidizer-rich, uni-element studies and the fuel-rich, multi-element studies of Hulka et al. owing to significant differences in hardware and experimental conditions.

*2.6.1.2.2.3. Wall Heat Flux*

Concurrent measurements of wall heat flux were obtained as described in an earlier section. The locations of both heat flux gauges (designated as Gauge A and Gauge B) are given in Table 2.6.3. For each of the combustion runs, thermocouple measurements from both gauges were obtained and reduced to obtain the wall heat flux level during the firing period. In this copper heat-sink chamber, heat flux to the wall varies with time during the firing. Initially, the heating level is high owing to the lower wall temperatures. As wall temperature rises, the wall heat flux decreases steadily during the firing. In most cases, the heat flux diminishes by a factor of two during the steady combustion period. Typical heat flux time-histories, from four combustion runs, for one of the heat flux gauges is shown in Fig. 2.6.12.

The variation of heating with respect to O/F ratio and axial position within the chamber is determined by comparing time-average values of the transient heating profiles (see Fig. 2.6.13). The results show that the highest heat fluxes are associated with the O/F ratio of 5 (nominal heating of 6 Btu/in$^2$-s) with heating being insensitive to location in the chamber. Heating

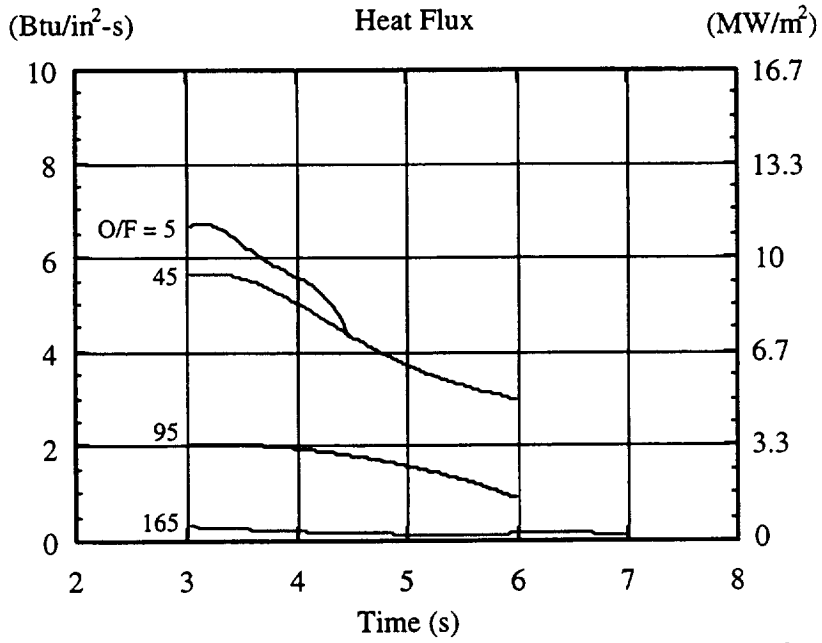


**Fig. 2.6.12. Typical time-history of heat flux for one of the gauges is shown for four combustion runs, each at a different O/F ratio. Gauge is located at x=1 in. for these runs.**

diminishes for higher O/F ratios as may be expected since less fuel is available for combustion and less energy is released. This is seen in both the low and high pressure experiments. The heat flux levels at the O/F of 165 are lowest, ranging from 0.1 to 0.4 Btu/in$^2$-s. The left graph in Fig. 2.6.13 (low pressure study) includes one data point with the small injector at a higher pressure of 634 psia, with gauges located at x=9 in. No significant pressure effect is observed in this range.

This study reveals that the near-injector heating (x = 1 in.) at O/F of 50 and 100 is higher than at downstream positions. Local flame impingement/attachment to the wall is a likely explanation for this phenomenon. This trend is also borne out at the higher pressures. The photograph of Fig. 2.6.10, which shows the injector flame rapidly expanding to the wall, supports this inference. It is possible to conclude from this that near-injector locations of a chamber experience larger heat fluxes owing to the spreading of the swirl coaxial flame.

The results for the O/F of 165 case (smaller injector) should be viewed as order-of-magnitude, however, because certain factors reduce the accuracy of this measurement. Initial heating due to the ignition torch is of the same order as the heating during the firing and preheats the chamber side walls non-uniformly to a temperature that is comparable to the adiabatic flame temperature of combustion temperature at O/F of 165. In some firings, wall cooling occurs instead of heating. The heat gauge with the present thermocouples is not designed to work optimally at these low heat flux levels. More sensitive thermocouples might be able to resolve this problem. Finally, it is noted that heat transfer coefficient could not be estimated in this work since near-wall gas temperature measurements are not available.

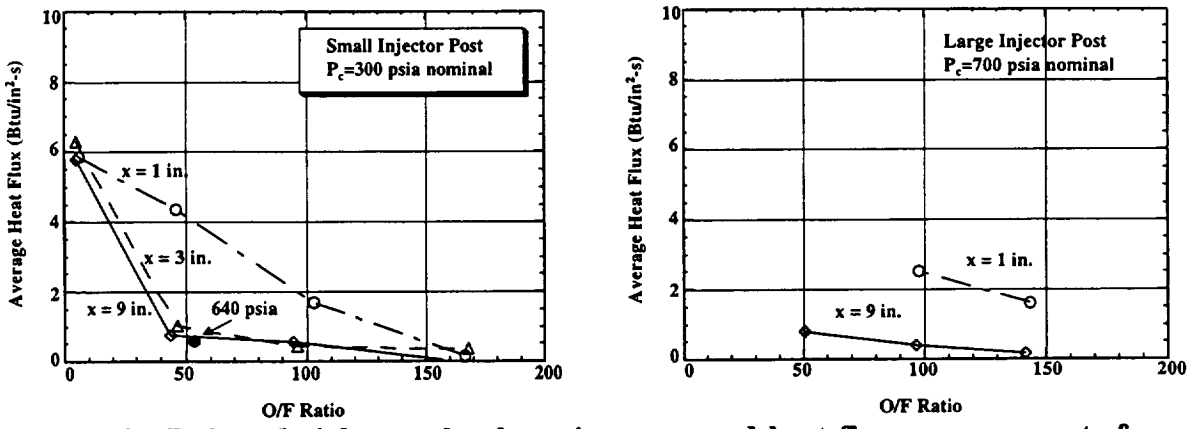


**Fig. 2.6.13. Left and right graphs show time-averaged heat flux measurements for small and large injector, respectively.**

A previous study of wall heat flux due to LOX/$GH_2$ swirl coaxial injectors was carried out by Petersen et al. [40] with a multi-element, cylindrical chamber operation at high pressures (1700 to 2400 psia) and flowrates (~65 lbm/s), and mixture ratios near 5.5. Wall heat fluxes of 25 Btu/in$^2$-s were observed for their baseline case, which is approximately four times the highest flux in the present study with the small injector. While a direct connection between the two studies is not immediately possible, further experiments using the present injector at higher pressures and element flowrates can be used to establish heat transfer scaling relationships.

The global results from the hot-fire experiments presented here demonstrate the viability of the present swirl coaxial injector for high mixture ratio rocket combustion. The present single-element studies at sub-critical and near-critical chamber pressures provide a characterization of this injector from the standpoints of performance, stability and heat transfer. In particular, the present injector provides for stable ignition, combustion, and flame holding over a wide range of oxidizer-to-fuel mixture ratio (by mass) from 5 to 170, and chamber pressures from 250 to 700 psia. Results from the combustion stability investigation demonstrate stable combustion with root-mean-square pressure fluctuations of 2% of chamber pressure or less, with weak acoustic coupling to longitudinal modes of the combustion chamber. Concurrent heat flux studies with this injector/chamber combination illustrate the thermal benefits of oxidizer-rich combustion conditions.

*2.6.1.2.2.4. LOX Drop Size and Velocity*

Measuring LOX drop size and velocity in a combustion zone is not a trivial exercise. Earlier attempts at making drop size and velocity measurements for a shear coaxial injector element yielded limited success [22, 24] due to the harsh and confined nature of the LOX flowfield. The swirl coaxial injector was deemed to be more pragmatic since the flow is more spread out and therefore, the LOX number density is lower. However, several attempts at making the measurements revealed that the flow condition choice is constrained by practical issues. These issues are noted prior to the discussion of the results since they have a bearing on the quality of the measurements.

Initial attempts at phase Doppler interferometry measurements within the combusting LOX spray revealed that the choice of chamber pressure and O/F ratio have an effect on the quality of drop measurements and therefore need to be chosen with care. The effect is

manifested through flame luminosity that increases proportionally with chamber pressure, and varies substantially depending upon the O/F ratio as well. Combustion at pressures much higher than 300 psia, or near the stoichiometric O/F ratio, leads to strong increases in broadband flame radiation. This causes signal-to-noise ratio (SNR) problems in drop measurements where the coherent light scattered by drops, particularly small ones, is masked by flame light admitted through the phase Doppler interferometry instrument's bandpass filters. In practice, over 80% of the drop realizations which are detected by the PDI instrument cannot be analyzed in situations with strong flame interference. The problem is mitigated and circumvented by maximizing laser beam power and carefully selecting the chamber operating conditions. A chamber pressure of nominally 300 psia, along with an oxidizer-rich O/F ratio for combustion, lead to significantly reduced flame light and much better SNR. For the swirl coaxial injector flowfield, it was observed that conducting measurements at an O/F ratio of 30 or greater considerably improved the visibility of the signal as compared to near-stoichiometric operating conditions owing to the difference in flame radiation.

The radiative and convective heat release of combustion in the near-injector region is also problematic in another respect. Combustion runs that are performed at pressures well above 300 psia result in excessive heating near the injector face to the extent that erosion and burning of the stainless steel injector tip occur during a single run. Combustion at 300 psia and O/F ratio of 5 with this injector does not damage the injector tip, but results in heating effects on the optical windows. Thermally-induced erosion of the chamber walls and window area seals causes material deposition on the window optical surface as well as surface damage to the quartz. This circumstance does not allow for repeatable and reliable drop measurements unless new windows are used for each combustion run. In light of the above, the approach taken was to circumvent the operational issues by selecting a suitable but thermally benign operating point. The oxygen/hydrogen atomization study is therefore performed at O/F ratio of 30 at a chamber pressure of 300 psia.

A LOX flowrate of 0.2 lbm/s with an O/F of 30 was selected for the study and corresponds to a LOX injection Weber number of 30,900; the low surface tension of LOX leads to higher Weber number than the cold flow studies discussed earlier. In choosing this flowrate, practical constraints again had to be taken into account again. While it was desirable to conduct experiments at the Weber numbers of the cold flow experiments, this was not possible with

LOX. For the $LN_2$ jacketed LOX supply tubing, 0.2 lbm/s was the lowest practical cryogenic flowrate that could be delivered by the facility while maintaining a suitably low and steady cryogenic injection temperature.

LOX drop size and velocity measurements from approximately fifty-five combustion runs are presented in Fig. 2.6.14 and Fig. 2.6.15. The first figure gives a survey of LOX atomization at radial positions which are 2 in. downstream of the injector face ($z/\delta = 150$), whereas the second figure is for a location further downstream at 3.5 in. from the injector face ($z/\delta = 260$). Optical access allowed for approximately three-fourths of the width of the chamber to be interrogated. The measurement region extended from 0.35 in. above the chamber centerline to 0.87 in. below the centerline, where the region below centerline is arbitrarily given a positive designation. The arithmetic mean and Sauter mean diameters are shown for each radial position along with corresponding values of mean drop velocity and the estimated mass flux. Each data point presented in the figures represents a single combustion run of fixed time duration where the number of drop samples acquired for the run varies from as few as five hundred to as many as seven thousand depending upon the local particle flux density in the flowfield. The lowest sample sizes are at the centerline of the spray.

The atomization survey in Fig. 2.6.14 indicates the familiar phenomenology of swirl sprays in which the majority of the spray flux is found off-centerline. This may be inferred from the flux estimates and the velocity measurements. The symmetry in the velocity profile encouragingly indicates that the limited radial scan may indeed be representative of the data at any azimuth. Repeated combustion runs at the same location also give quite comparable results, which suggests that the drop sample size for each combustion run is adequate for the present purpose. The mean drop sizes $D_{10}$ in the figure vary between 50 and 100 μm while the Sauter mean diameters $D_{32}$ vary from 80 to 160 μm, with the highest values being realized off-center. It should be noted that measurements outside a radius of 0.79 in. are affected to some degree by the presence of window purge flow of nitrogen. Based upon the measured water spray cone angle ($\theta$=38°) with this injector, it is estimated that the peak mass flux here for LOX should occur at approximately 0.67 in. from the centerline. This estimate is confirmed by the mass flux results. An integration of the flux profile, assuming azimuthal symmetry, indicates that the measurements account for only 8% of the injection flowrate.

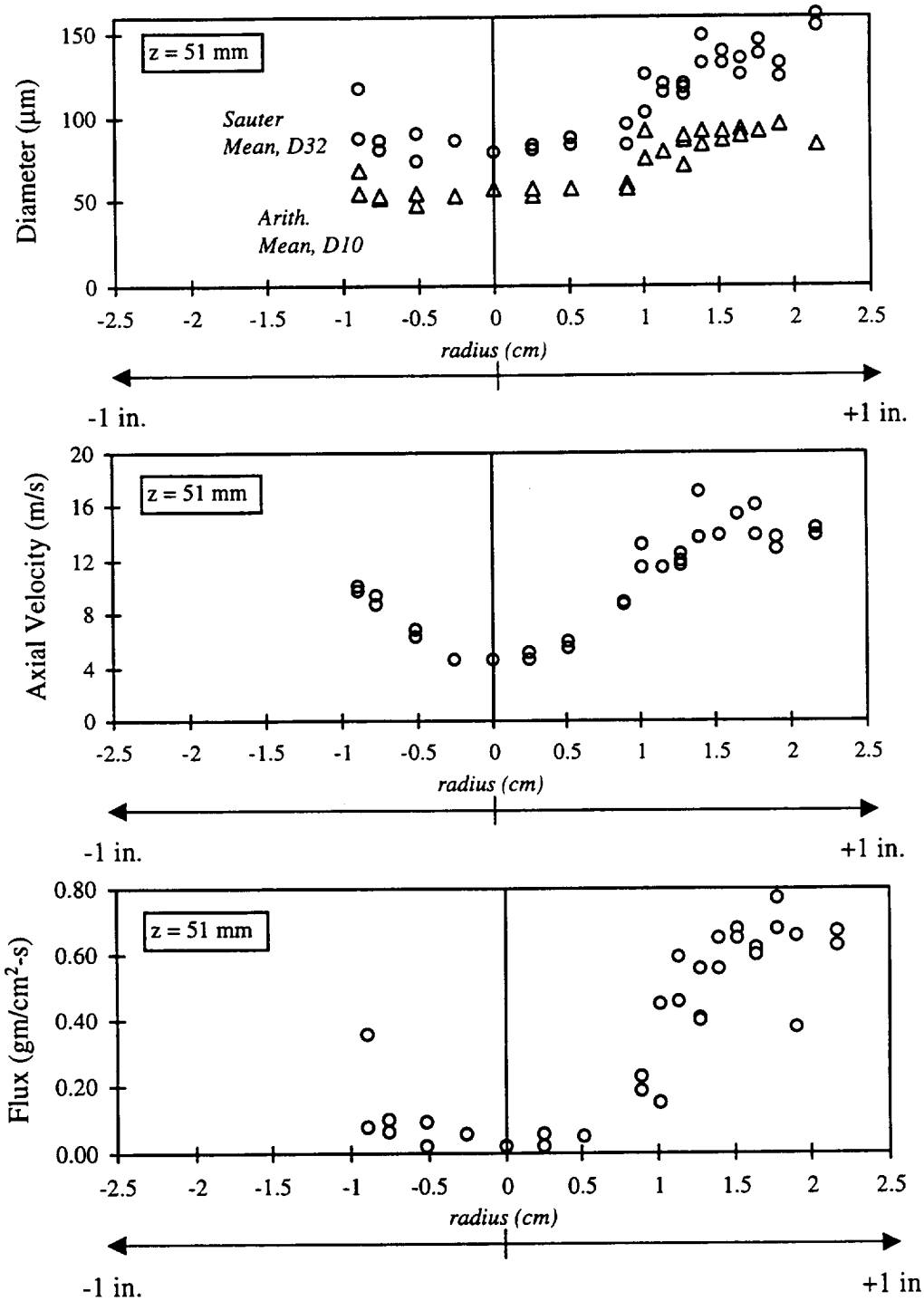


**Fig. 2.6.14. LOX drop measurements for axial location of 2 in. from injector face.**

In contrast to the above, the results at the downstream location of $z = 3.5$ in. are less definitive. Approximately 2000 or fewer drops are realized at the locations interrogated, and fewer than 500 in the region near the centerline. While there is a semblance of the original hollow-cone spray, the profiles of drop size, velocity, and flux are almost constant across the

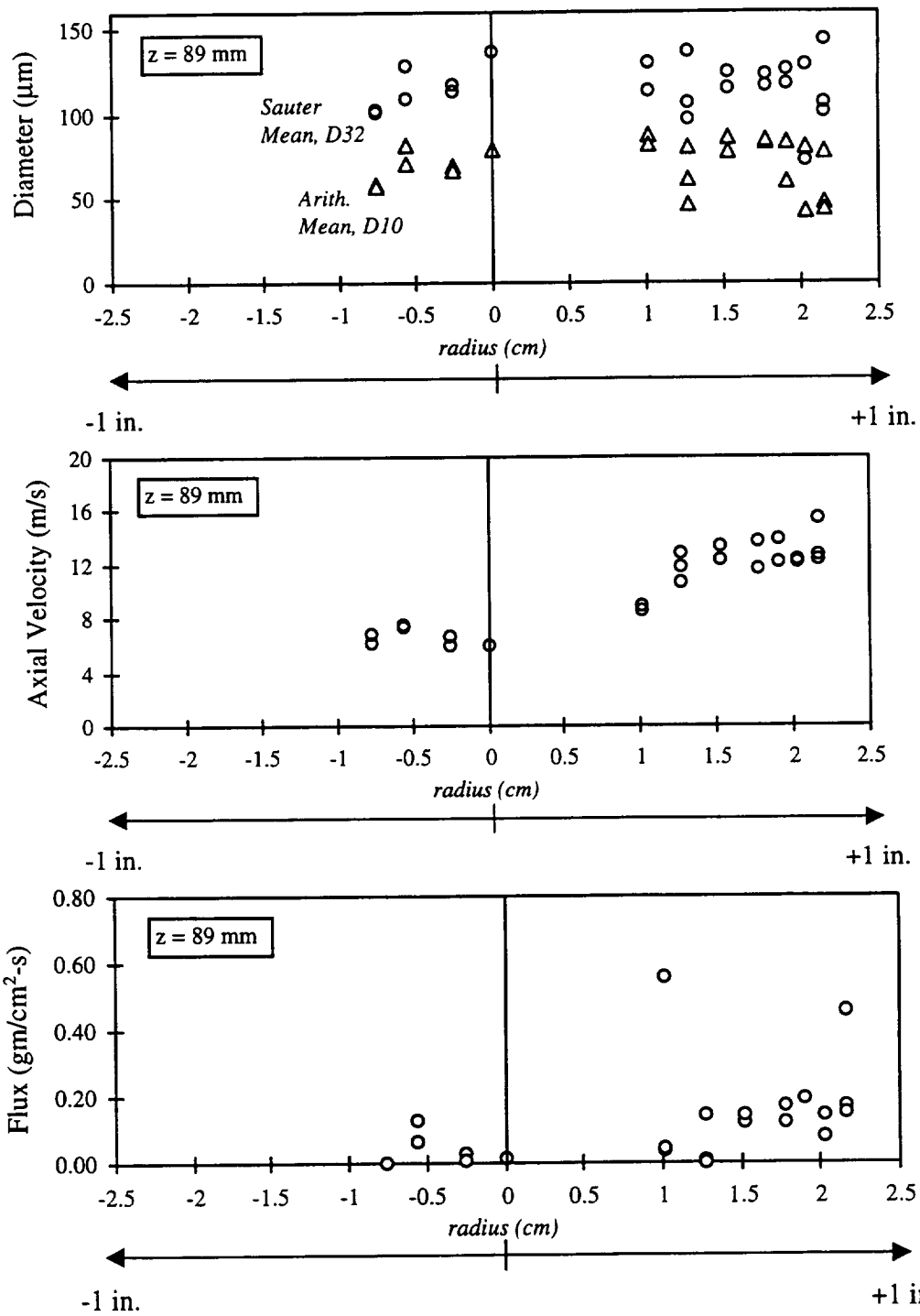


**Fig. 2.6.15. LOX drop measurements for axial location of 3.5 in. from injector face.**

chamber: $D_{32}$ ~ 130 $\mu$m, and $\bar{u}$ ~ 46 ft/s. The two anomalously high values of mass flux, out of twenty-two total, cannot be readily explained. It is noted that at this location the data scatter is greater owing to a smaller number of drop samples acquired during the combustion run.

## 2.6.2. LOX/$GH_2$ STOICHIOMETRIC CORE/DOWNSTREAM DILUTION STUDIES

In contrast to the direct injection approach discussed previously in this section, the stoichiometric core/downstream dilution approach, which is discussed next, involves near-stoichiometric combustion in a "can" recessed from the main injector face with downstream dilution of LOX from the main injector face for overall oxidizer-rich combustion. This type of approach is attractive because the same type of overall concept could also be used for fuel-rich combustion (where fuel would be injected at the main injector face). In this section, the experimental setup is detailed first followed by a discussion of the experimental results.

### 2.6.2.1. Experimental Setup

The experimental configuration for the second approach involving a stoichiometric core/downstream dilution for $LO_2/GH_2$ propellants is shown in Fig. 2.6.16. The swirl coaxial injector shown inside the cylindrical "can" on the left of the figure is the same element that was utilized for the direct injection approach discussed in Section 2.6.1. For the current set of experiments, this injector element was operated at a mixture ratio of 10 for $LO_2/GH_2$ propellants ($LO_2$ and $GH_2$ mass flowrates of 0.1 and 0.01 lbm/s, respectively). Downstream dilution of $LO_2$ was achieved via eight impinging doublet elements on the main injector faceplate. A detailed drawing of the injector faceplate for downstream $LO_2$ dilution is shown in Fig. 2.6.17. The impinging doublet elements are designed for downstream $LO_2$ dilution of 0.9 lbm/s, thus providing a total design stoichiometry of 100. The dimensions of the "can" geometry are L=3 in. and D= 0.875 in., for a L/D of 3.43. The impinging jet doublet elements are designed for a total included angle of 60 degrees, and are canted 20 degrees towards the center. The hole diameter

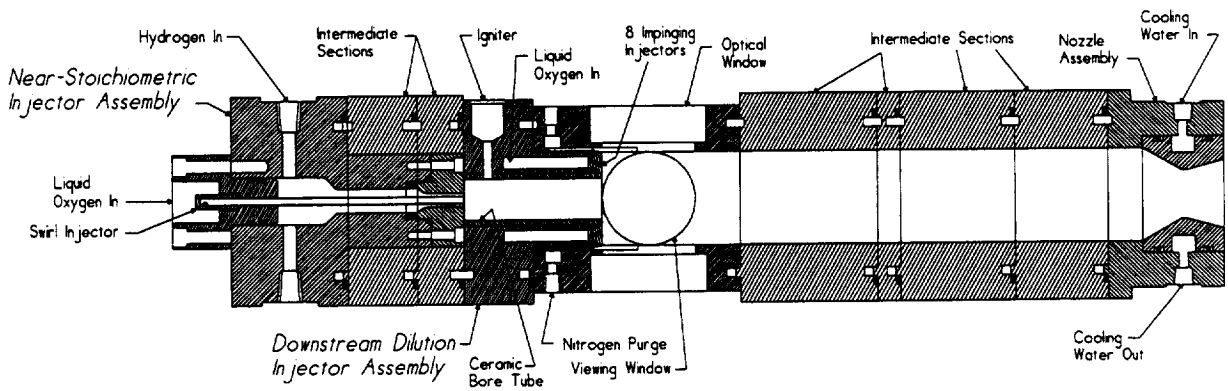


**Fig. 2.6.16. Rocket geometry for stoichiometric core/downstream dilution experiments.**

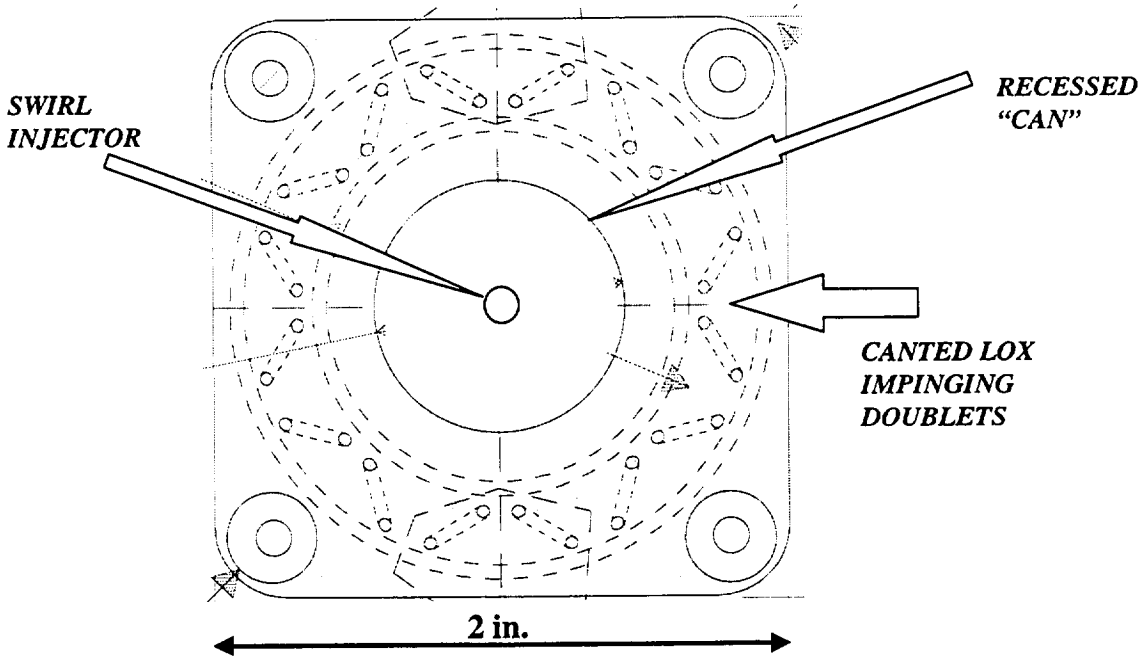


**Fig. 2.6.17. Injector face geometry for stoichiometric core/downstream dilution experiments.**

for the doublet elements is 0.041 in. For operation at higher mixture ratios than 100, the $GH_2$ flow through the main swirl coaxial injector element can be reduced.

The start-up procedure for the tests involved the following steps. A $GO_2/GH_2$ flame from a spark ignited igniter section (not shown in Fig. 2.6.16) was used to ignite the $LO_2/GH_2$ flow from the main swirl coaxial injector in the "can" cavity. The chamber pressure was verified for $LO_2/GH_2$ combustion before the staging of downstream $LO_2$ dilution.

### 2.6.2.2. Results and Discussion

A near-injector image of the combustion zone is shown in Fig. 2.6.18. The image was taken for an overall O/F of 99.4 for a chamber pressure of 354 psia. The field of view for the image is 2 in. The image clearly shows the LOX flow from three doublet impinging elements in the foreground. The two individual LOX jets from the central doublet are clearly visible in the image.

Experiments were conducted for overall O/F ranging from about 50 to 140. For all experiments, the LOX flow from the main shear coaxial injector element was maintained at 0.1 lbm/s. The LOX flow through the eight impinging elements, the hydrogen flow through the main swirl coaxial injector and the nozzle were varied to conduct the tests over the O/F range for

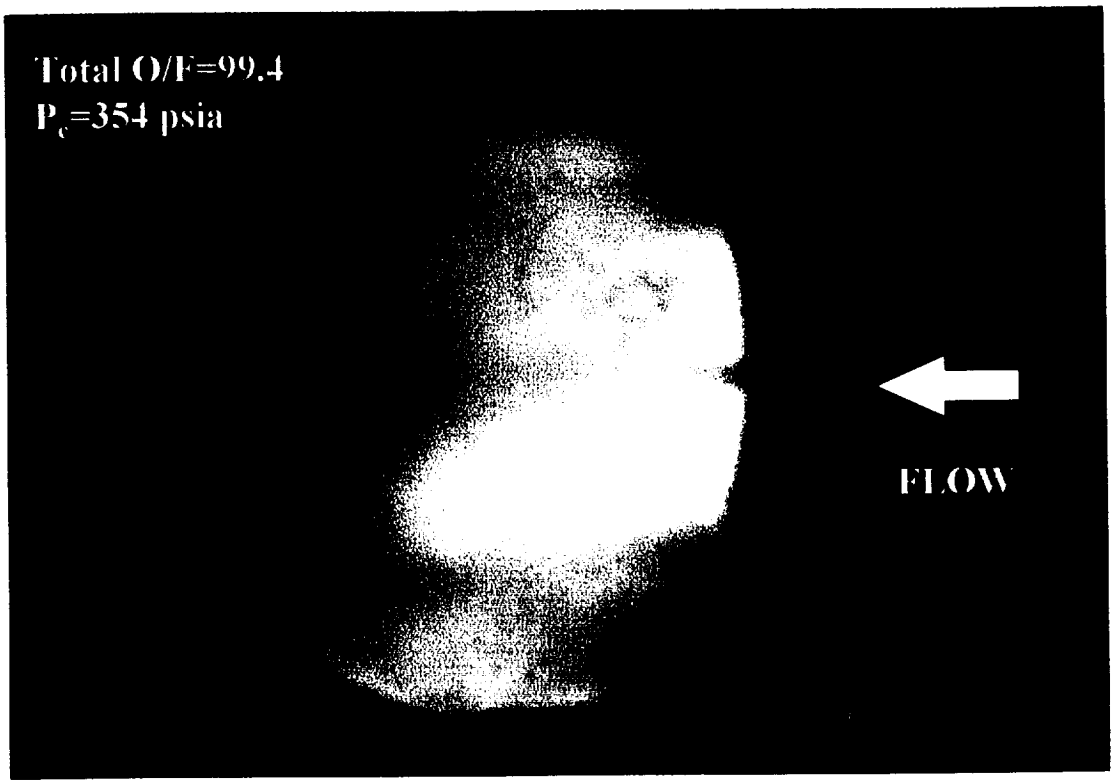


**Fig. 2.6.18. Photograph of near-injector face region for representative stoichiometric core/downstream dilution rocket firing.**

a chamber pressure of about 350 psia. For all experiments, a nominal (roughly 10% of total flow) nitrogen purge flow was introduced through the window cooling slots to cool the windows.

Examples of chamber pressure versus time for three distinct O/F cases are shown in Fig. 2.6.18. For all of these cases, the LOX downstream injection phase of the firing was staged after verification of ignition for the main "can" injector. This staging is evident in the pressure rise part of the chamber pressure traces in the figure. For all mixture ratio cases, overall steady state combustion was achieved within 1 s of propellant intoduction.

The performance results are shown in Table 2.6.5. c* efficiencies were calculated for both with and without the nitrogen purge flow. For all O/F cases, reasonable c* efficiencies were realized. This select set of experiments conducted for the stoichiometric core/downstream dilution approach shows that the approach is viable for high O/F LOX/$GH_2$ combustion. It is envisioned that for a full scale preburner configuration, multiple "can" geometries would be employed to uniformly distribute the combustion flowfield over the entire injector face. This design is attractive because it could also be used for fuel-rich preburner application.

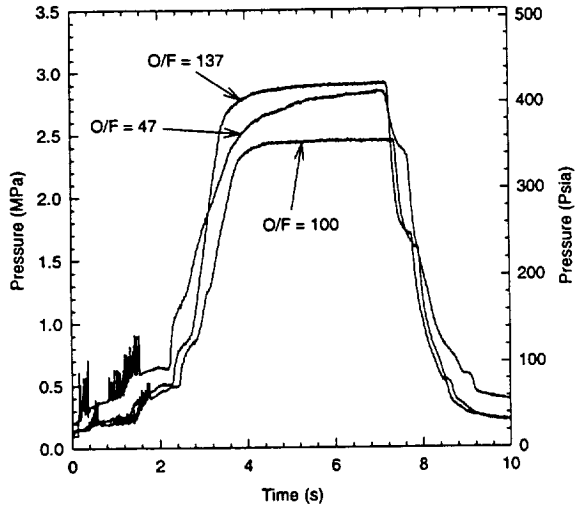


**Fig. 2.6.19. Pressure versus time traces for stoichiometric core/downstream dilution rocket firings at three overall oxidizer-rich conditions.**

**Table. 2.6.5. Performance Results for LOX/$GH_2$ Stoichiometric Core/Downstream Dilution Experiments.**

| Total LOX Flow (lbm/s) | LOX Dilution Inj. Pressure Drop (psia) | Overall O/F Ratio | Chamber Pressure (psia) | c* Efficiency (with purge) | c* Efficiency (without purge) |
|---|---|---|---|---|---|
| 0.331 | 31.8 | 47.1 | 409 | 0.909 | 0.974 |
| 0.694 | 85.8 | 99.4 | 355 | 0.928 | 0.963 |
| 0.674 | 110.4 | 96.5 | 356 | 0.941 | 0.978 |
| 0.715 | 91.9 | 103.2 | 353 | 0.913 | 0.946 |
| 0.726 | 79.6 | 104.8 | 361 | 0.928 | 0.961 |
| 0.707 | 79.9 | 102.1 | 362 | 0.942 | 0.976 |
| 0.726 | 82.0 | 105.4 | 360 | 0.929 | 0.962 |
| 0.732 | 81.6 | 106.2 | 360 | 0.926 | 0.958 |
| 0.759 | 92.4 | 108.0 | 367 | 0.917 | 0.950 |
| 0.955 | 142.2 | 137.0 | 421 | 0.957 | 0.985 |
| 0.904 | 132.7 | 129.5 | 415 | 0.964 | 0.995 |
| 0.998 | 131.7 | 141.5 | 408 | 0.904 | 0.930 |
| 0.954 | 131.3 | 138.3 | 411 | 0.940 | 0.967 |

## 2.6.3. LOX/RP-1 DIRECT INJECTION STUDIES

For LOX/RP-1 oxidizer-rich direct injection combustion studies, two injector geometries, viz. pintle and fuel-centered pintle injectors were studied. These studies are described individually in the following two sub-sections.

### 2.6.3.1. Pintle Injector Studies

Rocket engines using pintle injectors for storable propellants have been successfully employed for a range of propulsion applications. This includes the historic Lunar Module Descent Engine (LMDE) [41], the second stage Thor-Delta engine and a variety of thrusters for satellite applications. These designs have covered a wide range of thrust levels (5-250k lbf), chamber pressures (10 to 3,500 psia) and over twenty propellant combinations. Throughout this experience, engines using the pintle injector have never demonstrated vulnerability to combustion instability. In addition, recent tests with LOX/$LH_2$ [42] and LOX/RP-1 [43] at high thrust levels have demonstrated $c^*$ efficiencies in the 95-97% range.

The present interest in investigating pintle injector flowfield and performance characteristics is motivated by interest in the RP-1/LOX propellant combination. The overall goal of the research was to establish a data base on the flowfield characteristics of the injector for oxygen-rich as well as near-stoichiometric conditions. The interest in near-stoichiometric conditions stems from possible applications for the "bantam" class of thruster, whereas, investigations at oxygen-rich conditions provides guidance for designing oxidizer-rich preburners for future thrusters that employ the full-flow engine cycle. In addition, the research was directed towards providing a data base that could possibly explain the inherent stability of the injector.

Three pintle injectors were designed and fabricated based on discussions with TRW [44]. Experiments for these three injectors were conducted for both cold-flow and hot-fire conditions. The details of the design procedure and experiments involving these injectors are presented next.

#### 2.6.3.1.1. Injector Design

The pintle injector, illustrated for the configuration of this research project in Fig. 2.6.20, has a single centrally positioned injection element that protrudes into the combustion chamber. The central liquid, which may be either the fuel or the oxidizer, is turned 90 degrees and flows

$$\theta = f(TMR, BF)$$

$$TMR = \frac{(Mdot * U)_{RP}}{(Mdot * U)_{LOX}}$$

$$\text{Blockage Factor (BF)} = \frac{\Sigma \text{ Width of Slots}}{\text{Perimeter of Tube}}$$

$$\text{Effective Momentum Ratio (EMR)} = \frac{TMR}{BF}$$

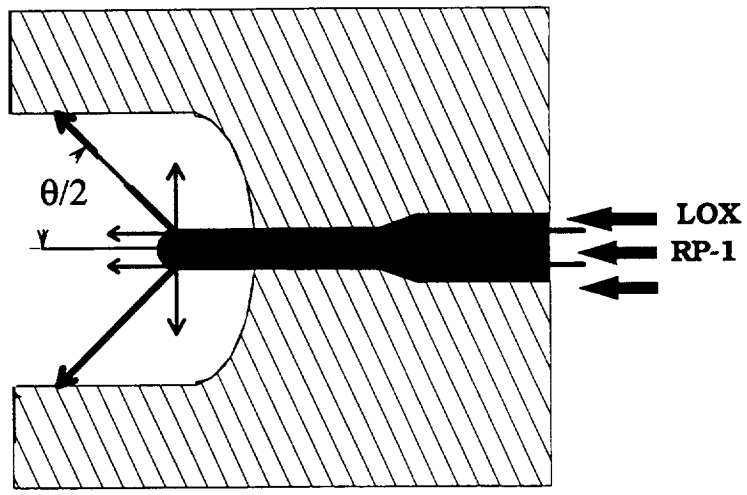


**Fig. 2.6.20. Pintle injector design characteristics.**

into the combustion chamber radially through a set of orifices. The second liquid flows axially through a continuous annulus around the pintle element. The two fluids impact to form a hollow spray cone whose characteristics are defined mainly by the momentums of the two impinging streams.

Pintle injectors for RP-1/LOX propellants can be designed with either central LOX/annular RP-1 or central RP-1/annular LOX. Here, based on momentum ratio and geometric constraints, the central RP-1/annular LOX configuration was chosen. The design of the central "pintle" geometry is crucial for achieving good mixing and combustion. Detailed discussions with TRW [44] yielded three "pintle" designs as shown in Fig. 2.6.21. All three injectors have the same outer diameter of 0.25 in, and are fabricated with Monel tubing and welded on nickel tips. The first injector has four horizontal slots with minimal blockage factor, the second injector has 24 vertical slots and the third injector has 24 horizontal slots. The slots were fabricated using electro-deposition machining (EDM). These three geometrically different pintle injectors were designed to cover a wide range of blockage factors (BF) and slot orientations with the goal of gaining insight on the effect(s) of geometry on performance.

2.6.3.1.2. Cold Flow Studies

Cold flow studies were conducted first to verify the functionality of the hardware and to understand the relationship between propellant momentum ratio and spray angle. The three variations of the pintle injector were characterized under cold flow conditions with water as a

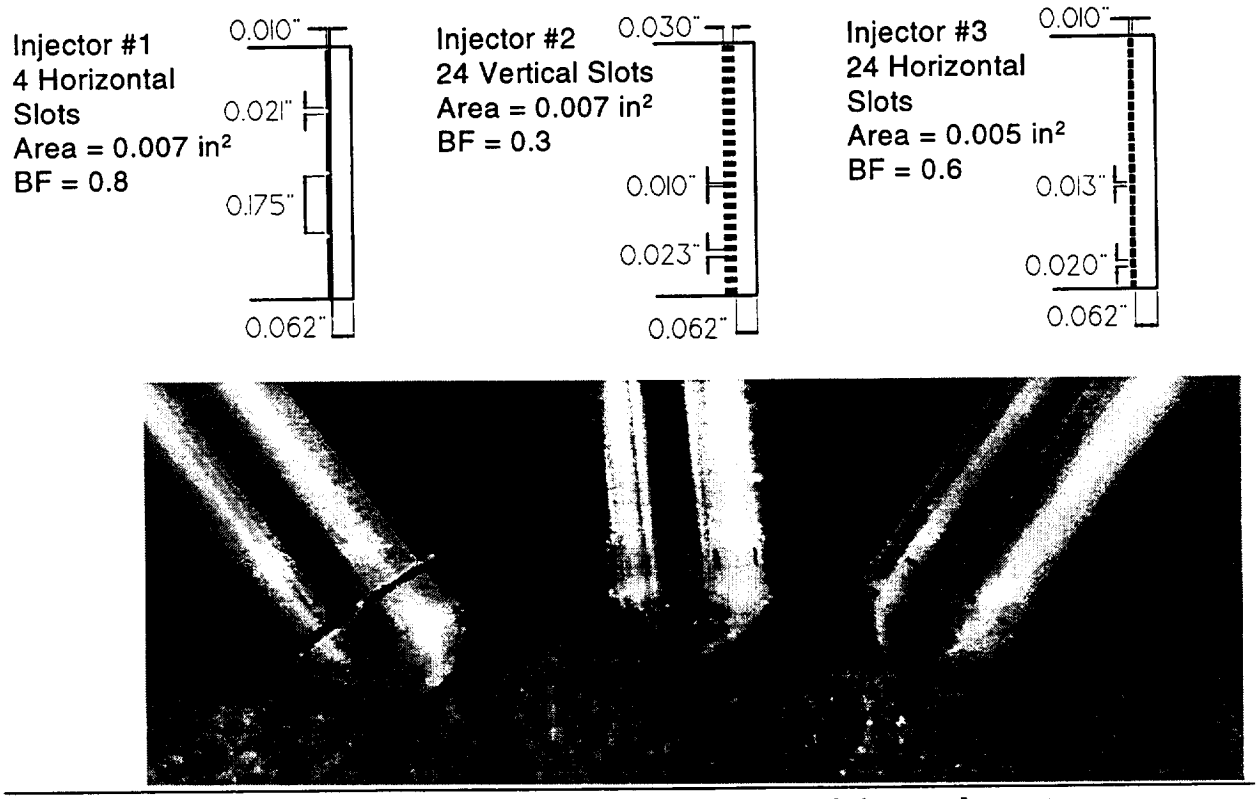


**Fig. 2.6.21. Pintle injector tip designs for three injector elements.**

simulant for both propellants. The matrix of 3 by 3 images shown in Fig. 2.6.22 are from the cold flow characterizations of the injectors. These images were obtained using a CID camera and stroboscopic lighting. The three images in the first column were taken by positioning the 35 mm camera directly beneath the pintle tip and flowing only through the central pintle. The first image for injector #1 shows four liquid sheets emanating from the four horizontal slots, whereas the next two images show 24 liquid jets. The middle and last column of images were taken by positioning the camera sideways with respect to the injector. The middle column of images for the same central and annular flows contrasts the effects of injector geometry on the resulting spray field. The spray cone angle for the first injector (4 horizontal slots) is seen to be larger than for the 24-slot injectors. Finally, the last column of images shows the spray field for flow conditions where the central to annular mass flowrate ratios, and hence, total momentum ratio (TMR; see Fig. 2.6.20 for definition), are higher than that for the images shown in the central column.

The spray half angle ,$\theta/2$, for various total momentum ratios measured from the images shown in Fig. 2.6.22 and others are depicted in Fig. 2.6.23. The measurements show that as

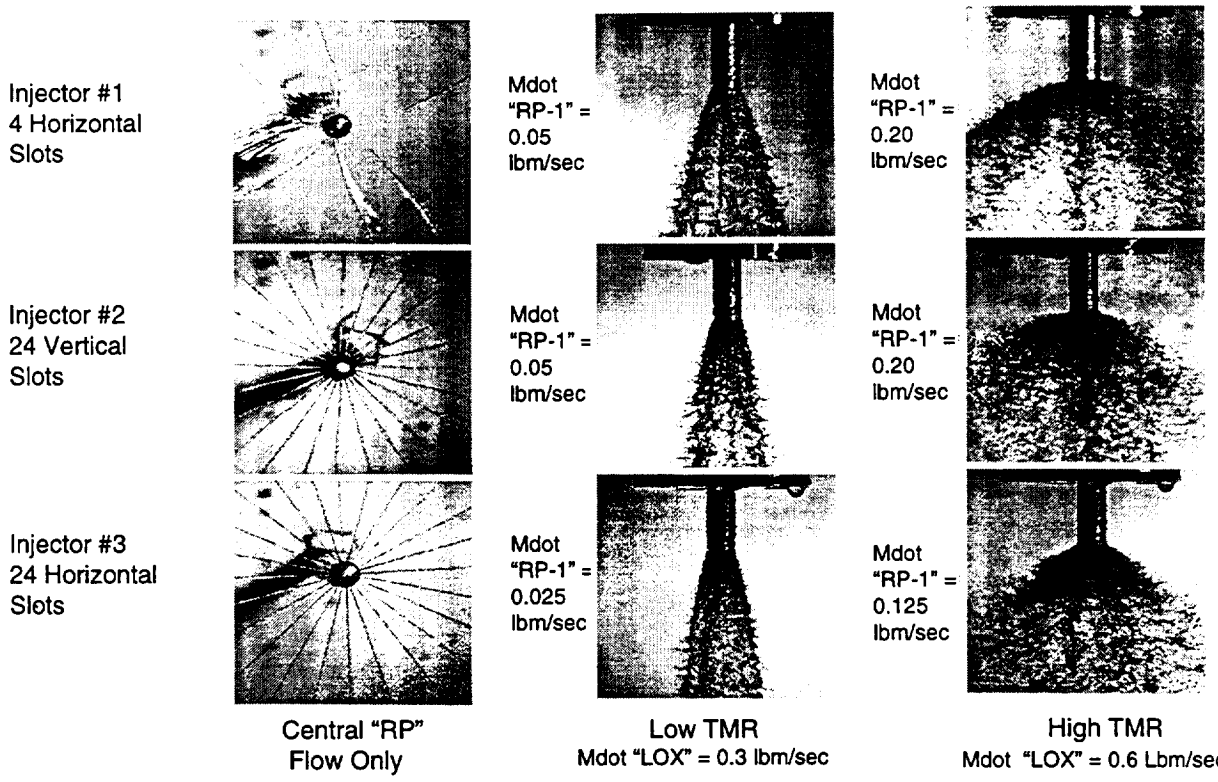


**Fig. 2.6.22. Cold flow visualizations for three pintle injectors.**

TMR increases, the spray angle increases at a less than linear rate. The measurements also indicate that the blockage factor (BF) does not have a significant influence on the spray angle for the range of blockage factors for the three injectors (0.3-0.8).

2.6.3.1.3. Hot Fire Studies

Since the pintle injector has a wide spray angle as compared to other traditional injectors such as shear or swirl coaxial injectors, the recirculation flow patterns in the chamber are extremely important. In order to address this issue, a new circular cross section (2 in. diameter) optically-accessible combustion chamber with a smooth contoured injector face was designed and fabricated specifically for the experiments involving the LOX/RP-1 pintle injector. Note that this chamber differs from the workhorse chamber utilized for the majority of the experiments reported here (see Section 2.2), and consequently a brief description is provided. The schematic of this new rocket chamber is shown in Fig. 2.6.24. The chamber is comprised of several sections that include an injector assembly, window/igniter assembly, blank sections, and a nozzle assembly. The injector assembly includes the pintle injector and a concave injector face that transitions smoothly to the round section as shown in the figure. The window-section allows

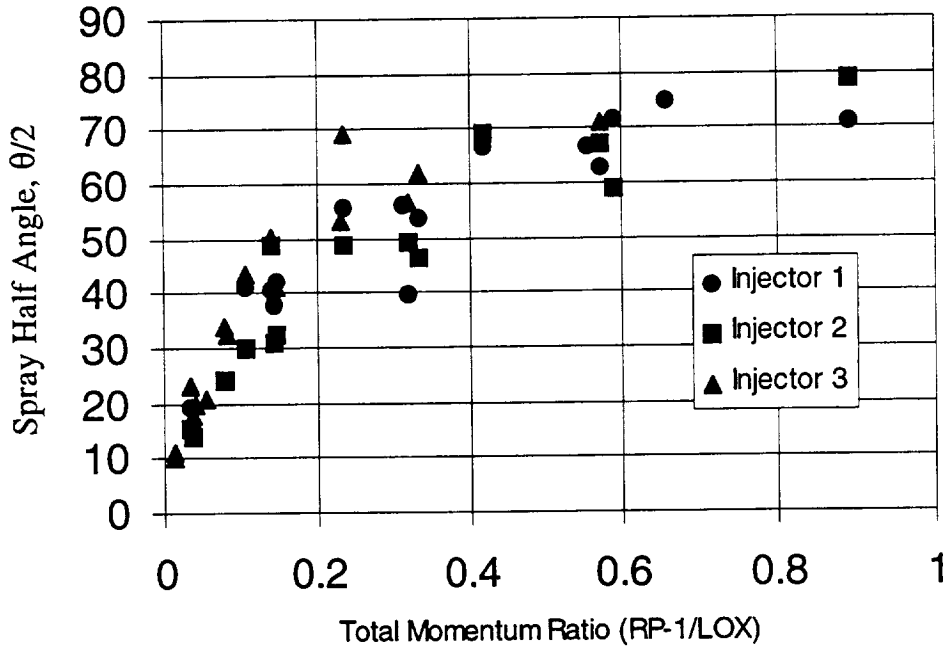


**Fig. 2.6.23. Spray Half Angle (θ/2) vs. Total Momentum Ratio.**

optical access into the combustion chamber for laser-based diagnostic techniques. Two circular 1 in. diameter quartz windows, 150° apart, and a 1 x 0.25 in. slot provide optical access into the rocket chamber. The circular windows were positioned 150° apart to facilitate phase Doppler interferometry measurements. The slot access which is 90° from one of the circular windows is for laser sheet introduction into the chamber. This feature allows the use of diagnostic techniques such as planar Mie scattering or Raman spectroscopy that require laser beam/sheet with 90° camera positioning. The size of the windows represents a compromise between maintenance of a circular cross section and improved optical access. The window section also has a port for the $GH_2/GO_2$ igniter (not shown here) that is used for ignition. Overall, the chamber is modular in design, i.e., the blank sections and the window section can be moved around to position the window section at various distances from the injector, and the chamber length can be varied by removing blank sections. The nozzle assembly is designed such that nozzles with various throats can be easily interchanged.

Twenty three successful firings including all three injectors and a wide range of O/F ratios were conducted as summarized in Table 2.6.6. All combustion pressure traces were stable for at least the final 2 seconds of the 3 second firings. The combustion pressures were all close to the target 300 psia indicating a reasonably predictable performance level. A panoramic

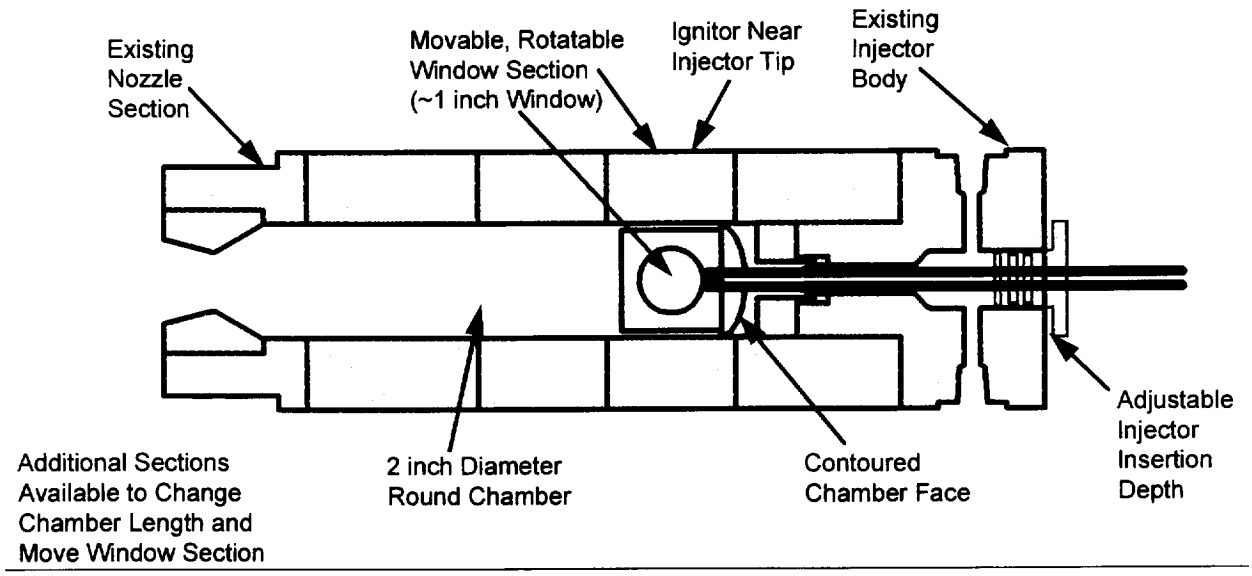


**Fig. 2.6.24. Rocket chamber for pintle injector experiments.**

photographic image of a rocket firing for the RP-1/LOX pintle injector is shown in Fig. 2.6.25. The flame luminosity of RP-1/LOX combustion is extremely high as evidenced by the light level that passed through a neutral density filter positioned in front of the window. Close-up photographs (not shown here) of the near-injector region indicated very high light intensity levels prohibiting any assessment of the injectors' flame holding characteristics.

These experiments were geared towards assessing the three geometric variations of the pintle injector under combustion conditions. As indicated in the table for the hot-fire

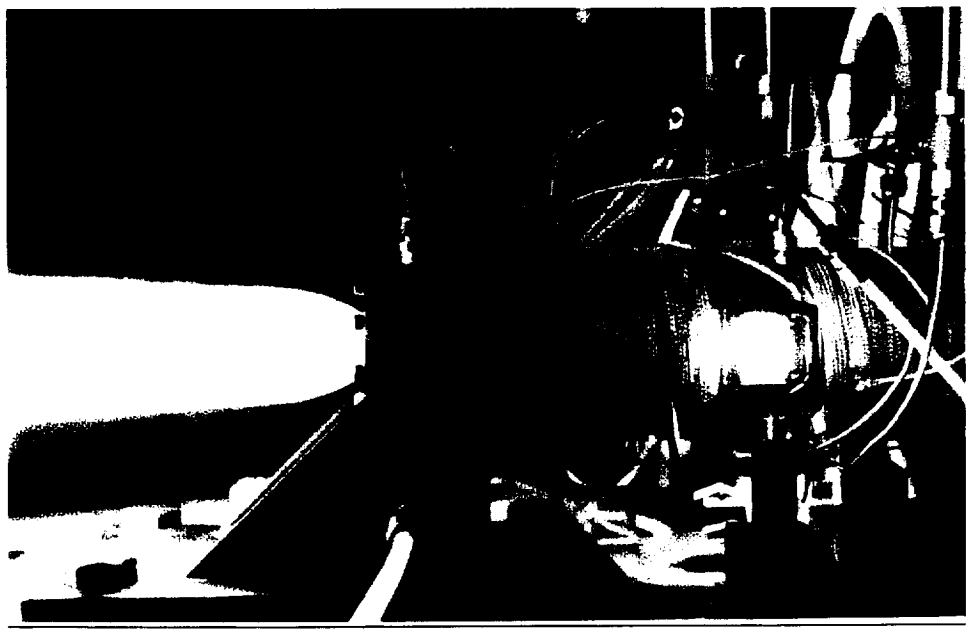

**Fig. 2.6.25. Panoramic photograph of LOX/RP-1 rocket firing for pintle injector.**

**Table. 2.6.6. Performance Results for LOX/RP-1 Pintle Injector Experiments.**

| Injector | Case # | Mass Flowrate (lbm/s) | | | O/F | TMR | $P_c$ (psia) |
|---|---|---|---|---|---|---|---|
| | | LOX | RP-1 | $GN_2$ | | | |
| *Injector # 1* | A1 | 0.37 | 0.14 | 0.11 | 2.60 | 0.77 | 298 |
| *(4 Slots)* | A1 | 0.41 | 0.14 | 0.11 | 2.84 | 0.66 | 312 |
| | A2 | 0.68 | 0.25 | 0.10 | 2.69 | 0.72 | 312 |
| | A2 | 0.70 | 0.25 | 0.10 | 2.77 | 0.65 | 307 |
| | A2 | 0.71 | 0.25 | 0.10 | 2.81 | 0.66 | 315 |
| | B1 | 0.97 | 0.34 | 0.10 | 2.86 | 0.66 | 315 |
| | B2 | 0.92 | 0.37 | 0.10 | 2.48 | 0.96 | 309 |
| | B3 | 0.68 | 0.41 | 0.10 | 1.66 | 1.83 | 303 |
| | B1 | 0.92 | 0.34 | 0.09 | 2.72 | 0.73 | 308 |
| | B4 | 0.91 | 0.15 | 0.08 | 6.00 | 0.14 | 277 |
| | | | | | | | |
| *Injector # 2* | D3 | 0.73 | 0.41 | 0.10 | 1.78 | 1.46 | 308 |
| *(24 Vertical* | D2 | 0.81 | 0.38 | 0.10 | 2.12 | 1.09 | 324 |
| *Slots)* | D1 | 0.82 | 0.34 | 0.10 | 2.39 | 0.8 | 312 |
| | D3 | 0.84 | 0.41 | 0.10 | 2.03 | 1.24 | 331 |
| | D4 | 0.85 | 0.15 | 0.10 | 5.52 | 0.15 | 298 |
| | D5 | 0.88 | 0.06 | 0.10 | 13.6 | 0.03 | 305 |
| | D5 | 0.93 | 0.06 | 0.10 | 14.4 | 0.03 | 304 |
| | | | | | | | |
| *Injector # 3* | C4 | 0.94 | 0.12 | 0.10 | 7.57 | 0.14 | 301 |
| *(24* | C3 | 0.63 | 0.27 | 0.10 | 2.38 | 1.29 | 326 |
| *Horizontal* | C3 | 0.65 | 0.27 | 0.10 | 2.43 | 1.42 | 339 |
| *Slots)* | C2 | 0.58 | 0.25 | 0.10 | 2.34 | 1.29 | 319 |
| | C1 | 0.68 | 0.22 | 0.10 | 3.09 | 0.82 | 322 |

experiments, all three injector geometries yielded stable ignition and combustion characteristics. Injector #2 was tested at mixture ratios up to 14.4, and the results showed that even at high mixture ratios, the combustion characteristics of the pintle injector were stable.

### 2.6.3.2. Pentad Injector Studies

In this section, the studies related to oxidizer-rich LOX/RP-1 combustion for a pentad impinging injector element are presented and discussed. The research impacts immediate and future technology development goals. For oxidizer-rich LOX/RP-1 propellants, the pentad impinging injector element was chosen in addition to the earlier described pintle injector because it is the most amenable injector design in terms of atomization/injector pressure drop requirements.

The design of the pentad injectors for oxidizer-rich conditions was based on standard practice found in many references (for example, see Ref. 45). The goal of the design procedure was to design high performing injector elements that had realistic pressure drop margins.

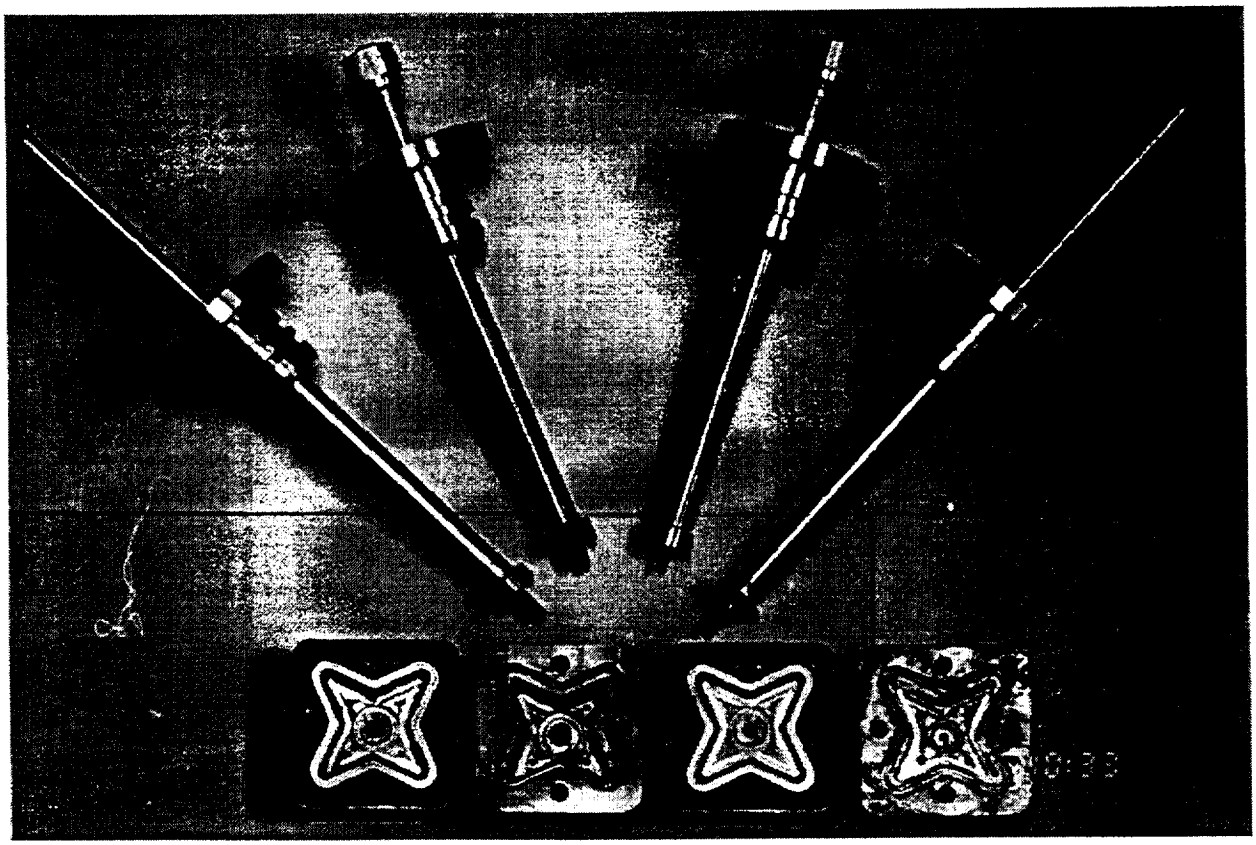

**Fig. 2.6.26. Photograph of pentad injectors designed for direct injection LOX/RP-1 experiments.**

A good pentad injector design requires that the orifice sizes are nearly equal and that the central propellant stream axial momentum is close to the radial momentum for the outer (4 holes) propellant within design pressure drop requirements. With the realization that the stoichiometric mixture ratio for LOX/RP-1 is 2.9, a "classic" pentad element for near-stoichiometric conditions would therefore be fuel-centered. However, here the goal was to design an oxidizer-rich pentad element for a mixture ratios of 50. Clearly, to equate propellant stream momentums for the oxidizer-rich case, it is necessary to design a fuel-centered injector. It should be noted that because of the disparity in propellant flowrates for either case, the injector design is not "ideal" in terms of equal hole sizes, stream momentums and pressure drops but represents an optimization of all three parameters.

The fuel-centered oxidizer-rich element for a mixture ratio of 50 was designed for a LOX flowrate of 1 lbm/s such that the LOX and RP-1 pressure drops would be 100 and 75 psid, respectively. The half-impingement angle for the injector element was set at 30°.

A photograph of four pentad injectors is shown in Fig. 2.6.26. From the left, the third element is the oxidizer-rich pentad element. The remaining three elements were designed and fabricated for other stoichiometric ratio/flowrate applications. The injector elements were designed such the central post screws onto the injector face from the back side. Additionally, all injector posts have two concentric tubes that are soldered onto the copper piece at the tip region of the post. This arrangement provides air (very low thermal conductivity) insulation between the two propellants, a feature that prohibits the RP-1 flow in the injector from freezing.

The oxidizer-rich LOX/RP-1 oxidizer-rich experiments were initiated for the target mixture ratio of 60. However, a delayed ignition occurred during the beginning of the first firing and damaged the window section of the rocket and a camera. Based on this mishap, all oxidizer-rich LOX/RP-1 experiments were terminated.

## 2.7. FUEL-RICH PREBURNER COMBUSTION AND INJECTOR TECHNOLOGY

In this section, research work carried out for fuel-rich combustion for both LOX/$GH_2$ and LOX/RP-1 propellant combinations are presented and discussed. The motivation for the current work is driven by the need to advance injector development technologies for fuel-rich preburner applications. For both propellant combinations, only the direct injection method was investigated. Recall from the last section on oxidizer-rich combustion that the direct injection method involves the injection of all the propellants from the main injector. For the two propellant combinations, viz. LOX/$GH_2$ and LOX/RP-1, the swirl coaxial injector element and oxidizer-centered pentad impinging jet injector were investigated, respectively. The injector design philosophy for the propellant combinations along with results obtained for rocket firing experiments are presented and discussed in the following two sections.

### 2.7.1. LOX/$GH_2$ DIRECT INJECTION STUDIES

In this section, the studies related to fuel-rich LOX/$GH_2$ combustion for a swirl coaxial injector element are presented and discussed. The research impacts immediate and future technology development goals. The gas generator of the proposed YRS2200 engine, which is one option for the X-33 RLV, operates at fuel-rich conditions for LOX/$GH_2$ propellants. In addition, the preburner for the SSME as well as one of the preburners of the conceptual full-flow staged combustion engine cycle operate under these conditions. The swirl coaxial injector element was chosen in favor of the shear coaxial injector element in the present study because earlier efforts indicated that mixing and combustion zone lengths are significantly reduced for the swirl element [25,29].

The key issue for preburner injector technology development is the design of an injector that produces uniform temperature mixed combustion product gases at the exit. The uniformity of temperature and species at the exit plane can be characterized by intrusive techniques such as thermocouple rakes and gas sampling probes. However, the significant evolution of laser-based diagnostic techniques over the last decade allows for the possibility of non-intrusive measurement of these important quantities in the harsh flowfield rocket environment. For temperature and species measurements in combustion environments, laser-based diagnostic

techniques have been successfully used [46]. Although these diagnostic tools, such as Raman spectroscopy and coherent anti-Stokes Raman spectroscopy (CARS), have not been extensively used for characterizing rocket flowfields, they are well established techniques in studying flames in atmospheric to moderately high (2 to 8 atm.) pressures [47-50]. In recent years, there has been some involvement of laser diagnostics in screening and development of rocket engine injectors for gaseous propellants (see Section 2.8). Use of Raman spectroscopy is well incorporated in these investigations where the technique is suitable [51-54]. Despite the complexity of the experimental systems, coherent anti-Stokes Raman spectroscopy (CARS) has been utilized for rocket plume temperature characterization [55], and laser induced fluorescence (LIF) for OH radical measurements in the near-injector region [56].

The number of studies of LOX/$GH_2$ combustion has been relatively small due to the extreme nature of the flowfield. The limited number of studies include phase Doppler interferometry measurements of LOX drop size and velocity [22] and flow visualization studies of injector flowfields at chamber pressures ranging from sub- to super-critical [27-28, 57]. In this section, the successful application of Raman spectroscopy for major species and temperature profile measurements under rocket firing conditions is also presented.

### 2.7.1.1. Experimental Setup

In this section, the swirl coaxial injector geometry, experimental flow conditions and Raman spectroscopy implementation issues are presented.

#### 2.7.1.1.1. Swirl Coaxial Injector Element

A swirl coaxial injector element was utilized for introducing the LOX/$GH_2$ propellants into the chamber. The schematic of the injector is shown in Fig. 2.7.1. As is evident, the central LOX post is the same as the one utilized for the oxidizer-rich studies described in Section 2.6. The injector was designed for a nominal liquid oxygen flowrate of 0.25 lbm/s. The swirl nut seen in the figure is used for imparting swirl to the liquid. The inner and outer diameters of the post measure 0.135 in. and 0.165 in., respectively. Cold flow measurements have shown that the swirl angle is 42°. For the fuel-rich experiments described here, an outer diameter of 0.5 in. was chosen for the hydrogen annulus.

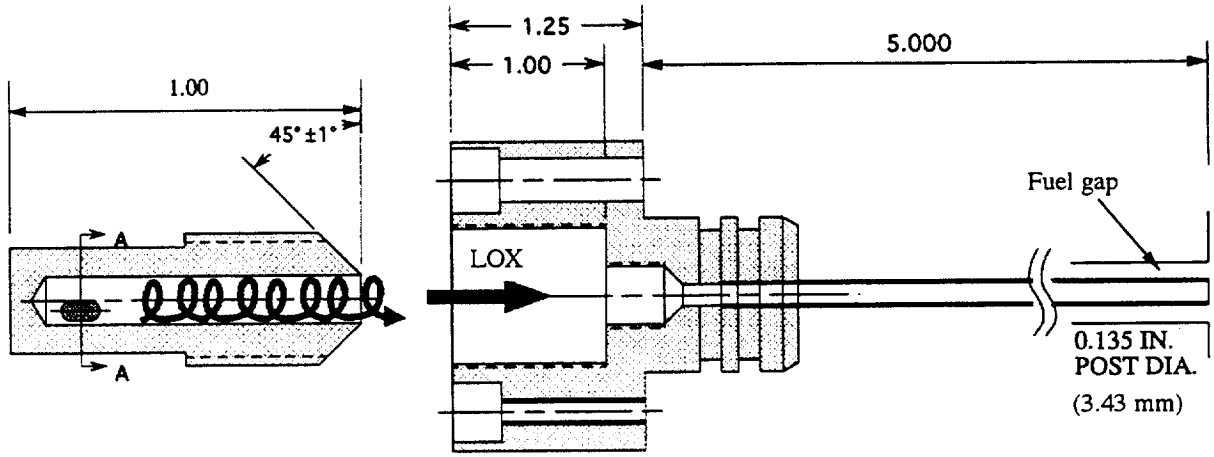


- **Industry-Scale Injector ($C_d$ = 0.32, $L/d$ = 20, Swirl Angle = 42°)**
  - **0.135 in. Post ID**
  - **0.165 in. Post OD**
  - **0.5 in. Annulus OD**

**Fig. 2.7.1. Schematic of swirl coaxial injector.**

2.7.1.1.2. Rocket Window Section for Raman Spectroscopy

A special optically-accessible window section was designed for the Raman spectroscopy experiments. A schematic of the rocket chamber indicating the special optically-accessible window section is shown in Fig. 2.7.2. Since the technique is applied in a "line" measurement configuration, the introduction of the laser beam into the chamber requires only a small access port. However, since the high energy beam is tightly focused to achieve high spatial resolution in the chamber, a quartz window placed near the vicinity of the focal point is immediately damaged. To circumvent this problem, a small quartz window (0.5 in. diameter; 0.25 in. thick) was attached at the end of a 0.5 in (O. D.) stainless steel tube that extended roughly 11 inches from the side wall of the chamber to introduce the laser radiation to the control volume. There was no need to use a window on the downstream side of the control volume. Thus, the laser beam simply exited from the control volume and was blocked by a beam stop that is placed at the end of a stainless steel tube similar to the laser access port. With this configuration, the laser beam cross-section at the quartz window location was increased, resulting in lower energy per unit area, without compromising the optical setup. For the present arrangement, the Raman signal is collected 90° from the incident laser beam. Consequently, a slotted optical access port

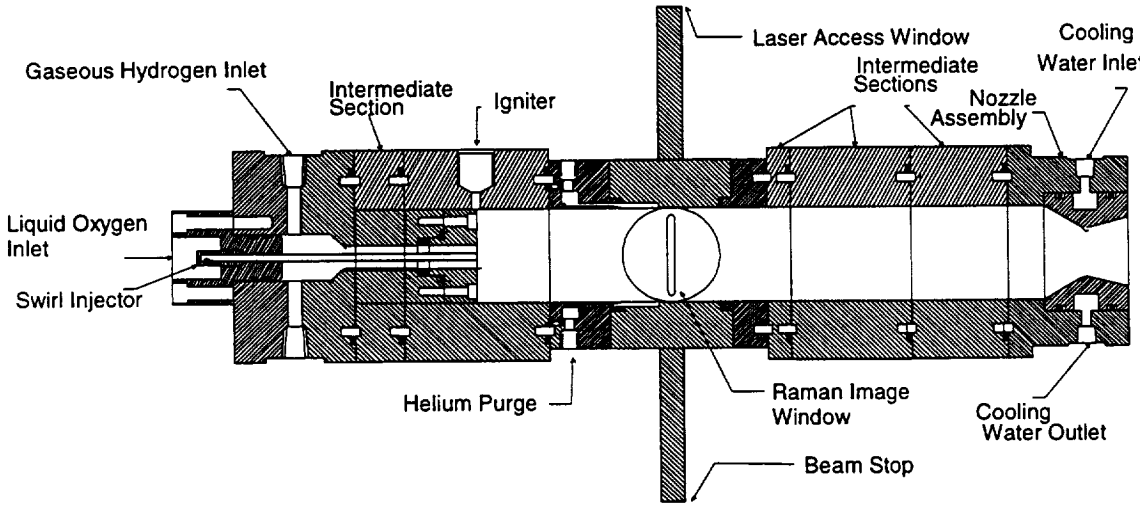


**Fig. 2.7.2. Cross-sectional view of the optically-accessible rocket.**

on the top of the window section was utilized for signal collection. All of the windows were protected from the extreme temperatures by a purge gas of helium.

2.7.1.1.3. Flow Conditions

Initial studies involving the injector element were conducted for a fixed LOX flowrate of 0.2 lbm/s over mixture ratios ranging from one to four. The goal of this phase of experimentation was to document the performance characteristics of the injector element. Detailed flow conditions for four mixture ratio conditions are shown in Table 2.7.1. The results show that the c* efficiency for these experiments decrease with increasing mixture ratio. It is evident from these results that for the fixed injector geometry case studied here, the lower performance is directly a consequence of poor atomization at the lower fuel/oxidizer momentum ratio. Performance at the higher mixture ratio would have increased if the hydrogen stream momentum were increased by decreasing the cross sectional area of the fuel annulus.

Raman spectroscopy was setup for making species and temperature measurements at an axial location of 5 in. from the injector face. This axial location corresponds to a length to diameter ratio of 37 based on the LOX post diameter of 0.135 in. and was chosen because it represented a sufficient length from the injector face for substantial vaporization of the LOX. Raman spectroscopy is only suited to liquid free flow regions since the orders-of-magnitude more intense Mie scattering from LOX drops overwhelms the weak Raman signal. Initial Raman measurements at this location indicated that only the mixture ratio case of one (Case A;

**Table 2.7.1. Rocket Test Firing Conditions.**

| CASE | A | B | C | D |
|---|---|---|---|---|
| LOX Flowrate lbm/s | 0.2 | 0.2 | 0.2 | 0.2 |
| $GH_2$ Flowrate lbm/s | 0.2 | 0.1 | 0.067 | 0.05 |
| $(O/F)_{mass}$ | 1 | 2 | 3 | 4 |
| $T_{adiabatic}$ K | 1257 | 2033 | 2628 | 3053 |
| $P_{chamber}$ psia | 429 | 392 | 398 | 412 |
| $c^*$ Efficiency | 1.0 | 0.96 | 0.86 | 0.80 |

Table 2.7.1) exhibited a totally LOX-free flowfield. Based on these investigatory experimental results, the technique was applied only for Case A (see Table 2.7.1) for detailed flowfield measurements at the 5 in. axial measurement location.

2.7.1.1.4. Raman Diagnostic Setup

Temperature and major species profiles corresponding to the Case A were obtained by linewise spontaneous vibrational-rotational Raman imaging. All of the measurements were done during the steady state part of the rocket firing. A sample chamber pressure trace for Case A indicating the Raman data collection timing is shown in Fig. 2.7.3.

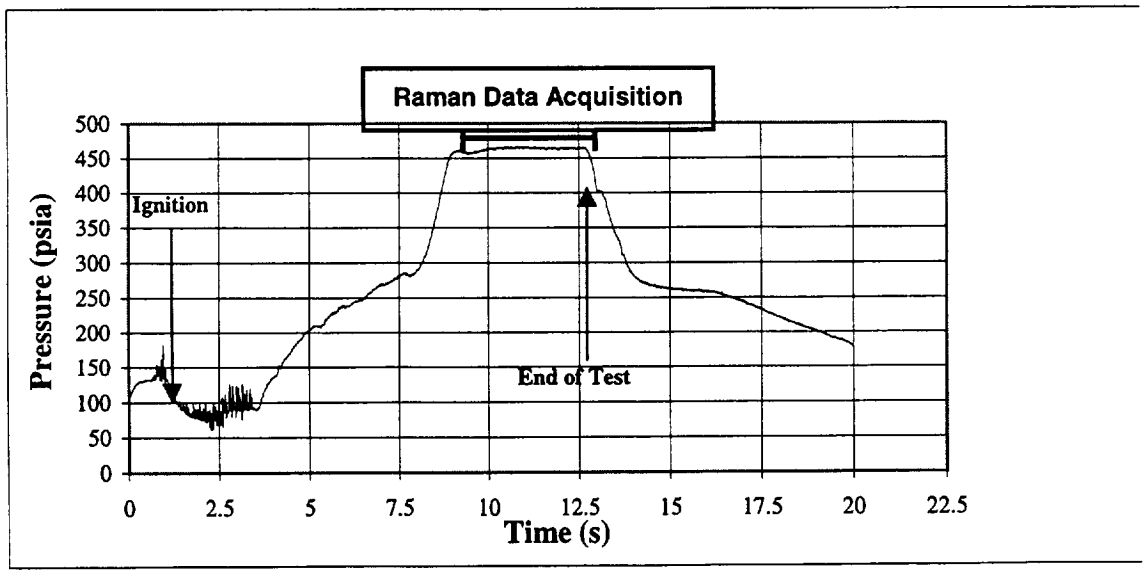


**Fig. 2.7.3. Sample pressure trace from a typical rocket test case.**

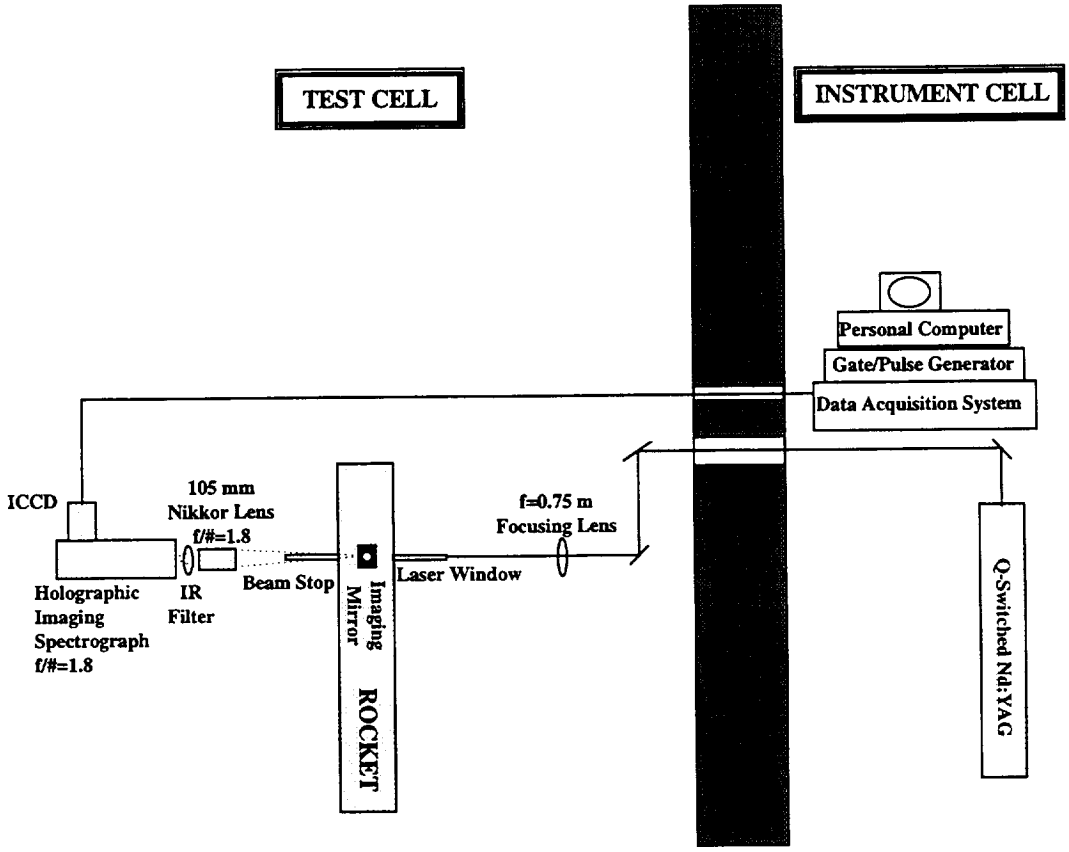


**Fig. 2.7.4. Schematic of Raman setup.**

Single shot Raman images were gathered while the chamber pressure was steady which took place approximately 5 seconds after ignition of the flow. This delay is associated with achieving good quality LOX conditions at the injector. A pulse laser operation frequency of 5 Hz was chosen to allow enough time for data transfer to occur. This 5 Hz frequency enabled roughly 15 single shot Raman images to be captured during each rocket firing.

A schematic of the Raman system is shown in Fig. 2.7.4. A Q-switched, frequency doubled Nd:YAG laser operating at 5 Hz was used as the 532 nm excitation source. The laser power output was measured to be about 300 mJ/pulse. The laser pulse polarization was rotated from the vertical to horizontal direction via two mirrors immediately following the laser. This allowed the collection optics to be in the correct polarization orientation. The laser beam was passed through the window section that separates the test cell from the instrument cell and reflected by two mirrors to position it in line with the rocket window section. The laser beam was focused to a 500 μm diameter at the center of the rocket cross section by an f=0.75 m

focusing lens. A linewise Raman image of the flame front was projected by a 3 in. diameter mirror placed above the rocket window section. The image was gathered and focused by an f/# 1.8, 105 mm Nikkor lens. An f/# 1.8 Kaiser Optic holographic imaging spectrograph in conjunction with an intensified charge-coupled device (ICCD, 576x384 pixel) camera was used to capture the Raman signals of major combustion species ($H_2$, $O_2$, $H_2O$). The system allowed simultaneous multi-species multi-point Raman measurements. The slit width of 500 μm and binning of four pixels in the radial dimension, corresponding to the 384 pixel direction, and of six pixels in the wavelength dimension, corresponding to the 576 pixel direction were used. The Raman signal-to-noise ratio was increased by discriminating against the Rayleigh interference by using of a notch filter centered at 532 nm (FWHM ≈ 18 nm) placed inside the spectrograph. The intense flame interference was reduced 50% by using a linear dichroic sheet polarizer aligned with the Raman signal polarization. Further discrimination against the flame luminosity was achieved by the use of a sharp IR filter.

#### 2.7.1.2. Results and Discussion

The major species mole fractions and temperature can be obtained from the wavelength averaged vibrational Raman signal intensity values. Raman signal intensity is related to the number density of the molecule, a constant and a temperature dependent function that relates the spectral bandwidth factor to the Raman signal strength as represented by equation 2.7.1.

$$S_i = n_i K_i f_i(T) \tag{2.7.1}$$

The constant in this equation accounts for the laser pulse energy, species Raman cross section, optical collection efficiency and optical solid angle.

Once the Raman signals from the different species are collected by the ICCD camera, they are converted into mole fraction and temperature profiles across the measured rocket combustion chamber using calibration curve fit values and assumption of ideal gas law behavior.

An example of a raw uncorrected Raman image is shown in Fig. 2.7.5 corresponding to a rocket firing for Case A (see Table 2.7.1). In this figure, the abscissa represents the wavelength of light, whereas the ordinate represents radial location. The intensity at each pixel represents light intensity at a given wavelength for a radial position. The three dimensional plot shown in Fig. 2.7.6 shows the intensity (in arbitrary units) for a typical instantaneous unprocessed image

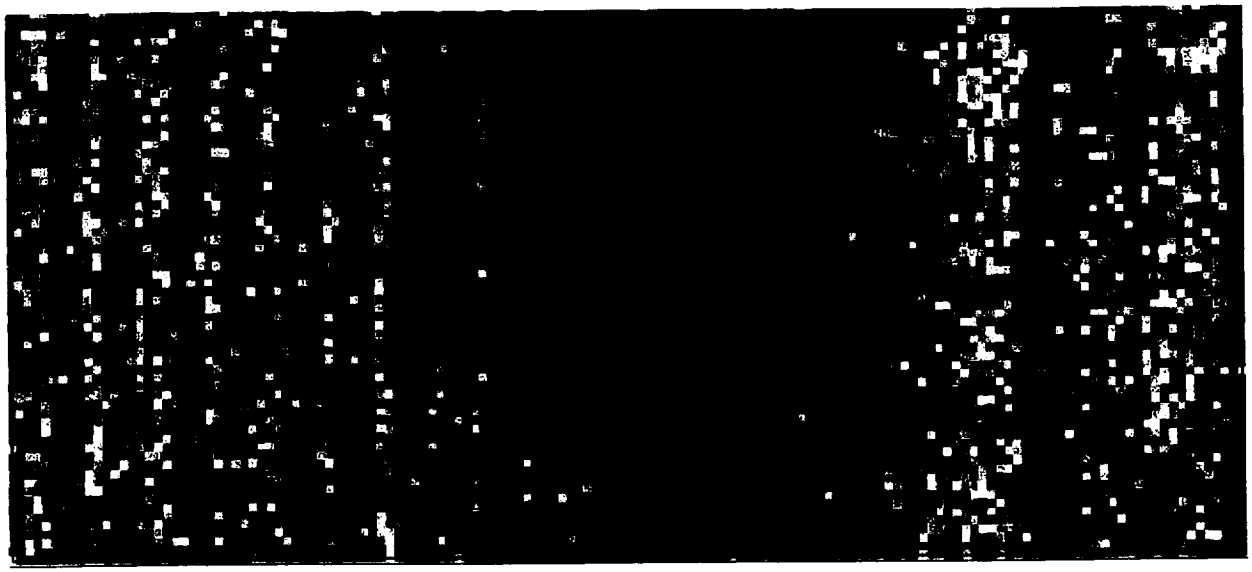

Fig. 2.7.5. A typical instantaneous unprocessed Raman image. Axial measurement location is 5 in. from the injector face. The abscissa and ordinate represent wavelength and radial location, respectively.

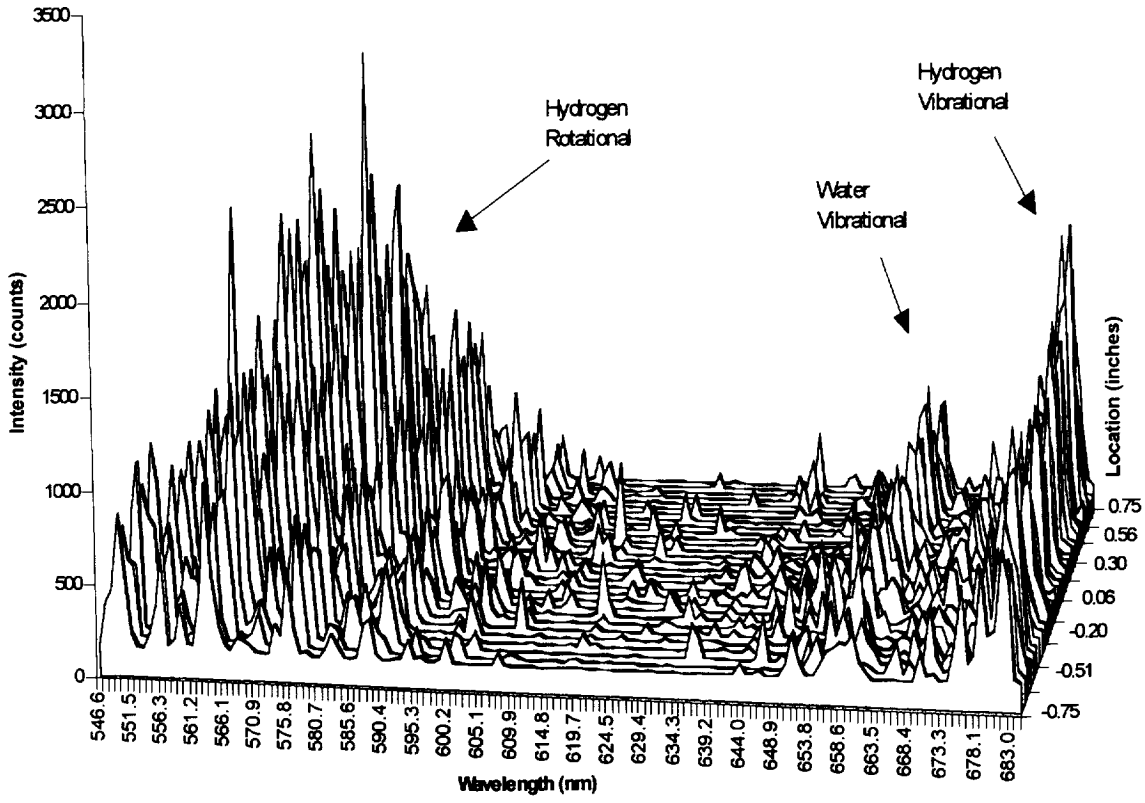


Fig. 2.7.6. A typical intensity levels for an instantaneous unprocessed Raman image. Axial measurement location is 5 in. from the injector face.

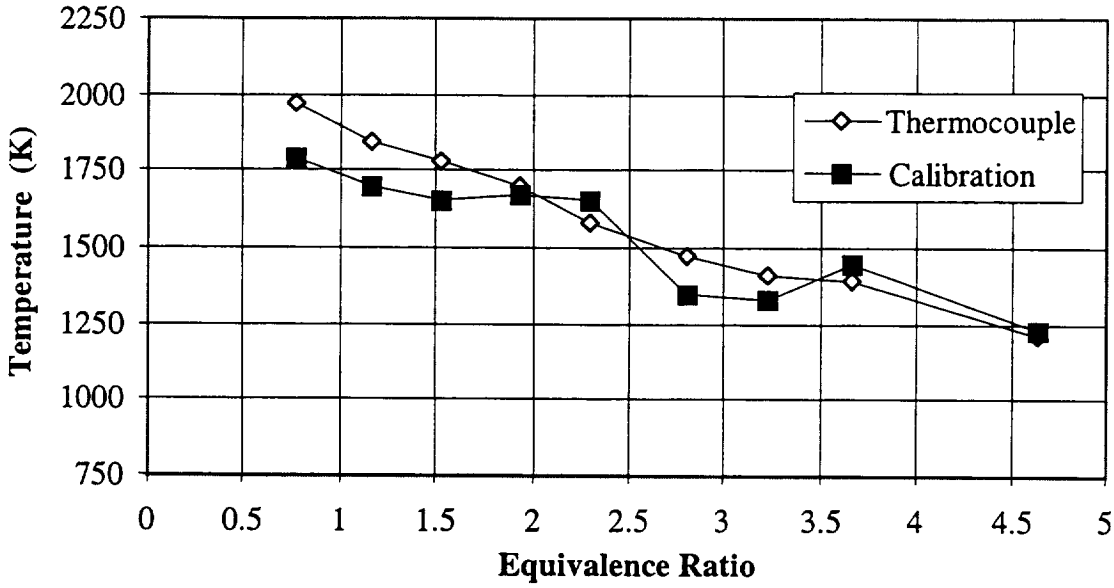


**Fig. 2.7.7. Calibration temperature comparison. Note S.I. units on graph.**

corresponding to Case A (see Table 2.7.1). In the figure, the Raman signal intensity is plotted versus the wavelength and radial location dimensions. As seen in the figure, Raman Stokes rotational hydrogen lines are also measured because of the relatively larger Raman cross section of hydrogen. The holographic grating reciprocal linear dispersion of 11.1 nm/mm allows the hydrogen vibrational Stokes lines and the rotational Stokes lines to be captured simultaneously on the camera. The efficiency of the grating combined with the efficiency of the camera at these wavelength regions introduce higher signal counts for the rotational hydrogen lines as compared to theoretical values. Theoretically, the S-branch rotational hydrogen Raman signal intensity should be about half the magnitude observed for the vibrational Raman signal intensity at 1200 K for a camera with uniform response for the entire wavelength domain. The Raman signal from water vapor is also seen in the figure. However, no signal from oxygen is evident (signal at 580 nm). This indicates that at this axial location all the oxygen is consumed.

To obtain the flowfield species mole fraction and temperature, the optical setup was first calibrated using a laminar hydrogen/air flame from a flashback-resistant flat flame Krupa style burner [58]. Mole fractions of hydrogen and air were varied to obtain various equivalence ratios. The temperature at these different flame conditions was measured with an uncoated B-type (Platinum-30% Rhodium vs. Platinum-6% Rhodium) thermocouple with a bead diameter of ~385 μm. The calibration results are displayed in Figs. 2.7.7 and 2.7.8. The accuracy of the

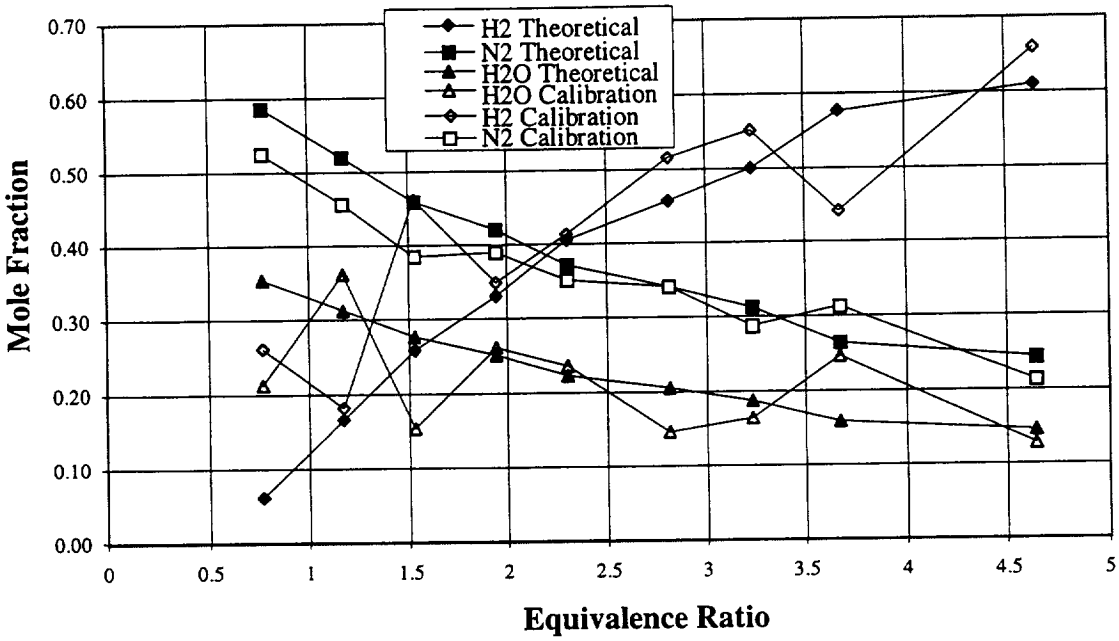


**Fig. 2.7.8. Calibration species mole fraction comparison.**

temperature and mole fraction measurements could be improved further by increasing the number of Raman signal accumulations during calibration data acquisition. The resultant uncertainty due to calibration measurements is estimated to be about 40% for the present results.

From the calibration values and with the assumption of ideal gas law, single shot temperature and mole fraction profiles of LOX/$GH_2$ combustion at the mixture fraction of one (Case A, Table 2.7.1) were obtained for the 5 in. axial measurement location. To the authors' knowledge, these measurements represent the first attempt for single shot temperature and major species mole fraction profile measurements of LOX/$GH_2$ propellant combustion in a rocket engine under relatively high pressure and temperature conditions. Sample instantaneous radial profiles of temperature and species mole fraction are shown in Figs. 2.7.9 and 2.7.10.

It should be noted that the adiabatic flame temperature predictions of 2250 R (1250 K) is close to the temperature measurements at the center region of the chamber. The temperature profiles indicate increased values close to the wall region of the chamber as compared to the central region. The measurements indicate larger noise at the edges of the Raman images (near the walls) which contribute to the uncertainty in the temperature values. This noise is believed to arise from the intense laser beam reflection from the laser window and the beam dump.

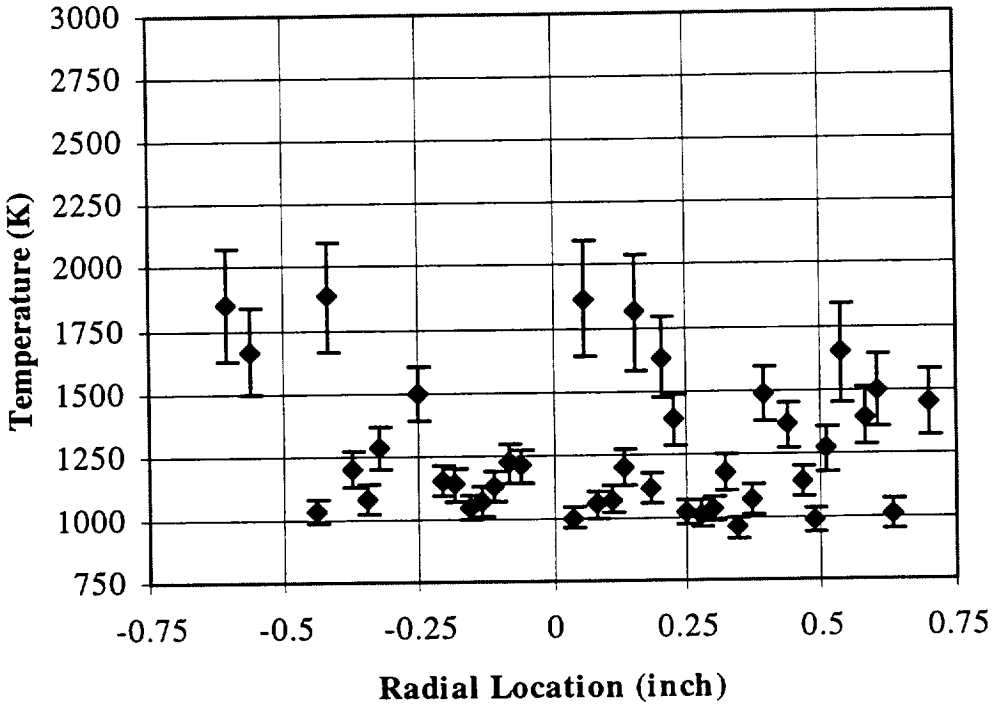


(a)

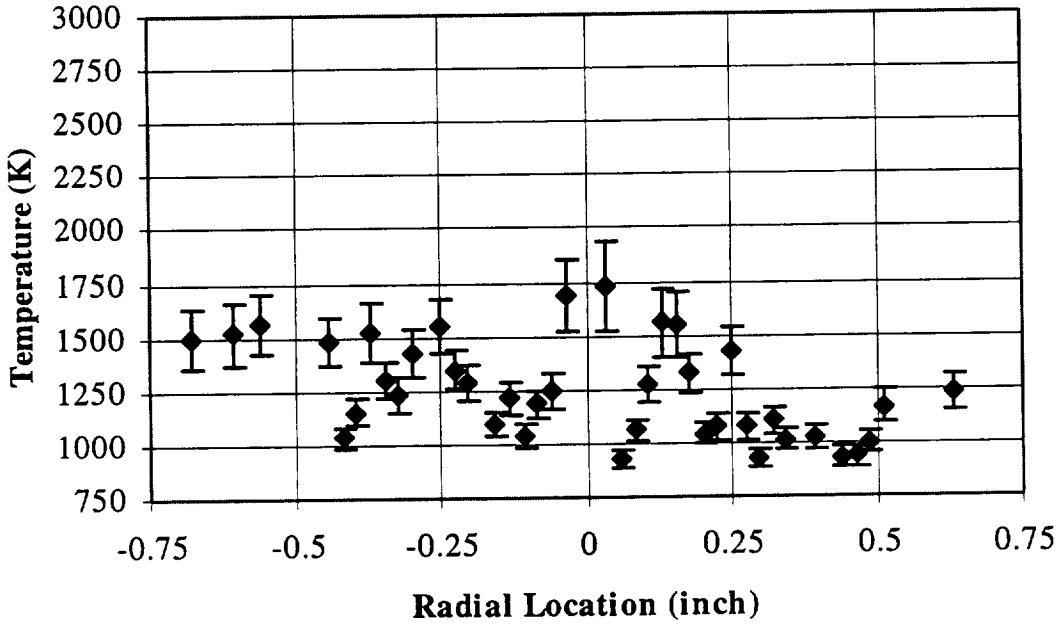


(b)

**Fig. 2.7.9. Examples of single shot temperature radial profiles. Note S. I. units on graph.**

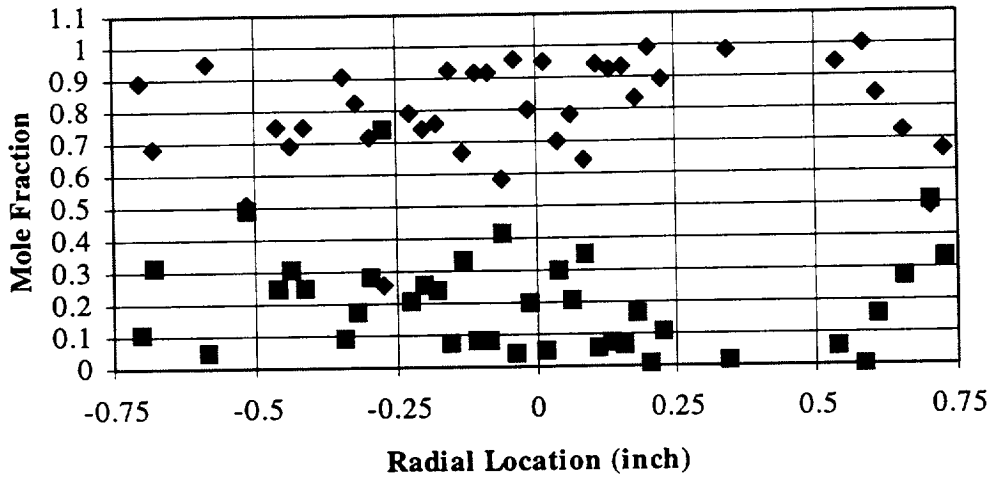


(a)

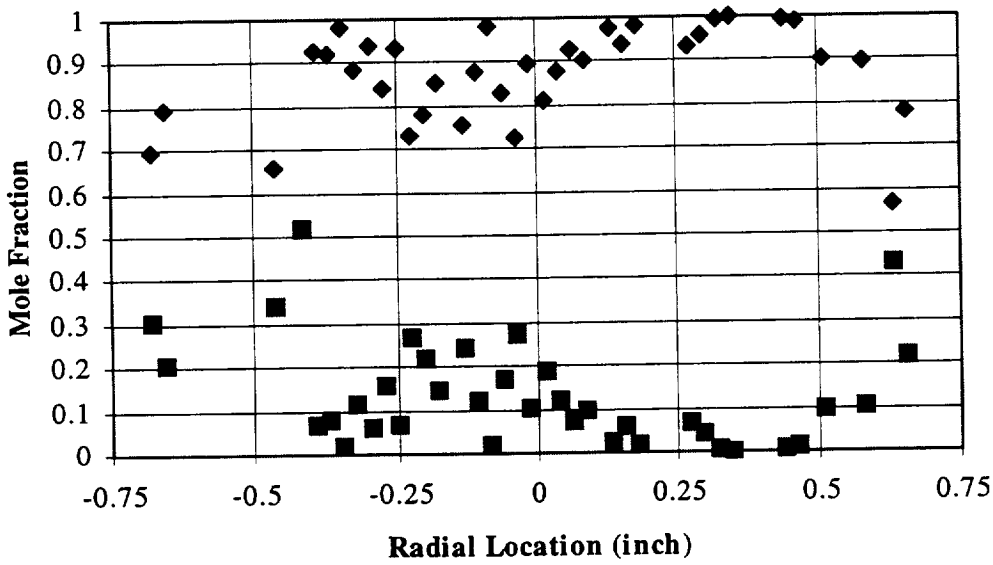


(b)

**Fig. 2.7.10. Examples of single shot species mole fraction radial profiles.**

The error bars associated with the single shot temperature values are derived from the equation below:

$$\delta n_i = \left\{ \sum_{i=1}^{N} \left( \frac{\partial n_i}{\partial X_i} \right)^2 \right\}^{1/2} \qquad (2.7.2)$$

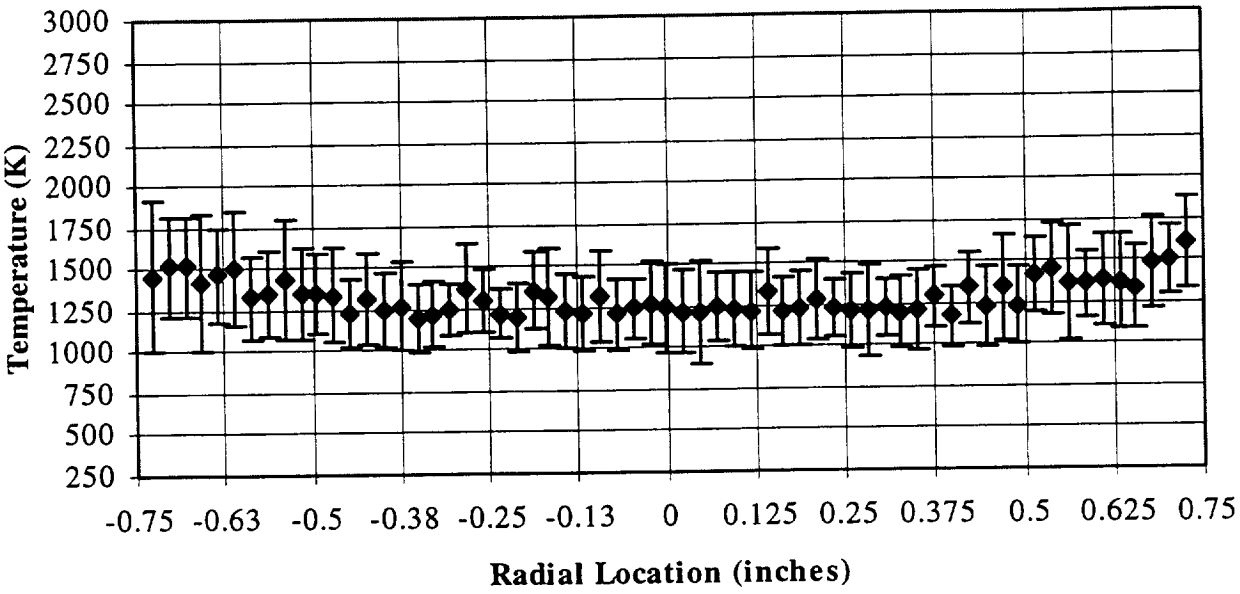


**Fig. 2.7.11. Average temperature profile from multiple single shot Raman images. Note S.I. units on graph.**

where $X_i$ represents the independent variables in equation 2.7.1, namely Raman signal intensity $S_i$, constant $K_i$ and temperature dependent function $f_i(T)$ for each specie [59]. Most of the error in single shot measurements arrive from the noisy operation of the intensifier. The combination of about 10% quantum efficiency and the high gain of the intensifier results in signal and background interference shot noise that dominates the uncertainty in the error estimates.

After the single shot temperature and mole fraction profiles were obtained, the temporally averaged results were obtained. Figures 2.7.11 and 2.7.12 display the resultant average temperature and mole fraction profiles from 26 single shot Raman images. The average temperature profile is much more uniform and is close to the adiabatic temperature value of 2250 R (1250 K). However, there is still a slight increase in the temperature at the wall regions of the rocket chamber compared to the central region. This anomaly of higher than adiabatic flame temperature values suggests the need for future investigations.

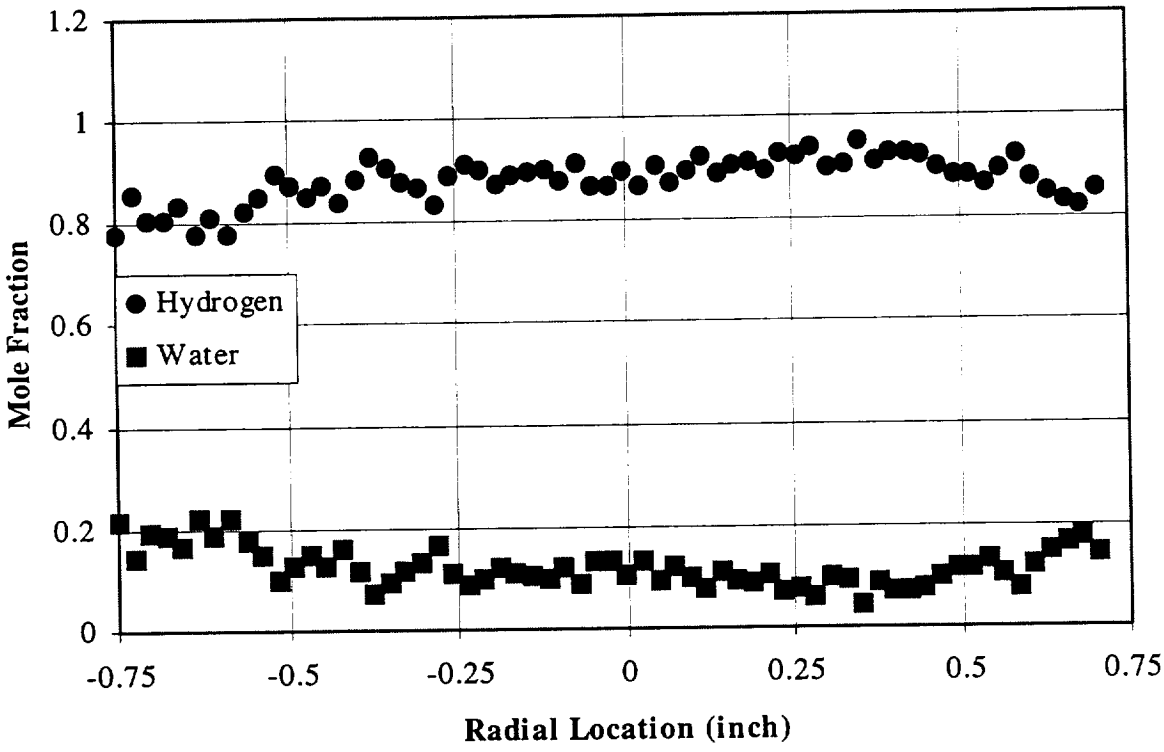


**Fig. 2.7.12. Average major species profiles from multiple single shot Raman images.**

## 2.7.2. LOX/RP-1 DIRECT INJECTION STUDIES

In this section, the studies related to fuel-rich LOX/RP-1 combustion for a pentad impinging injector element are presented and discussed. The research impacts immediate and future technology development goals. For fuel-rich LOX-RP-1 propellants, the pentad impinging injector element was chosen in favor of other injector element designs because it is the most amenable injector design in terms of atomization/injector pressure drop requirements.

### 2.7.2.1. Experimental Setup

In this section, the pentad impinging injector geometry, experimental flow conditions and experimental results are presented.

#### 2.7.2.1.1. Pentad Injector Element

The pentad injector element was chosen for fuel-rich direct injection studies for the LOX/RP-1 propellant combination because it is the most amenable injector design in terms of

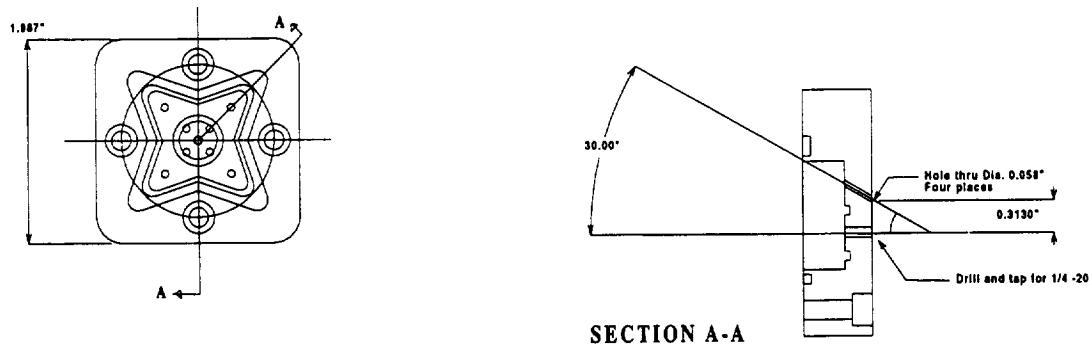


**Fig. 2.7.13. Pentad injector configuration for LOX/RP-1 propellants.**

atomization/injector pressure drop requirements. A schematic of the pentad injector configuration is shown in Fig. 2.7.13. The design of the pentad injectors for fuel-rich conditions was based on standard practice found in many references (for example, see Ref. 45). The goal of the design procedure was to design high performing injector elements that had realistic pressure drop margins. A good pentad injector design requires that the orifice sizes are nearly equal and that the central propellant stream axial momentum is close to the radial momentum for the outer (4 holes) propellant within design pressure drop requirements. With the realization that the stoichiometric mixture ratio for LOX/RP-1 is 2.9, a "classic" pentad element for near-stoichiometric conditions would therefore be fuel-centered. However, here the goals were to design fuel- rich pentad elements for mixture ratios about 0.5. Clearly, to equate propellant stream momentums for the fuel-rich case, it is necessary to design a oxidizer-centered injector. It should be noted that because of the disparity in propellant flowrates for the fuel-rich case, the injector design is not "ideal" in terms of equal hole sizes, stream momentums and pressure drops but represents an optimization of all three parameters. The oxidizer-centered fuel-rich element for a mixture ratio of 0.5 was designed for a RP-1 flowrate of 0.5 lbm/s such that the LOX and RP-1 pressure drops would be 50 and 100 psid, respectively. The half-impingement angle for the injectors was set at 30°.

A photograph of four pentad injectors is shown in Fig. 2.7.14. In the figure, elements are shown for both fuel-rich and oxidizer-rich conditions. The oxidizer-rich elements are discussed in Section 2.6.3. The injector elements were designed such the central post screws onto the injector face from the back side. Additionally, all injector posts have two concentric tubes that are soldered onto the copper piece at the tip region of the post. This arrangement provides air

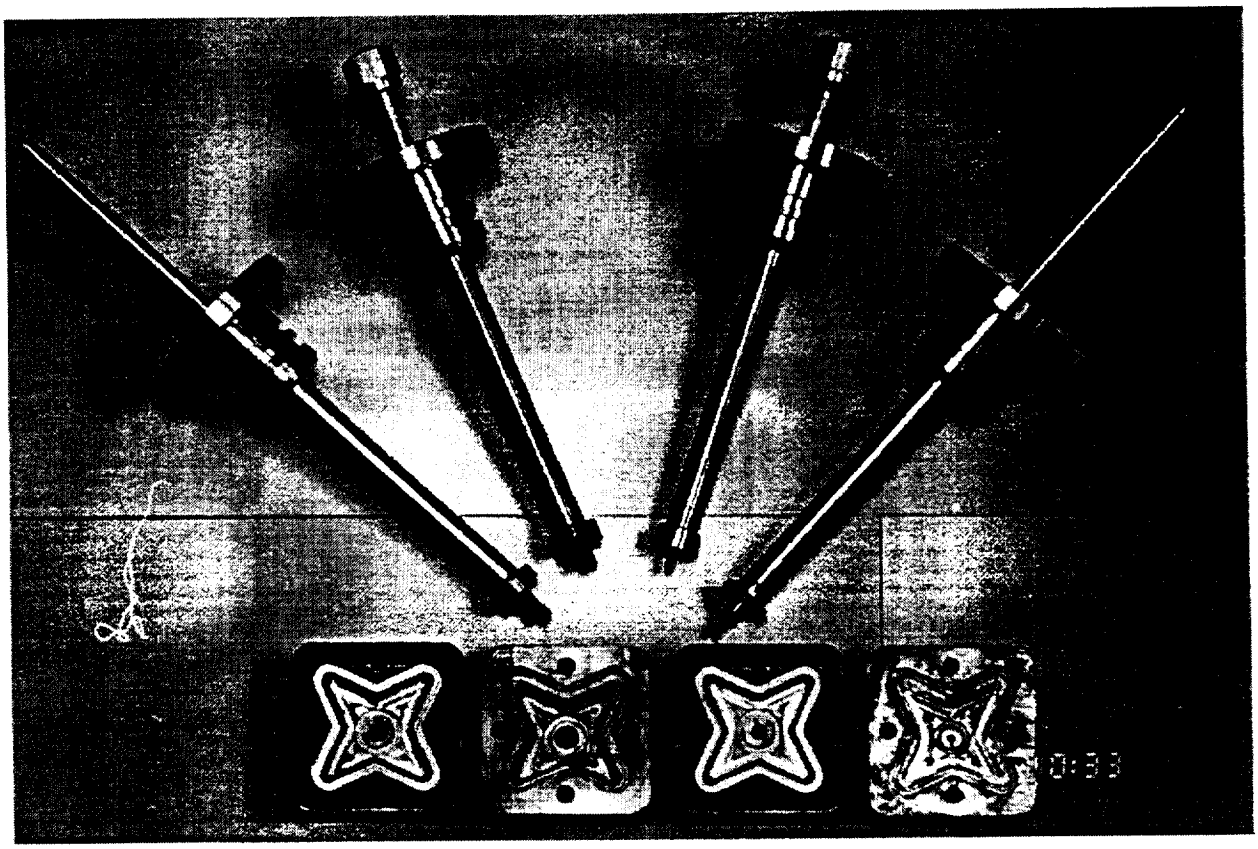

**Fig. 2.7.14. Photograph of pentad injectors designed direct injection LOX/RP-1 experiments. For all element designs, the central post screws onto the injector face from the back.**

(very low thermal conductivity) insulation between the two propellants, a feature that prohibits the RP-1 flow in the injector from freezing.

2.7.2.1.2. Flow Conditions

The fuel-rich experiments were conducted at the target flow mixture ratio of 0.5 at a nominal chamber pressure of 375 psia. Additionally, experiments were conducted at mixture ratios of 0.25 and 0.75. The flow conditions for the experiments are presented in Table 2.7.2.

### 2.7.2.2. Results and Discussion

The c* efficiency calculated for the uni-element injector experiments show that the element was high performing as expected. However, heavy soot deposition on the windows prevented any laser diagnostic measurements. The plume from the rocket nozzle also was dramatically "sooty" as the mixture ratio was lowered from 0.75 to 0.25. Afterburning of RP-1

**Table 2.7.2. Flow Conditions for LOX/RP-1 Fuel-Rich Studies**

| CASE | A | B | C |
|---|---|---|---|
| $LO_2$ Flow (lbm/s) | 0.125 | 0.25 | 0.375 |
| RP-1 Flow (lbm/s) | 0.5 | 0.5 | 0.5 |
| O/F | 0.25 | 0.5 | 0.75 |
| $LO_2$ velocity (ft/s) | 45 | 90 | 135 |
| RP-1 velocity (ft/s) | 136 | 136 | 136 |
| $T_{adiabatic}$ (K) | 1065 | 1215 | 1337 |
| $P_c$ (psia) | 363 | 373 | 370 |
| c* Efficiency | 0.98 | 0.93 | 0.96 |

fuel outside the rocket chamber was also noted. The global photograph of the rocket firing shown in Fig. 2.7.15 (a) illustrates the severe nature of the fuel-rich rocket firings. Near-injector face photography was attempted for all the flow conditions. Except for one frame near the beginning of a rocket firing, all the frames yielded little or no information because of heavy soot deposition on the windows. The single frame of use is shown in Fig. 2.7.15 (b). This photograph for a mixture ratio of 0.75 (see Table 2.7.2 for additional details) clearly depicts that the flame is attached to the central LOX orifice exit. Two of the RP-1 jets are seen to impinge into the flame region (the other two are behind and hence, can not be seen). This photograph indicates that a recirculation zone in the near-injector region feeds RP-1 vapor to the central LOX jet, thereby sustaining the flame.

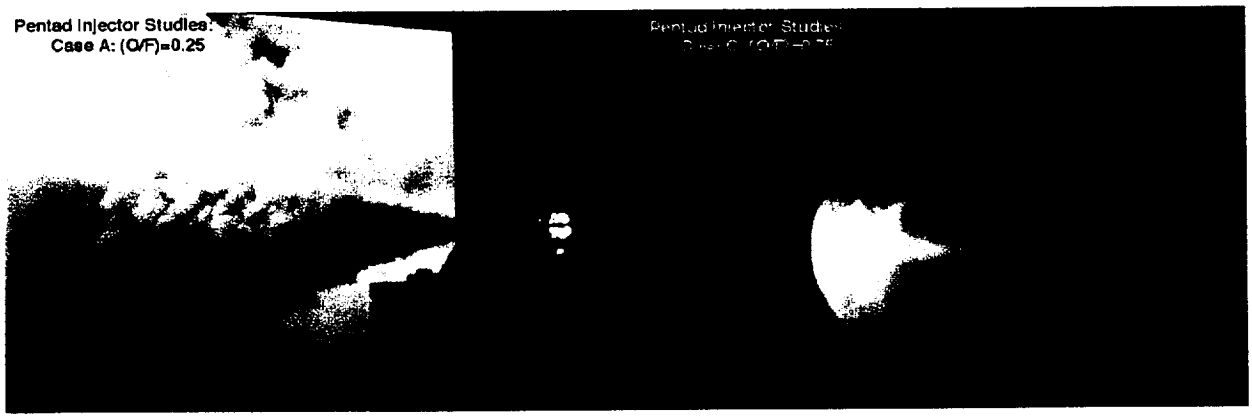


(a) (b)

**Fig. 2.7.15. Global (a) and near-injector face (b) photographs of the fuel-rich LOX/RP-1 pentad element injectors. The first photograph for a mixture ratio of 0.25 illustrates the sooty nature of the rocket plume. The bright region in the photograph is the window location. The near-injector photograph (b) for a mixture ratio of 0.75 indicates that the flame is located at the edge of the central LOX orifice. Clearly, a re-circulation zone near the injector face feeds RP-1 vapor to the central LOX jet.**

## 2.8. ADVANCED GAS/GAS INJECTOR TECHNOLOGY STUDIES

As mentioned in Chapter 1, the overall program was re-directed to include additional work items in direct support of Reusable Launch vehicle development goals. The experimental evaluation of the mixing and combustion characteristics of various injector concepts for gaseous propellants was included to support one of the engine concepts for the proposed Reusable Launch Vehicle (RLV) technology program. The full-flow engine concept includes full flow of both the fuel and the oxidizer through the preburners and consequently, gaseous propellant injection in the main chamber. At the time of the development sequence, the data base for gas-gas injectors was limited [60-64]. To fill this gap, NASA MSFC formed a Gas-Gas Injector Technology (GGIT) team which included NASA MSFC as the coordinating organization, Penn State University and NASA Lewis as the uni-element and multi-element testbeds, respectively, and Rocketdyne as the industrial partner. The scope of this program was changed to support GGIT team activities.

The plan of the GGIT team was to first identify a number of "team designed" gas/gas injector concepts. Penn State University and NASA Lewis would then conduct experiments to document the flowfield characteristics for both uni- and multi-element configurations. Based on the results of this first phase of experimentation, a second series of injector concepts would be investigated.

In the first phase of the program, the assembled team members selected and designed gas-gas injector concepts for uni-element and multi-element testing at Penn State and NASA Lewis. The team-selected injector configurations included the O-F-O triplet, F-O-F triplet and swirl coaxial elements. In addition, two Rocketdyne proprietary injector elements were also investigated.

Based on the results of this first phase of experimentation the team decided, for the second phase, to investigate the flowfield characteristics of various geometric variations of the shear coaxial injector. This second phase of experimentation also included geometric variations of one of the Rocketdyne proprietary injector elements.

In this section, the experiments are discussed in terms of chronological order, i.e., the first phase of experimentation is discussed first followed by the second phase. In the first phase, the injector design logic for the "team-selected" injector configurations is presented, followed by a discussion of the results. The discussion of the second phase of experimentation includes the

reasoning for picking the shear coaxial injector element for characterization, the design characteristics of the injector and the experimental results.

### 2.8.1. FIRST PHASE OF EXPERIMENTATION

The three injector concepts decided by the GGIT team were chosen based on performance, material compatibility (injector face heat transfer issues), stability, complexity, cost, durability, packaging and manifolding issues. In addition, as per Rocketdyne's suggestions, all three injector concepts were tied to Rocketdyne's specifications for the full scale rocket engine. The injector designs represented the "best" designs possible in terms of scaling issues and facility limitations.

Rocketdyne's specifications for the full scale rocket engine are summarized in Table 2.8.1. The propellant combination was oxygen/hydrogen for both the oxidizer and fuel preburners. The hot gaseous oxygen-rich and fuel-rich products from the preburners were to be introduced into the main chamber with the gas-gas injectors. The "optimum" geometries for the three chosen injector configurations were first designed for the full scale rocket conditions. This task carried out by NASA Marshall and Penn State personnel showed that the chosen injector configurations could be packaged and manifolded within Rocketdyne's specifications for the full scale engine conditions.

**Table 2.8.1. Rocketdyne's Specifications for Full Scale Rocket Engine**

| | |
|---|---|
| Chamber pressure ($P_C$) | 3000 psia |
| Nominal Mixture Ratio | 6 |
| OX Preburner Mixture Ratio | 156.5 |
| FUEL Preburner Mixture Ratio | 0.52 |
| OX-Rich Gas Injection Temperature | 1110 R |
| FUEL-Rich Gas Injection Temperature | 1100 R |
| OX Flow | 260 lbm/s |
| FUEL Flow | 43.33 lbm/s |
| Throat Diameter | ≈ 5.5 in. |
| Contraction Ratio | 2.5 to 4.5 |
| Chamber Diameter | 8.8 to 12 in. |
| FUEL $\Delta P/P_C$ | 10 to 15% |
| OX $\Delta P/P_C$ | 15 to 20% |
| Manifold/Dome Velocity Head | < 2% of Injector $\Delta P$ |

The chosen injector elements were then designed within the Penn State facility limitations. The Penn State and NASA Lewis experiments were conducted using room temperature $GO_2$ and $GH_2$ propellants at a chamber pressure of 1000 psia, and hence there were basic differences in fluid and flow properties between the experiments and full scale rocket conditions. The design logic for the three gas-gas injector configurations examined at Penn State in the uni-element rocket chamber are presented next. This description is followed by a summary of the experimental techniques employed for characterizing the combusting $GO_2/GH_2$ flowfields.

### 2.8.1.1. Injector Geometries

The three "team" injector elements were designed for implementation in the optically-accessible rocket chamber described in Section 2.2 (see Fig. 2.2.1 for details).

The following three injector geometries were designed for gaseous oxygen/gaseous hydrogen flow at a mixture ratio of six. The target chamber pressure was 1000 psia for oxygen and hydrogen flowrates of 0.25 lbm/s and 0.042 lbm/s, respectively.

#### 2.8.1.1.1. O-F-O Triplet Element

The basic schematic of the O-F-O triplet is shown in Fig. 2.8.1. The design of the injector considers the following geometric terms, diameter of OX orifice, $d_O$, diameter of FUEL orifice, $d_F$, impingement half-angle, $\theta$, and orifice spacing, s. In addition, the length to diameter ratio of the orifices is important in terms of flow development and packaging issues. These geometric parameters directly affect performance, face heat transfer issues and stability. Since the performance of the injector is related to gaseous propellant mixing, the matching of the propellant stream momentum is important. Previous work by Aerojet on gas-gas injectors [60] suggested that optimum mixing efficiency occured when:

$$(2.3\dot{m}_F V_F)/(\dot{m}_O V_O \sin\theta) = 2 \qquad (2.8.1)$$

where $\dot{m}$ and V are mass flowrate and velocity, and the subscripts O and F refer to oxidizer and fuel, respectively. Therefore, in terms of performance, the above equation was first used as a guideline for designing the individual O-F-O injector and full injector assembly layout for the full scale rocket specifications as suggested by Rocketdyne. This task was performed by personnel from NASA Marshall, Penn State and Rocketdyne. As a baseline for the O-F-O triplet, a $\theta$ of 30° was chosen. Since the number of elements, element design, injector face packaging and flow

manifolding are inherently interrelated, an iterative procedure was used to formulate the injector design for the full scale rocket specifications. At each step of the iterative procedure, the elements for the full scale conditions were designed such that the LHS of equation 2.8.1 was as close to the RHS within the flow (flowrate, injector pressure drop, etc.) specifications. The results of this endeavor showed that nominally 244 O-F-O triplet elements (optimized based on equation 2.8.1) could be packaged on a faceplate in either a "linear" or "ring" type arrangement within the proposed injector faceplate size and injector manifold pressure drop criteria. This design then represents the full scale design to which both the experimental results from the Penn State and NASA Lewis should be scaled.

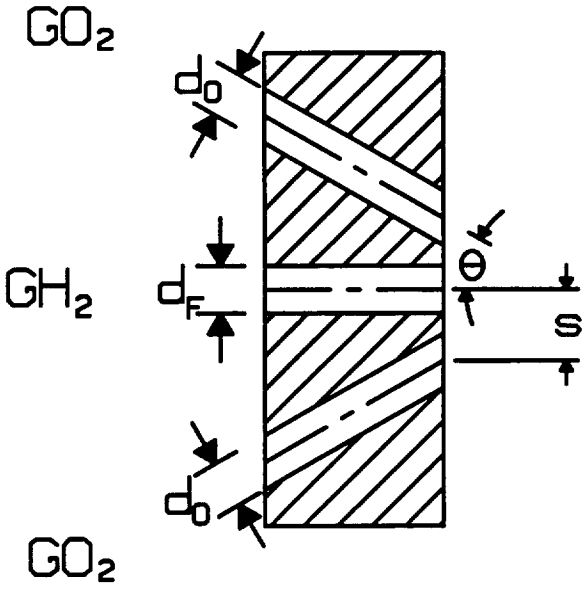


**Fig. 2.8.1. Schematic of O-F-O triplet injector for $GO_2/GH_2$ propellants.**

The next step involved optimizing the single O-F-O injector design for the Penn State experimental conditions for $GO_2/GH_2$ propellants. The Penn State design was for the same propellant O/F ratio of six at a $GO_2$ mass flowrate of 0.25 lbm/s and 1000 psia chamber pressure. The injector designs for the PSU test conditions and full scale engine conditions are compared in Table 2.8.2. Although exact similitude between all the Penn State and full scale rocket conditions could not be realized because of different flowrate, chamber pressure and propellant properties, both injectors were optimized based on the Aerojet correlation (i.e. momentum ratio) [60], and hence the experimental results obtained should be scalable to full scale conditions. Note also that the chamber pressure and mass flowrate per element ratios between the two injector designs essentially cancel to yield injectors that are geometrically within 50% of each other.

The assembly drawing for the O-F-O triplet injector is shown in Fig. 2.8.2. The injector assembly consists of a $GO_2$ manifold body, a $GH_2$ post that feeds through the $GO_2$ manifold body and screws to the injector faceplate. The $GO_2$ manifold body is an existing piece of hardware (see Fig. 2.2.1) that is used for the O-F-O triplet.

## Table 2.8.2. O-F-O Triplet Design Considerations

| (#) Parameter | PSU Conditions | Rocketdyne Rocket Specifications | RATIO (Rocket/PSU) | Comments PSU/Rocket |
|---|---|---|---|---|
| (1) Chamber Pressure ($P_C$) | 1000 psia | 3000 psia | 3.0 | facility maximum/specified |
| (2) O/F | 6 | 6 | 1.0 | specified/specified |
| (3) Number of Elements | 1 | 244 | 244 | uni-element/244 elem. from packaging |
| (4) $_{OX}$ Total | 0.25 lb/s | 260 lb/s | 1040.0 | facility maximum/specified |
| (5) $_{OX}$ Per Element | 0.25 lb/s | 1.0656 lb/s | 4.26 | specified/from packaging |
| (6) OX Mol. Weight | 32.0 | 30.65 | 0.96 | specified/specified |
| (7) OX Gamma | 1.4 | 1.31 | 0.93 | specified/specified |
| (8) OX Temperature | 540 R | 1110 R | 2.06 | specified/specified |
| (9) OX Density | 5.53 lb/ft$^3$ | 7.73 lb/ft$^3$ | 1.40 | specified/specified |
| (10) OX Sound Speed | 1084 ft/s | 1533 ft/s | 1.41 | specified/specified |
| (11) $_{FUEL}$ Total | 0.042 lb/s | 43.33 lb/s | 1040.0 | specified/specified |
| (12) $_{FUEL}$ Per Element | 0.042 lb/s | 0.18 lb/s | 4.26 | specified/from packaging |
| (13) FUEL Mol. Weight | 2.02 | 3.06 | 1.52 | specified/specified |
| (14) FUEL Gamma | 1.4 | 1.38 | 0.98 | specified/specified |
| (15) FUEL Temperature | 540 R | 1100 R | 2.04 | specified/specified |
| (16) FUEL Density | 0.35 lb/ft$^3$ | 0.78 lb/ft$^3$ | 2.23 | specified/specified |
| (17) FUEL Sound Speed | 4314 ft/s | 4959 ft/s | 1.15 | specified/specified |
| (18) Impingement Half-Angle | 30° | 30° | 1.0 | design point/design point |
| (19) $d_{OX}$ | 0.0999 in. | 0.1443 in. | 1.44 | rocket geometry ≈ 50% bigger |
| (20) $d_{FUEL}$ | 0.1269 in. | 0.1628 in. | 1.28 | rocket geometry ≈ 50% bigger |
| (21) Impingement Distance from Faceplate ($d_{impn}$) | 0.50 in. | 0.72 in. | 1.44 | $5d_{OX}/5d_{OX}$ |
| (22) Faceplate Thickness (l) | 0.31 in. | 0.4 in. | 1.29 | $l/d_{FUEL}$ same as for rocket/nominal |
| (23) OX $C_D$ | 0.85 | 0.85 | 1.0 | assumed/assumed |
| (24) FUEL $C_D$ | 0.85 | 0.85 | 1.0 | assumed/assumed |
| (25) OX Velocity | 489 ft/s | 715 ft/s | 1.46 | inj. velocities are within 50% |
| (26) FUEL Velocity | 1603 ft/s | 1857 ft/s | 1.16 | inj. velocities are within 50% |
| (27) FUEL/OX Vel. Ratio | 3.28 | 2.60 | 0.79 | velocity ratios are within 20% |
| (28) OX Mach # | 0.45 | 0.47 | 1.04 | Mach numbers are identical |
| (29) FUEL Mach # | 0.37 | 0.37 | 1.0 | Mach numbers are identical |
| (30) $\Delta P_{OX}/P_C$ | 0.15 | 0.15 | 1.0 | injector pressure drops are identical |
| (31) $\Delta P_{FUEL}/P_C$ | 0.10 | 0.10 | 1.0 | injector pressure drops are identical |
| (32) Momentum Ratio $(m_F V_F) / (m_O V_O \sin\theta)$ | 1.10 | 0.87 | 0.79 | momentum ratios are nearly identical |
| (33) RHS of Aerojet Corr. | 2.52 | 1.99 | 0.79 | BOTH INJECTORS ARE CLOSE TO AEROJET DESIGN CONDITIONS |

### 2.8.1.1.2. F-O-F Triplet Element

The basic schematic of the F-O-F triplet is shown in Fig. 2.8.3. The design of the injector considers the following geometric terms, diameter of OX orifice, $d_O$, diameter of FUEL orifice, $d_F$, impingement half-angle, $\theta$, and orifice spacing, s. In addition, the length to diameter ratio of the orifices is important in terms of flow development and packaging issues. These geometric parameters directly affect performance, face heat transfer issues and stability. Since the performance of the injector is related to gaseous propellant mixing, the matching of the

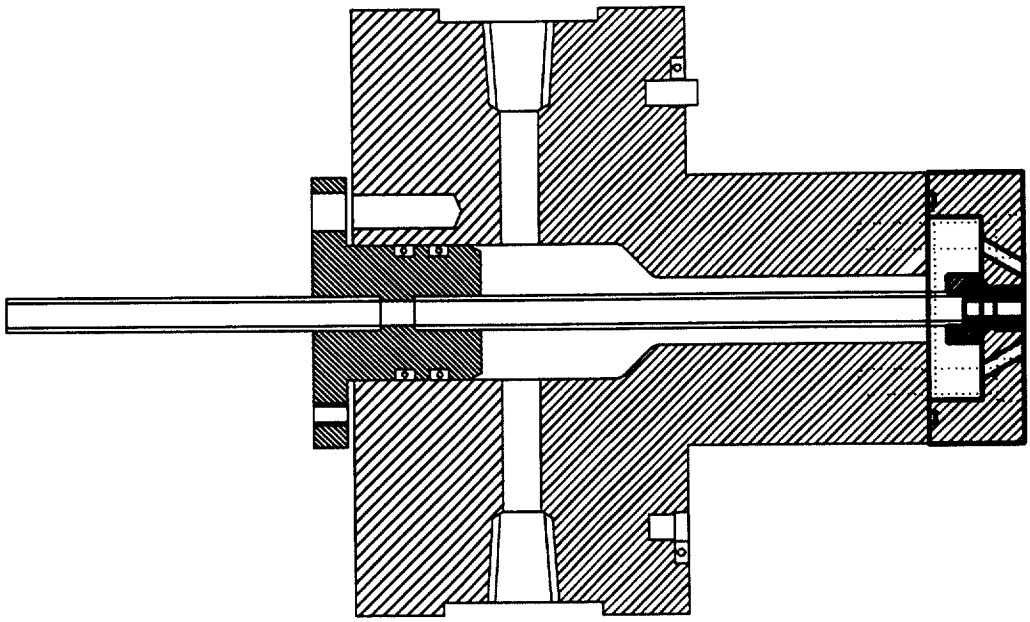

**Fig. 2.8.2. Assembly drawing for the O-F-O triplet injector. The injector assembly consists of a $GO_2$ manifold body, a $GH_2$ post that feeds through the $GO_2$ manifold body and screws to the injector faceplate.**

propellant stream momentum is important. Previous work by Aerojet [60] on gas-gas injectors suggested that optimum mixing efficiency occured when:

$$(2.3\dot{m}_O V_O)/(\dot{m}_F V_F \sin\theta) = 2 \qquad (2.8.2)$$

where $\dot{m}$ and V are mass flowrate and velocity, and the subscripts O and F refer to oxidizer and fuel, respectively. Therefore, in terms of performance, the above equation was first used as a guideline for designing the individual F-O-F injector and full injector assembly layout for the full scale rocket specifications as suggested by Rocketdyne. This task was performed by NASA Marshall, Penn State and Rocketdyne personnel. As a baseline for the F-O-F triplet, a $\theta$ of 30° was chosen. Since the number of elements, element design, injector face packaging and

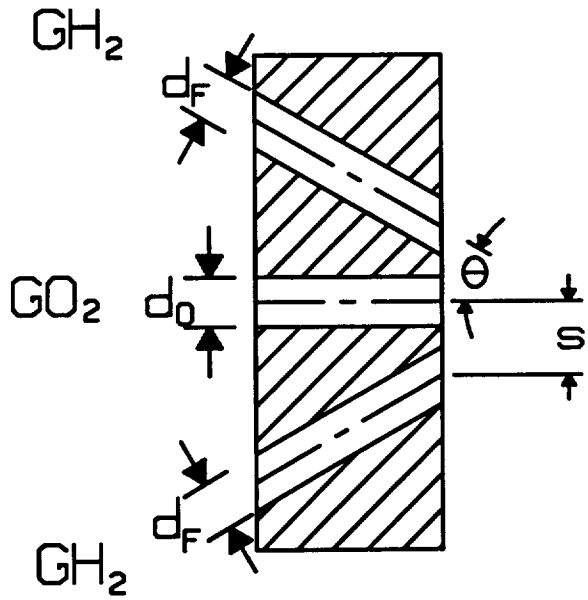


**Fig. 2.8.3. Schematic of F-O-F triplet injector for $GO_2/GH_2$ propellants.**

flow manifolding are inherently interrelated, an iterative procedure was used to formulate the injector design for the full scale rocket specifications. At each step of the iterative procedure, the elements for the full scale conditions were designed such that the LHS of equation 2.8.2 was as close to the RHS within the flow (flowrate, injector pressure drop, etc.) specifications. Unlike, the O-F-O triplet design, the F-O-F triplet could not be designed within the injector pressure drop criteria such that the LHS of equation 2.8.2 was about two (the best possible is about seven). The results of this endeavor showed that nominally 244 F-O-F triplet elements could be packaged on a faceplate in either a "linear" or "ring" type arrangement within the proposed injector faceplate size and injector manifold pressure drop criteria. This design then represents the full scale design to which both the experimental results from the Penn State and NASA Lewis should be scaled.

The next step involved optimizing the single F-O-F injector design for the Penn State experimental conditions for $GO_2/GH_2$ propellants. The Penn State design was for the same propellant O/F ratio of six at a $GO_2$ mass flowrate of 0.25 lbm/s and 1000 psia chamber pressure. The injector designs for the PSU test conditions and full scale engine conditions are compared in Table 2.8.3. Although exact similitude between all the Penn State and full scale rocket conditions could not be realized because of different flowrate, chamber pressure and propellant properties, both injectors were optimized based on the Aerojet correlation (i.e. momentum ratio) [60] and hence the experimental results obtained should be scalable to full scale conditions. Note also that the chamber pressure and mass flowrate per element ratios between the two injector designs essentially cancel to yield injectors that are geometrically within 50% of each other.

The assembly drawing for the F-O-F triplet injector is exactly the same as that for the O-F-O triplet arrangement shown in Fig. 2.8.2, except that the propellant flows are reversed.

2.8.1.1.3. Swirl Coaxial Element

The basic schematic of the swirl coaxial injector is shown in Fig. 2.8.4. The design of the injector considers the following geometric terms, OX post diameter, $d_O$, FUEL annulus inner diameter, $d_{Fi}$, and FUEL annulus outer diameter, $d_{Fo}$. Based on Aerojet's gas-gas injector research [60], propellant mixing increases with increasing swirl angle. The inner flow can be swirled either with tangential vanes or with a swirl nut with tangential slots. However, the physical dimensions of the injector increases for greater swirl angles for both methods. For the

**Table 2.8.3. F-O-F Triplet Design Considerations**

| (#) Parameter | PSU Conditions | Rocketdyne Rocket Specifications | RATIO (Rocket/PSU) | Comments PSU/Rocket |
|---|---|---|---|---|
| (1) Chamber Pressure ($P_C$) | 1000 psia | 3000 psia | 3.0 | facility maximum/specified |
| (2) O/F | 6 | 6 | 1.0 | specified/specified |
| (3) Number of Elements | 1 | 244 | 244 | uni-element/244 elem. from packaging |
| (4) $_{OX}$ Total | 0.25 lb/s | 260 lb/s | 1040.0 | facility maximum/specified |
| (5) $_{OX}$ Per Element | 0.25 lb/s | 1.0656 lb/s | 4.26 | specified/from packaging |
| (6) OX Mol. Weight | 32.0 | 30.65 | 0.96 | specified/specified |
| (7) OX Gamma | 1.4 | 1.31 | 0.93 | specified/specified |
| (8) OX Temperature | 540 R | 1110 R | 2.06 | specified/specified |
| (9) OX Density | 5.53 lb/ft$^3$ | 7.73 lb/ft$^3$ | 1.40 | specified/specified |
| (10) OX Sound Speed | 1084 ft/s | 1533 ft/s | 1.41 | specified/specified |
| (11) $_{FUEL}$ Total | 0.042 lb/s | 43.33 lb/s | 1040.0 | specified/specified |
| (12) $_{FUEL}$ Per Element | 0.042 lb/s | 0.18 lb/s | 4.26 | specified/from packaging |
| (13) FUEL Mol. Weight | 2.02 | 3.06 | 1.52 | specified/specified |
| (14) FUEL Gamma | 1.4 | 1.38 | 0.98 | specified/specified |
| (15) FUEL Temperature | 540 R | 1100 R | 2.04 | specified/specified |
| (16) FUEL Density | 0.35 lb/ft$^3$ | 0.78 lb/ft$^3$ | 2.23 | specified/specified |
| (17) FUEL Sound Speed | 4314 ft/s | 4959 ft/s | 1.15 | specified/specified |
| (18) Impingement Half-Angle | 30° | 30° | 1.0 | design point/design point |
| (19) $d_{OX}$ | 0.1413 in. | 0.2040 in. | 1.44 | rocket geometry ≈ 50% bigger |
| (20) $d_{FUEL}$ | 0.076 in. | 0.0976 in. | 1.28 | rocket geometry ≈ 50% bigger |
| (21) Impingement Distance from Faceplate ($d_{imp}$) | 0.54 in. | 0.75 in. | 1.39 | $5d_{OX}/5d_{OX}$ |
| (22) Faceplate Thickness (l) | 0.28 in. | 0.4 in. | 1.43 | $l/d_{FUEL}$ same as for rocket/nominal |
| (23) OX $C_D$ | 0.85 | 0.85 | 1.0 | assumed/assumed |
| (24) FUEL $C_D$ | 0.85 | 0.85 | 1.0 | assumed/assumed |
| (25) OX Velocity | 489 ft/s | 715 ft/s | 1.46 | inj. velocities are within 50% |
| (26) FUEL Velocity | 2230 ft/s | 2583 ft/s | 1.16 | inj. velocities are within 50% |
| (27) FUEL/OX Vel. Ratio | 4.56 | 3.61 | 0.79 | velocity ratios are within 20% |
| (28) OX Mach # | 0.45 | 0.47 | 1.04 | Mach numbers are identical |
| (29) FUEL Mach # | 0.52 | 0.52 | 1.0 | Mach numbers are identical |
| (30) $\Delta P_{OX}/P_C$ | 0.15 | 0.15 | 1.0 | injector pressure drops are identical |
| (31) $\Delta P_{FUEL}/P_C$ | 0.20 | 0.20 | 1.0 | injector pressure drops are identical |
| (32) Momentum Ratio $(m_O V_O) / (m_F V_F \sin \theta)$ | 2.63 | 3.32 | 1.26 | momentum ratios are nearly identical |
| (33) RHS of Aerojet Corr. | 6.05 | 7.64 | 1.26 | BOTH INJECTORS ARE NOT CLOSE TO AEROJET DESIGN CONDITIONS |

present design, the inner propellant flow was swirled with the aid of a swirl nut with tangential slots. Also, the mixing characteristics of the swirl coaxial injector is worst when the velocity ratio between fuel-to-oxidizer flow is ≈ 11 [60]. For velocity ratios greater or smaller than about 11, the mixing efficiency is reported to increase. In terms of utilizing the swirl component of the inner flow (oxidizer) to promote mixing and propellant spreading, momentum considerations indicate that the swirl coaxial injector be operated at lower fuel-to-oxidizer velocity ratios.

The aforementioned guidelines were used to design the individual swirl coaxial injector and full injector assembly layout for the full scale rocket specifications with the same iterative

procedure used for designing the O-F-O and F-O-F triplet elements. The design methodology for swirl coaxial injectors described in Ref. 60 was utilized for designing the injector. The results of this endeavor showed that nominally 270 swirl coaxial elements with a swirl angle of 75 degrees could be packaged on a faceplate in the "ring" type arrangement within the proposed injector faceplate size and injector manifold pressure drop criteria. This design then represents the full scale design to which both the experimental results from the Penn State and NASA Lewis should be scaled.

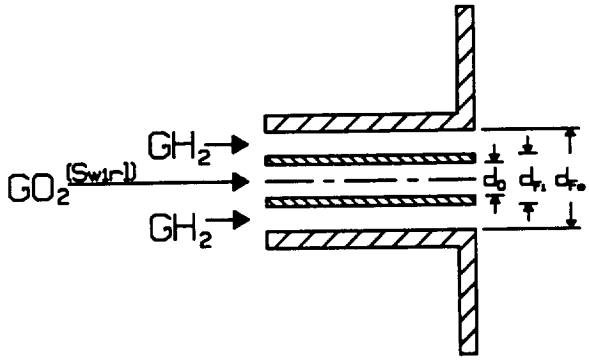


**Fig. 2.8.4. Schematic of swirl coaxial injector for $GO_2/GH_2$ propellants.**

The next step involved optimizing the single swirl coaxial injector design for the Penn State experimental conditions for $GO_2/GH_2$ propellants. The Penn State design was for the same propellant O/F ratio of six at a $GO_2$ mass flowrate of 0.25 lbm/s and 1000 psia chamber pressure. The injector designs for the PSU test conditions and full scale engine conditions are compared in Table 2.8.4. Note that the chamber pressure and mass flowrate per element ratios between the two injector designs essentially cancel to yield injectors that are geometrically within 50% of each other. In addition to the 75 degree swirl angle geometry, the effect of swirl angle on combustion was assessed by experimenting at other swirl angles, viz. 60 and 90 degrees.

The design of the $GO_2$ post for the swirl coaxial injector is shown in Fig. 2.8.5. The $GO_2$ post is designed to screw onto the injector assembly of the rocket chamber depicted in Fig. 2.2.1.

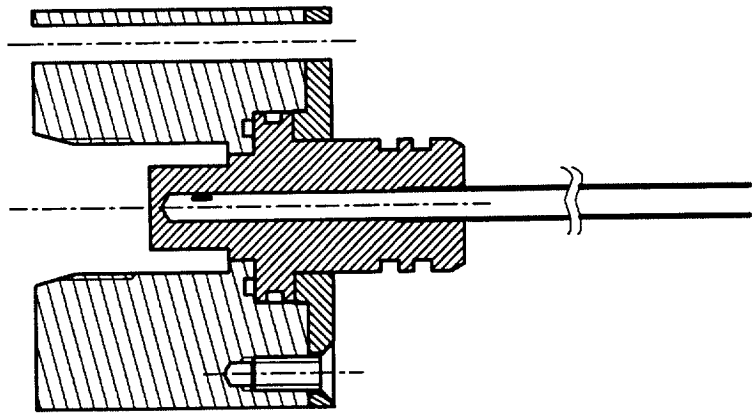

**Fig. 2.8.5. $GO_2$ post design for swirl coaxial injector. $GO_2$ post was designed to screw onto injector assembly shown in Fig. 2.2.1.**

## Table 2.8.4. Swirl Coaxial Injector Design Considerations

| (#) Parameter | PSU Conditions | Rocketdyne Rocket Specifications | RATIO (Rocket/PSU) | Comments PSU/Rocket |
|---|---|---|---|---|
| (1) Chamber Pressure ($P_C$) | 1000 psia | 3000 psia | 3.0 | facility maximum/specified |
| (2) O/F | 6 | 6 | 1.0 | specified/specified |
| (3) Number of Elements | 1 | 270 | 270 | uni-element/270 elem. from packaging |
| (4) $_{OX}$ Total | 0.25 lb/s | 260 lb/s | 1040.0 | facility maximum/specified |
| (5) $_{OX}$ Per Element | 0.25 lb/s | 0.963 lb/s | 3.85 | specified/from packaging |
| (6) OX Mol. Weight | 32.0 | 30.65 | 0.96 | specified/specified |
| (7) OX Gamma | 1.4 | 1.31 | 0.93 | specified/specified |
| (8) OX Temperature | 540 R | 1110 R | 2.06 | specified/specified |
| (9) OX Density | 5.53 lb/ft$^3$ | 7.73 lb/ft$^3$ | 1.40 | specified/specified |
| (10) OX Sound Speed | 1084 ft/s | 1533 ft/s | 1.41 | specified/specified |
| (11) $_{FUEL}$ Total | 0.042 lb/s | 43.33 lb/s | 1040.0 | specified/specified |
| (12) $_{FUEL}$ Per Element | 0.042 lb/s | 0.16 lb/s | 3.85 | specified/from packaging |
| (13) FUEL Mol. Weight | 2.02 | 3.06 | 1.52 | specified/specified |
| (14) FUEL Gamma | 1.4 | 1.38 | 0.98 | specified/specified |
| (15) FUEL Temperature | 540 R | 1100 R | 2.04 | specified/specified |
| (16) FUEL Density | 0.35 lb/ft$^3$ | 0.78 lb/ft$^3$ | 2.23 | specified/specified |
| (17) FUEL Sound Speed | 4314 ft/s | 4959 ft/s | 1.15 | specified/specified |
| (18) Full Swirl Cone Angle | 75° | 75° | 1.0 | design point/design point |
| (19) $d_{OX}$ | 0.2802 in. | 0.3843 in. | 1.37 | rocket geometry ≈ 40% bigger |
| (20) $d_{Fi}$ | 0.3302 in. | 0.4343 in. | 1.32 | rocket geometry ≈ 40% bigger |
| (21) $d_{Fo}$ | 0.3702 in. | 0.4743 in. | 1.28 | rocket geometry ≈ 40% bigger |
| (22) OX Post Wall Thickness | 0.025 in. | 0.025 in. | 1.0 | same OX post wall thickness fabrication limitation |
| (23) FUEL Annulus Gap Width | 0.020 in. | 0.020 in. | 1.0 | same FUEL annulus gap fabrication limitation |
| (24) OX $C_D$ | 0.1825 | 0.1825 | 1.0 | calculated/calculated |
| (25) FUEL $C_D$ | 1.0 | 1.0 | 1.0 | assumed/assumed |
| (26) OX Velocity | 342 ft/s | 501 ft/s | 1.46 | inj. velocities are within 50% |
| (27) FUEL Velocity | 782 ft/s | 1040 ft/s | 1.33 | inj. velocities are within 50% |
| (28) FUEL/OX Vel. Ratio | 2.29 | 2.08 | 0.91 | velocity ratios are within 10% |
| (29) Momentum Ratio $(m_F V_F) / (m_O V_O)$ | 0.38 | 0.35 | 0.92 | momentum ratios are nearly identical |
| (30) OX Mach # | 0.32 | 0.33 | 1.03 | Mach numbers are within 20% |
| (31) FUEL Mach # | 0.18 | 0.21 | 1.17 | Mach numbers are within 20% |
| (32) $\Delta P_{OX}/P_C$ | 0.20 | 0.20 | 1.0 | injector pressure drops are identical |
| (33) $\Delta P_{FUEL}/P_C$ | 0.023 | 0.030 | 1.3 | FUEL pressure drop may need to be increased with upstream orifice |

The post design includes a swirl nut that feeds the oxidizer tangentially into the central tube from a swirl chamber. The screw-on face plate shown in the rocket assembly (see Fig. 2.2.1) defines the outer diameter of the $GH_2$ fuel annulus, whereas the inner diameter of the $GH_2$ fuel annulus is defined by the outer diameter of the $GO_2$ post. The swirl injector was designed in this modular fashion such that swirl nut/$GO_2$ tube assemblies for different swirl angles could be easily interchanged. A photograph of the three swirl injector elements is shown in Fig. 2.8.6. The design specifics of the three swirl coaxial injector elements are tabulated in Table 2.8.5.

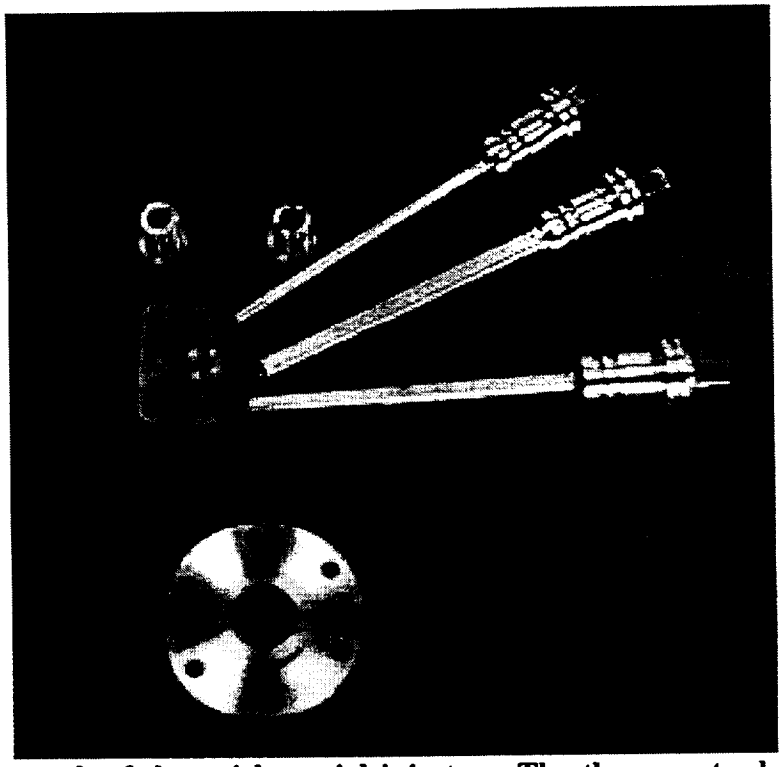

**Fig. 2.8.6. Photograph of the swirl coaxial injector. The three posts shown are for swirl angles of 60, 75 and 90 degrees. The photograph also shows the faceplate and two "nuts" that are used for varying the $GH_2$ annulus.**

### 2.8.1.2. Experimental Setup

Raman spectroscopy was employed as the major diagnostic technique for characterizing the mixing and combustion characteristics of the flowfield. In addition the injector face was instrumented with a thermocouple for injector face temperature measurements during the rocket firings. The implementation of these two techniques are discussed next.

#### 2.8.1.2.1. Raman Spectrometry

The Raman spectroscopy technique was developed and applied for making line images of the species field in the combustion chamber. Various optical configurations can be used for applying the Raman spectroscopy technique [46, 50]. Here an optical arrangement that stresses

**Table 2.8.5. Swirl Coaxial Injector Dimensions.**

| | $GO_2$ post diameter ($d_O$) | $GH_2$ annulus inner diameter ($d_{Fi}$) | $GH_2$ annulus outer diameter ($d_{Fo}$) |
|---|---|---|---|
| 60° Swirl | 0.210 in. (5.33 mm) | 0.250 in. (6.35 mm) | 0.290 in. (7.37 mm) |
| 75° Swirl | 0.277 in. (7.04 mm) | 0.317 in. (8.05 mm) | 0.357 in. (9.07 mm) |
| 90° Swirl | 0.370 in. (9.40 mm) | 0.410 in. (10.4 mm) | 0.450 in. (11.4 mm) |

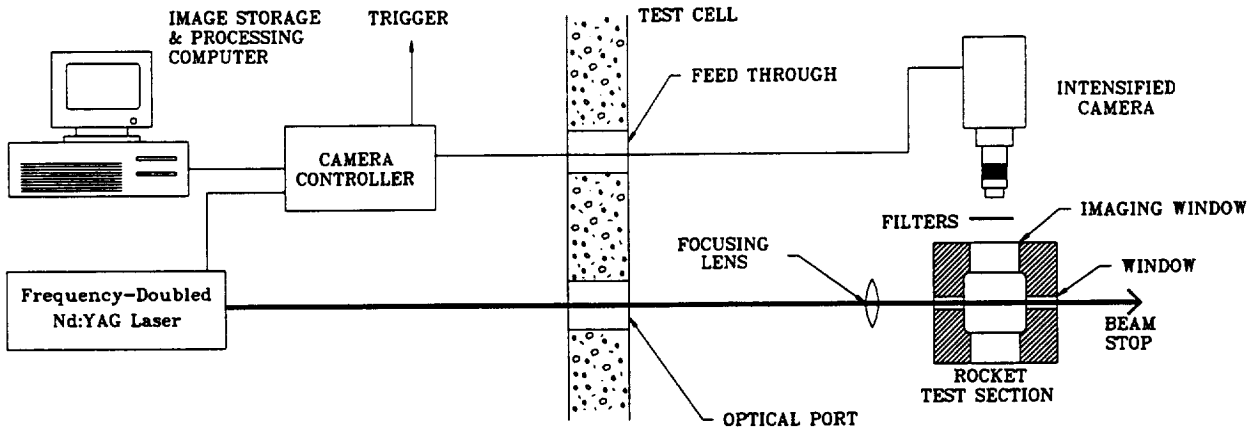


**Fig. 2.8.7. Experimental setup for Raman spectroscopy measurements.**

maximum collection of the weak Raman signal for making line images of the species field was developed. The experimental setup shown in Fig. 2.8.7 includes a frequency doubled Nd:YAG laser for Raman excitation and an intensified Charged Coulomb Device (CCD) camera for Raman signal detection. The frequency-doubled Nd:YAG laser delivers a pulse energy of 1 J at a wavelength of 532 nm. For the experiments reported here, the laser was operated to deliver 130 mJ per pulse (duration of 7 ns). The 10 mm diameter laser beam was focused using a 1500 mm lens to a waist of 0.3 mm downstream of the exit window. Inside the 25.4 mm (2 in.) cross section of the rocket chamber, the converging beam was nominally 1.3 mm in diameter. This optical arrangement prevented the quartz windows from being damaged by the high power laser beam. The full width at half maximum (FWHM) laser bandwidth is specified as less than 0.003 $cm^{-1}$.

The optics used on the receiving side are summarized in Table 2.8.6. The integrated slow scan intensified 16-bit CCD camera (14 bits were used) equipped with a f# 1.2, 50 mm focal length lens, was aligned 90° to the laser beam (see Fig. 2.8.7). For image analysis, only a portion of the total image (area of 144 x 10 pixels corresponding to a line image field of view of 1.79 x 0.157 in.

**Table 2.8.6. Receiving Side Optical Characteristics.**

| | |
|---|---|
| Camera Type | 12 Bit Intensified CCD Camera |
| Camera Readout Rate | 150 kHz |
| Camera Gate Width | 5 ns |
| Camera Lens | 50/1.2 with PK-12 Extension |
| Field of View | 45.5 x 4 mm |
| $GO_2$ Interference Filter | Center Wavelength - 581.2 nm; Bandwidth - 8.5 nm |
| $GH_2$ Interference Filter | Center Wavelength - 681.0 nm; Bandwidth - 9.7 nm |
| $H_2O$ Interference Filter | Center Wavelength - 661.3 nm; Bandwidth - 9.7 nm |
| $GN_2$ Interference Filter | Center Wavelength - 608.0 nm; Bandwidth - 9.4 nm |

(45.5 x 4 mm)) corresponding to the laser beam region was utilized. This optical arrangement was iteratively reached and represents a near optimum configuration for signal strength with respect to equipment limitations. For the wavelength of the laser used here ($\lambda$=532 nm), the center wavelength for the shifted Stokes Vibrational Q-branch signal from $GO_2$, $GH_2$, $GN_2$ and $H_2O$ species are 580, 681, 607 and 660 nm, respectively [46]. For each species measurement, a 10 nm (nominally; see Table 2.8.6 for specifics) bandpass filter centered at the aforementioned wavelengths was placed in front of the camera. In addition, for each species measurement, a high pass cutoff filter was placed in front of the camera to further isolate the Raman signal from the Rayleigh scattered light. Note that the choice of the interference filter bandwidth affects the temperature sensitivity of the Stokes bandwidth factor. For example, with Nd:YAG laser (532 nm) excitation for $GN_2$ species, the temperature dependence of the Stokes bandwidth factor to interference filter bandwidth shows that a filter centered at 607.3 nm with a bandwidth of 5 nm effectively makes the species measurement temperature independent to within 5% [46]. Alternately, the Stokes bandwidth factor increases non-linearly by about 40% for the $GN_2$ species temperature range from 300 to 3000K with a 10 nm bandwidth filter centered at 607.3 nm [46]. Clearly, for species field concentration measurements, the filters should be chosen to make the measurement temperature independent; otherwise careful filter calibration is necessary. For the experiments reported here, off-the-shelf low cost filters were chosen.

2.8.1.2.2. Injector Face Thermocouple Instrumentation

Temperature measurements of the injector face (injector face plate is made of oxygen-free copper) were made for all injector elements. The temperature was measured with the aid of a type "K" thermocouple silver brazed at a location 0.425 in. from the injector centerline. The temperature measurements were sampled at 200 Hz.

### 2.8.1.3. Results and Discussion

Since the target pressure of 1000 psia was relatively high, initial experiments were first conducted at lower chamber pressures of 300, 500 and 700 psia. These initial experiments indicated extremely high heat transfer rates to the wall for both the O-F-O and F-O-F triplet injector elements (melting in the wall region was observed). However, although the heat transfer rates for the swirl coaxial injector elements was high, they were not high enough to damage the

rocket. Consequently, Raman spectroscopy measurements of the flowfield were made for only the swirl coaxial injector elements.

Temperature measurements of the injector face (injector face plate is made of oxygen-free copper) are shown in Fig. 2.8.8 for the three swirl coaxial injectors. The temperature was measured with the aid of a type "K" thermocouple silver brazed at a location 0.425 in. from the injector centerline. The temperature measurements sampled at 200 Hz for the 2 sec. duration rocket firings show that the injector face temperature is lowest for the 60° swirl injector, and nominally the same for the 75° and 90° $GO_2$ swirl angle injector elements. The high injector face temperatures indicate that the energy release for the swirl coaxial injector element is close to the face, and hence, the possible use of this type of injector for actual rocket engines will require injector face cooling schemes that can alleviate the excessive injector face heat transfer rates.

The first set of experiments at a nominal chamber pressure of 1000 psia indicated that due to the large difference in index of refraction between the high temperature $GO_2/GH_2$ combustion products and the cold(er) nitrogen flow employed for purging the window section,

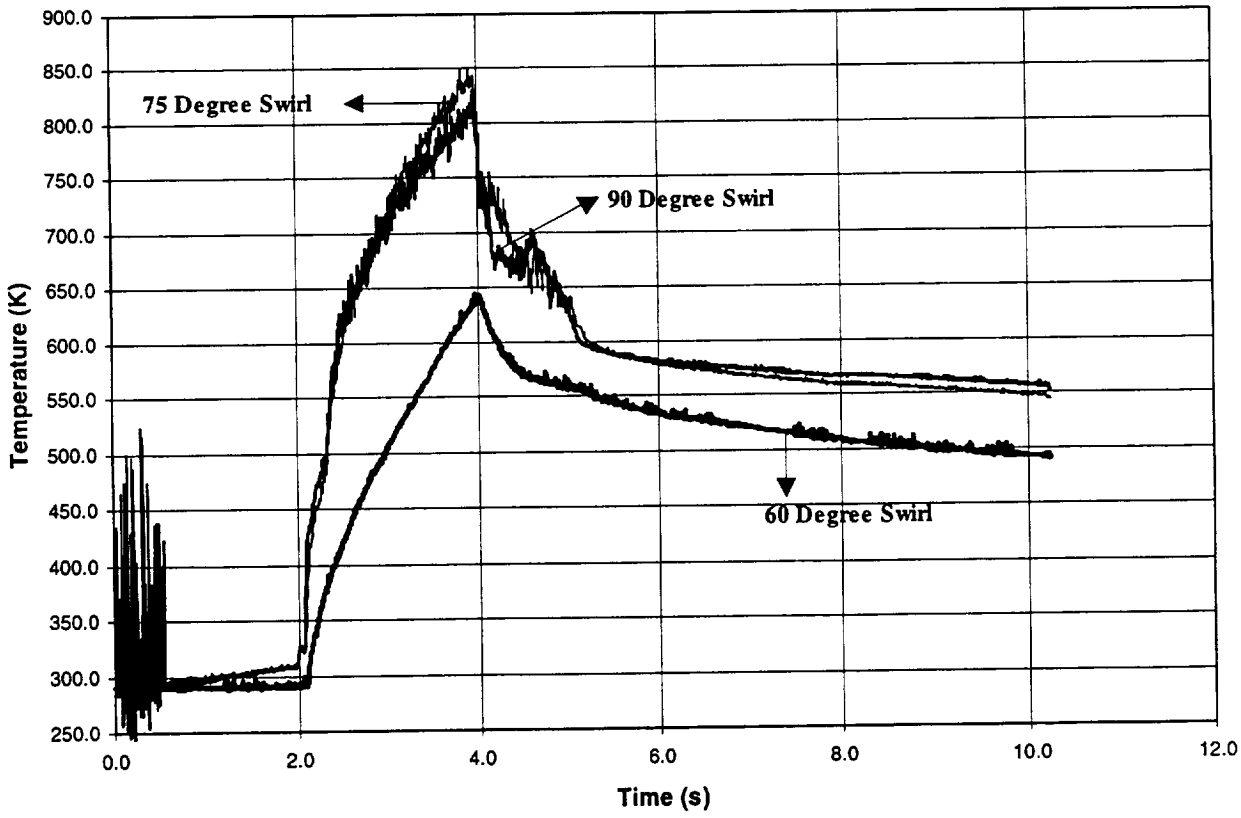


**Fig. 2.8.8. Injector face temperature for the three swirl coaxial injectors. Thermocouple is located 0.425 in. from injector centerline.**

the laser beam steered/bloomed through the chamber cross-section and severely compromised the Raman experiments. Fortuitously, helium has an index of refraction close to that of the high temperature $GO_2/GH_2$ combustion products. The experimental results presented next were obtained by using helium instead of nitrogen as the window purge gas. Unfortunately, helium does not have a Raman cross-section due to its monatomic structure, and hence its concentration can not be measured using Raman spectroscopy.

Radial line images of the species Raman signal at an axial location of 3.5 in. from the injector face for the three geometric variations (60°, 75°, and 90°), of the swirl coaxial injector are shown in Figs. 2.8.9-2.8.11. In these three figures, both a representative instantaneous image and the averaged image (nominally 10-20 image average) for each measured species, viz. $GH_2$, $GO_2$ and $H_2O$, are shown. The instantaneous images highlight the highly turbulent nature of the combusting flowfield. Analysis of the instantaneous flow structure in the combusting flowfield was not possible because the current experimental setup only provided the Raman signal from only one species at one time. The averaged images were obtained by averaging the instantaneous images for each species and correcting for both the flame luminosity levels and background scattering. Note that the gray-scales for each species was scaled from minimum to maximum, and therefore the gray-scale should not be used to compare the relative Raman signal strength. The measurements showed that $GH_2$ and $H_2O$ were present at all radial locations at the 3.5 in. measurement location. Here, the Raman signal obtained for the $GO_2$ measurement setup was "weak". Furthermore, each instantaneous $GH_2$ measurement (of both the vibrational and one of the rotational lines) always showed $GH_2$ at <u>all</u> radial locations. Since oxygen and hydrogen cannot occupy the same location at the same time, this suggests that $GO_2$ was not present at the 3.5 in. measurement location. The relatively weak signal measured using the $GO_2$ measurement setup is believed to be from a rotational line (S-branch) of $GH_2$ that can be detected if the gas temperature is high [46]. Hence, for all three geometric variations of the swirl injector, combustion was complete within 3.5 in. from the injector face.

To quantify the Raman spectroscopy measurements, the experimental setup was calibrated for $GO_2$ and $GH_2$ species at standard temperature and pressure conditions. The experimental setup was also calibrated *in-situ* for $H_2O$ using a steam/$GN_2$ flow. The calibrations of the major species provided a basis for extracting the radial profiles of species mole fraction from the corrected

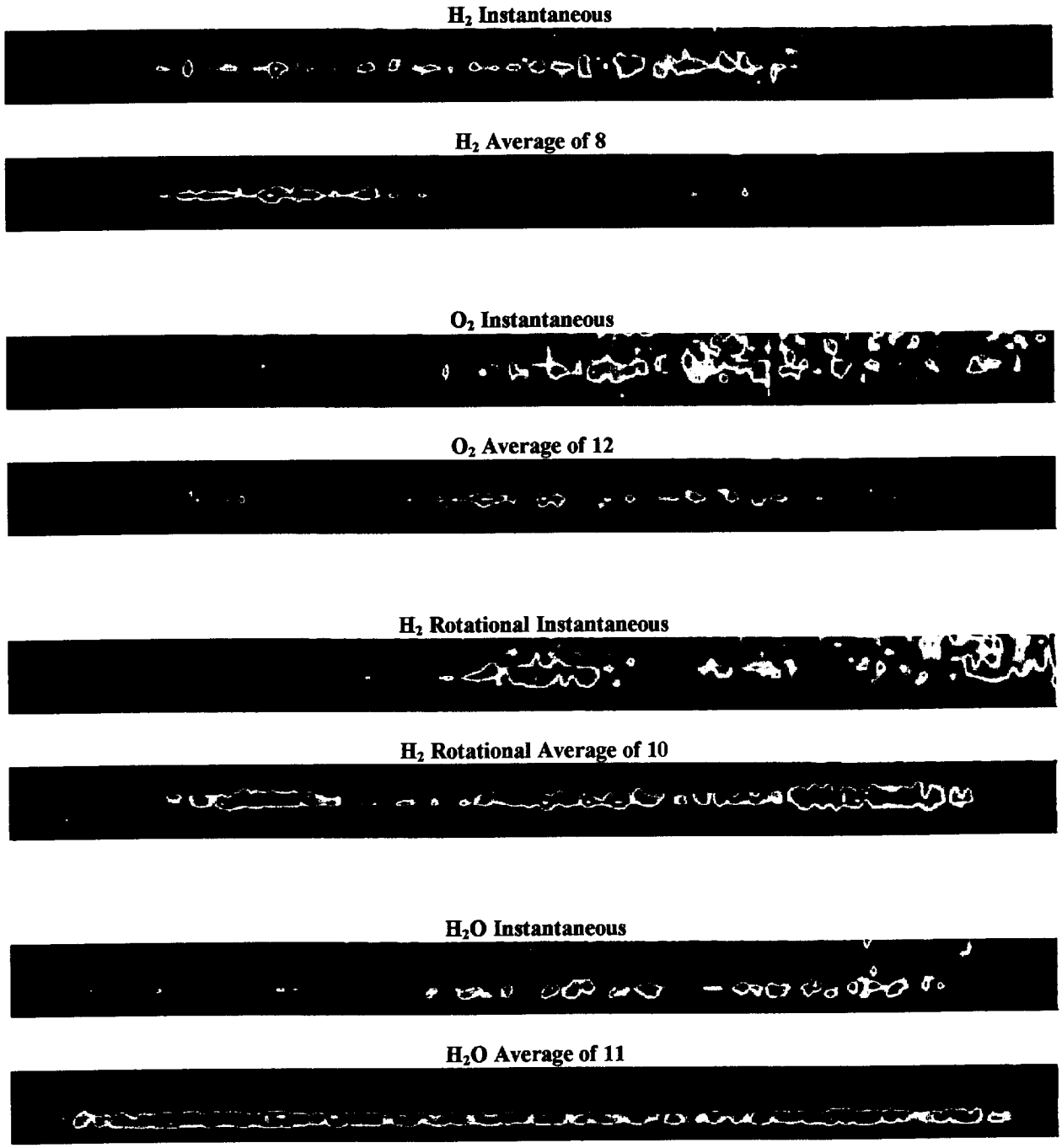


**Fig. 2.8.9. Raman line images of major species for the $GO_2/GH_2$ 60° swirl coaxial injector. Radial species profiles are for an axial measurement location of 3.5 in. from injector face at a chamber pressure of 993 psia.. For each species, instantaneous and average images are shown. Note that the $GO_2$ signal is not from $GO_2$ but is argued to be from a rotational line of $GH_2$ that is within the bandwidth of the $GO_2$ filter.**

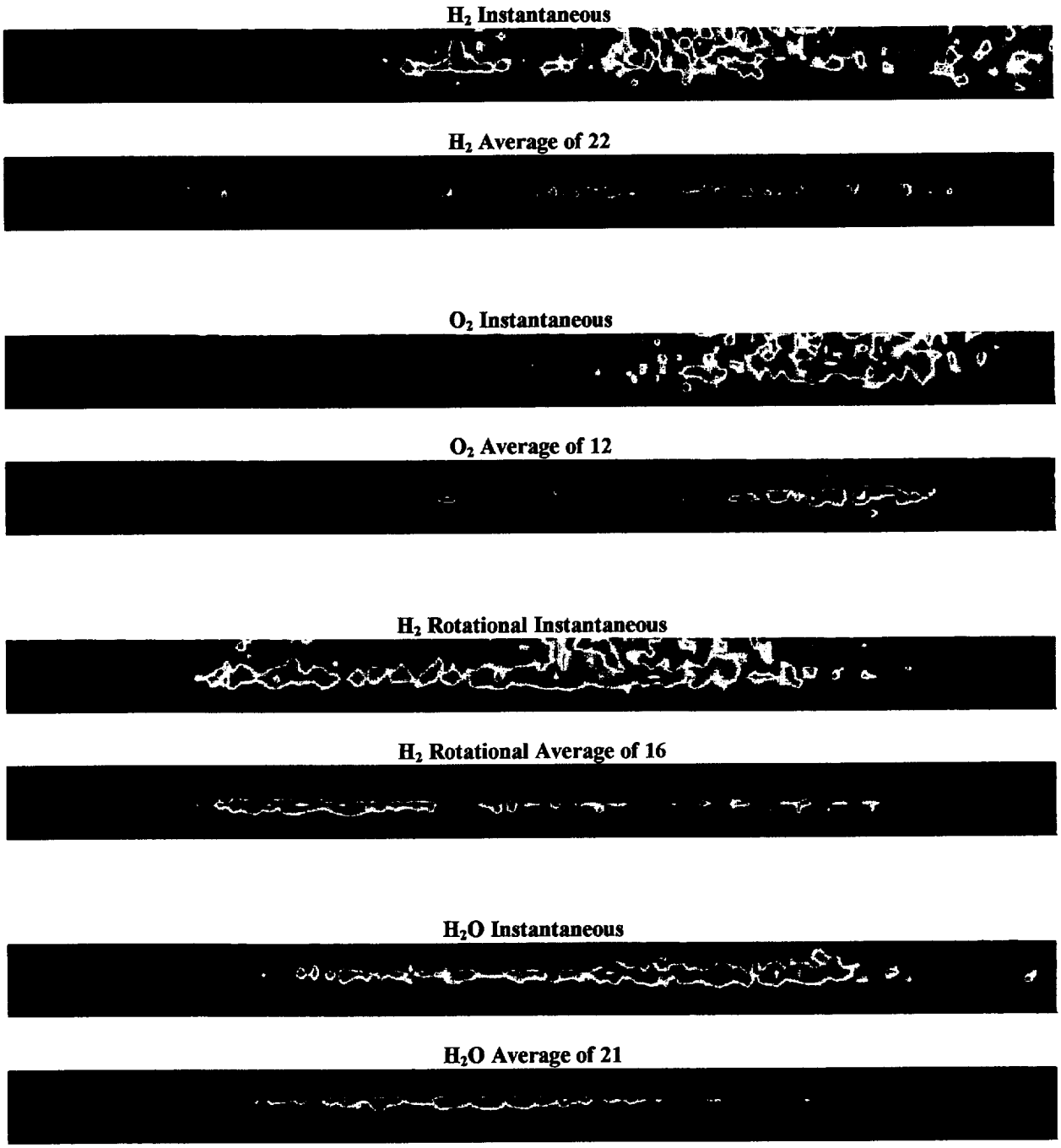


**Fig. 2.8.10. Raman line images of major species for the $GO_2/GH_2$ 75° swirl coaxial injector. Radial species profiles are for an axial measurement location of 3.5 in. from injector face at a chamber pressure of 1039 psia.. For each species, instantaneous and average images are shown. Note that the $GO_2$ signal is not from $GO_2$ but is argued to be from a rotational line of $GH_2$ that is within the bandwidth of the $GO_2$ filter.**

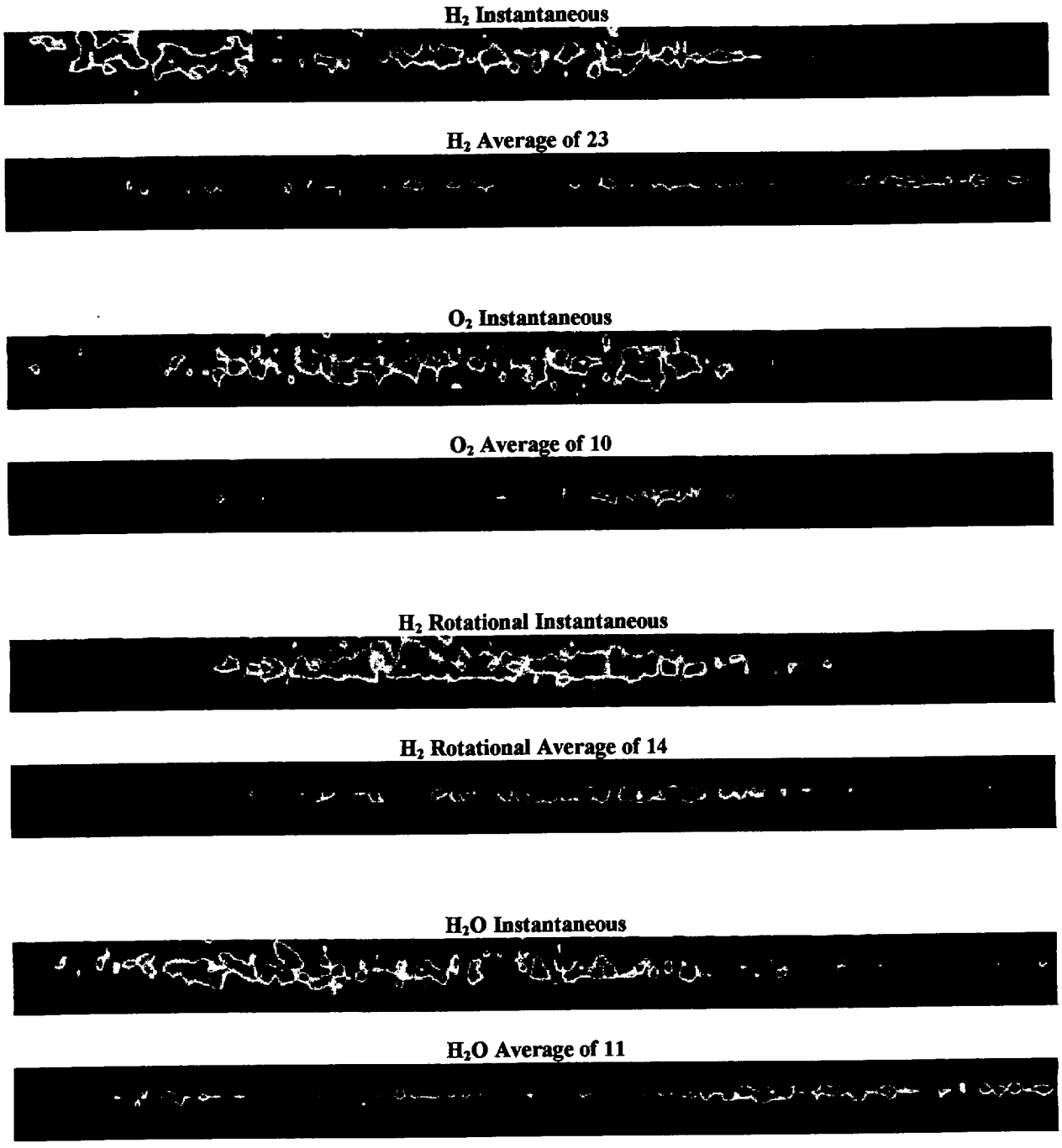


**Fig. 2.8.11. Raman line images of major species for the $GO_2/GH_2$ 90° swirl coaxial injector. Radial species profiles are for an axial measurement location of 3.5 in. from injector face at a chamber pressure of 995 psia.. For each species, instantaneous and average images are shown. Note that the $GO_2$ signal is not from $GO_2$ but is argued to be from a rotational line of $GH_2$ that is within the bandwidth of the $GO_2$ filter.**

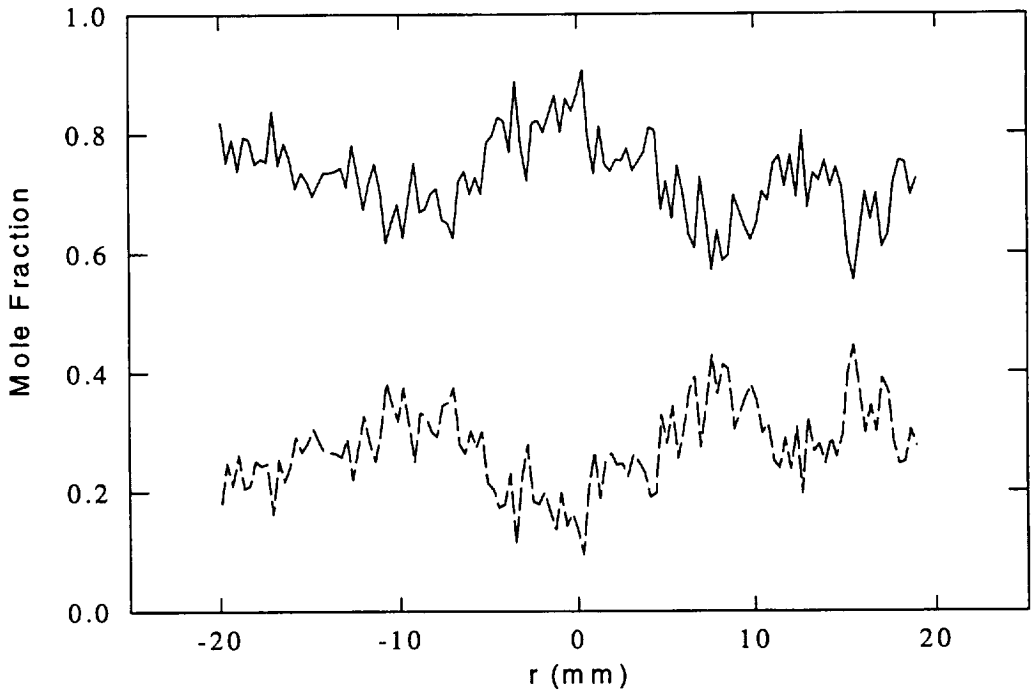


**Fig. 2.8.12. Average $GH_2$ and $H_2O$ mole fraction radial profiles at an axial measurement location of 3.5 in. from injector face for 60° swirl injector. Mole fraction results are obtained from the Raman line images shown in. Fig. 2.8.9. $P_c$=993 psia.**

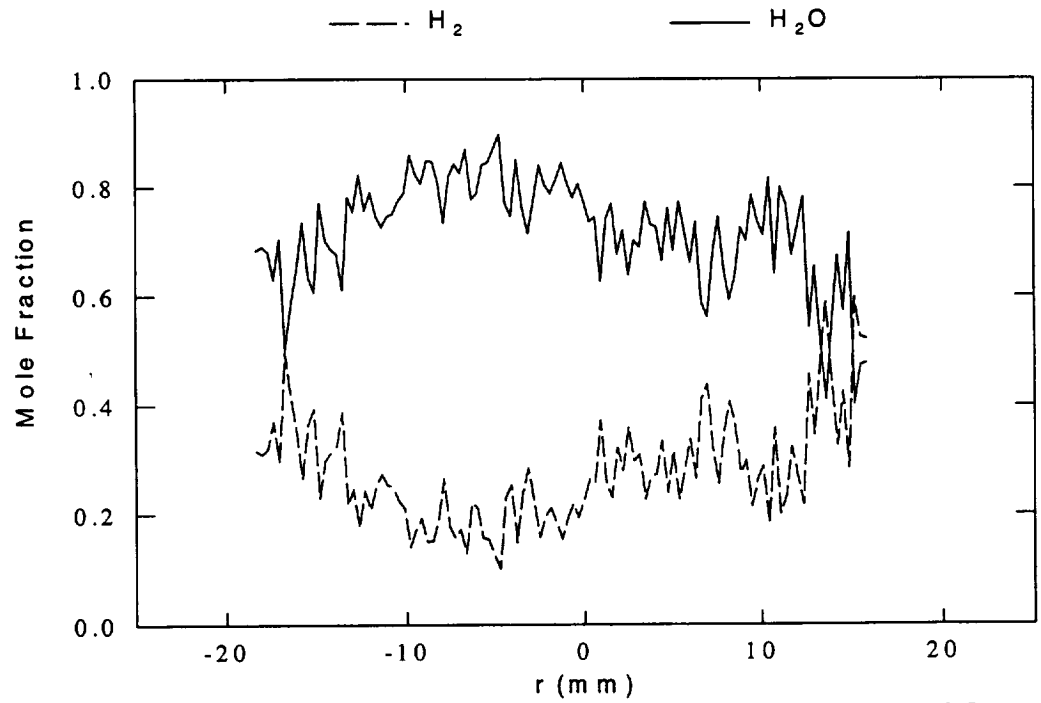


**Fig. 2.8.13. Average $GH_2$ and $H_2O$ mole fraction radial profiles at an axial measurement location of 3.5 in. from injector face for 75° swirl injector. Mole fraction results are obtained from the Raman line images shown in. Fig. 2.8.10. $P_c$=1039 psia.**

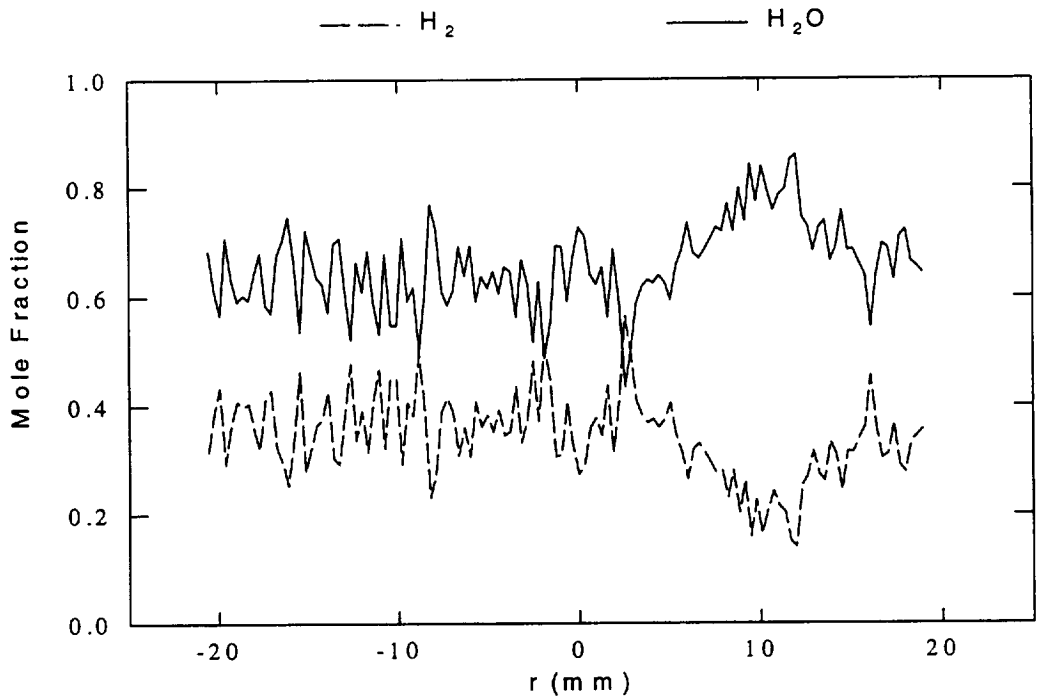


**Fig. 2.8.14. Average $GH_2$ and $H_2O$ mole fraction radial profiles at an axial measurement location of 3.5 in. from injector face for 90° swirl injector. Mole fraction results are obtained from the Raman line images shown in. Fig. 2.8.11. $P_c$=995 psia.**

average Raman images described earlier, as shown in Figs. 2.8.12-2.8.14 for the tested swirl coaxial injectors. The species mole fraction results are semi-quantitative since the Stokes bandwidth factor for the filters used for the experiment was temperature dependent. The results showed that all three species were nearly uniformly distributed in the radial direction indicating that combustion was complete or near-completion. Clearly, these measurements show that the swirl coaxial injector element is an efficient injector in terms of its mixing, combustion and performance characteristics. However, from the Raman measurements at one axial location, viz. 3.5 in. from the injector face, the superiority of one geometric variation over the others can not be quantified. The injector face temperature measurements indicated that increased $GO_2$ swirl levels promote mixing and combustion, and hence it is expected that, in contrast to the 60° swirl injector, combustion is complete closer to the injector face for the 90° swirl injector. In any case, the results indicate that the generic swirl injector is an efficient injector, and actual implementation of this type of injector will require trade off studies between injector face temperature requirements and mixing/combustion efficiency limits, i.e. necessary chamber length to achieve complete combustion.

### 2.8.2. SECOND PHASE OF EXPERIMENTATION

The first set of experiments for the swirl coaxial injector showed that although mixing and combustion was complete close to the injector face, the face heat flux was very high. Based on theses results involving the swirl coaxial injector element, the GGIT team decided to investigate the shear coaxial injector element for the second phase of experimentation. The experiments conducted for this phase again investigated the mixing and combustion characteristics of the injector with the aid of Raman spectroscopy.

#### 2.8.2.1. Shear Coaxial Injector Elements

The GGIT team decided that the flowfield characteristics for various geometrically different shear coaxial injector elements needed to be studied for the second phase of experimentation. Four geometric variations of the shear coaxial injector elements were designed for implementation in the optically-accessible rocket chamber described in Section 2.2. (see Fig. 2.2.1 for details).

The shear coaxial injector element geometries were designed for gaseous oxygen/gaseous hydrogen flow at a mixture ratio of six. The target chamber pressure was 1000 psia for oxygen and hydrogen flowrates of 0.25 lbm/s and 0.042 lbm/s, respectively.

The design phase of the shear coaxial injector elements involved vigorous discussions between all GGIT team members. The discussion led to the decision that four shear coaxial injector elements with gaseous hydrogen to gaseous oxygen velocity ratios between 4 and 8 needed to be designed and fabricated. The common parameters for all four geometric variations of the injector element are summarized in Table 2.8.7. Based on these common parameters, four shear coaxial injector elements were designed and fabricated. The specifics of each design are presented in Table 2.8.8.

#### 2.8.2.2. Raman Spectroscopy Setup

Raman spectroscopy was employed as the major diagnostic technique for characterizing the mixing and combustion characteristics of the flowfield. During the time period between the first and second phases of experimentation, the technique had been further refined. Specifically, in contrast to the earlier implementation of the technique with filters for each species, the technique now employed a spectrometer. The major gain with this new setup was due to the possibility of *simultaneously* measuring all major species.

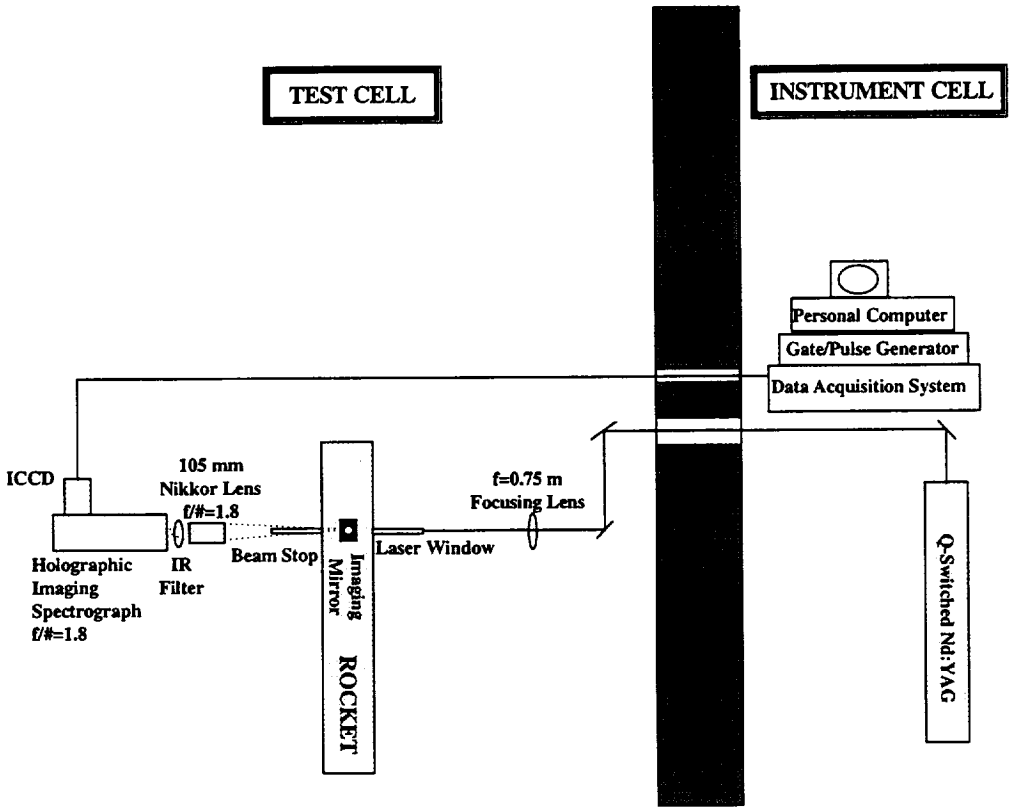


**Fig. 2.8.15. Schematic of improved Raman set-up with spectrometer for simultaneous measurement of all major species.**

conjunction with an intensified charge-coupled device (ICCD, 576x384 pixel) camera was used to capture the Raman signals of major combustion species ($H_2$, $O_2$, $H_2O$). The system allowed simultaneous multi-species multi-point Raman measurements. The slit width of 500 μm and binning of four pixels in the radial dimension, corresponding to the 384 pixel direction, and of six pixels in the wavelength dimension, corresponding to the 576 pixel direction were used. The Raman signal-to-noise ratio was increased by discriminating against the Rayleigh interference by using of a notch filter centered at 532 nm (FWHM ≈ 18 nm) placed inside the spectrograph. The intense flame interference was reduced 50% by using a linear dichroic sheet polarizer aligned with the Raman signal polarization.

### 2.8.2.3. Results and Discussion

The averaged and background luminosity corrected Raman signals at the axial measurement location of 5 in. from the injector face for the four geometric variations (see Tables 2.8.7 and 2.8.8 for details), of the shear coaxial injector are shown in Figs. 2.8.16. In the figures, the abscissa and ordinate represent the wavelength of light and radial location,

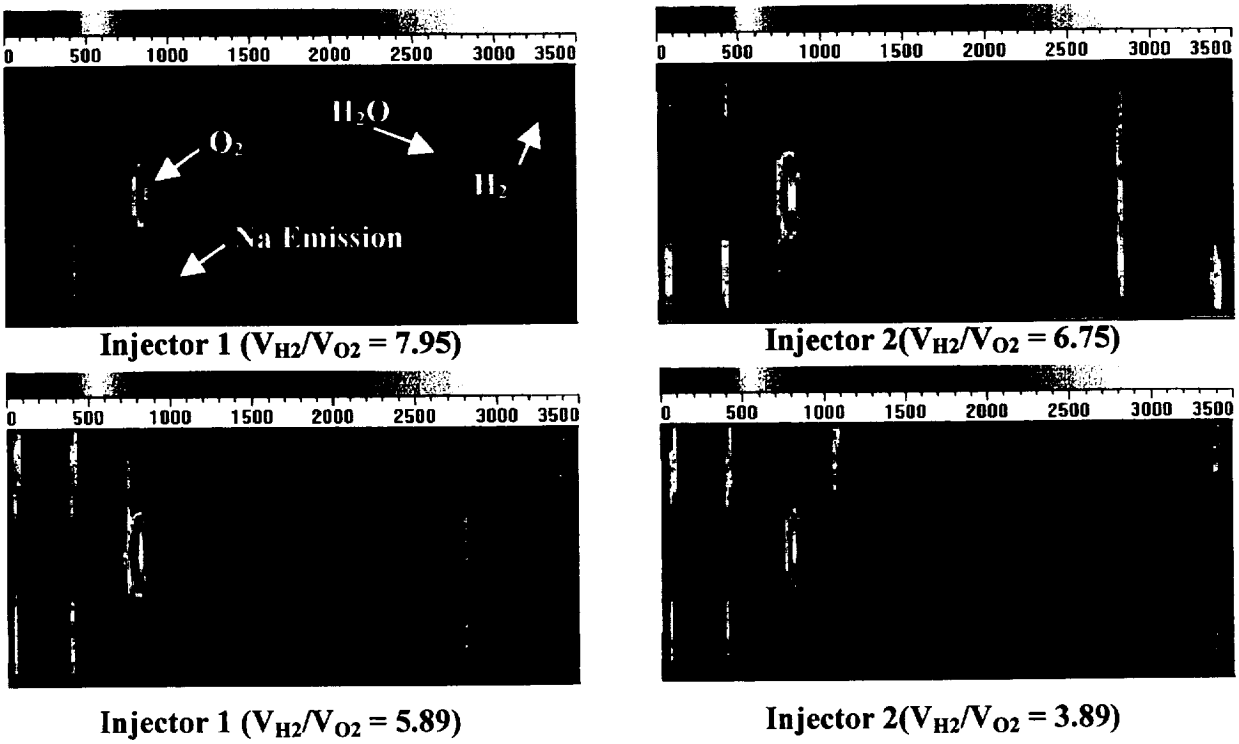


**Fig. 2.8.16. Comparison of flame background corrected averaged Raman species measurements for four geometric variations of the shear coaxial injector. For target flow conditions, see Tables 2.8.7 and 2.8.8.**

respectively. The central ordinate location corresponds to the axis of the shear coaxial injector element. The wavelength locations of oxygen, hydrogen and water vapor are indicated in one of the results. The averaged images were obtained by averaging multiple instantaneous images for each flow condition and correcting for both the flame luminosity levels and background scattering. Note that the scale for each of the results is consistent, and therefore, the levels can be compared between the different results. The measurements showed that $GO_2$ always prevails in the central part of the flowfield. Comparison of the results for the four gaseous hydrogen to gaseous oxygen velocity ratio cases shows that the least amount of oxygen is present for the highest velocity ratio case (velocity ratio of 8). This is consistent with the realization that mixing, and consequently combustion, increases with increasing hydrogen to oxygen velocity ratio. The results also indicate the presence of $H_2$ and $H_2O$ away from the central region of the flowfield. Complementary face temperature measurements (not shown here) indicate a moderate temperature increase of about 100 K for all studied shear coaxial injector geometries. These results indicate that mixing and combustion for the shear coaxial injector in an uni-element configuration are relatively gradual.

# III. ANALYTICAL STUDIES

## 3.1. INTRODUCTION

Our focus in this second major section of the report is on the analysis of combustors for cryogenic rocket engines. As in the experimental section, it places an emphasis on the detailed phenomena that take place in the combustor to provide understanding and insight into practical design features. The analytical results are intended to complement the experiments reported above through providing interpretation, while also relying on the experimental measurements as a validation source. The approach taken is to use computational fluid dynamic solutions of the complete equations of motion. Computational capabilities are approaching the point where they can begin to be used in the design of practical rocket combustors, and the present study gives a very practical basis for assessing and extending their maturity while simultaneously complementing the experiments.

The specific topics covered are in general similar to those discussed in the experimental section although they are considerably restricted in scope. It was the assumption at the start of the effort that computational capabilities were not sufficiently advanced to allow complete three-dimensional studies of two-phase reacting flow problems. Although considerable progress has been made in the intervening time, three-dimensional solutions remain largely beyond current computational capabilities. All results presented herein are therefore two-dimensional (generally axisymmetric) in nature. Analysis of the complex three-dimensional injectors tested in the experimental section has there not been attempted. In the two-dimensional regime, both steady and unsteady flowfields have been simulated, and both two-phase and single-phase solutions have been considered.

Another difference between the experimental tasks and the analytical tasks is that most of the analyses consider hydrogen and oxygen propellants. In general, the hydrocarbon propellants considered in the experimental section have not been modeled because of the much more complex chemical kinetics. In the hydrogen-oxygen case, both $GO_2/GH_2$ and $LOX/GH_2$ predictions have been included. As a brief summary of capabilities, axisymmetric computations for the gas-gas case are reasonably well in hand. The kinetics are well established; the necessary grid resolution is not a problem; and results are generally realistic [65-68]. The primary uncertainties involve turbulence and turbulent combustion. Although our understanding of both turbulence and turbulent combustion is elementary, engineering models for turbulence are

calibrated well enough to provide semi-quantitative confidence in the results. Engineering models for turbulent combustion are much less well developed, but their impact is lessened by the fast kinetics of the hydrogen-oxygen system, especially in the absence of the familiar nitrogen diluent that is missing in the rocket combustor.

Analogous axisymmetric computations of the LOX spray combustion process in the LOX/$GH_2$ case involve considerably larger uncertainties. The primary problem in LOX spray computations is in establishing the droplet size distribution. Although numerous models exist for estimating atomization properties, their reliability is very low except in very specialized situations. In particular, it is clear that atomization models from one configuration or regime cannot be reliably extrapolated to another. An important issue here is the degree of applicability of atomization measurements taken under cold flow conditions to the desired hot flow environment. Our results simultaneously show that the predictions of spray combustion calculations are quite sensitive to the initial drop size distribution. Not only does the mean drop size influence the results, but also the distribution likewise is a very sensitive parameter. Consequently, the state of spray combustion computations is much less mature than that of single-phase solutions. Our results described herein are based on measured initial drop sizes in an attempt to minimize this influence.

In addition to the hydrogen-oxygen modeling results, we also describe a global analysis of a combined hydrogen-hydrocarbon manifold problem. These results are given below. We start by describing the computational model that was used for all the analyses. We then describe individual problems in sequence.

## 3.2. DESCRIPTION OF COMPUTATIONAL MODEL

The computational model involves the Navier-Stokes equations coupled with auxiliary transport equations for the individual species and a two-equation model of turbulence. For cases with liquid spray, the drops are handled by a Lagrangian particle tracking procedure. The equations for the gas phase case can be expressed in their traditional conservative form as:

$$\Gamma\frac{\partial \mathbf{Q}_p}{\partial t}+\frac{\partial \mathbf{E}}{\partial x}+\frac{\partial \mathbf{F}}{\partial y}=\mathbf{L}(\mathbf{Q}_p)+\mathbf{H}_{gas}+\mathbf{H}_{liq} \tag{3.2.1}$$

For convenience, the equations are written in vector form, starting from the continuity equation, the momentum equations, the energy equation, the species equations, and the turbulence equations.

In Eq. 3.2.1, we have chosen to use the vector of primitive variables, $\mathbf{Q}_p=(p+2k/3,u,v,T,Y_i,k,\varepsilon)^T$, as the primary dependent variable. Here all variables have their standard meaning: $\rho$ is the density; $u$ and $v$ are the Cartesian velocity components; $T$ is the temperature; $Y_i$ is the mass fraction of the $i^{\text{th}}$ species with the implication that the species variable, $i$, runs from one to the total number of species; and $k$ and $\varepsilon$ are the dependent variables in the two-equation turbulence model. Note that the thermodynamic pressure is replaced by a modified pressure, $p+2k/3$ to include the effects of turbulence. The selection of $\mathbf{Q}_p$ as the primary dependent variable is particularly convenient for reacting flows because it allows us to compute the temperature at the new time step and then obtain the enthalpy of the mixture from the temperature, rather than having to invert this relation as is normally done.

To retain the classical form of the equations, the time derivative is multiplied by the Jacobian matrix, $\Gamma=\partial\mathbf{Q}/\partial\mathbf{Q}_p$ to switch from the conservative variables, $\mathbf{Q}=(\rho,\rho u,\rho v,\rho e,\rho Y_i,\rho k,\rho\varepsilon)^T$. This Jacobian, $\Gamma$, is a sparse matrix that contains only the thermodynamic properties of the fluid(s) of interest. For most computations, the physical properties in this Jacobian are replaced by artificial properties that provide improved convergence in the low speed flows that are typical of combustion problems.

This preconditioning procedure is discussed elsewhere. For the present system, the following preconditioning matrix was used:

$$\Gamma = \begin{pmatrix} \rho'_p & 0 & 0 & \rho'_T & 0 & 0 & 0 \\ \rho'_p u & 0 & 0 & \rho'_T u & 0 & 0 & 0 \\ \rho'_p v & 0 & 0 & \rho'_T v & 0 & 0 & 0 \\ \rho'_p h^0 & \rho u & \rho v & \rho'_T h + \rho h_T & 0 & \frac{5}{3}\rho & \frac{\rho}{\sigma}(h_j - h_N) \\ \rho'_p Y_i & 0 & 0 & \rho'_T Y_i & \rho & 0 & 0 \\ \rho'_p k & 0 & 0 & 0 & 0 & 0 & 0 \\ \rho'_p \varepsilon & 0 & 0 & 0 & 0 & 0 & 0 \end{pmatrix} \tag{3.2.2}$$

In this expression, $\rho'_p$ and $\rho'_T$ are artificial fluid properties that are used to speed convergence. They have been defined as,

$$\rho'_p = \frac{\gamma \mathrm{Re}^2}{u_r} \quad \text{and} \quad \rho'_T = 0$$

where $Re$ is the cell Reynolds number, $u_r$ is a reference velocity and $\gamma$ is the ratio of specific heats.

The flux vectors, $\mathbf{E}$ and $\mathbf{F}$, that appear in Eq. 3.2.1 are given by

$$\mathbf{E} = \begin{Bmatrix} \rho u \\ \rho u^2 + p \\ \rho uv \\ \rho u h^o \\ \rho u Y_i \\ \rho uk \\ \rho u\varepsilon \end{Bmatrix} \qquad \mathbf{F} = \begin{Bmatrix} \rho v \\ \rho uv \\ \rho v^2 + p \\ \rho v h^o \\ \rho v Y_i \\ \rho vk \\ \rho v\varepsilon \end{Bmatrix} \tag{3.2.3}$$

where the stagnation enthalpy is denoted as, $h^o$.

The terms on the left hand side of Eq. 3.2.1 include the viscous operator, $\mathbf{L}(\mathbf{Q}_p)$ and two source vectors, $\mathbf{H}_{gas}$, and $\mathbf{H}_{liq}$. The viscous operator is given by

$$\mathbf{L}(\mathbf{Q}_p) = \frac{\partial}{\partial x}\left(\mathbf{R}_{xx}\frac{\partial \mathbf{Q}_p}{\partial \mathbf{x}} + \mathbf{R}_{xy}\frac{\partial \mathbf{Q}_p}{\partial y}\right) + \frac{\partial}{\partial y}\left(\mathbf{R}_{yx}\frac{\partial \mathbf{Q}_p}{\partial \mathbf{x}} + \mathbf{R}_{yy}\frac{\partial \mathbf{Q}_p}{\partial y}\right) \tag{3.2.4}$$

where $\mathbf{R}_{xx}$, $\mathbf{R}_{xy}$, $\mathbf{R}_{yx}$, and $\mathbf{R}_{yy}$, are diffusion matrices with the general form,

$$\mathbf{R}_{xx} = \begin{pmatrix} 0 & 0 & 0 & 0 & 0 & 0 & 0 \\ 0 & \frac{4}{3}\mu & 0 & 0 & 0 & 0 & 0 \\ 0 & 0 & \frac{4}{3}\mu & 0 & 0 & 0 & 0 \\ 0 & \mu u & \mu v & \lambda & 0 & 0 & 0 \\ 0 & 0 & 0 & 0 & \rho D_{ij} & 0 & 0 \\ 0 & 0 & 0 & 0 & 0 & \mu_k & 0 \\ 0 & 0 & 0 & 0 & 0 & 0 & \varepsilon \end{pmatrix} \tag{3.2.5}$$

Note that the first row and the first column of all the diffusion matrices are zero indicating that there is no diffusion term in the continuity equation, and that the pressure does not appear in the diffusion terms.

The first of the source vectors, $\mathbf{H}_{gas}$, contains the terms that appear in the standard gaseous equations, including axisymmetric terms, sources in the species equations and production and dissipation terms in the turbulence model equations. This vector is defined as,

$$\mathbf{H}_{gas} = (0 \quad -\rho uv/y \quad 0 \quad 0 \quad \dot{\omega}_i \quad S_k \quad S\varepsilon)^T \tag{3.2.6}$$

while the liquid source term contains mass, momentum and energy transport effects between the two phases,

$$\mathbf{H}_{liq} = (S_c \quad S_{mx} \quad S_{my} \quad S_e \quad S_{Yi} \quad 0 \quad 0)^T \tag{3.2.7}$$

The terms in this expression include the local liquid mass vaporization rate, the gas-liquid momentum and energy exchange, and the additional species accumulation in the gas phase from liquid vaporization. The liquid source term, $\mathbf{H}_{liq}$, is determined by integrating the contributions of mass, momentum and energy exchange from a Lagrangian treatment of a dilute, multi-disperse distributed liquid phase flow comprised of a large number of contributing particles. The governing equations for the liquid phase analysis are discussed below. For calculations

involving only the gaseous phase, the liquid-phase source term, $\mathbf{H}_{liq}$, is set to zero and the computation proceeds directly from the equations in this section. When spray drops are present, the auxiliary liquid phase equations described in the following section must be solved in conjunction with these gas phase equations.

As implied above, a standard $k$-$\varepsilon$ turbulence model is chosen to simulate the effects of turbulence. The model was augmented by both a low Reynolds number formulation and a wall-layer formulation to account for near wall effects. For computations involving the combustion of hydrogen and oxygen, an 8-specie, 18-reaction, $H_2/O_2$ chemical kinetics model was used. The approximate kinetic model for kerosene-oxygen combustion is described in detail below. The thermo-physical properties for each species were evaluated from appropriate temperature dependent functions with mixture viscosity and thermal conductivity obtained from Wilke's law. Diffusion coefficients for the individual species are obtained from Chapman-Enskog theory.

For gas phase constituents, we close the system by using the perfect gas equation of state for each species. For spray distributions, the gas phase computation is unchanged except for the addition of mass and momentum by the vaporization process. As each liquid drop passes through the flowfield, the vapor trail it deposits along its trajectory is assumed to mix instantaneously with the existing gases in the local control volume, and to obey gas kinetics following its evaporation.

### 3.2.1. NUMERICAL ALGORITHM

The complete numerical model is solved by an approximate implicit numerical algorithm. Spatial differencing of the convection terms is accomplished by either central differences or upwind-biased differencing of first-, second- or third-order formal accuracy. Diffusion terms are handled by central differencing. For the central difference case, the implicit formulation is solved by means of the tri-diagonal alternating direction implicit (ADI) method of Douglas and Gunn. For upwind differencing, either ADI or line Gauss-Seidel (LGS) is used. The code also includes an option for using the LU (symmetric point Gauss-Seidel) method, but this method is well known to be inferior to the other two methods in highly stretched grids, and is seldom chosen. A specially adapted preconditioning matrix is used to control the eigenvalues of the system to provide uniformly efficient convergence at all Mach numbers, especially the low speeds representative of combustion conditions. In addition, this preconditioning minimizes the

adverse effects of low Reynolds numbers and high aspect ratio cells that are characteristic of grids for turbulent flows.

Time accurate computations are accomplished by means of a dual-time algorithm. This enables the preconditioned pseudo-time marching procedure to be applied to time accurate problems in a manner analogous to that used for steady state problems.

### 3.2.2. MODELING PHILOSOPHY FOR DISTRIBUTED LIQUID PHASE

The modeling of the liquid spry considers the vaporization and dynamic motion of a large number of drops that determine the source terms for the gas phase. The primary difficulty in utilizing a Lagrangian treatment of the liquid phase is the significant computational resources required. Since tracking the individual drops of a physical spray is clearly beyond computational capabilities, we instead track a large number of parcel which are individually representative of a group of identical physical drops. Appropriate drop size and velocity distributions can be superimposed on the drop parcel distribution by statistical means. Clearly, the gas phase variables depend on the location of the liquid particles and the local vaporization rate (mass addition). The motion of the liquid particles in turn depends on the local gas phase properties such as temperature, velocity, and viscosity. Both sets of equations must be solved simultaneously in a coupled fashion to determine the steady state solution.

Common difficulties associated with the implementation of a mixed Eulerian/Lagrangian tracking procedure include the following:

The large number of particles needed to give an accurate representation of the particle distribution function at all points in space can require excessive computational resources both in terms of time and memory. This is particularly critical when coupled with a multi-dimensional, multi-species CFD code.

A large number of computational parcels must be used to ensure that a statistically significant sampling of point sources is considered when computing the source terms, especially near the outer edges of the spray distribution.

Mapping the instantaneous particle locations of the drops into the appropriate Eulerian grid for the gas phase mesh can become costly when dense, nonuinform meshes are used.

There must be a balance between the number of drops tracked and the convergence level of the gas phase equations. In general, doubling the accuracy of a statistical function such as the drop number density requires a one order of magnitude increase in the sample size. Consequently, as the gas phase solution converges, the required number of drops in the sample size increases very rapidly.

One factor that offsets much of the difficulty encountered with a Lagrangian approach is that all of our liquid-phase solutions are for steady-state conditions. It is not necessary to store the entire particle flowfield when only steady solutions are desired. Instead, each liquid drop parcel can be tracked from the inlet to the exit (or until it vaporizes completely) during a single time step. This circumvents the need for storing the locations and properties of all the drops. Instead, a series of individual drops can be tracked through the flowfield at each time step. Of course, this approach is not applicable during the transient phase, but becomes accurate as the gas flowfield approaches a steady state. The variables associated with the individual drop characteristic are scalars and are not stored variables. The mass, momentum and energy contributions are allocated throughout the trajectory to the appropriate local gas phase cells as the parcels traverse the flowfield. The inter-phase source terms contained in $\mathbf{H}_{liq}$ are the only quantities impacting the gas phase and are the only vector variables that must be stored in memory.

This is opposite to the case of the unsteady solution for which the instantaneous liquid phase variables (including their diameter and velocity components, etc.) must be stored for the entire field of drop parcels because the gas phase flowfield is changing every time, and the drops must pass through the time-varying field. The number of particles used in either the steady or the unsteady Lagrangian approaches is similar, but in the steady solution, none of the properties of the distributed phase need be stored. Thus, the storage requirement of the steady solution is not an issue in assessing its cost. The only issue with using the Lagrangian method in a steady solution is its impact on central processor time. For the present computations, typical flowfields are based on the contributions of several million particles.

The final issue in computing Lagrangian flows effectively is an efficient allocation of the inter-phase source terms from the instantaneous particle trajectories in space to the appropriate Eulerian cells in the discretized mesh. Typically, gas phase coordinate systems are mapped form

the physical grid to an equally spaced computational mesh. The tracking procedure for the Lagrangian particles keeps track of the physical coordinates of the particle, but it is necessary to have an efficient method for allocating the mass, momentum and energy contributions from the liquid phase to the appropriate gas phase cell. This is accomplished by taking into account the equally distributed character in the computational plane as noted in the next section.

### 3.2.3. LIQUID PHASE EQUATIONS OF MOTION

The liquid drop spray is described by a three-dimensional Lagrangian formulation that involves mass, momentum and energy transfer equations of the individual drop. Established empirical sub-models are used for the various physical processes associated with the liquid phase such as spray atomization and drop vaporization. The dynamic equations of motion for each drop can be written in vector form as

$$\frac{d\mathbf{Q}}{dt} = \mathbf{H}_d$$

where the primary vector, $\mathbf{Q}_d = (d, u_d, v_d, w_d, T_d)^T$, and the source term vector, $\mathbf{H}_d = \left(\dot{m}_{vap} / \pi \rho_l d^2, F_x / m_d, F_y / m_d, F_z / m_d, S_e\right)^T$. Here $d$ represents the drop diameter, and the subscript $d$ implies conditions of the drop. In the source term, $m_d$ refers to the mass of the drop, while $\dot{m}_{vap}$ is the instantaneous mass vaporization rate. The drag forces acting on the drop are obtained from standard drag curve results for spherical particles. The effects of gas/liquid drop turbulence interactions are modeled by using stochastic methods available in the literature.

Because the gas phase is treated as an axisymmetric flow, the liquid drops must be tracked in a fully three-dimensional physical space. Specifically, the paths of the individual drop trajectories in the Lagrangian treatment of the liquid phase are fully three dimensional, but their contribution to the gas phase is axisymmetric in the statistical mean. To accomplish this, the equivalent radial coordinate is used to rotate the three-dimensional trajectories to axisymmetric coordinates.

The drop parcel locations in axisymmetric space are computed from the contravariant velocities after the method of Sabnis as,

$$\frac{d\xi}{dt} = \hat{U} = \xi_x u_d + \xi_y v_d$$

$$\frac{d\eta}{dt} = \hat{U} = \eta_x u_d + \eta_y v_d$$

where $\xi$ and $\eta$ are the transformed axial and radial directions in computational space. The physical variables are updates using the known liquid phase velocities and current liquid phase time step. This formulation in computational space allows the appropriate cell index to which the liquid phase source terms are to be allocated by an integer division as opposed to a search routine. This minimizes the time required to identify where the contribution of any given drop trajectory is to be allocated in the gas phase solution.

## 3.3. CHARACTERIZATION OF REPRESENTATIVE FLOWFIELD

We begin by presenting representative results to characterize the overall flowfield in the gas/gas, hydrogen-oxygen case. By comparing these predictions with experimental data, we then document the level of accuracy that can be realized with the model. The computations mimic the uni-element coaxial gas/gas injector experiments described in Ref. 51. These experiments were conducted at Penn State under NASA MSFC Contract NAS8-38862, "An Experimental Study of Characteristic Combustion-Driven Flow for CFD Validation." The computational domain starts inside the co-axial injector passage and proceeds downstream to an assumed uniform outlet region in the vicinity of the nozzle. Note that the nozzle was not included in the computations. To obtain proper initial conditions for the $GH_2$ and $GO_2$ flowfields in the injector, preliminary computations were conducted for each channel, and were used as upstream boundary conditions for the chamber calculations. The lip region of the $GO_2$ post between the $GH_2$ and $GO_2$ co-axial passages was resolved by means of grid stretching. Representative grid sizes were nominally 151×101, with the computational domain beginning upstream inside the injector and extending downstream to the end of the chamber at an axial location of $x$=245.6 mm.

To provide an initial description of the overall combusting flowfield resulting from the $GO_2/GH_2$ shear coaxial injector, the global characteristics of the flowfield as determined by the CFD solutions are presented first. The velocity, temperature and OH concentration fields downstream of the shear coaxial injector are given in Fig. 3.3.1 (a-c). The velocity contours in Fig. 3.3.1 (a) show that the high velocity $GH_2$ jet from the annulus of the coaxial injector decelerates very rapidly after the $GH_2$ enters the combustor. Farther downstream, there is a gradual acceleration of the flow as a result of heat addition.

The temperature contours in Fig. 3.3.1 (b) show the overall heating pattern more clearly. A narrow annulus of hot gas starting from very near the injector face indicates that the $GH_2$ and $GO_2$ begin to react almost as soon as they enter the chamber. (A more detailed picture of this near-injector region is given later.) With increased distance downstream, a larger and larger fraction of the gas becomes heated by the flame, giving rise to the overall flow acceleration noted in Fig. 3.3.1 (a). Although the temperature profile spreads over most of the chamber, there remain substantial temperature striations as the gas exits through the nozzle.

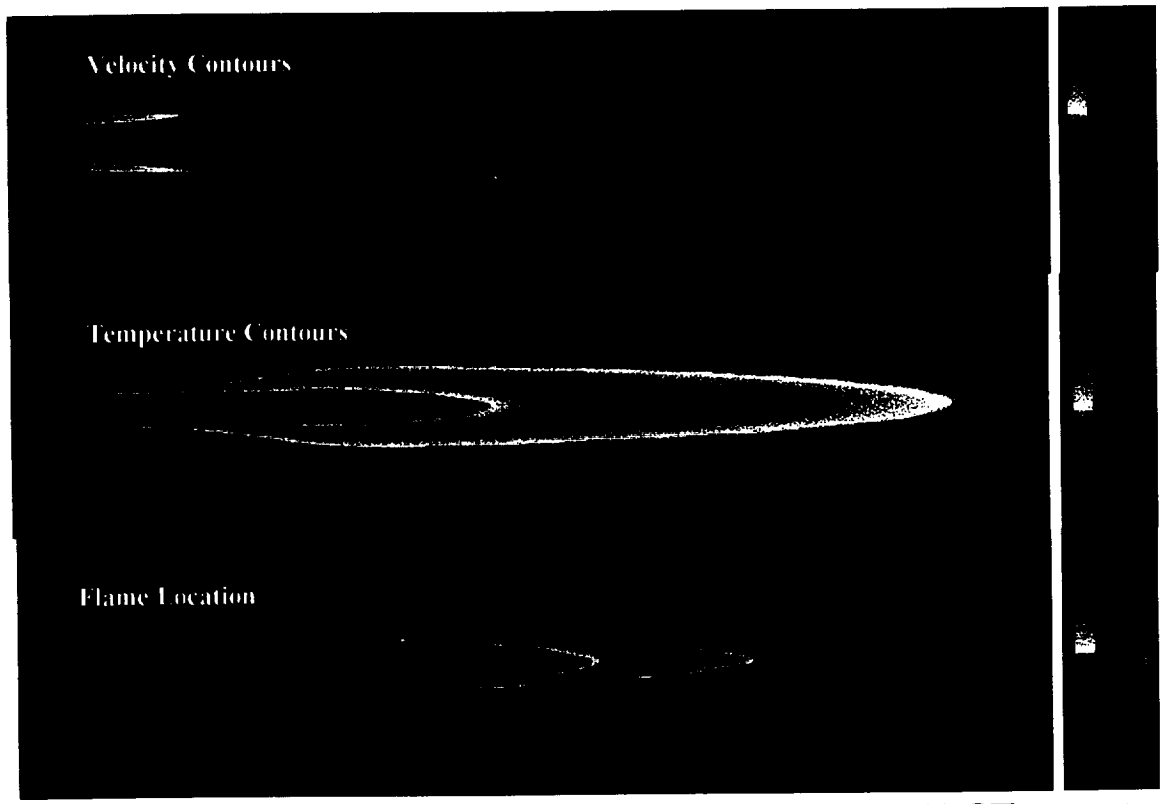


**Fig. 3.3.1. CFD predictions of the (a) velocity, (b) temperature and (c) OH concentration fields for the combusting $GO_2/GH_2$ flowfield downstream of the shear coaxial injector in the rocket chamber. Flow is from left to right.**

The OH concentration profiles in Fig. 3.3.1 (c) serve as a reasonably accurate marker for the flame, and show that the combustion is nearly complete after a distance of about x=185 mm. This flame configuration suggests the combustion process is reasonably efficient, a suggestion verified by experimental $c^*$ measurements discussed earlier. In addition $GO_2$ concentration profiles (presented later) indicate that most of the $GO_2$ has been burned, again indicating good combustion efficiency.

The global picture of the combustion process given by these computational predictions is one of a long annular flame that starts near the shadow of the splitter plate between the $GO_2$ and $GH_2$ streams and then spreads modestly in radius with increasing distance downstream.

These results are for an O/F ratio of 2.0, and at this condition, the flame consumes all the oxygen and closes at the centerline when all the $GO_2$ has been burned. As the O/F ratio is increased, the flame length increases, eventually extending out of the computational domain. This global picture of the flame characteristics is useful in understanding the experimental results presented below.

## 3.4. COMPARISON OF CFD PREDICTIONS WITH FLOWFIELD MEASUREMENTS FOR GAS/GAS CASE

LDV measurements of the velocity field and Raman spectroscopy measurements of the major species fields in a flowfield analogous to that described in Fig. 3.3.1 were measured at three axial measurement locations, viz. 25.4, 50.8 and 127 mm from the injector face. In particular, each image illustrates (by color) the radial extent of species at the stated axial location at one instant of time. These instantaneous images show that at this axial station, $GO_2$ species is present only in the region downstream of the $GO_2$ post, whereas $GH_2$ species diffuses considerably in the radial direction. The $H_2O$ species is present in the shear layer between the $GO_2$ and $GH_2$ flows. The instantaneous images also highlight the highly turbulent nature of the combusting shear layer.

To quantify the Raman spectroscopy measurements, the experimental setup was calibrated for $GO_2$, $GH_2$ and $GN_2$ species at standard temperature and pressure conditions. A similar calibration for $H_2O$ was obtained in a simple laboratory setup involving steam/air flow (393K). Using these calibrations, radial profiles of the major species mole fractions were extracted from the corrected/averaged Raman images. Computational predictions of the $GO_2$ and $GH_2$ mole fraction profiles at the three axial locations are compared to the experimental measurements in Figs. 3.4.1 and 3.4.2. Similar comparisons for the mean velocity and rms velocity profiles are presented in Figs 3.4.3 and 3.4.4. For all inset graphs in Figs. 3.4.1-3.4.4, the ordinate shows the radial distance from the centerline normalized with the $GO_2$ post radius.

At the first axial measurement location, $x$=25.4 mm, the radial profiles of $GO_2$ and $GH_2$ mole fraction (Figs 3.4.1 and 3.4.2) show that at 3.3 $GO_2$ post diameters downstream (25.4 mm), propellant mixing and combustion is limited to the thin shear layer between the two propellant flows. The $GO_2$ flow does not diffuse radially outward, whereas the $GH_2$ flow does diffuse radially outward but fails to penetrate the dense $GO_2$ central region. The $H_2O$ mole fraction (not shown) peaks at a radial location ($r/r_o \approx 1.2$) near the intersection of the $GO_2$ and GH2 mole fraction radial profiles. It is emphasized that the species mole fraction results are semi-quantitative since the Stokes bandwidth factor for the filters used for the experiment were temperature dependent. Note that due to the non-linear dependence of the Stokes bandwidth factor on temperature, the error in the radial profiles of species mole fraction is highest in the narrow high temperature zone corresponding to the shear layer mixing region between the two propellant streams, and minimal in

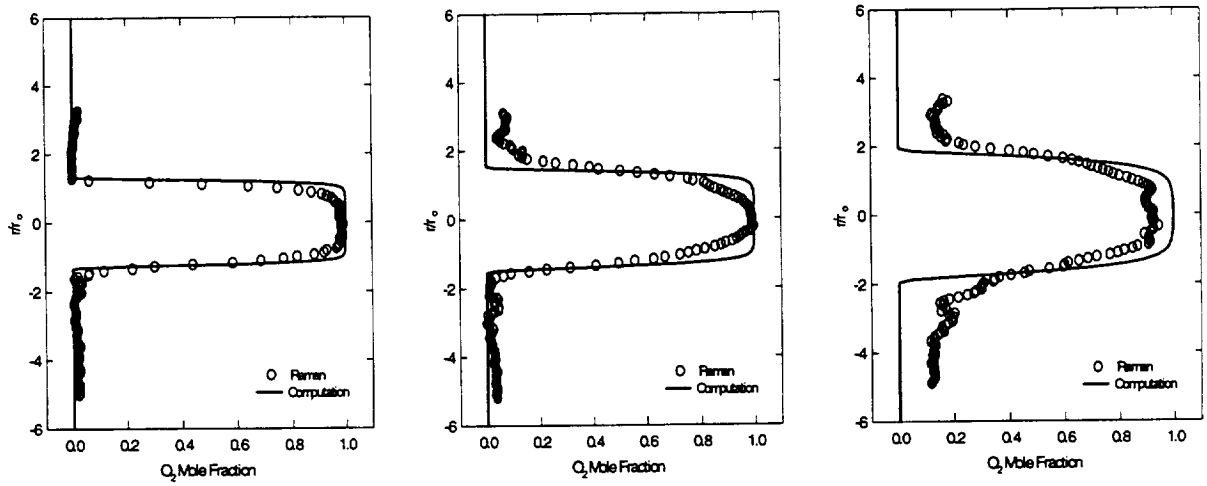


(a) $x$=25.4 mm (b) $x$=50.8 mm (c) $x$=127 mm

**Fig. 3.4.1. Comparison between measured and calculated $GO_2$ (a-c) mole fraction profiles for three axial locations from injector face.**

other low temperature (<1500K) regions. The complementary CFD species profile results agree reasonably with the experimental results. The slight difference between the measurements and calculations in the shear layer region probably stems from the measurement inaccuracy discussed earlier and the fact that the experimental results represent average quantities in a highly turbulent flowfield.

The corresponding radial profile of the axial component of the velocity (Fig. 3.4.3) indicates that the velocity of the central high density $GO_2$ flow remains nearly the same as the $GO_2$

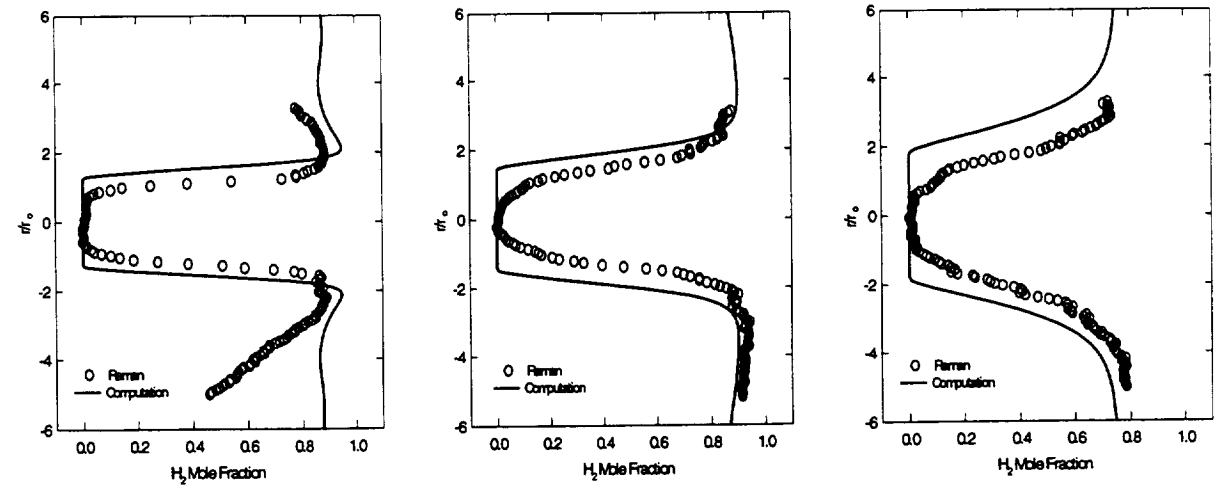


(a) $x$=25.4 mm (b) $x$=50.8 mm (c) $x$=127 mm

**Fig. 3.4.2. Comparison between measured and calculated $GH_2$ (a-c) mole fraction profiles for three axial locations from injector face.**

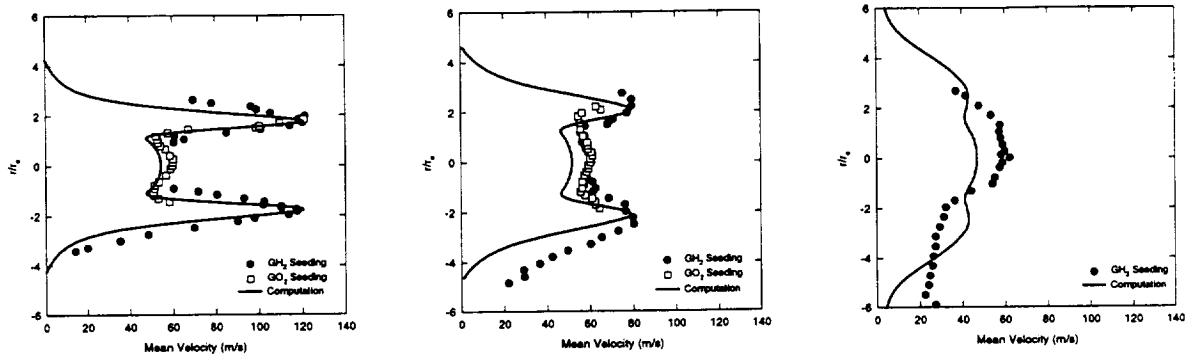


(a) $x$=25.4 mm (b) $x$=50.8 mm (c) $x$=127 mm

**Fig. 3.4.3. Comparison between measured and calculated mean (a-c) velocity profiles for three axial locations from injector face.**

injection velocity (≈51 m/s), whereas due to rapid radial diffusion, the 120 m/s peak velocity of the annular $GH_2$ flow is lower than the $GH_2$ annular injection velocity of 177 m/s. Notice that the velocity profile (corresponding to the $GH_2$ annular flow region) peaks at a radial location ($r/r_o \approx 2$) further out than the mixing shear layer region. The root mean square (rms) velocity profile (Fig. 3.4.4 indicates that in the central core, the rms velocity is about 6 m/s yielding a turbulent intensity value of about 0.1, or 10%. In the peak velocity region, the mean velocity is about 120 m/s with a corresponding root mean square velocity of about 30 m/s resulting in a turbulent intensity of about 0.25 or 25%. The higher turbulent intensity value here is probably a result of both combustion and the unsteady nature of the flow. The CFD predictions of the mean and rms velocity agree reasonably well with the measurements at this axial measurement location.

Farther downstream at an axial location of 50.8 mm from the injector face (6.6 $GO_2$ post diameters), the radial profiles of $GO_2$ and $GH_2$ mole fraction (Figs. 3.4.1 and 3.4.2) show that as

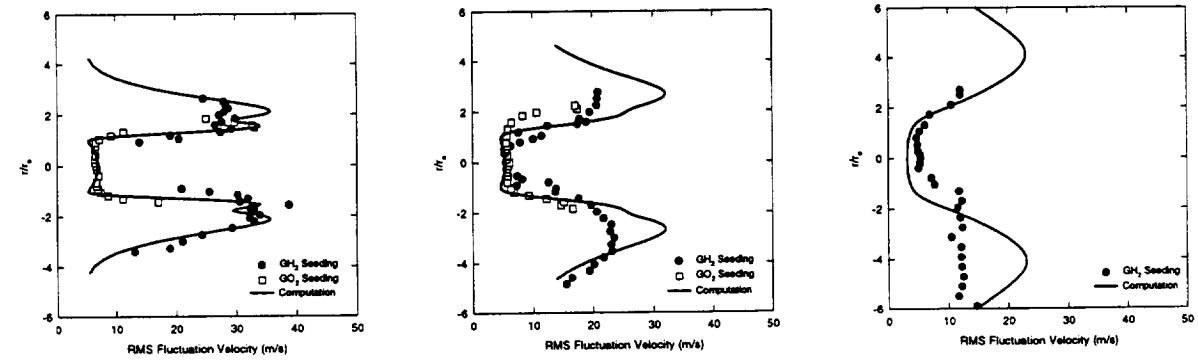


(a) $x$=25.4 mm (b) $x$=50.8 mm (c) $x$=127 mm

**Fig. 3.4.4. Comparison between measured and calculated and root mean square (a-c) velocity profiles for three axial locations from injector face.**

compared to the first measurement location, the mixing shear layer has radially shifted outward by a small amount. The half width at half maximum (HWHM) of the $GO_2$ mole fraction is at $r/r_o \approx 1.2$, suggesting that the central $GO_2$ flow is diffusing radially at a slow rate.

The corresponding velocity (Fig. 3.4.3) in the central $GO_2$ part of the flowfield is still nearly the same as that of the $GO_2$ injection velocity (≈51 m/s), whereas the peak velocity of the annular low density $GH_2$ flow has now decelerated to 80 m/s (from an injection velocity of 177 m/s). Again, the radial location of the shear-mixing layer is closer to the centerline than the $GH_2$ peak velocity location. The rms velocity profile (Fig. 3.4.4) shows that the turbulent intensity measured in the peak velocity region at the second axial location (mean velocity and rms velocity are 80 m/s and 20 m/s, respectively) is similar to the results at the first axial location. The CFD predictions of the species mole fraction, and mean and rms velocity agree qualitatively with the measurements at this axial measurement location.

Finally, at the farthest downstream measurement location, $x$ =127 mm (16.4 $GO_2$ post diameters), the mole fraction profiles (Figs. 3.4.1 and 3.4.2) indicate the presence of non-combusted $GO_2$ in the central part of the flowfield and unreacted $GH_2$ radially outwards. The CFD results also indicate the presence of unburnt $GO_2$ and $GH_2$, but differ quantitatively with the experimental results.

The corresponding mean velocity profile (Fig. 3.4.3) shows that the velocity in the center region of the flowfield corresponding to unreacted $GO_2$ is close to the $GO_2$ injection velocity, whereas away from the center region, the velocity decreases with radial distance. In comparison to the results upstream, the mean velocity and the rms velocity (Fig. 3.4.4 away from the centerline are lower, however the rate of drop off is significantly higher for the mean velocity, resulting in a turbulent intensity (or large scale unsteadiness) of about 0.4 or 40% (mean velocity and rms velocity are 25 m/s and 10 m/s, respectively). Agreement between the experimental and CFD results for this axial location is qualitative.

Clearly, both the measurements (up to 127 mm (16.4 $GO_2$ post diameters)) and the predictions of the species and velocity fields indicate that whereas the low density annular $GH_2$ flow rapidly diffuses radially outward to fill the chamber, the high density central $GO_2$ flow does not diffuse significantly with downstream distance, resulting in a shear layer with low mixing efficiency as attested by the measured high $GO_2$ mole fraction levels ($GO_2/GH_2$ combustion

products for a mixture ratio of four are $GH_2$ and $H_2O$, each at a mole fraction of 0.5). However, since the $c^*$ efficiency for the rocket is very high, near complete combustion is achieved by the nozzle entrance, and hence, additional flowfield measurements between the furthest current axial station and the nozzle entrance are desirable.

The agreement between the CFD results and experimental measurements presented here indicates that experimentally validated CFD codes are at a point where they can begin to be used as design tools for predicting gaseous propellant combustion in rocket chambers. In addition, CFD can provide additional flowfield details that cannot be measured easily, such as details related to flame holding. CFD results on the flame-holding mechanism for the shear coaxial injector are presented in section 3.10.

# 3.5. TRI-PROPELLANT DROP BURNING AND HYDROCARBON COMBUSTION PROCESSES

## 3.5.1. BACKGROUND AND JUSTIFICATION

Results reported from the Russian literature have indicated performance advantages for adding 'small' amounts of hydrogen to a kerosene engine. Similarly, experimental results from Japan have likewise indicated that the addition of hydrogen improved both the efficiency and the stability of a hydrocarbon engine. Our original interest in analyzing the tri-propellant problem was to provide some fundamental basis upon which to understand and interpret these reported favorable effects of hydrogen on the RP-1 combustion process, as similar reports had been circulating for many years. Accordingly, the primary analytical effort was concentrated on the combustion characteristics of a single RP-1 drop in a gaseous hydrogen environment and the changes in its combustion characteristics when a small amount of hydrogen was added.

Extensive numerical experiments with a mixture of hydrogen and oxygen surrounding a kerosene drop indicated that upon ignition, the hydrogen would immediately (or very rapidly) burn with the oxygen to leave an RP-1 drop surrounded by a warm oxidizer gas with a small fraction of water diluent. The hydrocarbon drop then subsequently burned in this warm, vitiated oxidizer environment. This finding, which is clearly intuitively plausible, suggests that hydrogen does not materially improve the burning characteristics of kerosene except through its effect on increasing the surrounding temperature. It is true that hydrogen might have a notable effect on kerosene combustion if it were intimately mixed with the kerosene prior to combustion, but the cited engine results appeared to be more analogous to the model of a kerosene drop in a sea of oxygen-hydrogen, than a mixture of kerosene and hydrogen surrounded by oxidizer. Thus our results in this area proved negative from the viewpoint of supporting RP-1 combustion improvement by hydrogen addition.

Follow-up engine tests in Japan that were conducted and published while the present effort was underway indicated that the addition of an inert gas (helium) was just as effective in improving combustion efficiency and engine stability as was hydrogen. Since the addition of either hydrogen or helium had the same effect, it was clear that it was not the combustion characteristics of the hydrogen that led to the improvements. The explanation for the effect of gas addition was now traced to its impact on the atomization process since both the hydrogen and

the helium in the Japanese tests were introduced through the RP-1 injectors. The addition of a gas into the liquid stream resulted in finer atomization and improved the engine combustion characteristics. Thus, the effect proved to be a mechanical effect, not a chemical effect as was thought earlier.

The engine tests in Russia, however had used separate injection elements for the hydrogen and kerosene, so improved kerosene atomization characteristics should not have been the explanation for their reported performance increases. Even though the reported findings were similar, the sources of the effect were clearly different. Further literature research conducted during the present effort ascertained that the reason that for the performance improvement in the Russian engines was simply that a large amount of hydrogen had been added to the kerosene. The hydrogen addition ranged between 10 and 20 % by weight so that hydrogen was the largest fuel constituent by moles. Consequently, the majority of the energy supplied to the engine in the Russian tests came from the hydrogen, not the kerosene. The reported efficiency improvements thus arose because the engine was more like a hydrogen engine than a kerosene engine, and the improvement in $I_{sp}$ with hydrogen is well known.

Finally, our own experiments, reported in chapter 2 of the present report indicated that hydrogen had no favorable effects on the combustion properties of RP-1. The combination of the present analytical and experimental efforts in conjunction with a more precise interpretation of the Russian and Japanese tests, therefore conclusively demonstrate that hydrogen has no favorable effect on the kerosene combustion process. There are several ways that hydrogen addition can improve engine performance, but not through its effect on the combustion process. The preliminary findings of the analytical predictions thus appear to be well founded. In the following sub-sections, the analytical studies are described in detail along with representative results.

### 3.5.2. DEVELOPMENT OF RP-1/HYDROGEN COMBUSTION KINETICS MODEL

The first step in assessing the burning characteristics of an RP-1/hydrogen mixture was to develop a representative chemical kinetics model for the hydrocarbon-hydrogen system. The model had to be detailed enough to take into account the presence of varying amounts of elemental hydrogen, while being economical enough to allow repetitive computations. In assembling this kinetic system, we enlisted the help and advice of appropriate researchers at

**Table 3.5.1. RP-1 Global Combustion Kinetics Model; Single-Step Model**

| GLOBAL MECHANISM | A | B | E/R | POWER DEPENDENCIES |
|---|---|---|---|---|
| Single Step Model | | | | |
| $C_{13}H_{28} + 20\ O_2 \rightarrow 13\ CO_2 + 14\ H_2O$ | 3.8 E11 | 0 | 1.511 E4 | $[C_{13}H_{28}]^{0.25}[O_2]^{1.5}$ |
| $C_{11}H_{14} + 14.5\ O_2 \rightarrow 11\ CO_2 + 7\ H_2O$ | 2.0 E11 | 0 | 1.511 E4 | $[C_{11}H_{14}]^{-0.1}[O_2]^{1.85}$ |

MSFC and industrial laboratories to avoid any unnecessary duplication of previous work. The help obtained from these individuals is gratefully acknowledged. In assembling this kinetics model we also drew on our existing soot formation expertise developed under other funding to assess the potential effects of soot formation on the effective heat release. Soot formation processes in kerosene engines can be of importance for both combustion and heat transfer reasons.

A detailed review of available literature on chemical kinetic modeling of hydrocarbon fuels and a survey of selected individuals working in the field have been used as the basis for identifying a practical combustion model for tri-propellant engines. Existing chemical kinetic models are available for various levels of sophistication, and clearly, the most detailed are beyond the complexity that can be used in CFD codes. The task in choosing the present model for mixtures of RP-1 and $H_2$ was to identify a model that contained sufficient detail to be capable of predicting the effects of hydrogen on the combustion of kerosene. This, of course, presupposes the model is capable of predicting the combustion of kerosene alone. A second goal in the study was to identify models of two different levels so that the simpler one could be used for parametric analysis and computations, while the more complex and costly one could be used as a check on the former. Six different models have been considered and are discussed below.

**Table 3.5.2. RP-1 Global Combustion Kinetics Model; Two-Step Model**

| GLOBAL MECHANISM | A | B | E/R | POWER DEPENDENCIES |
|---|---|---|---|---|
| Two-Step Model | | | | |
| $C_{13}H_{28} + 13.5\ O_2 \rightarrow 13\ CO + 14\ H_2O$ | 4.7 E11 | 0 | 1.511 E4 | $[C_{13}H_{28}]^{0.25}[O_2]^{1.5}$ |
| $C_{11}H_{14} + 9\ O_2 \rightarrow 11\ CO + 7\ H_2O$ | 2.4 E11 | 0 | 1.511 E4 | $[C_{11}H_{14}]^{-0.1}[O_2]^{1.85}$ |
| $CO + 0.5\ O_2 \rightarrow CO_2$ | 3.5 E14 | 0 | 2.014 E4 | $[CO][H_2O]^{0.5}[O_2]^{0.25}$ |

**Table 3.5.3. RP-1 / $H_2$ Combustion Kinetics Model**

| ELEMENTARY MECHANISM | A | | B | E/R | |
|---|---|---|---|---|---|
| Wet CO Mechanism | | | | | |
| $OH + H_2 = H_2O + H$ | 2.2 | E13 | 0 | 2.57 | E3 |
| $O + H_2O = OH + OH$ | 6.8 | E13 | 0 | 9.26 | E3 |
| $O + H_2 = H + OH$ | 1.8 | E10 | 1.0 | 4.48 | E3 |
| $H + O_2 = O + OH$ | 2.2 | E14 | 0 | 8.46 | E3 |
| $OH + M = O + H + M$ | 8.0 | E19 | -1.0 | 5.221 | E4 |
| $O_2 + M = O + O + M$ | 5.1 | E15 | 0 | 5.791 | E4 |
| $H_2 + M = H + H + M$ | 2.2 | E14 | 0 | 4.833 | E4 |
| $H_2O + M = H + OH + M$ | 2.2 | E16 | 0 | 5.287 | E4 |
| $CO + OH = H + CO_2$ | 1.5 | E7 | 1.3 | -0.40 | E3 |
| $CO + O_2 = CO_2 + O$ | 3.1 | E11 | 0 | 1.893 | E4 |
| $CO + O + M = CO_2 + M$ | 5.9 | E15 | 0 | 2.06 | E3 |
| $H_2O_2$ Mechanism | | | | | |
| $M + H_2O_2 = OH + OH + M$ | 1.2 | E17 | 0 | 2.291 | E4 |
| $H_2O_2 + OH = H_2O + HO_2$ | 1.0 | E13 | 0 | 0.91 | E3 |
| $HO_2 + HO_2 = H_2O_2 + O_2$ | 1.0 | E13 | 0 | 0.50 | E3 |
| $HO_2 + OH = O_2 + H_2O$ | 5.0 | E13 | 0 | 0.50 | E3 |
| $HO_2 + O = O_2 + OH$ | 5.0 | E13 | 0 | 0.50 | E3 |
| $HO_2 + H = OH + OH$ | 2.5 | E14 | 0 | 0.96 | E3 |
| $HO_2 + H = O_2 + H_2$ | 2.5 | E13 | 0 | 0.35 | E3 |
| $HO_2 + H_2 = H_2O_2 + H$ | 7.3 | E11 | 0 | 9.42 | E3 |
| $H + O_2 + M = HO_2 + M$ | 1.5 | E15 | 0 | -0.50 | E3 |
| $HO_2 + CO = CO_2 + OH$ | 1.5 | E14 | 0 | 1.193 | E4 |

Four are given on the attached Tables 3.5.1 to 3.5.4, while the remaining two are referenced to the literature. The models we have chosen for use are given in Tables 3.5.2 and 3.5.4.

The global kinetics model for hydrocarbon fuels that was identified from the literature and adapted for use in kerosene flames is given in Tables 3.5.1 to 3.5.4. A number of more detailed models for heavy hydrocarbons were reviewed for potential use as a check on the global model. A parametric study of representative $GO_2$/hydrocarbon flame solutions was obtained for fuels similar to kerosene. Methods for coupling the hydrogen with the hydrocarbon analysis have also been identified to enable computations of the tri-propellant problem. Finally, a grid system has been chosen for the drop problem.

## Table 3.5.4. RP-1/$H_2$ Multi-Step Global Combustion Kinetics Model

| GLOBAL MECHANISM | A | B | E/R | POWER DEPENDENCIES |
|---|---|---|---|---|
| RP-1 | | | | |
| $C_{13}H_{28} \rightarrow 6.5\ C_2H_4 + H_2$ | 1.0473 E12 | 0 | 3.5229 E3 | $[C_{13}H_{28}]^{1.0}$ |
| $C_{13}H_{28} + 6.5\ O_2 \rightarrow 13\ CO + 14\ H_2$ | 1.2900 E9 | 1 | 2.5160 E4 | $[C_{13}H_{28}]^{0.5}[O_2]^{1.0}$ |
| $C_{13}H_{28} + OH \rightarrow 6.25\ C_2H_4 + 0.5\ CO +$ | 2.0000 E17 | 0 | 1.4919 E4 | $[C_{13}H_{28}]^{1.0}[OH]^{1.0}$ |
| $0.5\ H_2O + H_2$ | 1.7982 E10 | 0 | 3.5000 E4 | |
| $C_{11}H_{14} \rightarrow 5.5\ C_2H_2 + 1.5\ H_2$ | 4.4963 E9 | 1 | 2.6785 E4 | $[C_{11}H_{14}]^{1.0}$ |
| $C_{11}H_{14} + 5.5\ O_2 \rightarrow 11\ CO + 7\ H_2$ | 1.4721 E17 | 0 | 1.4510 E4 | $[C_{11}H_{14}]^{0.5}[O_2]^{1.0}$ |
| $C_{11}H_{14} + OH \rightarrow 5.25\ C_2H_2 + 0.5\ CO +$ | | | | $[C_{11}H_{14}]^{1.0}[OH]^{1.0}$ |
| $0.5\ H_2O + 1.25\ H_2$ | | | | |
| Secondary Fuel | | | | |
| $C_2H_2 + 6\ OH \rightarrow 4\ H_2O + 2\ CO$ | 4.7850 E15 | 0 | 1.3883 E4 | $[C_2H_2]^{1.0}[OH]^{1.0}$ |
| $C_2H_2 + 2\ OH \rightarrow 2\ CO + 2\ H_2$ | 2.8000 E16 | 0 | 0 | |
| $C_2H_4 + 6\ OH \rightarrow 2\ CO + 2\ H_2O + H_2$ | 2.2020 E15 | 0 | 1.2079 E4 | $[C_2H_2]^{1.0}[OH]^{1.5}$ |
| $C_2H_4 + 2\ OH \rightarrow 2\ CO + 3\ H_2$ | 2.1129 E27 | -3.0 | 6.3062 E3 | $[C_2H_4]^{1.0}[OH]^{1.0}$ |
| $C_2H_2 + O_2 = 2\ CHO$ | 4.0000 E12 | 0 | 1.4092 E4 | |
| $C_2H_4 + M = C_2H_2 + H_2 + M$ | 2.0893 E17 | 0 | 3.9810 E4 | $[C_2H_4]^{1.0}[OH]^{1.5}$ |
| | | | | $[C_2H_2]^{1.0}[O_2]^{1.0}$ |
| | | | | $[C_2H_4]^{1.0}[M]^{1.0}$ |
| Soot Reactions | | | | |
| $\left\{\begin{matrix} C_{13}H_{14} \\ C_9H_{11}OH \\ C_{12}H_{16} \end{matrix}\right\} = HC \bullet$ soot | -4.0465 E17 * | -2.0 | 1.6110 E4 | $[HC]^{1.43}[O_2]^{-0.5}$ |
| $soot + O_2 \rightarrow CO_2$ $\quad [soot] = -12 P_{O_2} A_t \left[\frac{K_A X}{1+K_Z P_{O_2}} + K_B^{(1-X)}\right]$ | | | | |
| $X = \left[1+K_T/(K_B P_{O_2})\right]^1$ | | | | |
| $K_i = A_i \exp\{-E_i/RT\},\ 1 = A, B, T, Z$ | | | | |
| i = A | 2.0000 E1 | 0 | 1.5090 E4 | |
| B | 4.4600 E-3 | 0 | 7.6490 E3 | As indicated by the equation for |
| C | 1.5100 E5 | 0 | 4.8820 E4 | [soot] |
| D | 2.1300 E1 | 0 | -2.0630 E3 | |

where $A_t = 6(C_s/\rho_s \bullet D_s)$ $\left(cm^2\ surface/cm^3\right)$ $P_{O_2}$ = partial pressure of $O_2$ (atm),

$C_s = \left(g \bullet soot/cm^3\ of\ gas\right)$ $\rho_s = \left(g \bullet soot/cm^3\ of\ soot\right)$ $D_s$ = diameter of soot (cm),

[soot] = mass of soot/volume of gas ($g/cm^3$).

* Sign on A indicates rate of formation of soot

**Table 3.5.4 (continued). RP-1/$H_2$ Multi-Step Global Combustion Kinetics Model**

| ELEMENTARY MECHANISM | A | B | E/R |
|---|---|---|---|
| Wet CO Mechanism | | | |
| $H_2 + O_2 = OH + OH$ | 1.7000 E13 | 0 | 2.4070 E4 |
| $OH + H_2 = H_2O + H$ | 2.1900 E13 | 0 | 2.5900 E3 |
| $OH + OH = O + H_2O$ | 6.0230 E12 | 0 | 5.5000 E2 |
| $O + H_2 = H + OH$ | 1.8000 E10 | 1.0 | 4.4800 E3 |
| $H + O_2 = O + OH$ | 1.2200 E17 | -0.91 | 8.3690 E3 |
| $M + O + H = OH + M$ | 1.0000 E16 | 0 | 0 |
| $M + O + O = O_2 + M$ | 2.5500 E18 | -1.0 | 5.9390 E4 |
| $M + H + H = H_2 + M$ | 5.0000 E15 | 0 | 0 |
| $M + H + OH = H_2O + M$ | 8.4000 E21 | -2.0 | 0 |
| $CO + OH = H + CO_2$ | 4.0000 E12 | 0 | 4.0300 E3 |
| $CO + O_2 = CO_2 + O$ | 3.0000 E12 | 0 | 2.5000 E4 |
| $CO + O + M = CO_2 + M$ | 6.0000 E13 | 0 | 0 |
| $H_2O_2$ Mechanism | | | |
| $M + H_2O_2 = OH + OH + M$ | 1.2600 E17 | 0 | 2.2900 E4 |
| $H_2O_2 + O_2 = HO_2 + HO_2$ | 3.9800 E13 | 0 | 2.1440 E4 |
| $H_2O_2 + H = H_2 + HO_2$ | 1.5850 E12 | 0 | 1.9120 E3 |
| $H_2O_2 + OH = H_2O + HO_2$ | 1.0000 E13 | 0 | 9.0600 E2 |
| $HO_2 + OH = O_2 + H_2O$ | 5.0100 E13 | 0 | 5.0300 E2 |
| $HO_2 + O = O_2 + OH$ | 5.0100 E13 | 0 | 5.0300 E2 |
| $HO_2 + H = OH + OH$ | 2.5000 E14 | 0 | 9.5630 E2 |
| $HO_2 + H = O_2 + H_2$ | 2.5100 E13 | 0 | 3.5230 E2 |
| $H + O_2 + M = HO_2 + M$ | 1.5800 E15 | 0 | -5.0340 E2 |
| $HO_2 + CO = CO_2 + OH$ | 1.0000 E10 | 0 | 0 |

The hydrocarbon fuel that is typically used as a rocket propellant is a type of kerosene with a typical average molecular weight of about 175 and effective composition given by $CH_{1.97}$. As is typical of hydrocarbon fuels, RP-1 is a mixture of many different types of hydrocarbons. At present we are treating it as a mixture of aliphatics and aromatics. Detailed kinetic mechanisms for polymers of this size have yet to be developed, so a global decomposition mechanism must be selected for the fuel.

The simplest approach is to use a single-step global decomposition mechanism as suggested by Westbrook and Dryer [69]. The single-step model (see Table 3.5.1) assumes full combustion to water and carbon dioxide and so does not give the proper heat release in most flames. The heat release can be adjusted for specific regimes to provide thermodynamically realistic results. This model has 5 species and 2 reactions.

A two-step model (Table 3.5.2) that includes an equilibrium $CO\text{-}CO_2$ reaction gives much improved heat release as it allows for the recombination of CO and $CO_2$, and so has been chosen as our "workhorse" model. This model has 6 species and 3 reactions. This model, however, omits the effects of the shifting equilibrium in the water reaction, while in addition, being insensitive to the presence of hydrogen as a second fuel. Accordingly, a more detailed model is required to model the role of hydrogen on the hydrocarbon combustion.

A first approach toward including the effects of hydrogen on the RP-1 flame is to include the elementary $H_2O_2$ and the wet CO reaction mechanisms as shown in Table 3.5.3. This reaction set again includes the global decomposition mechanism for the RP-1, while including the detailed effects of the presence of hydrogen. Because it omits the detailed decomposition of the fuel, some of the effects of hydrogen will be omitted, but it should give a reasonable representation. A similar model obtained from the work of Wang et al. [70, 71] has been used to obtain a similar detailed description of the water gas and hydrogen reactions, as given in Table 3.5.4. This model is currently the one chosen for most of the detailed combustion studies. Computations with this model are used to determine how the hydrogen affects the combustion process, and comparisons with the model in Table 3.5.2 show under which conditions this simpler model can be used.

In addition to the models given here, the ongoing work by Kundu [72] on jet engine fuels has resulted in two kinetics models, one with 16 species and the other with 8. Since these

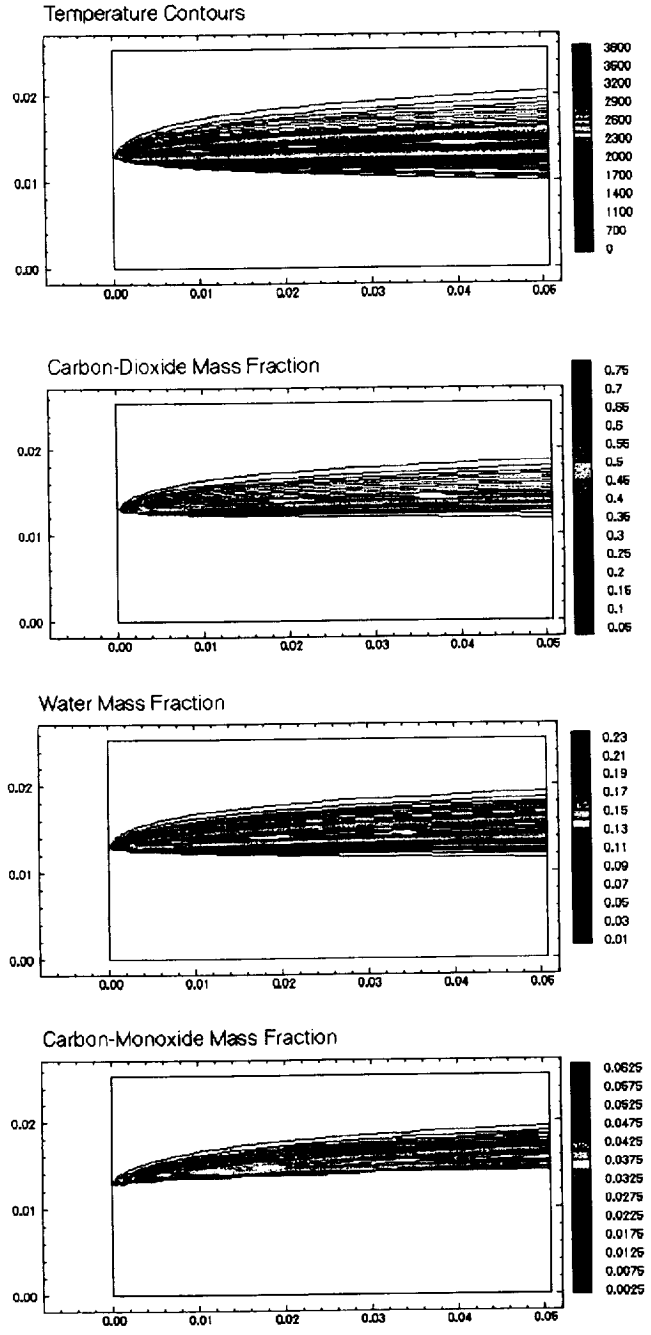


**Fig. 3.5.1. Representative laminar diffusion flame solution.**

include NO reactions as well, they can be simplified for use in the present rocket application. A brief assessment of these models ascertained that they provided no significant improvements in efficiency or accuracy over the models discussed above.

Finally, we note the more detailed models that have been used for methane-air CFD computation [73], and for one-dimensional methane and propane combustion modeling [74, 75]. These are too large in size to be considered for routine computations in the present analysis, but the results of more detailed analyses of this type can lead to improved global models [76].

A representative flowfield solution of a 2D, laminar diffusion flame with gaseous fuel and oxidizer is shown in Fig. 3.5.1. The two-step model (Table 3.5.2) with six species and three reactions was used in the computation. Temperature contours reveal a flame temperature of about 3600 K. The species contours indicate that small amounts of CO persist in the flame at this condition. In addition, several representative parametric studies of the effects of inlet gas temperatures, velocities and chamber pressure on the flame characteristics have been performed using the combustion model.

### 3.5.3. SINGLE RP-1 DROP COMBUSTION ANALYTICAL RESULTS

The effects of hydrogen addition on RP-1 combustion characteristics are addressed by studying isolated RP-1 drops in a convective environment. The idea is that if the combustion characteristics of a single drop are altered by the presence of hydrogen, these same changes would then very likely affect the spray combustion process in the engine. Understanding the role of hydrogen in the combustion mechanism, along with the recent empirical understanding of its mechanical role in altering drop size, should provide sufficient design intuition for later engine testing.

The approach followed is based primarily on CFD modeling of the drop combustion process, but a very important component of the study is a companion set of experiments. The CFD results are expected to provide the detailed understanding of the combustion process, while the experiments are used to establish their global validity. In addition to the CFD model, an analytical drop vaporization/ combustion model is also used.

The CFD model solves the complete Navier-Stokes equations coupled with species diffusion and finite-rate chemical kinetics for the combustion process. The simplified

hydrocarbon reaction set described in the previous section is used to describe the combustion. The complex mixture of hydrocarbon components that make up RP-1 is replaced by a single model hydrocarbon, $C_{13}H_{28}$, whose pyrolysis and combustion are treated by means of a global two-step reaction process. Transport properties of the gas are computed as functions of the local thermodynamic conditions and species concentrations. These properties include individual binary diffusion coefficients for each species. Because the conditions of interest correspond to small drops moving at relatively slow speeds with respect to the gas, laminar flow has been assumed. This, of course, amplifies the need for realistic molecular properties. The oxidizer is taken as gaseous oxygen.

The liquid phase is modeled as a spherical drop whose vaporization is controlled by the heat transfer from the burning gas phase. This non-distorted drop assumption is justified by an order of magnitude analysis for the conditions appropriate to the current work. In addition, this approximation was also verified directly from the experiments in which visual photography was used to monitor the rate of change of the burning drop. The interface between the liquid and the gas is treated by means of mass and energy balance boundary conditions. Convection inside the drop was ignored as it would most likely not impact the qualitative manner in which hydrogen affected the relative vaporization/ combustion rate.

We begin by presenting the results of CFD computations that replicate the conditions of the experiments. The comparison of these initial computations with the experimental results provides confidence in the computational results. The computations are then extended to a wide range of conditions with carefully controlled parametric changes so as to explain the experimental results and to further investigate the effects of hydrogen addition on a burning RP-1 drop.

The experiments described in Chapter 2 considered the combustion of a single drop of RP-1 in a flowing stream of gas. Two separate conditions were measured to detect the effects of hydrogen on drop combustion. First, the drop was burned in a pure oxygen stream to provide a reference condition. Then, drops were burned in co-flowing hydrogen-oxygen streams to deduce the changes caused by hydrogen addition.

### 3.5.3.1. CFD Comparisons with Experiments

The computations contain a wide range of O/F conditions from infinity through 32. The lower limit of this range is determined by the Japanese and Russian experiments that went up to hydrogen flow rates that were 10% of the RP-1 flow rate by mass. Three particular types of computation are considered. The first is the reference condition of an RP-1 drop in pure oxygen. The second series considers the combustion of an RP-1 drop in a pre-burned mixture of hydrogen and oxygen at several O/F levels. The third series attempts to compute the simultaneous combustion of hydrogen, oxygen, and RP-1, however, the reaction rate of hydrogen is so fast that the "simultaneous" combustion computations turn out to be sequential rather than simultaneous, and this third series degenerates to RP-1 burning in hydrogen-oxygen products. This step suggests that the only way that hydrogen can impact the combustion process in the engine is through changing the "ambient" conditions of the drops. Because the third series effectively degenerates to the second series and the pure oxygen environment of the first series is a special case of the second with the hydrogen content set to zero, most of our attention concerns the second series. Accordingly, we consider the combustion of an RP-1 drop in a flowing mixture of oxygen and oxygen-hydrogen combustion products. The percentage of hydrogen is varied parametrically starting from zero (pure oxygen). The effect of the hydrogen, then, is to increase the ambient temperature and to deplete slightly the oxygen mole fraction in the free-stream.

We begin by comparing the CFD predictions with the experimental measurements for the case of an RP-1 drop vaporizing in a convective environment of pure gaseous oxygen. As initial conditions, a 530 μm diameter RP-1 drop was introduced into a 300 K oxygen flowfield with a relative velocity of 1.33 m/s with respect to the drop. These conditions closely approximate those in the experiments and correspond to an initial drop Reynolds number of 42 based on the drop diameter, the relative velocity, and the far-field density and velocity. The drop measurement locations in the experiments are substantially downstream from the porous oxygen faceplate inlet, where the oxygen gas is essentially stagnant, so the relative velocity between the gas and the drop is equal to the drop velocity. This observation is verified by the measured velocity change of the drops in the experiments. Throughout the experiment, the drop velocity remains constant, but its diameter changes due to vaporization, so the Reynolds number

**Table 3.5.5. Summary of Flow Conditions for Computational Modeling Experiments.**

| Conditions | O/F | $d_o$ | $T_\infty$ | $u_{rel}$ | $\rho_\infty$ | $\mu_\infty$ | $Re_i$ | $\frac{d\left(\overline{d^2}\right)}{dt}_i$ |
|---|---|---|---|---|---|---|---|---|
| pure oxygen | $\infty$ | 530μm | 300 K | 1.33 m/s | $1.3\ \frac{kg}{m^3}$ | $2.18\cdot10^{-5}\ \frac{kg}{m-s}$ | 42.0 | $1.44\ \frac{mm^2}{s}$ |
| | | 350 μm | " | " | " | " | 27.8 | |
| | | 200 μm | " | " | " | " | 15.9 | |
| hydrogen/oxygen mixture | 80 | 250μm | 1566 K | 6 m/s | $0.22\ \frac{kg}{m^3}$ | $6.43\cdot10^{-5}\ \frac{kg}{m-s}$ | 5.08 | $1.51\ \frac{mm^2}{s}$ |
| | | 150 μm | " | " | " | " | 3.05 | |
| | | 100 μm | " | " | " | " | 2.03 | |
| pure oxygen | $\infty$ | 530 μm | 300 K | 6 m/s | $1.3\ \frac{kg}{m^3}$ | $2.18\cdot10^{-5}\ \frac{kg}{m-s}$ | 189 | $1.75\ \frac{mm^2}{s}$ |
| hydrogen/oxygen mixture | 128 | " | 1148 K | " | $0.34\ \frac{kg}{m^3}$ | $5.6\cdot10^{-5}\ \frac{kg}{m-s}$ | 19.3 | $1.45\ \frac{mm^2}{s}$ |
| | 32 | " | 2400 K | " | $0.19\ \frac{kg}{m^3}$ | $1.26\cdot10^{-5}\ \frac{kg}{m-s}$ | 4.8 | $1.7\ \frac{mm^2}{s}$ |
| hydrogen/oxygen mixture | 80 | " | 1566 K | 6 m/s | $0.22\ \frac{kg}{m^3}$ | $6.43\cdot10^{-5}\ \frac{kg}{m-s}$ | 10.3 | $1.51\ \frac{mm^2}{s}$ |
| | " | " | " | 1.33 m/s | " | " | 2.3 | $1.27\ \frac{mm^2}{s}$ |
| pure oxygen | $\infty$ | 200 μm | 300 K | 0.6 m/s | $1.3\ \frac{kg}{m^3}$ | $2.18\cdot10^{-5}\ \frac{kg}{m-s}$ | 7.2 | $1.08\ \frac{mm^2}{s}$ |
| | " | " | 1150 K | 6 m/s | $0.32\ \frac{kg}{m^3}$ | $5.3\cdot10^{-5}\ \frac{kg}{m-s}$ | 7.3 | $1.6\ \frac{mm^2}{s}$ |
| | " | " | 2400 K | 16 m/s | $0.16\ \frac{kg}{m^3}$ | $7\cdot10^{-5}\ \frac{kg}{m-s}$ | 7.3 | $2.2\ \frac{mm^2}{s}$ |

decreases with time. A summary of the experimental conditions for the RP-1/pure oxygen environment is given as the first entry in Table 3.5.5.

A history of the drop diameter squared as a function of time in the pure oxygen environment is shown in Fig. 3.5.2. As an approximation, the computations consider a series of fixed drop sizes that are treated in a quasi-steady fashion to obtain steady-state solutions. The instantaneous vaporization rates of a series of drop diameters can be expanded in a Taylor

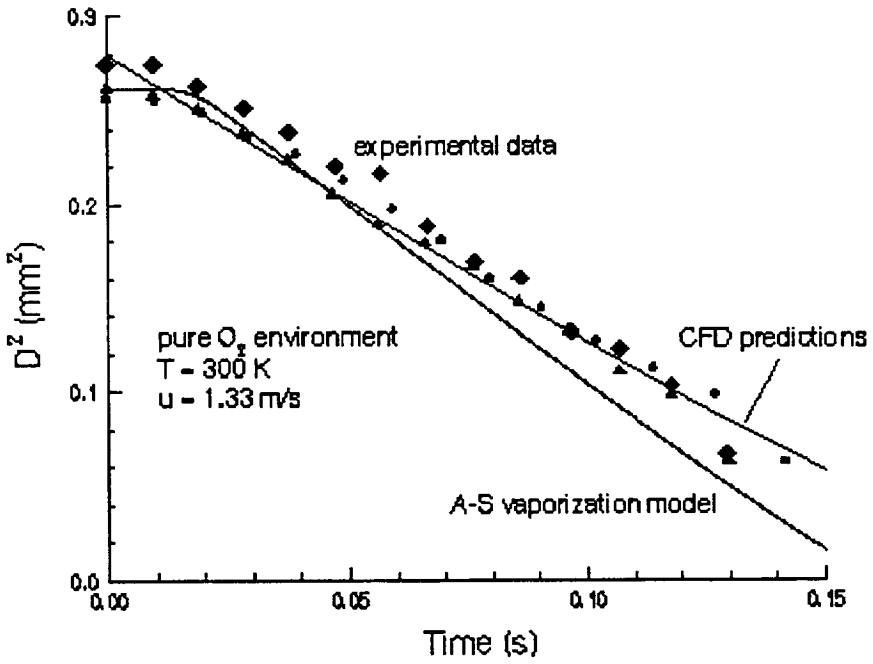


**Fig. 3.5.2. Comparison of analytical and experimental combusting single RP-1 drop diameter squared vs. time for a convective pure oxygen environment (O/F ratio = ∞). Experimental results are given by various symbols, and the detailed CFD results with Navier-Stokes/finite rate chemistry as well as the Abramzon-Sirignano vaporization model are indicated by the solid and dotted lines, respectively. The approximate averaged (numerical and analytical) curve slope = 1.44 mm$^2$/s; $d_i$ = 530 μm, $T_\infty$ = 300 K, u = 1.33 m/s, $Re_i$ = 42.**

series in time to obtain the drop time-history curves. The detailed CFD predictions are indicated by the solid line, and results predicted using the Abramzon-Sirignano vaporization model are given by the dotted line. The experimental measurements taken for a series of drop runs are indicated by numerous symbols. As the drops are introduced into the oxygen environment, they are initially ignited by a localized high temperature region. A flame zone surrounds the drop (at these Reynolds numbers which are less than 50) for the duration of the drop lifetime. A visualization of the flame sheath surrounding the drop is presented below. The heat released from the combustion between the vaporized RP-1 and the external oxygen in the flame zone vaporizes additional liquid fuel in a continuing cycle as the drop diameter gradually decreases in time. The agreement between the detailed CFD predictions, the simplified drop model calculations, and the experimental data is quite good. We do note, however, that the Abramzon-Sirignano predictions are highly sensitive to property values. For these predictions, a one-third averaging procedure has been employed and other choices give considerably different results.

The average value of the change in drop area as a function of time (slope of curves) determined from the CFD predictions is approximately 1.44 $mm^2/s$.

The measurements for the case of an RP-1 drop burning in a mixture of hydrogen and oxygen were conducted for a smaller RP-1 drop and a larger free-stream velocity than in the pure oxygen case. These changes were dictated by safety considerations. For the hydrogen-oxygen-RP-1 tests, the initial drop diameter was 250 μm (as compared to 530 μm for the pure oxygen case), and the relative velocity was 6 m/s (as compared to 1.33 m/s). The effective O/F ratio of the stream was 80. A summary of these operating conditions is provided as the second entry in Table 3.5.5. The temperature increase arising from the hydrogen combustion at O/F = 80 raises the temperature from 300 K in Fig. 3.5.2 to 1565 K here. This approximates the well-mixed flame temperature assuming complete combustion of the added hydrogen. This temperature corresponds well with preliminary experimental measurements of the gases in the drop chamber.

To model this experiment, we start by immersing the drop in a pre-burned mixture of hydrogen and oxygen at the same conditions as the experiment ($V_{rel}$ = 6 m/s, d = 250 μm, O/F = 80, and Re = 5). The primary effect of hydrogen in such a calculation is the density and viscosity change in the free-stream resulting from the temperature increase. This effect will be discussed shortly. The results of the CFD computations are compared with those of the experiments in Fig. 3.5.3. As for the pure oxygen results given in Fig. 3.5.2, these comparisons show the variation of the square of the drop diameter as a function of time. In addition, the predictions of the simplified Abramzon-Sirignano model are also included. As before, the experimental results are indicated by closed symbols, the CFD predictions are indicated by the solid line, and the Abramzon-Sirignano calculations are given by the dotted line. As can be seen, the agreement between the numerical computations and the experimental data is again good. The average numerical value for the change in drop area for the mixed hydrogen-oxygen case as a function of time is 1.51 $mm^2/s$, which is only marginally higher than the pure oxygen environment rate. This suggests that the hydrogen has little effect on the evaporation and combustion of the RP-1 drop. It is important to note, however, that the convective conditions between the pure oxygen vaporization environment and the premixed oxygen-hydrogen environment shown in Figs. 3.52 and 3.5.3 are not the same because of the difference in drop

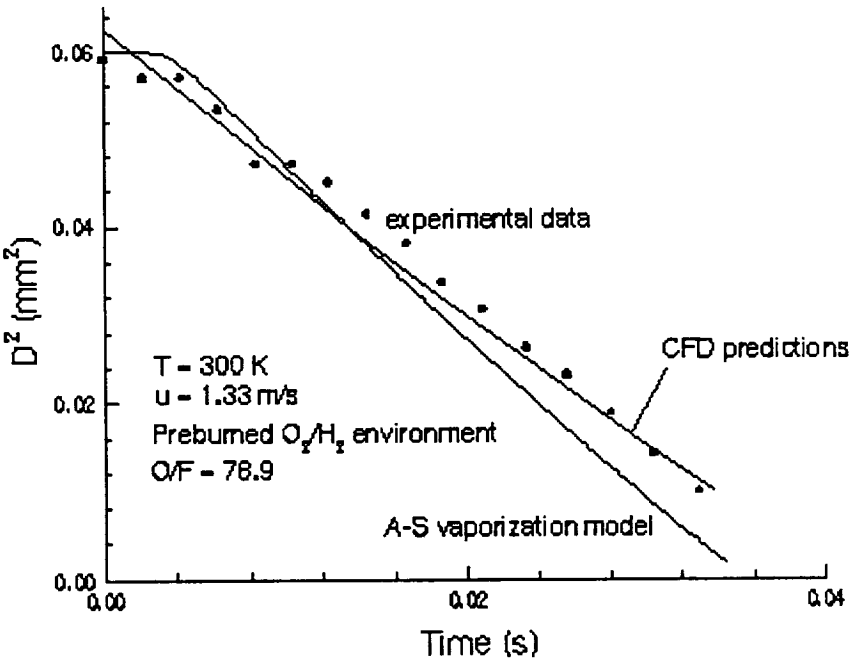


**Fig. 3.5.3. Comparison of analytical and experimental combusting single RP-1 drop diameter squared vs. time for a convective preburned oxygen/hydrogen mixture environment (O/F ratio = 80). Experimental measurements are given by symbols, and the detailed CFD results with Navier-Stokes/finite rate chemistry, as well as the Abramzon-Sirignano vaporization model are indicted by the solid and dotted lines, respectively. the approximate averaged (numerical and analytical) curve slope = 1.51 mm$^2$/s; $d_i$ = 250 μm, $T_\infty$ = 1566 K, u = 6.0 m/s, $Re_i$ = 5.**

velocity and Reynolds number. Additional computations to investigate this issue are presented shortly.

It is important to underscore the significance of the relationship between the CFD calculations and the experiments. The experimental measurements are invaluable in validating the CFD results that can then be used to conduct parametric studies of the effect of free-stream conditions on drop vaporization and combustion. Note that the agreement between the experiments and the CFD model is quite good for two very different convective environments. The fact that the CFD model and experiments match so well for both cases provides additional confidence in the accuracy of the numerical results and the experimental measurements.

### 3.5.3.2. Effect of Freestream Conditions on Reynolds Number

A comparison of the two experimental conditions summarized in Table 3.5.5 reveals the differences in the gas phase conditions and Reynolds number that exist during the drop lifetime.

It is interesting to note the observed close agreement in the surface regression rate between each of the conditions (both experimentally observed and numerically modeled) in spite of these variations in drop environment. This can be explained by a number of offsetting factors in the operating conditions that act to minimize differences in the global vaporization rate. The relative velocity ratio of 4.5 (6 m/s to 1.33 m/s), and initial diameter ratio of 0.47 (250 μm to 530 μm) were dictated by experimental safety conditions. The remaining differences in conditions arise either directly or indirectly from the freestream temperature ratio of 5.2 (1156K to 300 K) which results from the combustion of the added hydrogen with a small portion of the freestream oxygen.

For the current experiments, we are concerned primarily with O/F ratios greater than 50. Based on an ideal equation of state (which is valid under the present experimental conditions), the farfield density approximately exhibits a $\rho \sim 1/T$ dependence and the viscosity increases gradually based on a dilute gas temperature dependence as $\mu \sim T^{2/3}$. These relations are approximately true since molecular weight variations are minimized by the high O/F ratios. The gas density decreases dramatically while the dynamic viscosity increases for the experiment with hydrogen addition relative to the pure oxygen experiment. The density ratio and viscosity ratio between the hydrogen/oxygen mixture experiment and the pure oxygen experiment were 0.17 and 2.94, respectively (see Table 3.5.5). This indicates the Reynolds number of the experiment with hydrogen addition is substantially lower than that with pure oxygen. The overall Reynolds number dependence between the two experiments can be approximated as

$$\frac{Re_{mix}}{Re_{O_2}} = \frac{u_{mix}}{u_{O_2}} \frac{d_{mix}}{d_{O_2}} \left( \frac{T_{mix}}{T_{O_2}} \right)^{-5/3} \tag{3.5.1}$$

where Re is the drop Reynolds number, u and d are the drop relative velocity and diameter, and T is the freestream gas temperature. The subscripts mix and $O_2$ refer to the hydrogen/oxygen mixture and pure oxygen experiments described previously. Note that Eqn. 3.5.1 shows the strong Reynolds number dependence on freestream gas temperature. The relative velocity remains constant throughout each test, but the drop Reynolds number decreases in time because of the reduction in drop diameter as it vaporizes. Experimental results have shown almost no

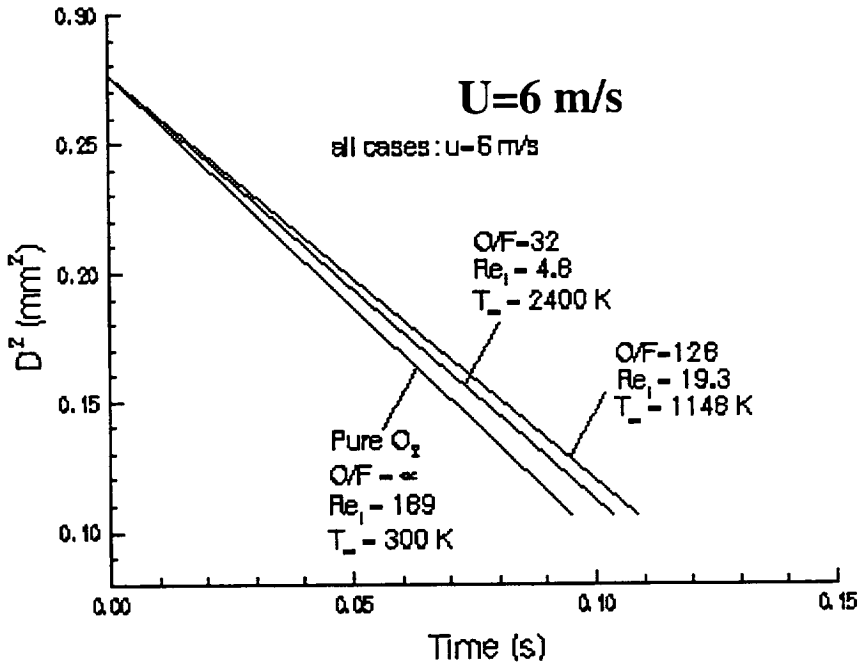


**Fig. 3.5.4. Effect of hydrogen addition (various O/F ratios) on drop diameter squared vs. time for a constant drop relative velocity of 6 m/s; pure oxygen (O/F ratio = ∞, $T_\infty$ = 300 K, $Re_i$ = 189) vs. an O/F ratio of 32 ($T_\infty$ = 2400 K, $Re_i$ = 4.8) and O/F ratio = 128 ($T_\infty$ = 1148K, $Re_i$ = 19.3).**

change in drop surface regression rate for the hydrogen-oxygen versus oxygen-only experiments, but the substantial change in Reynolds number between the two cases must be kept in mind.

Figure 3.5.4 presents computational results of drop lifetime as a function of various premixed O/F ratios using the detailed CFD model. The initial drop size is taken to be 530 μm with an initial velocity of 6 m/s (similar to the hydrogen/oxygen experiments with a large initial drop size). Three different farfield conditions are considered: O/F = ∞ (pure oxygen, $T_\infty$ = 300 K, $Re_i$ = 189); O/F = 32 ($T_\infty$ = 2400 K, $Re_i$ = 4.8); and O/F = 128 ($T_\infty$ = 1148 K, $Re_i$ = 19.3). Each line in Fig. 3.5.4 shows the variation of the square of the drop diameter in time. There is only a slight change in the drop lifetime for these cases where initial drop diameter and velocity are equal (but Reynolds number variations are significant). Both cases in which hydrogen addition is included vaporize slightly more slowly than the pure oxygen case, although the vaporization rate increases with temperature. This again suggests that the addition of hydrogen has little effect on vaporization and combustion of the RP-1 drop. This comparison corresponds closely to the physical situation within a combustion chamber system. In the

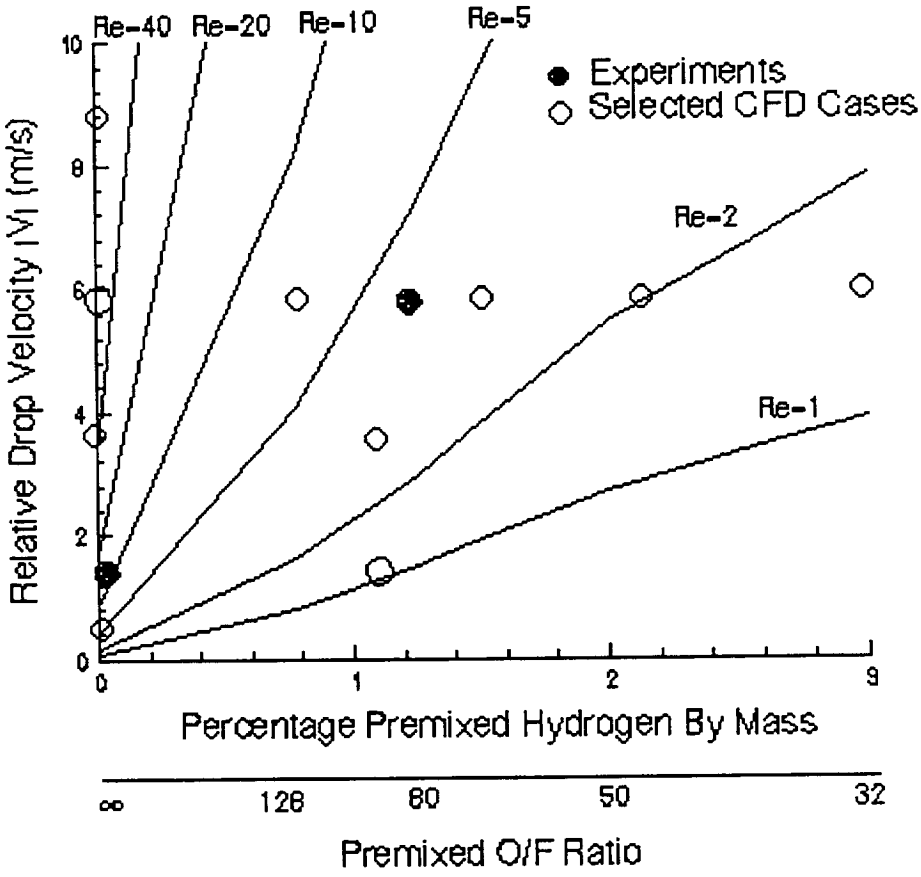


**Fig. 3.5.5. Drop Reynolds number dependence on relative velocity and pre-combusted O/F ratio for a 200 μm RP-1 drop. Symbols indicate experimental and selected computational conditions considered in current work.**

absence of hydrogen effects on atomization, both the drop size and velocity are fixed parameters, and the effect of hydrogen addition is to alter only the freestream environment by combustion.

Figure 3.5.5 shows the Reynolds number dependency between the relative velocity and premixed O/F ratio for a representative 200 μm RP-1 drop. Other sizes may change the magnitude but not the overall shape of the plot. The solid circle and crossed circle symbols indicate the conditions of the pure oxygen and hydrogen-oxygen experiments. Other symbols indicate different computational cases. Note that for a constant relative velocity, the drop Reynolds number decreases with increased hydrogen addition due to the density and property effects noted earlier. In order to follow a line of constant Reynolds number for different O/F ratios, the relative velocity must increase to counteract changes due to higher gas temperature.

### 3.5.3.3. CFD Flowfield Predictions

Noting these Reynolds number differences for the experimental conditions in Table 3.5.5, some of the details of the flowfields corresponding to the predictions in Figs. 3.5.2 and 3.5.3 are given in Figs. 3.5.6 and 3.5.7. These figures show the carbon dioxide mass fraction contours surrounding the drops at each of three instants during the drop lifetime. The carbon dioxide concentrations serve as a good indicator of the flame location. Figure 3.5.6 shows the flowfield surrounding the drop for the pure oxygen case of Fig. 3.5.2. From top to bottom, the $CO_2$ profiles correspond to the initial drop size, 500 μm, and two intermediate sizes, 350 μm and 200 μm. in all cases, the relative velocity is 1.33 m/s. The corresponding Reynolds numbers are 38, 28, and 16. The red regions indicate high concentrations of carbon dioxide at approximately the stoichiometric value of combustion between oxygen and the model hydrocarbon. As the drop gradually decreases in size, the wake region becomes smaller and the flowfield becomes more symmetric, approaching the Stokes limit. At all three Reynolds numbers, the flame surrounds the drop and the overall size of the combustion envelope decreases with the drop diameter.

The carbon dioxide contours for the corresponding premixed hydrogen-oxygen conditions of Fig. 3.5.3 are given in Fig. 3.5.7. Again, three results are shown for these conditions: d = 250 μm, 150 μm, and 100 μm, corresponding to the initial drop size and two intermediate sizes in the experimental measurements. The relative velocity here is constant at 6 m/s, and the O/F ratio of the pre-burned convective stream is 80 (both conditions identical to the experiments). Again, the flame completely envelops the drop at all conditions, but qualitatively, the present hydrogen-oxygen results are quite similar to the pure oxygen results of Fig. 3.5.4.

The corresponding temperature contours for these six conditions (three drop sizes at each flow condition) are given in Figs. 3.5.8 and 3.5.9. Again, the results are qualitatively similar. Note freestream gas temperature is increased in the hydrogen/oxygen mixture to the combusted value of 1566 K. There is again clear evidence that the flame surrounds the drop at all conditions, with the high temperature gases restricted to the drop wake. Overall, however, we conclude that there are no significant differences in the flame structure around the drop when hydrogen is mixed with the oxidizer.

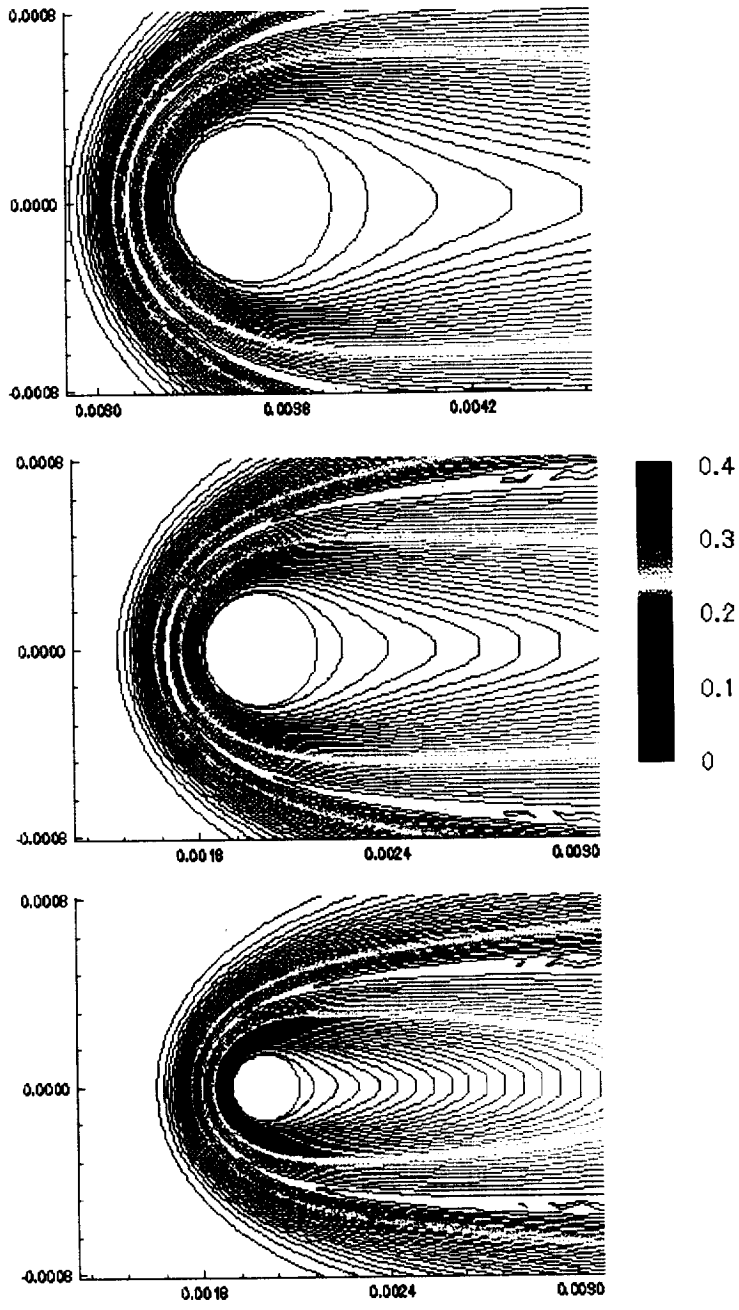


**Fig. 3.5.6. CFD computations of carbon dioxide mass fractions surrounding drops of 500 μm, 350 μm, and 200 μm (top to bottom figures) for the pure oxygen experimental conditions given in Fig. 3.5.2. The instantaneous Reynolds numbers are 39, 28, and 16 (with $u = 1.33$ m/s and $T_\infty = 300$ K). High $CO_2$ mass fractions serve as a qualitative indicator of flame location.**

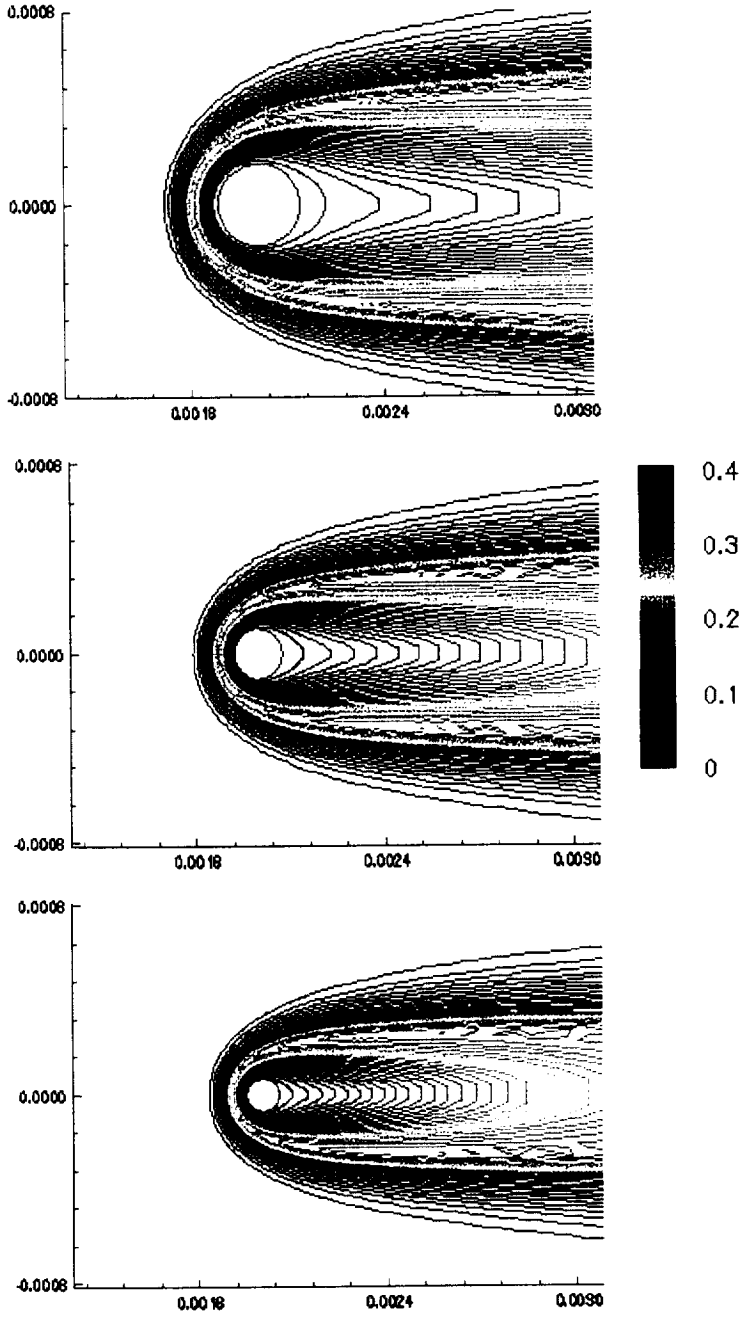


**Fig. 3.5.7. CFD computations of carbon dioxide mass fractions surrounding drops of 250 μm, 150 μm, and 100 μm (top to bottom figures) for the premixed O/F = 80 experimental conditions given in Fig. 3.5.3. The instantaneous Reynolds numbers are 5, 3, and 2 (with u = 6 m/s and $T_\infty$ = 1566 K).**

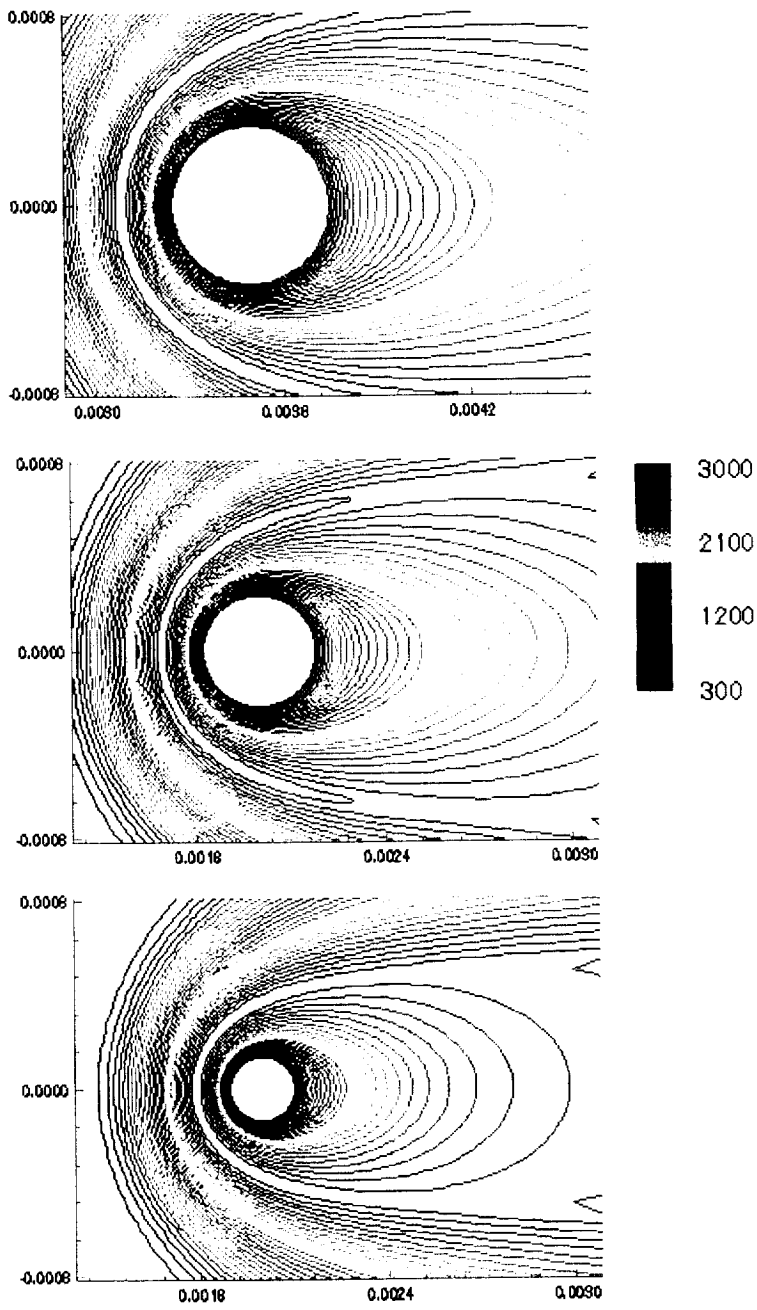


**Fig. 3.5.8. CFD computations of gas temperature surrounding drops of 500 μm, 350 μm, and 200 μm (top to bottom figures) for the pure oxygen experimental conditions given in Fig. 3.5.2. The Reynolds numbers are 39, 28, and 16 (with u = 1.33 m/s and $T_\infty$ = 300 K).**

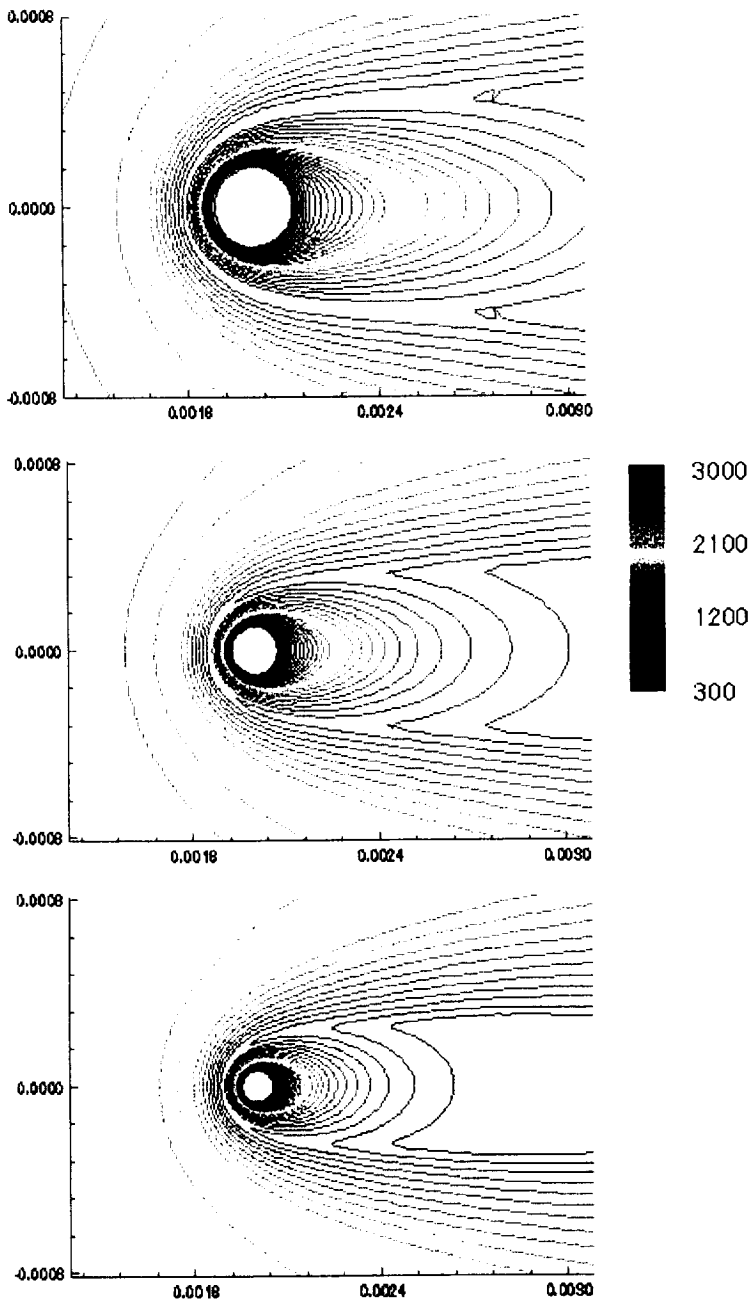


**Fig. 3.5.9. CFD computations of gas temperature surrounding drops of 250 μm, 150 μm, and 100 μm (top to bottom figures) for the premixed O/F = 80 experimental conditions given in Fig. 3.5.3. The Reynolds numbers are 5, 3, and 2 (with u = 6 m/s and $T_\infty$ = 1566 K). Note the freestream gas temperature in higher due to hydrogen addition.**

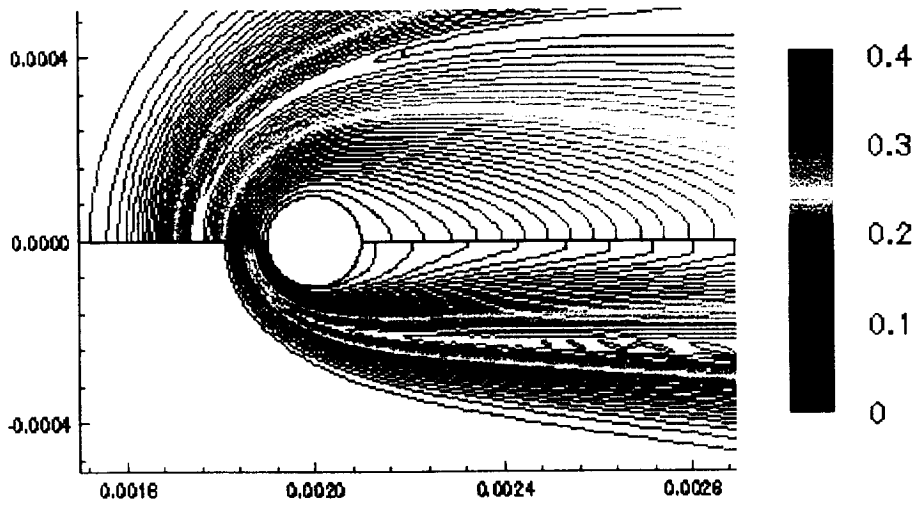


**Fig. 3.5.10. CFD computations of carbon dioxide mass fractions surrounding a 200 μm RP-1 drop at a Reynolds number of 7 for two different convective conditions: $T_\infty$ = 300 K, u = 0.6 m/s (top half) and $T_\infty$ = 1150 K, u = 6 m/s (bottom half). The higher temperature farfield is representative of an O/F ratio = 80. Closer flame location implies the effect of hydrogen addition on RP-1 drop vaporization and combustion is significant if considered at constant Reynolds number.**

The above results correspond to the experimental conditions, but because of limitations in the experiments, multiple parameters have been changed and these mask the physical changes that are taking place. To separate these effects, we compare in Fig. 3.5.10 the results of two computations at the same Reynolds number, but with different freestream temperatures. These are done using the full CFD computations. To minimize differences, we use pure oxygen for the oxidizer in both cases, but in the upper half of the figure, the temperature is 300 K, while in the lower half, it is 1150 K. Thus, freestream changes arise only from temperature, rather than from molecular weight or species concentration changes. This assumption is validated later. For this comparison, the diameters are both 200 μm, but the velocities differ by a factor of 10 to counterbalance the temperature change. In the upper portion of the figure, the velocity is 0.6 m/s, and in the lower portion, it is 6 m/s. Both conditions correspond to a Reynolds number of 7, which is approximately the conditions considered earlier. The carbon dioxide mass fractions are shown to obtain some qualitative idea of the flame position surrounding the drop.

This single parameter variation quickly shows the effect of changes in the freestream temperature. The higher temperature (bottom half) forces the flame much closer to the drop, reflecting the fact that the incoming gases do not have to be heated as much before combustion

starts. As a result of the flame being closer, the surface regression rate is considerably higher. The drop lifetime obtained from the computation with a freestream temperature of 1150 K is about 25% shorter than that for the 300 K case. An additional calculation at a freestream temperature of 2100 K showed a further decrease in drop lifetime.

These calculations with increased freestream temperature show that the drop behaves in qualitatively the same manner as it does when hydrogen is added. Thus, it appears that it is the freestream temperature change induced by the presence of hydrogen, and not the direct presence of hydrogen, that causes drop lifetime to decrease when hydrogen is added. The overall conclusion regarding the effect of hydrogen addition is therefore somewhat convoluted. The net effect is generally nearly zero, but there are two competing factors that result in this apparent lack of sensitivity to the presence of hydrogen, and one of these two effects is not what it seems. Adding hydrogen increases the freestream temperature and this indirect effect dramatically increases the vaporization rate and reduces the drop lifetime if the parametric range of drop Reynolds number is not changed. The actual presence of hydrogen has no effect apart from the temperature increase. This increase vaporization rate is, however, generally not seen under engine conditions or representative experiments because they, generally speaking, compare results at the same relative drop velocity, not the same drop Reynolds number. When experiments are conducted at the same pressure and flow conditions (apart from temperature) the drop relative velocity is approximately unchanged by the addition of hydrogen. The increased temperature and the changes in flowfield composition therefore result in a reduction in drop Reynolds number that approximately offsets the changes arising because of the freestream temperature. Higher freestream temperature increases the vaporization rate and draws the flame closer to the drop. Lower Reynolds numbers allow the flame to move away from the drop and the vaporization rate decreases. The two effects nearly counteract one another, and experimental observations report no change in the hydrodynamic flowfield including flame standoff distance, drop lifetime, and etc. The overall effects thus appear to be quite well understood.

As intimated above, the location of the flame in relation to the drop is determined by the thermodynamic state of the farfield gases (the temperature) and the hydrodynamic nature of the flowfield (the Reynolds number). The magnitude of the inertial and viscous terms impact the velocity field and the resultant fuel/oxidizer mixing, and are closely coupled in determining the flame standoff distance and shape. A more detailed summary of the flame structure and standoff

**Table 3.5.6. Flame Standoff Distance.**

| Gas Composition | d | Re | $R_{f/d}$ |
|---|---|---|---|
| Pure oxygen | 500 μm | 38.7 | 0.304 |
| O/F = ∞ | | | |
| $T_\infty$ = 300 K | 350 μm | 27.8 | 0.365 |
| U = 1.33 m/s | 200 μm | 15.9 | 0.502 |
| Hydrogen/oxygen Mixture | 250 μm | 5.08 | 0.290 |
| O/F = 80 | | | |
| $T_\infty$ = 1566 K | 150 μm | 3.05 | 0.373 |
| U = 6 m/s | 100 μm | 2.03 | 0.485 |

distance at the experimental conditions considered in Figs. 3.5.2 to 3.5.9 is presented in Table 3.5.6 for several representative drop diameters. The upper portion of Table 2 corresponds to the pure oxygen experimental conditions shown in Fig. 3.5.2 while the lower portion corresponds to the mixture of hydrogen and oxygen at O/F = 80 given in Fig. 3.5.3.

Table 3.5.6 includes three data points in time beginning with approximately the initial injected drop diameter and two intermediate drop sizes near the middle and at the end of the measured drop lifetimes under both experimental conditions. Also included are the instantaneous drop diameter, Reynolds number, and flame standoff distance at the front stagnation point of the drop non-dimensionalized by the instantaneous drop diameter. As noted earlier, the ambient conditions are dramatically different between each of the experimental conditions (see Table 3.5.5). In spite of these differences, however, the nondimensionalized flame standoff distance is nearly identical between each of the relative vaporization times, as can be seen in the last column of Table 3.5.6. This implies, therefore, that the drop heat transfer per unit area and surface regression rate are quantitatively the same in both of the experimental operating conditions. This explains the minimum differences in surface regression rate measured in the experiments despite the effect of hydrogen and combustion on the surrounding drop environment, which was observed in the experimental measurements.

In the above results, the impact of Reynolds number effects due to temperature and property variations have been noted. The two remaining issues affecting drop vaporization rate

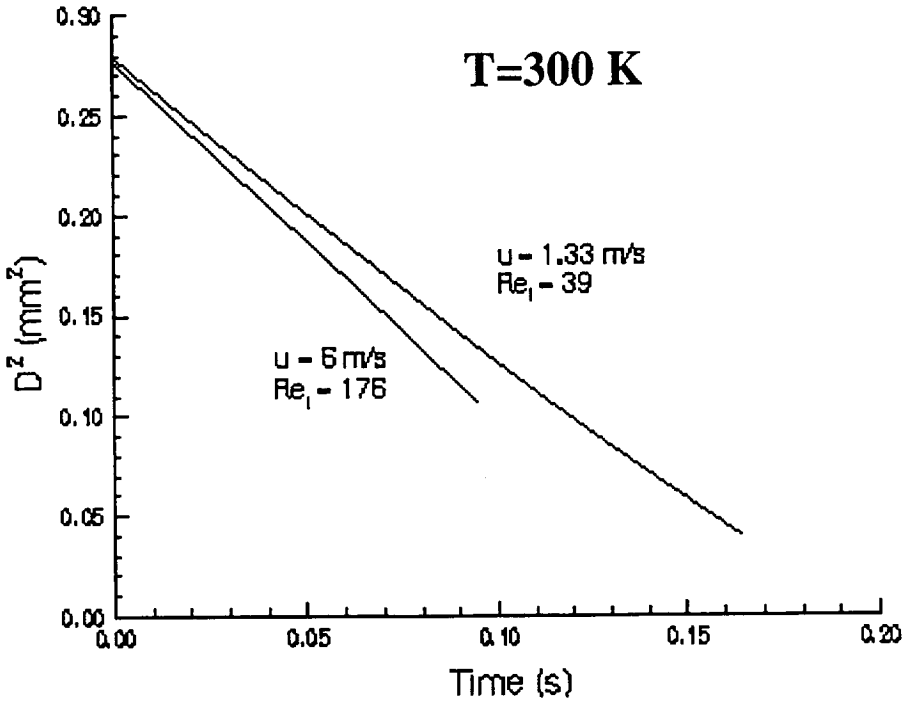


**Fig. 3.5.11. Comparison of CFD computations of RP-1 drop diameter squared vs. time for a convective pure oxygen environment (O/F Ratio = ∞, $T_\infty$ = 30 K, $d_i$ = 530 μm) for drop relative velocities of u = 1.33 m/s ($Re_i$ = 42) and u = 6 m/s ($Re_i$ = 189).**

and combustion are variations in relative velocity and species concentrations. These effects have been investigated using the complete CFD model and are shown in Figs. 3.5.11 and 3.5.12.

Fig. 3.5.11 shows the time history of the square of the drop diameter in a pure oxygen environment ($T_\infty$ = 300 K) for a 520 μm RP-1 drop injected with an initial relative velocity of 1.33 m/s and 6 m/s. These correspond to initial Reynolds numbers of 39 and 176, respectively. As expected, the increased convective effects due to the higher relative velocity increase the surface regression rate from an average value of 1.44 mm$^2$/s to 1.75 mm$^2$/s (approximately a 21% increase). Contour plots of the carbon dioxide mass fractions for this case are presented in Fig. 3.5.12. The upper half of Fig. 3.5.12 shows the solutions for the case where the drop relative velocity is 0.6 m/s ($Re_i$ = 7.4), while the lower half corresponds to a relative velocity of 6 m/s ($Re_i$ = 71.5). The instantaneous drop diameter for both cases is 200 μm and the freestream temperature is 300 K. The higher relative velocity (and higher Reynolds number) forces the flame closer to the drop surface so that the corresponding surface regression rate is substantially increased. This is reflected in the drop lifetime results shown in Figs. 3.5.11. Similar trends would be expected for different convective conditions.

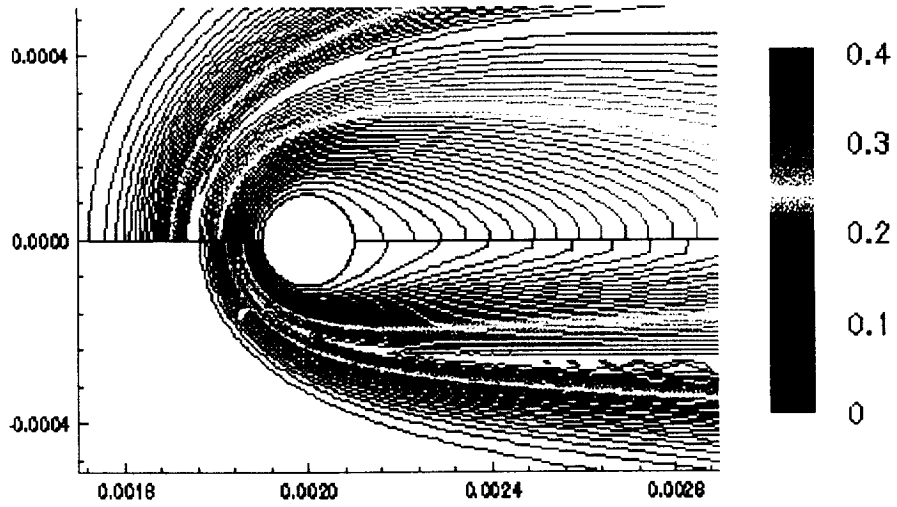


**Fig. 3.5.12. CFD computations of carbon dioxide mass fractions surrounding a 200 μm RP 1 drop in a pure oxygen environment (O/F Ratio = ∞) for two different convective conditions: u = 0.6 m/s (top half) and u = 6 m/s (bottom half). The Reynolds numbers are 7.4 and 71.5, respectively. Closer flame location at the higher relative velocity indicates increased RP-1 drop vaporization rate at higher relative velocities.**

A summary of the experimental and computational findings for drop vaporization rate as a function of Reynolds number and hydrogen addition (O/F ratio) are shown in Fig. 3.5.13. The horizontal axis shows the Reynolds number on a logarithmic scale and the vertical axis shows the vaporization rate normalized to the initial conditions of the hydrogen/oxygen experiments on a linear scale. Several parametric cases are shown using different symbols. Pertinent operating conditions are included in the figure legend. The overall general trend is that the magnitude of surface regression rate (equivalently the vaporization rate) increases with increasing Reynolds number at a uniform rate indicating a $d^2$-law dependence. The pure oxygen environment experiment is indicated by the solid square symbols, and the hydrogen-oxygen mixture experiment is given by the open diamonds. For each of these experiments, note that the magnitude of the vaporization rate is approximately equal (as noted earlier), in spite of the different initial and intermediate Reynolds numbers. For the case of constant Reynolds number, the drop vaporization rate increases dramatically with increasing hydrogen addition (decreasing O/F ratio). This can be noted by the progress from the open diamond symbols corresponding to an O/F ratio of 80 (1.25% hydrogen addition) to the open triangle symbols corresponding to an O/F ratio of 32 (3% hydrogen addition) (see legend in Fig. 3.5.13). This increase is somewhat larger than the effect of hydrogen addition at constant drop velocity, which more closely

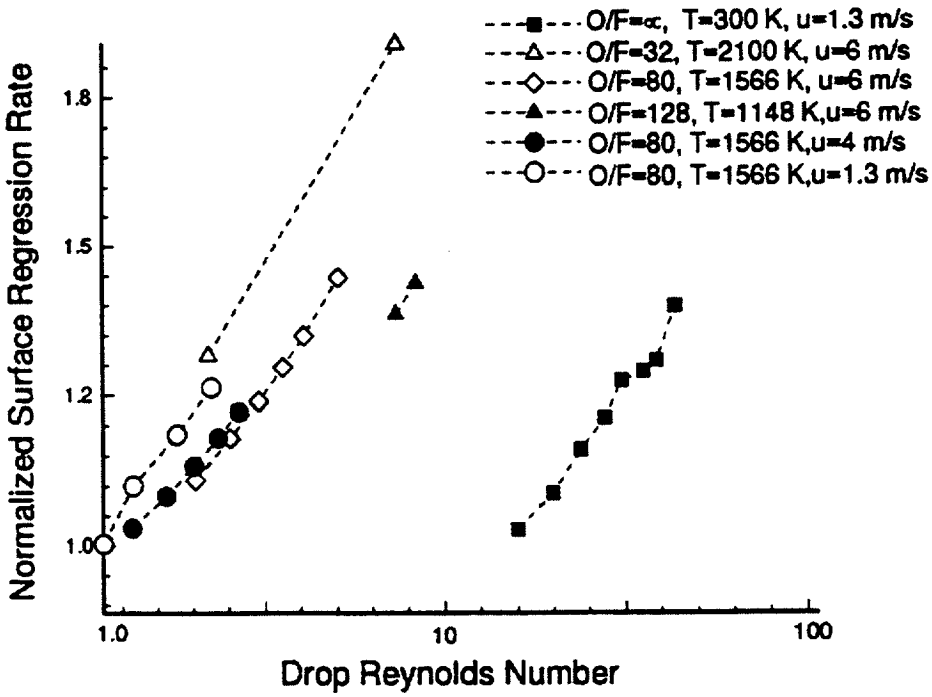


**Fig. 3.5.13. Parametric summary of normalized drop surface regression velocity as a function of drop Reynolds number for various freestream conditions.**

corresponds to the conditions that would be observed in practice. The velocity effects are apparent by comparing the conditions at an O/F ratio of 80 with relative velocities of 1.3, 4, and 6 m/s, respectively. This re-emphasizes the major conclusion that the effect of hydrogen addition on the vaporization and combustion of a single RP-1 drop significantly increases the vaporization rate based on hydrodynamic scaling at constant Reynolds number, but the effect is substantially less pronounced under the more physically realistic design parameter of fixed relative velocity.

## 3.6. ANALYTICAL STUDIES OF TRI-PROPELLANTS - HYDROGEN - RP-1 MANIFOLD ANALYSIS

Hydrocarbon fuel is attractive for an ETO propulsion mission because its energy density is higher than that of hydrogen. Hydrocarbon fuels permit a smaller tankage volume than does hydrogen and this reduction in size is particularly important during the lift-off phase of a launch mission. The sacrifice in specific impulse as compared to hydrogen, however, becomes increasingly important with velocity, and hydrogen eventually becomes the preferred fuel. Accordingly, a common compromise is to use hydrocarbon at lift-off and then transition to hydrogen in flight. This approach is common for booster-sustainer systems in staged vehicles where the two stages contain completely independent engines and fuel systems. A potential simplification that would provide the advantages of hydrocarbon fuel at lift-off and those of hydrogen later on is one in which a single engine would initially burn hydrocarbon fuel, and then switch to hydrogen. There are two potential approaches for achieving such a goal. In one, the engine has two completely separate fuel systems; one for hydrogen and the other for the hydrocarbon fuel. The shortcomings of such a system is that it is heavy, bulky and difficult to package. The second possibility is to flow the two fuels through the same fuel manifold and injectors in sequential fashion. Although this concept had been suggested at the start of the present Cooperative Agreement, the potential difficulties to be encountered in implementing it had not been considered in detail. The purpose of the present task was to identify in a qualitative sense the types of difficulties that might be encountered.

Originally the task was identified as a combined analytical-experimental task, but because of lessening interest in tri-propellant systems in industry; the task was deferred indefinitely in the realignment of November 1995. Prior to the realignment, some simple representative analyses of the dual-fuel, common manifold system had been completed. These initial results are summarized in the present section. The specific problem to be considered concerns the characteristics of the flowfield that would be encountered in the fuel manifold of a dual-fuel-engine using a common manifold. Specific issues of interest concerned heat transmission characteristics between the cryogenic hydrogen and the last vestiges of the hydrocarbon fuel, including physical characteristics at the interface between the two fuels and the effects of residual hydrocarbon left in the manifold.

### 3.6.1. BACKGROUND AND PARAMETER SIZING

The objective of the common manifold analysis was to identify the global characteristics of $H_2$/RP-1 common-manifold flows and to define an appropriate experimental configuration for experimental testing at a bench scale. The bench-top experiments were to be based conducted with a representative hydrocarbon such as RP-1, and liquid nitrogen to simulate the effects of cryogenic hydrogen. The dominant qualitative characteristics of this two-fluid transient were defined and a tentative geometry for initial testing was identified. These are discussed in this section.

To fix the key parameters in the dual-manifold problem, representative scales, flow rates and pressure drops were first estimated for typical liquid engines. Our analysis for the common manifold flows was limited to the fuel and oxidizer preburners in a full-flow cycle engine. These preburners give two different sets of conditions, both of which should be realistic. The sizes are based on a nominal 100,000-lb. engine.

The following strategy was used for fixing flow areas, injector sizes and flow rates. The oxidizer preburner was designed to operate at an O/F of 50 for RP-1 and an O/F of 160 for $H_2$. The fuel preburner was designed for O/F = 0.2 for RP-1 and O/F = .48 for $H_2$. The injector orifices were designed for an injector $\Delta p$ equal to 10% of the chamber pressure when operating on RP-1. The injector $\Delta p$ for hydrogen was then scaled up to the level necessary to get the required mass flow of $H_2$ through these same (RP-1) injector orifices. A summary of the design is given in Table 3.6.1.

### 3.6.2. REPRESENTATIVE CHARACTERISTIC TIMES

The global behavior of the flow in the manifold is governed by a series of characteristic times. The first of these is the manifold fill time, $\tau_{fill}$. This is a reference time that describes how long it takes to fill the manifold volume with hydrogen when it is flowing at its design flow rate. For a typical oxidizer preburner, where the manifold size is expected to be relatively large compared to the flow rate, the fill time is estimated to be about 70 milliseconds. For a fuel preburner where the flow rates would be much higher, but the manifold volume would be similar in size, the fill time is estimated to be only about 5 ms.

**Table 3.6.1. Preburner Sizes, Flow Rates and Pressure Drops for Common Manifold Analysis.**

| | Ox Preburner | | | | Fuel Preburner | | |
|---|---|---|---|---|---|---|---|
| | RP-1 | $H_2$ | $O_2$ | | RP-1 | $H_2$ | $O_2$ |
| $\dot{m}$ (lbm/s) | 4.0 | 1.5 | 240 | | 100 | 41.5 | 20 |
| # elements | 240 | 240 | 240 | | 100 | 100 | |
| $P_c$ (psia) | 4000 | 4000 | | | 4000 | 4000 | |
| Injector $\Delta p$ (psid) | 400 | 844 | | | 40 | 1035 | |
| Manifold Volume ($in.^3$) | 50 | 50 | | | 85 | 85 | |
| $\tau_{fill}$ (s) | $390\times10^{-3}$ | $70\times10^{-3}$ | | | $25\times10^{-3}$ | $5\times10^{-3}$ | |
| $\tau_{mixed}$ (s) | | $700\times10^{-3}$ | | | | $50\times10^{-3}$ | |
| $\tau_{recirc.\ outflow}$ (s) | | $170\times10^{-3}$ | | | | $14\times10^{-3}$ | |
| $\tau_{recirc.\ man.}$ (s) | | 5 | | | | 0.5 | |

Characteristic times for the switchover from kerosene to hydrogen in the manifold are clearly related to the manifold fill time, but also depend upon numerous other factors. While these can be estimated in various ways, two different methods have been used to make such estimates in the present work. The first is a lumped-parameter analysis based on a stirred-reactor mixing calculation, while the other involves using representative CFD computations. In both approaches, the hydrogen flow rate is turned on at time zero with an appropriate increase in pressure head corresponding to the injector pressure drop given in Table 3.6.1. The hydrogen then starts to flow into the manifold at a relatively slow rate that gradually increases to its steady state value as the residual kerosene is flushed out of the chamber. The characteristic times of interest are determined by the time required for hydrogen to flow out of the injector, or the time for the hydrogen concentration at a given location in the manifold to reach unity.

The characteristic time estimates based on the lumped-parameter analysis assume that the incoming hydrogen mixes instantaneously with the residual RP-1 in the manifold. We denote this time by $\tau_{mixed}$. The mass concentration of hydrogen leaving the injectors as a function of time is shown in Fig. 3.6.1. The time scale here is non-dimensionalized by the fill time $\tau_{fill}$.

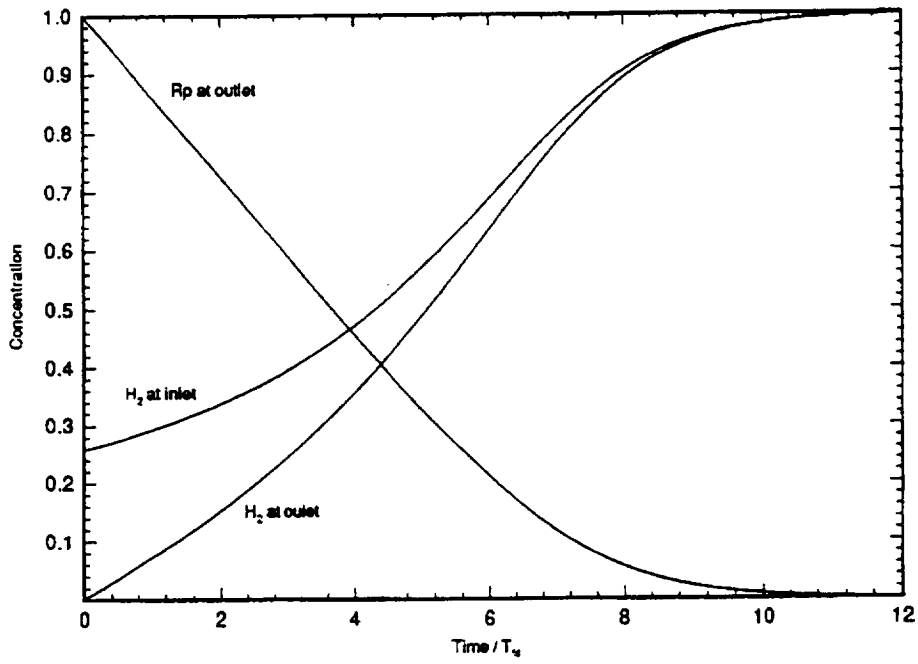


**Fig 3.6.1. Concentration of $H_2$ and RP-1 at both the inlet and exit. These results assume the hydrogen mixes instantaneously with the RP-1.**

These results show that it takes some 10 fill-times to reach full (95%) hydrogen flow in the instantaneously mixed case. Also included in Fig. 3.6.1 are plots of the hydrogen inflow rate and the RP-1 outflow rate as a function of time. These results show that the oxidizer preburner requires nearly a second, while the full preburner requires about 50 msec, to reach full hydrogen flow. These times indicate that experimental measurements, especially at the oxidizer preburner conditions, should be relatively straightforward. The characteristic times quoted are those for which the flow at the injector outlet reaches a concentration of 95% hydrogen. Since the fraction of hydrogen increases asymptotically, it takes correspondingly longer to reach pure hydrogen outflow. For this fully mixed calculation, the concentration at any point inside the manifold is always identically equal to the concentration at the exit, and so these two characteristic times are equal.

The characteristic flow times obtained from computational analysis include the effects of strong recirculation regions set up within the manifold as well as finite rate mixing between the two fluids. They do not, however, include the possible effects of small-scale 'fingering' at the interface that could possibly dominate mixing. These CFD computations are based on unsteady axisymmetric flow, and use a geometry and representative grid like that shown on Fig. 3.6.2 (a).

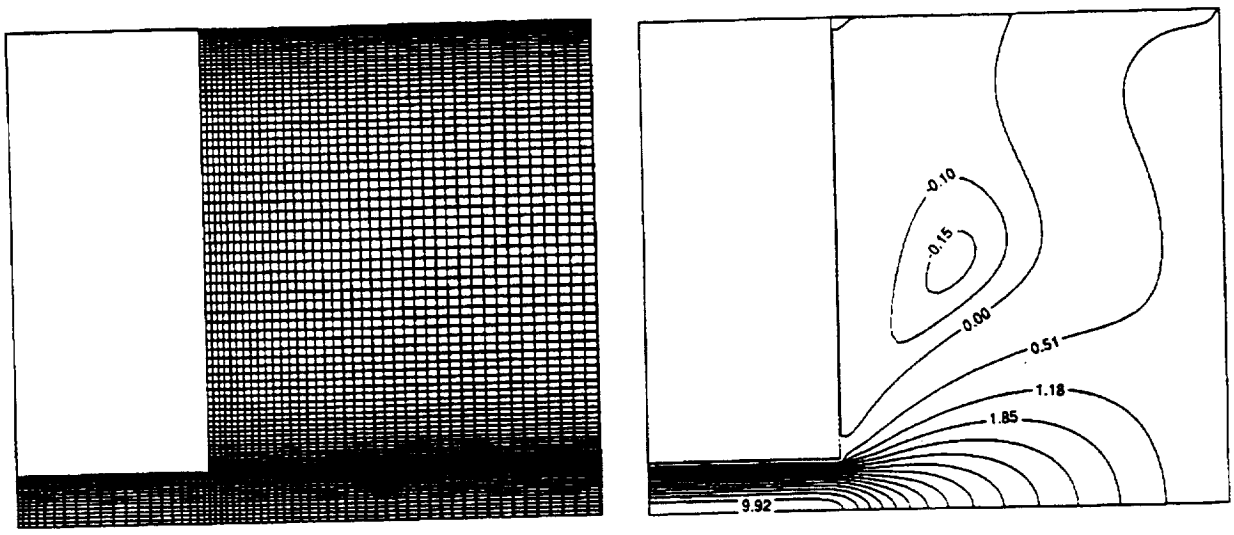


**(a) manifold geometry with grid** **(b) representative steady state flow**

**Fig. 3.6.2. Representative manifold grid and steady state flow conditions (for single fluid).**

To preserve axisymmetry, the manifold has a central feed and is shaped to match conditions in Table 3.6.1. Axial velocity contours for a representative steady flow condition (for a single fluid) is given on Fig. 3.6.2 (b). The flowfield pattern shown here proved to be rather difficult to set up, and because of the CPU requirements needed for these unsteady calculations, the results have been summarized from only a few runs.

The incorporation of finite mixing rates and recirculation effects causes the characteristic time required to reach 95% hydrogen at the outflow to differ sharply from the time to reach 95% hydrogen concentration at all points inside the manifold. As compared to the lumped-parameter estimates, the hydrogen concentration at the outlet reaches 95% in less time, while the concentration inside the manifold requires more time to get to 95%, especially inside the recirculation regions. Representative RP-1 concentration contours at four different times for the oxidizer preburner conditions are given in Fig. 3.6.3, while plots of the hydrogen concentration at several points inside the manifold and at the exit are given in Fig. 3.6.4 as functions of time. (The numbers at the various points in the top half of Fig. 3.6.4 indicate the location to which the concentration plots in the bottom half of the figure correspond.) The time for the outflow to change to 95% hydrogen is about 170 ms for the oxidizer preburner, while for the fuel preburner, it is about 15 ms. These numbers are given in Table 3.6.1 as $\tau_{recirc.}$ . The time required to
$outflow$

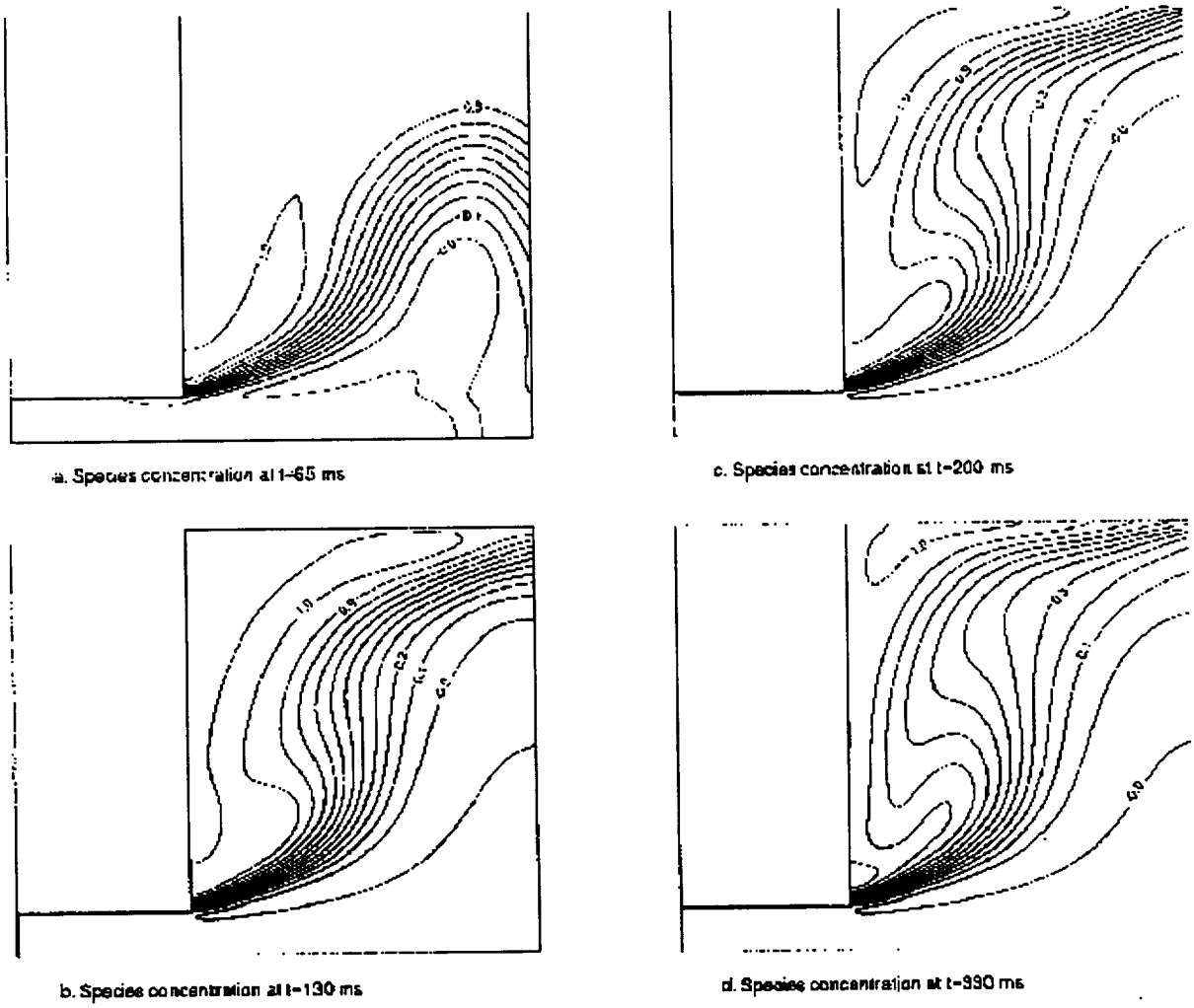


**Fig. 3.6.3. Representative RP-1 concentration contours at four different times**

reach 95% hydrogen inside the manifold varies strongly with location as the various curves on Fig. 3.6.4 show.

The numbers included in Table 3.6.1 have been estimated from solutions like those shown in Figs 3.6.3 and 3.6.4. This time constant, which is referred to as $\tau_{recirc.}$, describes the $_{man.}$ time to empty the manifold of residual RP-1. As can be seen from Fig. 3.6.4, this time is much larger than that required to reach a high percentage hydrogen flow at the outlet. These computations have been obtained for constant property fluids.

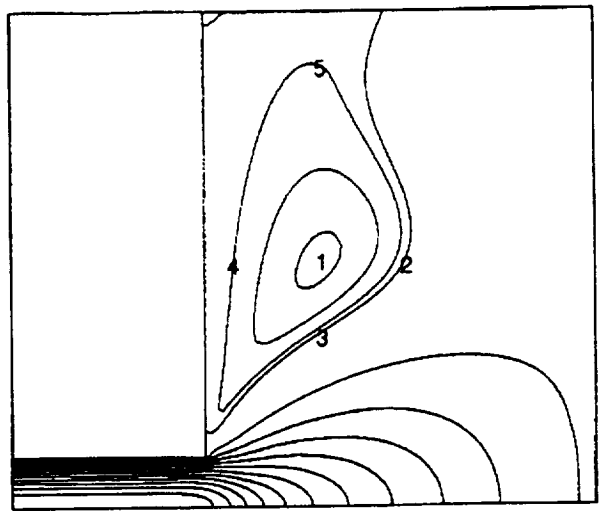


a. Velocity profile with measurement points.

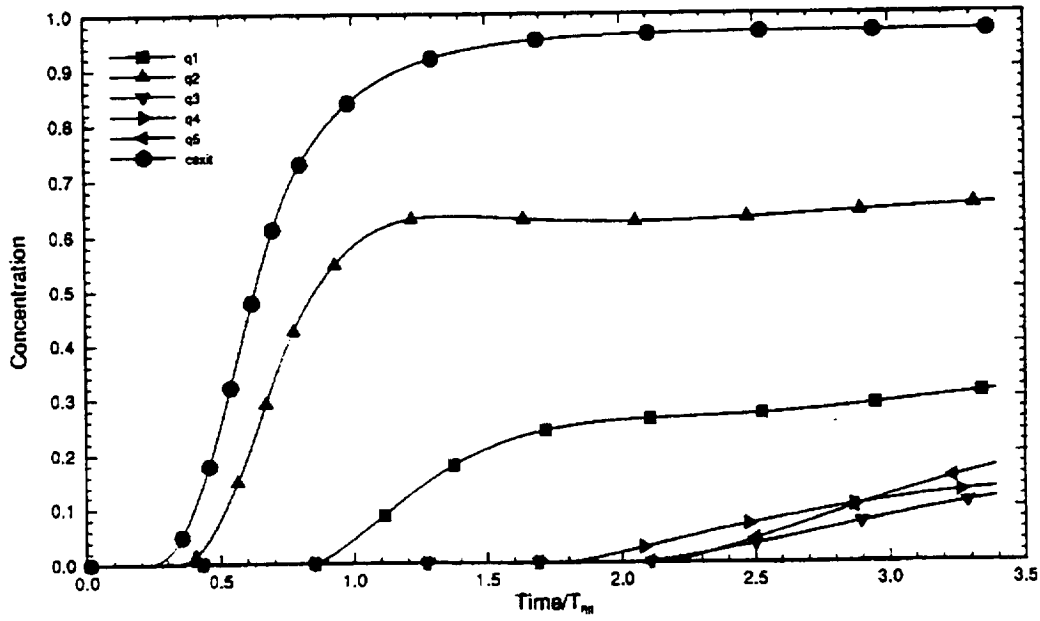


b. Concentration of $H_2$.

**Fig. 3.6.4. Hydrogen concentration in manifold.**

### 3.6.3. TENTATIVE BENCH-TOP EXPERIMENT

A tentative experimental configuration for testing the flow characteristics in a dual-fuel manifold was devised. A schematic of the configuration is shown in Fig. 3.6.5. The experiments were not conducted because of the realignment of the program as discussed in Chapter 1. However, a description of the intended experiments is provided here. Because the emphasis on

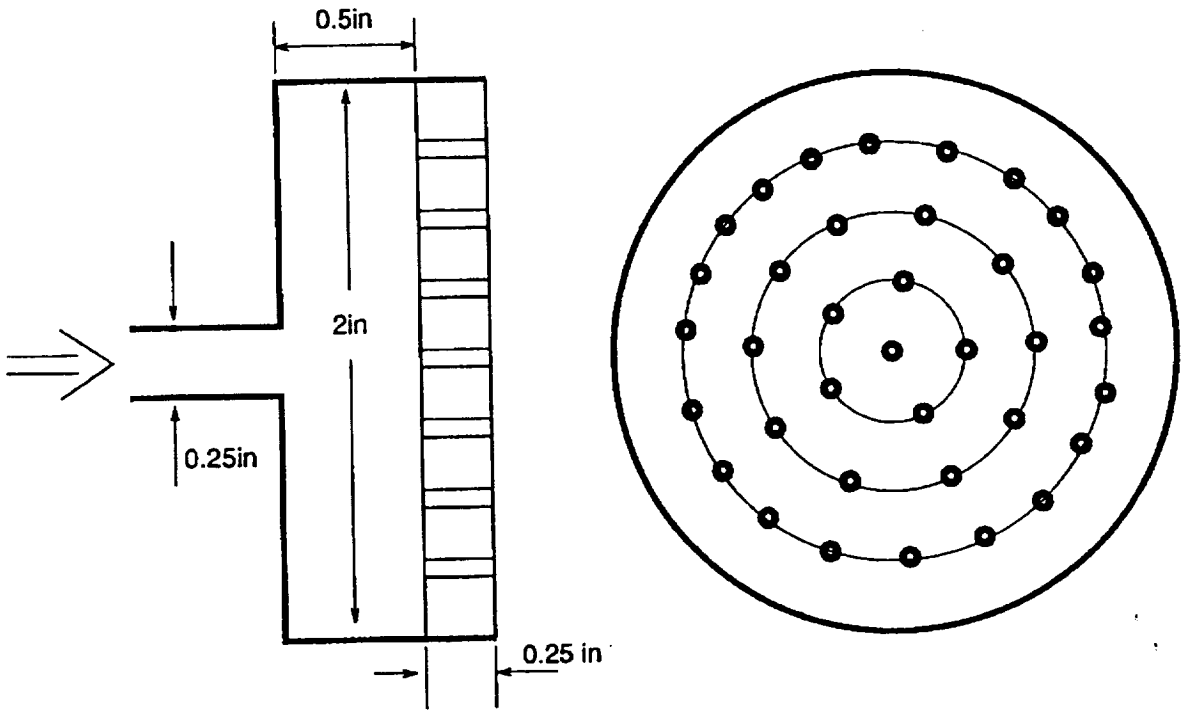


**Fig. 3.6.5. Proposed experimental configuration.**

this proposed experiment was intended to identify global characteristics of manifold flowfields, the experimental configuration, like the analysis, was chosen to be axisymmetric and to have a configuration analogous to the computational domain given in Fig. 3.6.1. The experiment was designed to use a central supply port feeding a cylindrical manifold with concentric rings of "injectors." This simplified experimental geometry would keep the flowfield simple enough that the dominant characteristics and controlling parameters could be identified. In addition, the axisymmetric geometry allows the analyses to be evaluated while also enabling the computational results to be used as an aid in understanding the experimental findings.

Because the characteristic times were expected to range from 100 milliseconds to a few seconds (as noted above), laser induced fluorescence (LIF) visualizations were intended as the primary diagnostic technique. Initial experiments involving the technique would use a combination of dyed and clear water for deducing the rate of decay of dye in the chamber as the clear water entered. Use of a fluorescent dye would enable simple quantitative measurements as well as qualitative pictures for use in understanding the flowfield and guiding the modeling.

## 3.7. OXYGEN RICH ROCKET COMBUSTION TECHNOLOGY—HIGH O/F DIRECT INJECTION ANALYSIS

This section begins by comparing LOX/$GH_2$ model predictions with experimental measurements from the uni-element rig. The primary purposes of these comparisons are to demonstrate how two-phase flow reacting models must be "calibrated" for applications to other situations. In these computations, we have compared drop-size predictions with measurements for both shear and swirl coaxial injectors, and, for the swirl injector, we have compared the predicted flame location with the experimental measurements.

The computational model used is a combination of our $GO_2/GH_2$ gas-gas model and the drop tracking model used for the downstream LOX injection. The initial mean drop size is obtained from experimental results, while the size distribution is taken as an upper limit distribution. (As noted in earlier publications, existing empirical correlations for drop size that have been developed from cold flow will provide drop size predictions ranging over several orders of magnitude, depending on the particular correlation chosen.) For the shear coaxial injector, the drop generation is distributed over an intact core region of about five LOX-post diameters, while for the swirl coaxial injector, the drops are all taken to originate from the inner corner of the LOX post. The observed intact core in the shear coaxial injector case extended through most of the length of the uni-element rig, but the predicted gas velocities beyond this distance were very low, suggesting very little drop stripping would take place there. Accordingly, a shorter intact core region was specified. The initial drop mean velocities for the shear coaxial injector were in the axial direction with a momentum per drop equal to that in the LOX post. A random 3-D perturbation ($u'$, $v'$, $w'$) of 10% of the mean was added to the initial velocity of each drop. Drop size was also specified randomly in a manner so as to give an upper limit distribution after many drops. Drop size and velocity were uncorrelated.

The initial drop velocities for the swirl coaxial injector were primarily oriented around the vicinity of the observed spray cone, but in keeping with experimental measurements, some drops were allowed inside the cone to fill the region near the axis. Again, the initial drop distributions were distributed around a mean corresponding to the axial plus swirl momentum of the liquid in the LOX post, the latter being deduced from the observed initial spray angle and

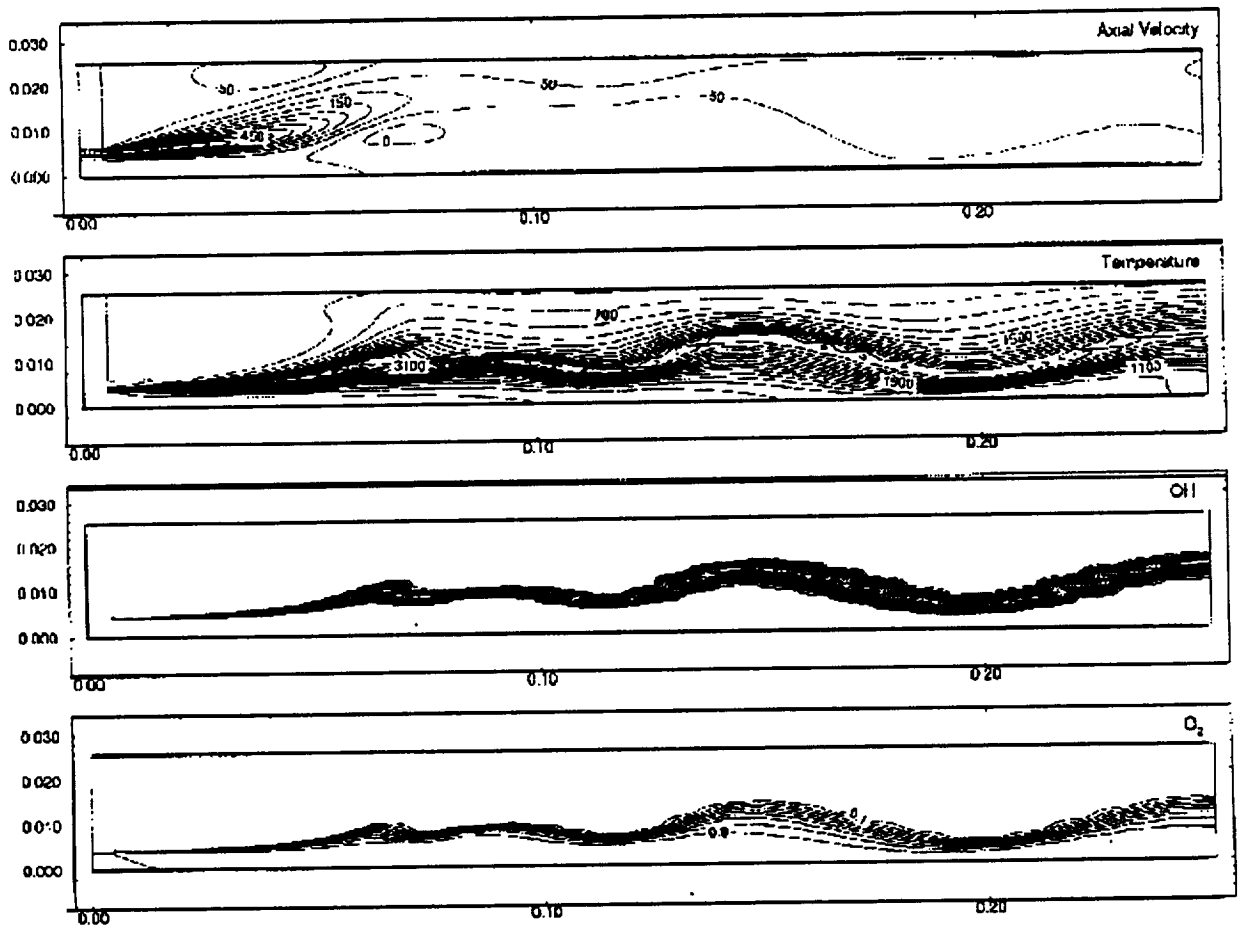


**Fig. 3.7.1. Calculated shear coaxial injector flowfield for LOX/$GH_2$ propellants at O/F=5.**

momentum arguments. Again, the initial velocity of each drop was chosen randomly about this mean (axial plus swirl), and the drop size and velocity were uncorrelated.

Representative results for the shear coaxial injector case are given on Figs. 3.7.1-3.7.5 for an O/F ratio of 5. Fig. 3.7.1 shows the predicted velocity, temperature, OH and $GO_2$ concentrations. The flame location is most aptly marked by the peak OH concentration which shows that the flame bulges away from the axis about 60 mm downstream of the injector faceplate. This apparently arises because the expansion produced by the upstream combustion forces the drops to move radially outward, taking the flame with them. The flowfield does, however, contain large scale unsteadiness that can also be seen in the figure. This unsteadiness has not been fully resolved in the computations, but has also been observed in the experiments. Comparison with gas-gas shear coaxial injector computations on Fig. 3.7.2 shows that the present LOX flame is noticeably further from the centerline than was the case with $GO_2$.

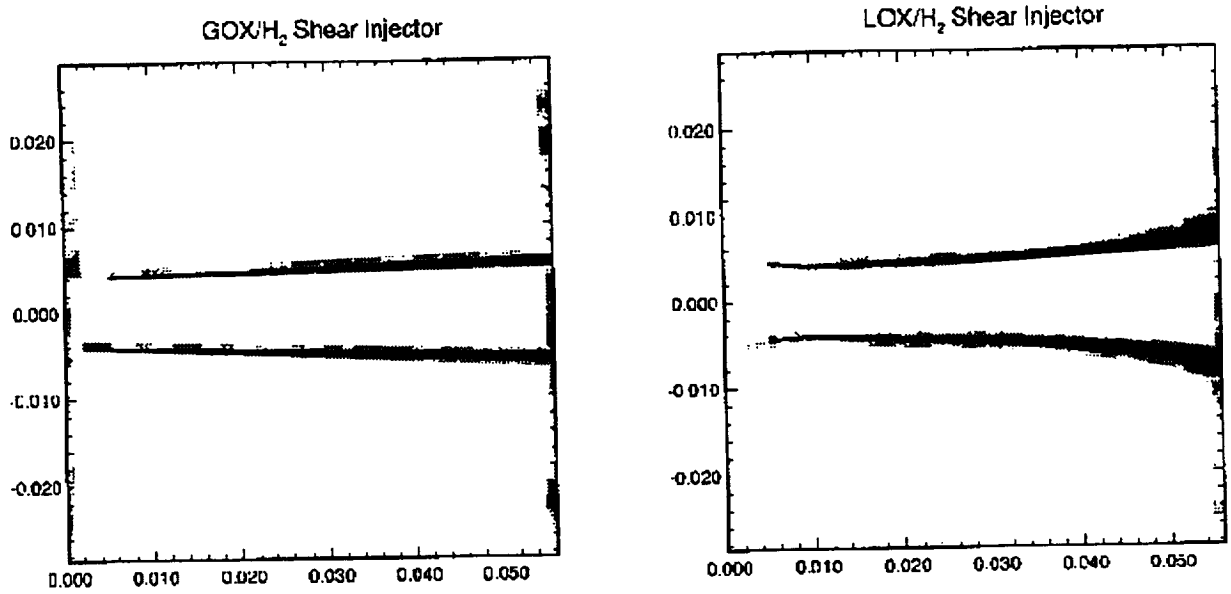


**Fig. 3.7.2. Computer flame fronts for $GO_2/GH_2$ and $LOX/GH_2$ shear coaxial injectors.**

Similarly, the large recirculation zone on the outer wall is fore-shortened by about a factor of two as compared to $GO_2$ calculations at similar O/F ratios. All in all, the LOX produces faster mixing than does the analogous $GO_2$ case.

Comparisons between the measured and predicted mean drop diameters (Sauter mean) at axial locations of 3 and 6 inches are given on Fig. 3.7.3. The predictions start from an initial

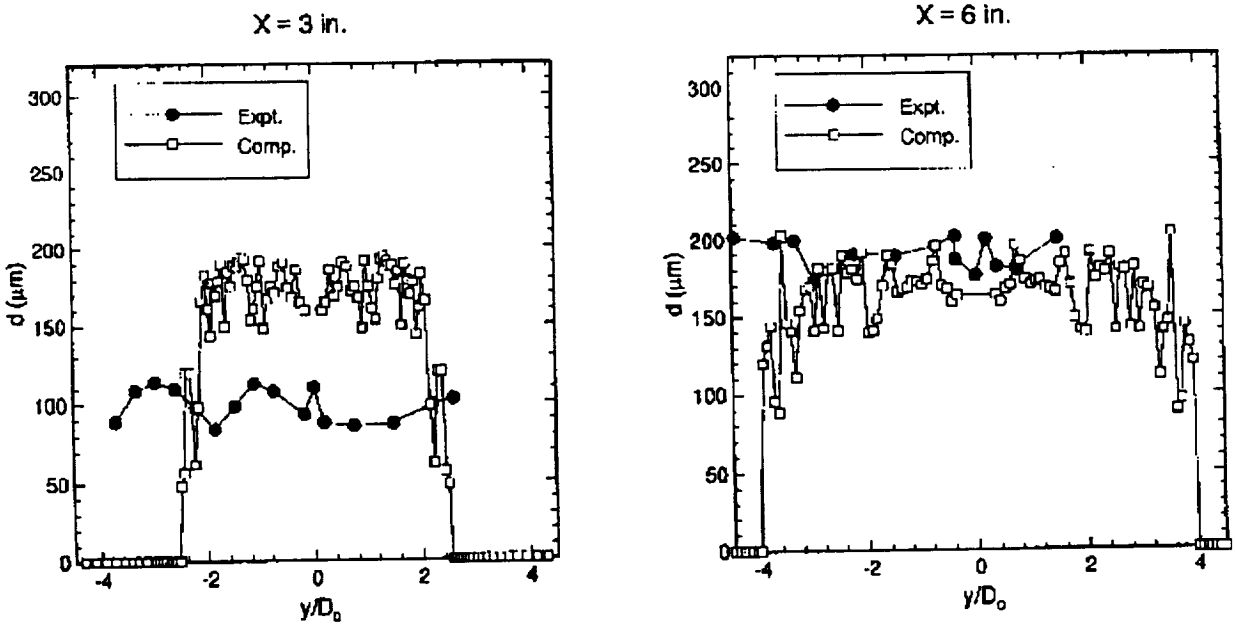


**Fig. 3.7.3. Radial variation of Sauter mean diameter ($D_{32}$) for $LOX/GH_2$ shear coaxial injectors operating at an O/F=5.**

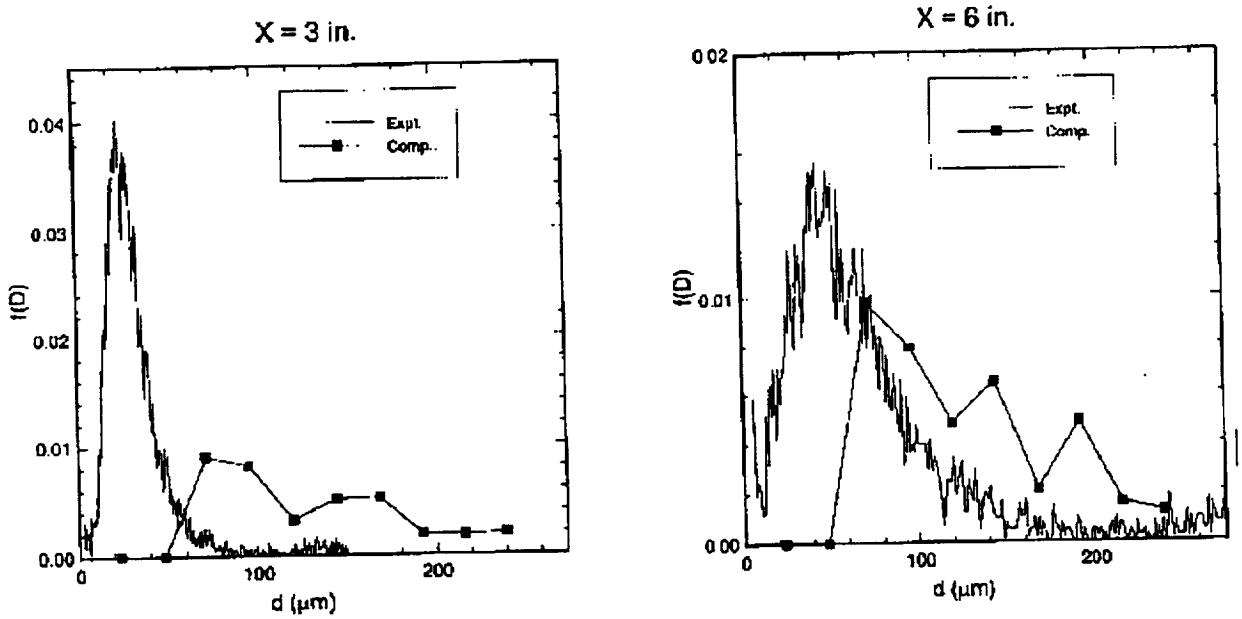


**Fig. 3.7.4. Comparison of drop size pdf between experimental and computational results. LOX/$GH_2$ shear coaxial injector at O/F=5. At each axial station, results are for r/D=1.48.**

drop diameter of 250 μm, and show a mean drop size of about 180 μm at x = 3 inches while the measurements indicate a size of about 100 μm at this same location. At x = 6 inches, the predicted drop size is nearly the same or perhaps slightly smaller at about 170 μm with a slight radial variation (larger drops near the centerline and smaller near the periphery). The experimental results indicate a mean drop size of about 180 μm at this position. Although

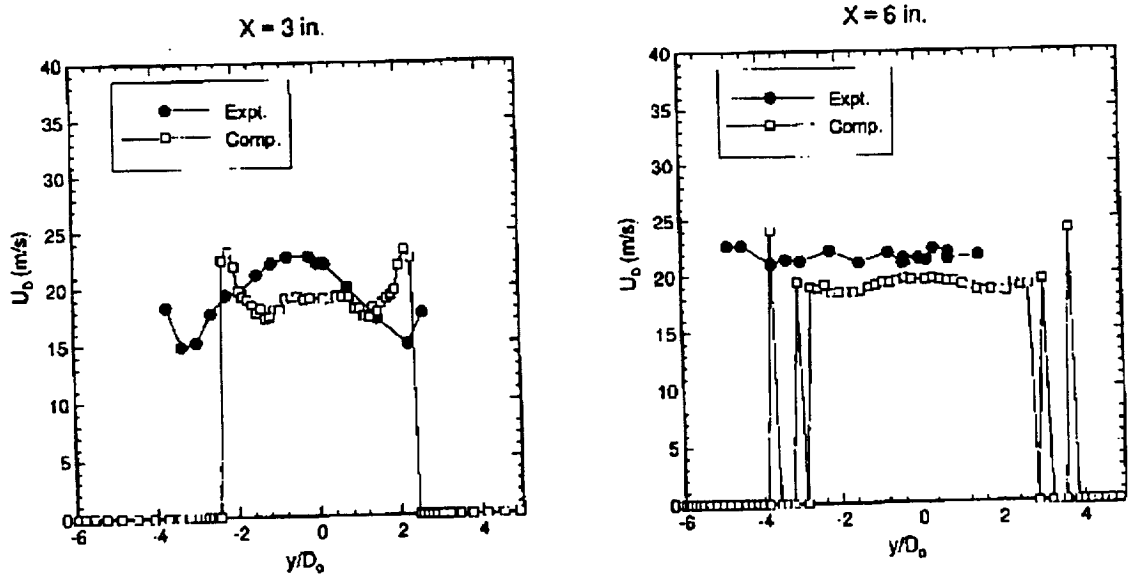


**Fig. 3.7.5. Comparison of drop mean velocity between experimental and computational results. LOX/$GH_2$ shear coaxial injector at O/F=5.**

the comparison at x = 6 inches is reasonable, it should be noted that the measurements at this station were in part used in choosing the initial drop sizes, so this agreement is more a calibration than a prediction. Unfortunately, the predicted trend with axial distance is opposite from experiment. A possible reason for the increasing drop size with distance in the experiment may be that many of the larger drops are non-spherical and so are rejected at x = 3 inches where the rejection rate is high (acceptance rate of about 25%). The higher acceptance rate at x = 6 inches suggests that this measurement may be more accurate. Representative comparisons with smaller initial drop sizes that matched the data at x = 3 inches (but were too small at x = 6 inches) were also computed. The flowfield results are only weakly dependent on the drop size.

The radial extent of the predicted drop locations in Fig. 3.7.3 is slightly smaller than that seen in the experiments, but, again, the amount of dispersion is primarily determined by the degree of randomness in the initial drop velocities. Additional comparisons of this type are given for the swirl coaxial injector case.

Fig. 3.7.4 compares the predicted and measured drop size distributions. At x = 6 inches, the comparisons are qualitatively correct, although the smaller drops (which are very plentiful in the experimental measurements) have all been vaporized and burned in the predictions. (Recall that the Sauter mean diameters for these two cases are approximately the same.) The results at x = 3 inches totally miss the small mean sizes observed in the experiment, as was noted above.

Finally, Fig. 3.7.5 shows the predicted drop mean velocities in comparison to the measurements. Here, the results are qualitatively accurate. Both experiment and prediction indicate a very small change in drop velocity with axial distance, and both give velocities in the 20 m/s range.

Results for the swirl coaxial injector are given on Figs. 3.7.6-3.7.9 for an O/F ratio of 20. Fig. 3.7.6 shows the velocity, temperature, OH and $GO_2$ concentration contours. As in the case of swirling gaseous oxidizer injection, the swirling LOX increases the flame width and decreases its length as compared to the shear coaxial injector case (compare with Fig. 3.7.1). The flame now moves farther from the centerline than in the shear coaxial injector case, a reflection of the centrifugal effects on the drop trajectories.

Drop size comparisons for this swirling LOX case are given on Fig. 3.7.7 (a). Here, data is available at only one axial station, x = 2 inches and has again been used as a calibration.

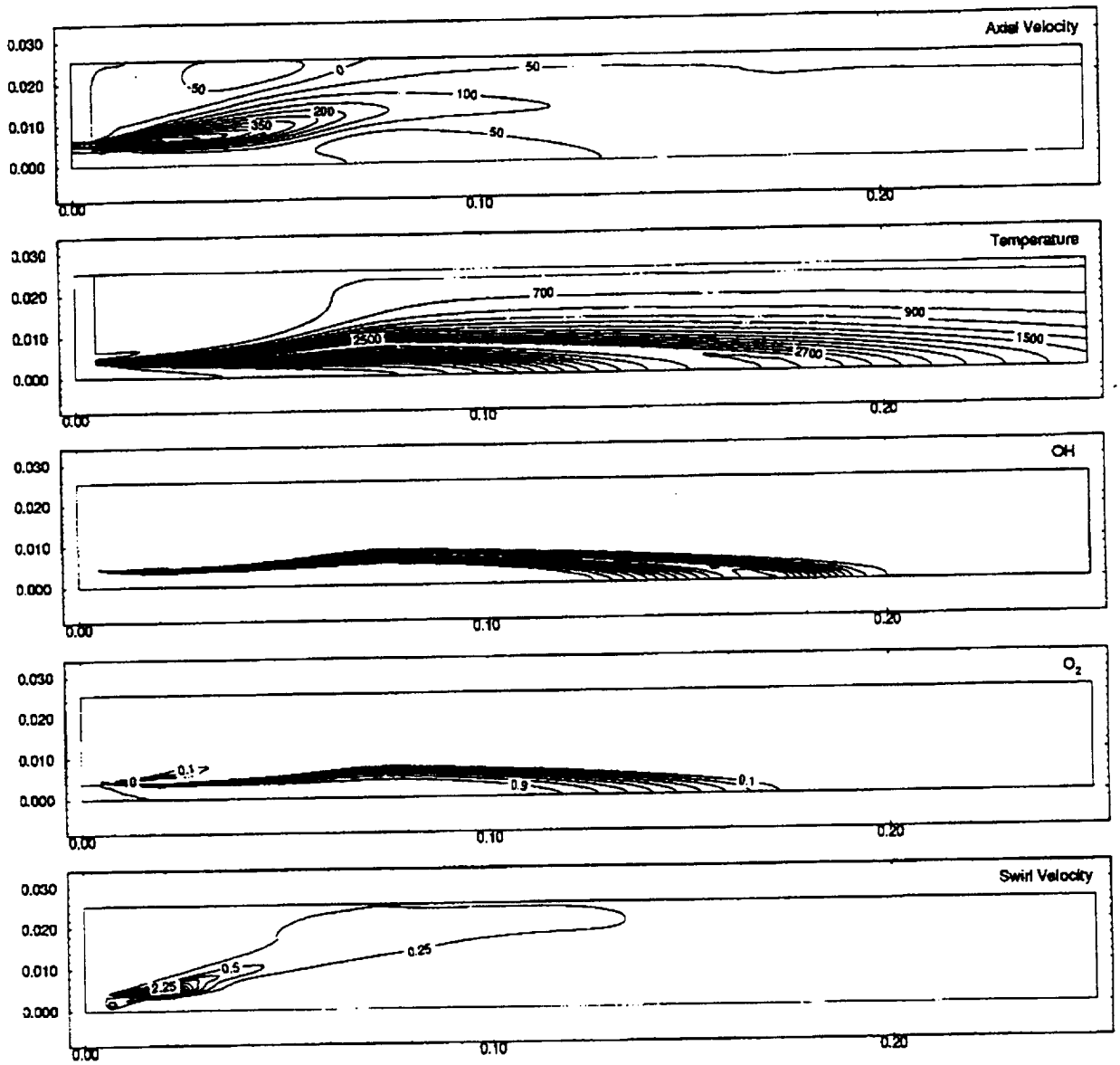


**Fig. 3.7.6. Calculated swirl coaxial injector flowfield for LOX/$GH_2$ propellants at O/F=20.**

The experimental measurements of the Sauter mean drop size is in the neighborhood of 300 μm, and an upstream mean of 350 μm has been used for these predictions. The predicted drop size distribution shows a weak radial variation at this axial location. The fluctuations at the extremes in radius arise because of an insufficient number of drops to obtain good statistical averages in the fringes of the spray. Similarly, the hole in the middle corresponds to the lack of a sufficient number of drops to give mean results in this inner "fringe" of the spray. Clearly, hot flow measurements like the present ones are a crucial input for CFD model development prior to attempting full scale engine predictions. Thus, the primary use of the present measurements has

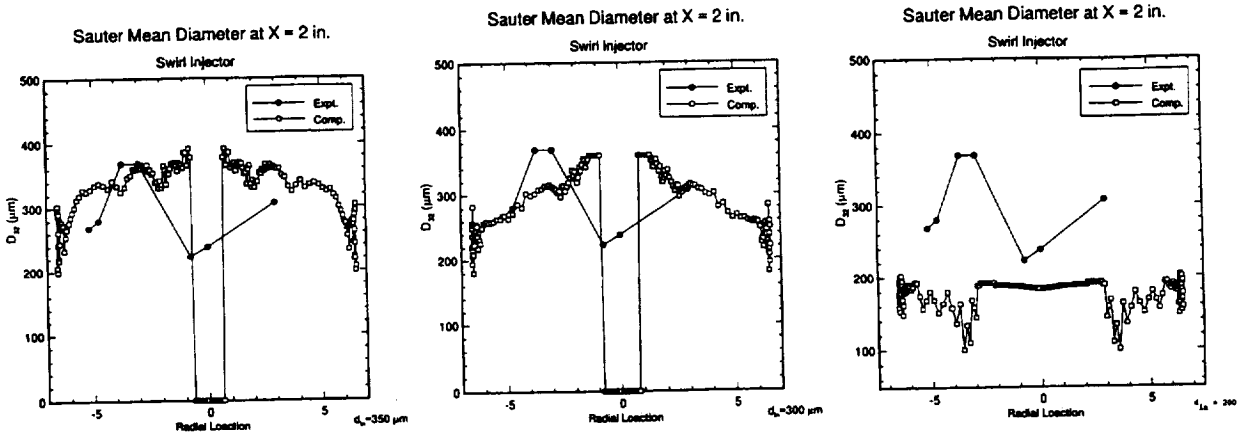


(a) 350 μm (b) 300 μm (c) 200 μm

**Fig. 3.7.7. Calculated Sauter mean diameter versus radial location for three different inlet drop diameters.**

been to adjust constants in the drop size model to be able to fit the measurements. Two such adjustments are shown in Figs. 3.7.7 (b) and (c) where the initial mean drop size has been decreased to 300 μm and 200 μm, respectively so the effect of initial drop size can be observed. The 300 μm case is quite similar to the 350 μm calculation. It produces similar drop sizes near the middle peak, but the radial gradient is stronger, and the drops over most of the combustor are smaller than in the 350 μm case. The 200 μm case produces a more uniform distribution of noticeably smaller drops. A smaller number of drops have been used in these last two calculations, and the statistical averages are less well resolved.

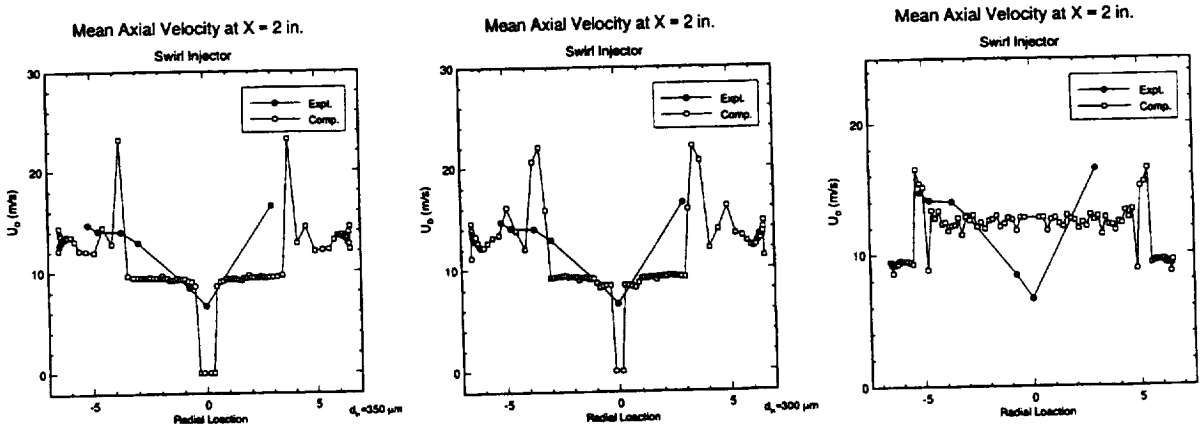


(a) 350 μm (b) 300 μm (c) 200 μm

**Fig. 3.7.8. Calculated mean drop velocity versus radial location for three different inlet drop diameters.**

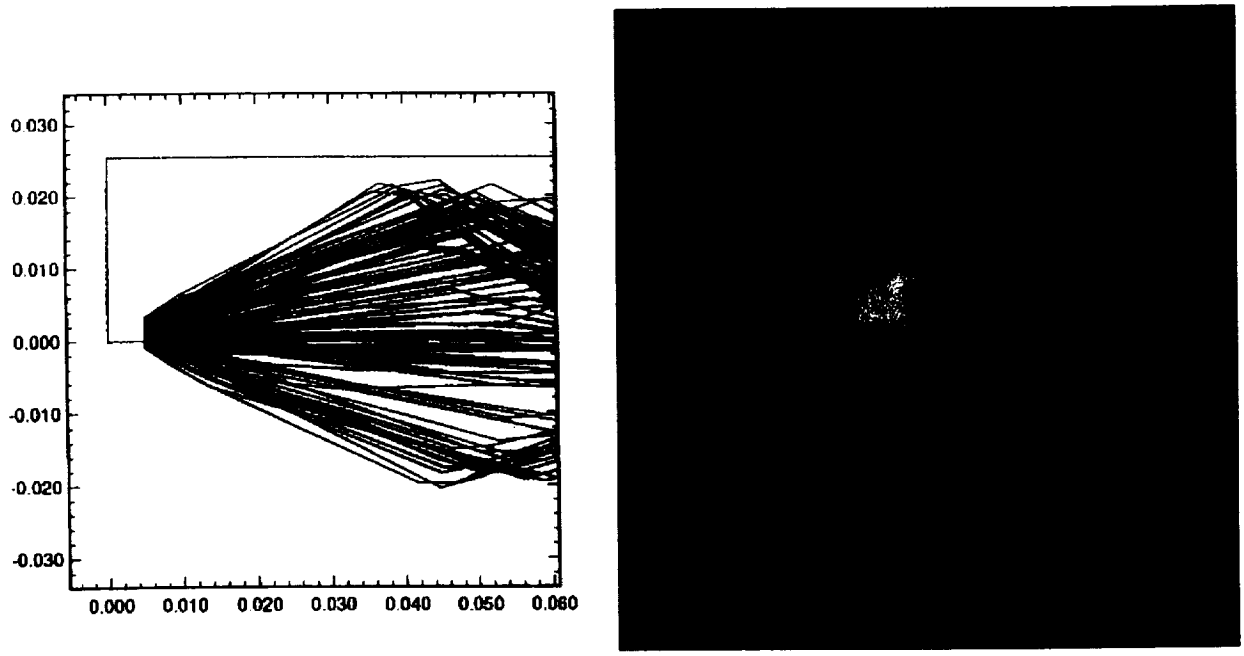


**Fig. 3.7.9. LOX drop field for swirl injector (flow is from left to right).**

The corresponding drop velocity predictions are compared to the experimental measurements in Fig. 3.7.8 (a) for the 350 μm case. Again, the fluctuations at the edge are the result of incomplete statistics in the fringes of the spray, and have no significant effect on the mean flow computation. Qualitative agreement is again seen in the velocity predictions. Corresponding results for the 300 and 250 μm cases are given in Figs. 3.7.8 (b) and (c).

The shape and location of the flame in the swirl coaxial injector experiment can also be used to verify the accuracy of the computational model. Fig. 3.7.9 (a) shows a series of computed drop trajectories that trace out the predicted spray location in the computation. (Note that specular reflection was assumed for any drops hitting the wall). Fig. 3.7.9 (b) shows an experimental visualization of the LOX drops in the presence of combustion. The silhouette of the spray pattern is quite similar. Here, the initial angle of the drops was matched to that of the measurements, but the remainder of the silhouette is determined from this upstream condition. Note that the experimental spray appears to expand outward just before reaching the wall, but overall the comparison is reasonable.

## 3.8. OXYGEN RICH ROCKET COMBUSTION TECHNOLOGY— NEAR STOICHIOMETRIC CORE/DOWNSTREAM DILUTION

Current interest in full-flow cycle liquid rocket engines has raised the need for vaporizing the entire liquid oxygen (LOX) flow prior to entry into the turbine. There are at least two distinct ways for accomplishing this. In the first, the entire LOX flow is passed through the gas generator and burned at very high O/F ratios with a small amount of hydrogen to produce a cool, GOX-rich mixture. In the second, a small fraction of the LOX is passed through the gas generator and burned at near-stoichiometric ratios to form a stream of hot gaseous products which are then used to vaporize the remainder of the LOX. There are potential technology-development issues associated with either approach. In the former, the combustion process takes place at O/F ratios of from 150 to 200 (see previous section). One major issue involves demonstrating unequivocally that the flame in the preburner can be maintained in stable fashion at these conditions. In the second approach, the near-stoichiometric combustion occurs at O/F ratios at which we have much experience, but effective methods must be identified for spraying the LOX into the hot gases downstream of the preburner in a fashion that ensures complete vaporization before entering the turbomachinery. The gas stream temperature should be uniform without temperature and O/F streaks that could lead to unacceptable thermal loading or safety concerns.

The present section focuses on the analysis of the second concept which we refer to as downstream dilution. The geometry we envision is a conventional preburner with multiple injectors at the head end that produce the near-stoichiometric hot gases close the injector face. The LOX is sprayed into the preburner downstream of this location to dilute the hot combustion gases to acceptable temperature levels and to bring the overall O/F ratio to the desired 150 to 200 level. The success of this downstream dilution concept depends upon identifying acceptable methods for injecting the liquid oxygen into the hot combustion gases. Three different geometries have been investigated in the LOX-rich preburner work to assess the global physics of downstream dilution of LOX injection and to test our drop tracking model. The present section summarizes the findings for these three potential configurations. The three geometries considered are:

⇒ Axial injection near the outer chamber wall from the injector faceplate,

⇒ Peripheral injection radially inward through a porous outer chamber wall,

⇒ Annular injection radially outward from a pipefeed system located in the center of the chamber.

In each case, modeling of the cylindrical dilution chamber begins downstream of the pre-burner flame zone which produces hot gases (3000 K) by combusting hydrogen with a small portion of the LOX feed in an approximately stoichiometric ratio. Liquid oxygen is then injected into a mixing chamber downstream of the preburner chamber where it is vaporized by the hot incoming gases.

We note at the outset that a splash plate could be used to mechanically disperse the LOX drops upon injection into the chamber. Mechanical devices of this type are effective in promoting mixing, but they also introduce potential difficulties, and increase the net pressure drop. The present approach is to identify the global levels of mixing that can be accomplished without intrusive mechanical devices. Mechanical devices can always be added to the design after it has been optimized if they are needed.

The injection is treated as a distributed liquid source using a specified drop diameter and mass distribution functions at each point. The spray is injected in a fan with random contributions in the axial and radial velocities of each drop. The individual drops are tracked in Lagrangian fashion and contributed mass, momentum, and energy to the gas phase modeled in an Eulerian approach.

In the axial injection design, dilution LOX injectors are presumed to be grouped around each individual LOX-hydrogen injection element. To enable the initial combustion to occur at near-stoichiometric O/F ratios, the LOX/$H_2$ injectors are recessed into the injector face in a "can" configuration. The hot combustion gases then expand into the main preburner chamber. The LOX injectors used to introduce the dilution liquid are positioned surrounding the "can" exit and are oriented at a canted angle which causes the liquid streams to impinge directly onto the hot combustion gases as shown in Fig. 3.8.1 (a).

In the radial injection design, the dilution oxygen is sprayed radially inward from the outer periphery of the combustion chamber so that the drops penetrate in a direction

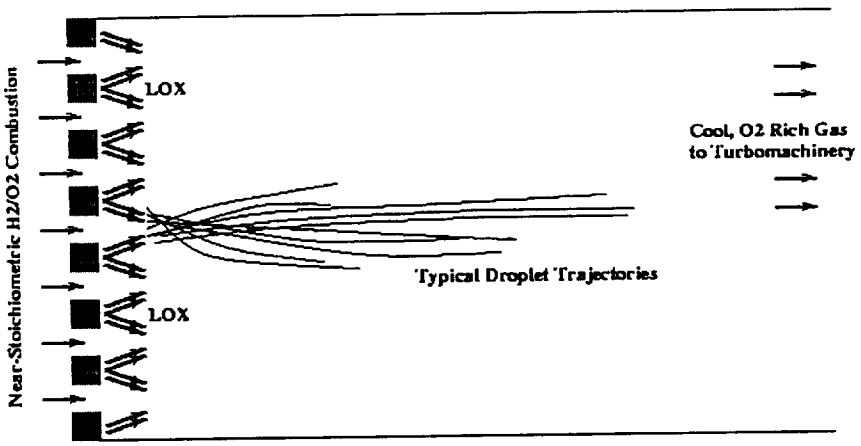


**(a) Geometry with axial liquid injection**

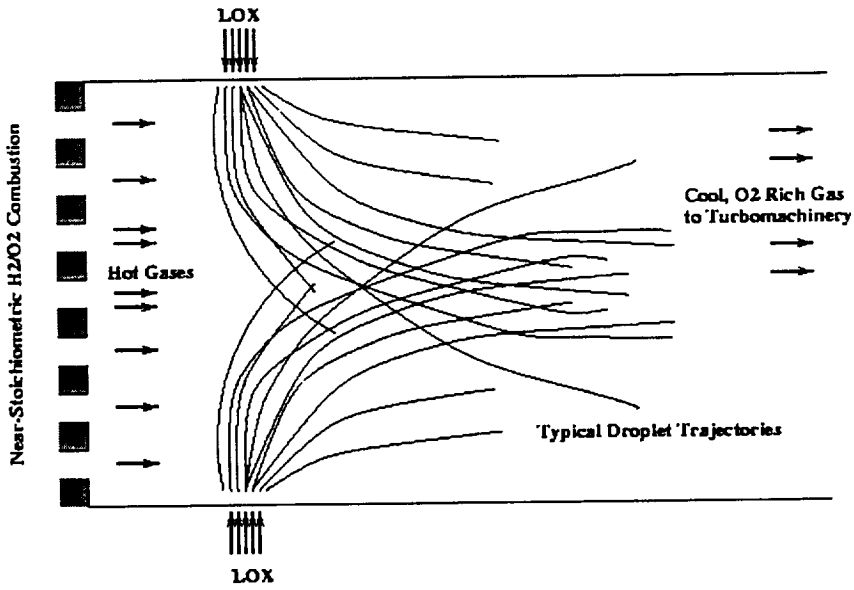


**(b) Geometry with radial liquid injection**

**Fig. 3.8.1.** Schematic of proposed oxygen-rich preburners.

perpendicular to the flow of the combustion products, as shown in Fig. 3.8.1 (b). This radial injection is assumed to be located far enough downstream of the injector face that the initial near-stoichiometric combustion process has been completed by the location at which the LOX enters. Some exploratory radial injection computations from a pipe on the centerline of the mixing chamber were also computed and are summarized briefly. Overall, the trade-offs between the axial and radial injection configurations give considerable insight into the design issues for such a downstream dilution chamber.

The present study is based upon a detailed computational model of the gas/liquid flow. In all cases, the near-stoichiometric combustion gases are taken to enter as a completely burned,

uniform stream. The trajectories of the vaporizing LOX drops are then followed through this hot gas flow field as they move from the injection location toward the downstream end of the chamber. The key issue is to identify the critical parameters that promote rapid vaporization, efficient mixing and temperature uniformity in the gases entering the turbomachinery.

The two generic geometrical configurations considered lend themselves to two distinct applications. First, the computational analysis provides an estimate of the relative effectiveness of the two injection configurations and their responsiveness to various design parameters in the problem. Second, the analyses also serve as a tool for designing a diagnostic experiment to verify the analysis and to prove the effectiveness of the design. In this regard, we note that experimental verification of the feasibility of the downstream dilution concept is preferably done first under laboratory-scale conditions, rather than at component sub-scale level. Such lab-scale tests would ideally document the details of drop sizes, velocities, trajectories, and vaporization rates to provide reliable design data for component-level design.

Here we note that, to be effective, the radial injection concept requires the use of a relatively large, nearly full-scale chamber with many injector elements. Radial injection in a chamber of small radius will impinge on the opposite wall, and give no information on the effectiveness of the design at full scale. Axial injection can, however, be accomplished readily on a single element scale, and the differences between single-element tests and multi-element tests should be relatively small. Thus, one of the uses of the axial injection modeling is to aid in the design of an experimental apparatus which will test the downstream dilution concept and validate computational methods like the present one.

### 3.8.1. COMPUTATIONAL FORMULATION

The computational model is the same as that outlined earlier in this chapter. A brief summary for these particular computations is repeated here with slightly more detail in the liquid spray model. The model is based on a mixed Eulerian-Lagrangian framework for the gas and liquid phases respectively. We begin by outlining the Eulerian gas phase model formulation and governing equations. This is followed by a brief description of the liquid phase equations of motion and relevant details of the Lagrangian computational model and inter-coupling terms between the gas and liquid phases.

### 3.8.1.1. Gas Phase Equations of Motion

The equations describing the gas phase are the axisymmetric Navier-Stokes equations coupled with auxiliary transport equations for species concentrations, turbulent kinetic energy and turbulent dissipation. These may be written in their traditional conservative form as follows:

$$\frac{\partial Q}{\partial t}+\frac{\partial E}{\partial x}+\frac{\partial F}{\partial y}=H+H_{liq}+L(Q_v) \tag{3.8.1}$$

The flux vectors are defined as:

$$Q=\begin{pmatrix}\rho\\ \rho u\\ \rho v\\ e\\ \rho k\\ \rho\varepsilon\\ \rho Y_i\end{pmatrix} \qquad E=\begin{pmatrix}\rho u\\ \left(\rho u^2+p_t\right)\\ \rho uv\\ (e+p_t)u\\ \rho uk\\ \rho u\varepsilon\\ \rho uY_i\end{pmatrix} \qquad F=\begin{pmatrix}\rho v\\ \rho uv\\ \left(\rho v^2+p_t\right)\\ (e+p_t)v\\ \rho vk\\ \rho v\varepsilon\\ \rho vY_i\end{pmatrix}$$

$$H=\begin{pmatrix}0\\ -\rho uv/y\\ 0\\ S_h\\ S_k\\ S_\varepsilon\\ S_y\end{pmatrix} \qquad H_{liq}=\begin{pmatrix}S_c\\ S_{mx}\\ S_{mr}\\ S_e\\ 0\\ 0\\ S_y\end{pmatrix} \qquad Q_v=\begin{pmatrix}p+\frac{2}{3}\rho k\\ u\\ v\\ T\\ k\\ \varepsilon\\ Y_i\end{pmatrix} \tag{3.8.2}$$

Here, the spatial variables $x$ and $y$ represent the axial and normal coordinates, and $u$ and $v$ represent the corresponding velocity components. The density and pressure are given by $\rho$ and $p$, and the total energy is defined as $e = \rho RT/(\gamma - 1)+1/2\ \rho\ (u^2+v^2+w^2)$, where R and $\gamma$ assume their usual definitions as the gas constant and specific heat ratio. The turbulent kinetic energy, dissipation rate, and species mass fractions are given by $k$, $\varepsilon$, and $Y_i$ respectively. The subscripts $i$=1, 2, ...$N$-1 represent individual species, where $N$ is the total number of chemical species considered. For simplicity, we close the system using the perfect gas relationship for the

equation of state. The diffusion operator $L$ has its standard definition and is given elsewhere [77].

The source vector $H$ contains the source terms due to combustion, turbulence, and axisymmetry. The source terms in the $k$ and $\varepsilon$ transport equation correspond to the standard $k$-$\varepsilon$ model with additional low Reynolds number terms included for near-wall effects [78]. The liquid phase analysis appears within the inter-phase coupling terms in the source vector $H_{liq}$. These symbolic terms represent the local liquid mass vaporization rate, the gas/liquid momentum and energy exchange, and the additional species accumulation in the gas phase from liquid vaporization.

Most generally, the source term $H_{liq}$ is determined by integrating the contributions of mass, momentum, and energy exchange from a Lagrangian treatment of a dilute, multi-disperse distributed liquid phase flow comprised of a large number of contributing particles. The governing equations for the liquid phase analysis are discussed in the following section.

### 3.8.1.2. Liquid Phase Modeling Philosophy

The modeling of the liquid spray considers the vaporization and dynamic motion of a large number of drops that determine the source terms to the gas phase. The primary difficulty in utilizing a Lagrangian treatment of the liquid phase is the significant computational resources required. Since tracking the individual drops of a physical spray is clearly beyond computational capabilities, we instead track a large number of parcels which are individually representative of a large number of identical physical drops. Appropriate drop size and velocity distributions can be superimposed on the drop parcel distribution by statistical means. Clearly, the gas phase variables depend on where the particles of liquid are located and the local vaporization rate (mass addition). The motion of the liquid particles in turn depends on the local gas phase properties such as temperature, velocity, and viscosity. Both sets of equations must be solved simultaneously in a coupled fashion to determine the steady state solution.

The common difficulties associated with the implementation of a mixed Eulerian-Lagrangian tracking procedure may be summarized as:

⇒ The computational time and memory requirements for the large number of particles needed to give good representation of the particle distribution functions at all points in space can

be excessive, especially when coupled with a multi-dimensional, implicit, multi-species, Eulerian CFD code.

⇒ A large number of computational parcels must be used to ensure that a statistically significant sampling of point sources are considered when computing the source terms.

⇒ It can be difficult to map the instantaneous particle locations in physical space to the appropriate grid cells in the Eulerian gas phase mesh when nonuniform grids are employed.

### 3.8.1.3. Lagrangian Tracking Procedure

With regard to memory requirements, because we seek only steady state solutions in the current paper, it is not necessary to store information about the particles throughout the flow field. Since the steady state solution is approached by an arbitrary, nonphysical pseudo-time transient, the source term contribution from an individual liquid drop parcel can be computed throughout its lifetime in a single pass while following the drop trajectory from its injection point.

The variables associated with the individual drop characteristics are scalars and are not stored variables. The mass, momentum, and energy contributions are allocated throughout the trajectory to the appropriate local gas phase cells as the parcels traverse the flow field. The inter-phase source terms contained in $H_{liq}$ are the only quantities impacting the gas phase and are the only vector variables required to be stored in memory.

This approach is directly opposite to unsteady solutions where all of the instantaneous liquid phase variables for each drop parcel (such as diameter and velocity) must be constantly retrieved from memory, updated, and again stored in memory. Such memory intensiveness is the primary drawback of a Lagrangian analysis, and is removed by the approach taken in the current work. The number of particles utilized in the current Lagrangian analysis is independent of memory and is therefore only limited by computational time. This dramatic increase in efficiency permits a much larger number of parcels to be considered. The abundance of parcels addresses the other critical concern in coupled Eulerian-Lagrangian analyses which requires that a sufficient number of particles are considered to ensure that a statistically significant sampling of point sources are used when computing the source terms. Typically, several million particles are present within the whole flow field in the steady-state solution.

The remaining issue in computing Lagrangian flows effectively is to efficiently allocate inter-phase source terms from the instantaneous particle locations in space to the appropriate Eulerian cells within the discretized gas phase grid. Typically, gas phase coordinate systems are mapped from the physical grid to a nondimensional, computational square mesh. Even though the instantaneous drop parcel physical coordinates are known at any instant in time, can be expensive to determine the index of the cell within which the parcel resides because a mesh search might be needed if the grid spacing is nonuniform. This is especially true when grid stretching is used to resolve gas phase flow field gradients. The procedure used to efficiently determine the computational cell location is discussed in conjunction with the liquid phase equations of motion presented in the following paragraphs.

### 3.8.1.4. Liquid Phase Equations of Motion

The liquid drop spray is described by a three-dimensional Lagrangian formulation that involves mass, momentum and energy transfer equations for the individual drops. Established empirical sub-models are used for the various physical processes associated with the liquid phase such as spray atomization and drop vaporization. The dynamic equations of motion for each drop can be written in vector form as

$$\frac{dQ_d}{dt} = H_d \tag{3.8.3}$$

where the vectors $Q_d = \left[d, u_d, v_d, w_d T_d\right]^T$ and $H_d = \left[\dot{m}_{vap} / \left(\pi \rho_l d^2\right), F_x/m_d, F_y/m_d, F_z/m_d, S_e\right]^T$.

Here, $d$ is the drop diameter, $u_d$, $v_d$, and $w_d$ are the $x$, $y$, and $z$ components of the drop velocity, and $T_d$ is the liquid temperature. In the source term, $m_d$ is the drop mass, $\rho_l$ is the liquid density, and $\dot{m}_{vap}$ and $S_e$ are the instantaneous vaporization and energy balance at the drop surface. The drag forces acting on the drops are estimated by standard drag curve results for spherical particles, given by the expression

$$F_i = \frac{\pi d^2}{8} \rho v_{rel,i} |V_{rel}| C_D \tag{3.8.4}$$

where $i$ represents a coordinate direction, and the relative velocities are defined as $v_{rel,i} = v_i - v_{d,i}$. The resultant relative velocity is given by $V_{rel} = \sqrt{u_{rel}^2 + v_{rel}^2 + w_{rel}^2}$. The effects

of gas/liquid drop turbulence interactions is modeled using stochastic methods which are widely employed [79]. The marching time step of the drop trajectory may vary based on drop lifetime, drop heating, drop acceleration, and the resident Eulerian cell grid dimension. This variation ensures computational robustness and reduces statistical scattering within small gas phase cell volumes.

The Lagrangian treatment of the liquid phase is fully three-dimensional in terms of the paths of the individual drop trajectories, but it is axisymmetric in the statistical mean to match the gas phase. Although three-dimensional effects are expected to be present in local regions, they are not expected to dominate the global effects in the dilution chamber, so the axisymmetric results are expected to provide the type of qualitative understanding that is needed for this conceptual design phase. Extension of the gas phases to three-dimensional geometries is straightforward.

Because the gas phase is treated as an axisymmetric flow, the liquid drops must be tracked in physical space and then transformed into an axisymmetric coordinate system. To accomplish this, the equivalent radial coordinate $y_r\sqrt{y^2+z^2}$ is used to rotate the three-dimensional trajectories to axisymmetric coordinates.

The drop parcel locations in axisymmetric space are computed from the contravariant velocities as [80]:

$$\frac{d\xi}{dt} = \hat{U} = \xi_x u_d + \xi_y v_d^* \tag{3.8.5}$$

$$\frac{d\eta}{dt} = \hat{V} = \eta_x u_d + \eta_y v_d^* \tag{3.8.6}$$

where $\xi$ and $\eta$ represent the axial and radial directions in axisymmetric computational coordinates, $\xi_x$, $\xi_y$, $\eta_x$ and $\eta_y$ are the local interpolated grid cell metrics, and $v_d^*$ is the equivalent axisymmetric normal velocity given by $v_d^* = \frac{\overline{vy} + \overline{wz}}{y_r}$. The physical space variables are updated using the known liquid phase velocities and current liquid phase time step as $x_i^{n+1} = x_i^n + \overline{u}_{d,i}\Delta t$. Using these expressions, the appropriate cell index to which the liquid phase

source terms are allocated may be simply found as $i = nint(\xi)$ and $j = nint(\eta)$. This approach has been validated on a trapezoidal mesh where the grid indices $i$ and $j$ may be prescribed analytically as a function of $x$ and $y$. This procedure dramatically increases computational efficiency and permits the grid indices to be determined with minimal additional computational effort.

### 3.8.1.5. Lagrangian Source Term Treatment

The mass source term $S_c$ of Eq. 3.8.2 which represents the mass vaporized per unit volume per unit time, is given by

$$S_c = \sum_k n_k \dot{m}_{vap,k} / dV \tag{3.8.7}$$

where $\dot{m}_{vap,k}$ is the vaporization rate from a single drop of diameter $d_k$ and density $\rho_k$, $n_k$ is the number of drops, and $dV$ is an appropriate differential cell volume in space. A wide number of available vaporization models for the individual drops may be employed from the literature. The vaporization rate $\dot{m}_{vap}$ from a single drop in the above expressions is treated here using the Priem-Heidmann vaporization model [81].

Similarly, the sources in the momentum equations include the momentum carried by the vapor as it enters the gas phase, less the drag exerted on the gas by the liquid phase

$$S_{m,i} = \sum_k \left( n_k \dot{m}_{vap,k} u_{i,k} - \frac{1}{6} \pi \rho_k d_k^3 n_k \frac{du_{i,k}}{dt} \right) \Big/ dV \tag{3.8.8}$$

where the subscript $i$ represents tensor notation for each coordinate direction and the $u_{i,k}$ are the drop velocities.

The source term for the energy equation may be written

$$S_e = \sum_k n_k \dot{m}_{vap,k} \left[ \bar{c}_{p,v} \left( T_k - T_g \right) - \lambda \right] / dV \tag{3.8.9}$$

where $T_k$ is the entering temperature of the vapor, $T_g$ is the ambient temperature of the gas, $\bar{c}_{p,v}$ is the appropriately averaged specific heat of the vapor/gas mixture surrounding the drop and $\lambda$ is the latent heat of vaporization.

The summations given in Eqs. 3.8.7-3.8.9 represent the localized contributions to a region in space from a large number of representative parcels which are injected into the flow field and assume steady state local Eulerian values over a long period of time.

## 3.8.2. RESULTS AND DISCUSSION

### 3.8.2.1. Preburner Geometries

Fig. 3.8.1 shows the two primary preburner geometries described earlier. The first design considers a recessed region for the primary combustion followed by direct injection of the LOX into the recirculation zone formed by the inlet of the injector face. The second configuration injects the LOX radially inward from the outer wall. As noted previously, the radial injection geometry is modeled as a preburner of full scale diameter and is intended to simulate the flow field downstream of a large number of individual upstream injector elements. In the computational model, it is assumed that these elements produce an equilibrium mixture of hot gases at near-stoichiometric conditions. The computations start downstream of this combustion zone with a uniform flow of hot gases through the upstream boundary that represents the products of combustion.

In contrast to the preburner geometry simulated in the radial injection configuration, the axial injection configuration is representative of a single element. The near-stoichiometric combustion takes place in a confined region that separates it from the downstream LOX dilution spray as shown in the figure. The mixing in this configuration is predominantly axial, and the scale-up of this axial injection concept to larger sizes would be accomplished by adding more primary injection elements. The model used for this single-element configuration starts with a uniform flow of combusted gases entering through the recessed upstream boundary. The LOX spray is injected through the recirculation region downstream of the recessed injector section.

The primary parameters studied are the mass flow rate of LOX and the injection characteristics of the spray. These variables include the overall O/F ratio, variations in the Sauter mean diameter of the injected spray, and variations in the liquid injection velocity.

The drops are injected into the computational domain in pre-atomized fashion. The injection element is modeled as producing a cone-shaped spray of drops with random, three-dimensional variations in initial velocity about the specified mean direction. A schematic of this

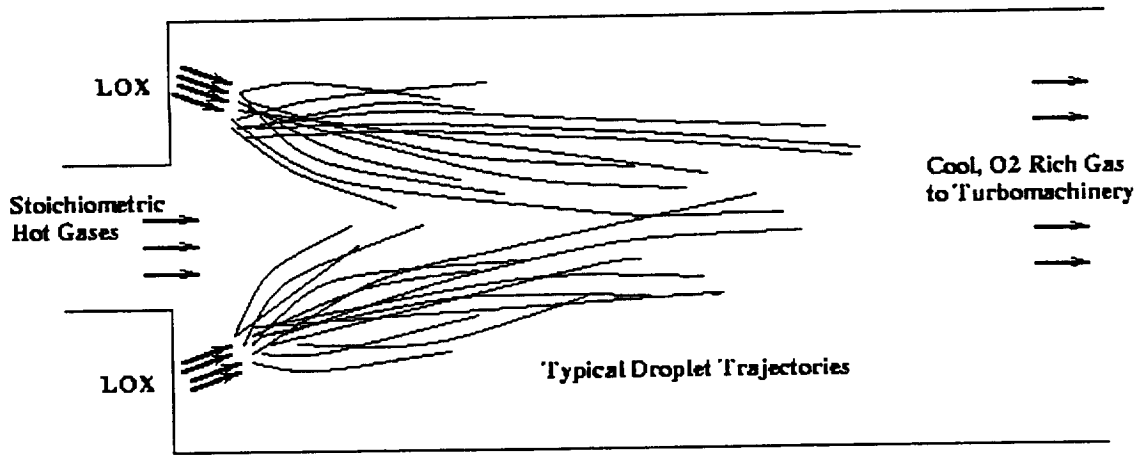


**Fig. 3.8.2. Schematic of single element preburner in axial geometry.**

process for the experimental design is shown in Fig. 3.8.2. The drop size distribution is based on a specified Sauter mean and an upper limit drop distribution function. Both the mean and the distribution are enforced by sampling randomly from the distribution as the drops are injected. Typical computations maintain several million computationally tracked particles within the flow field. The spatial locations of the liquid particles are used to compute the statistical results at local cells in the Eulerian CFD grid.

### 3.8.2.2. Axial Injection Cases

The first set of results utilizes a simplified axial injector geometry. The total amount of liquid mass vaporized into the gas phase can be determined by integrating the mass flow rate at every axial location. This integrated value is shown in the schematic at the top of Fig. 3.8.3. For this case, approximately 50 kg/s is added to the hot inlet gas flow of 10 kg/s. As the cross-sections of the axial velocity profiles indicate, the gas phase velocity decreases locally in the cooler regions. Corresponding contour plots of temperature (not shown) indicate the presence of strong regions of cooler gas near regions where the vaporization of the injected LOX is high, as expected. The cooler regions diffuse outward and spread as unvaporized drops are dispersed more widely throughout the flowfield. As more cold vapor is produced through vaporization, the temperature of the gas decreases to a value of approximately 200 K.

The computational domain for the axial LOX injection geometry with the recessed core geometry was outlined previously in Fig. 3.8.2. In this configuration, the near-stoichiometric combustion takes place in a recessed chamber around each injector element. The resulting high-

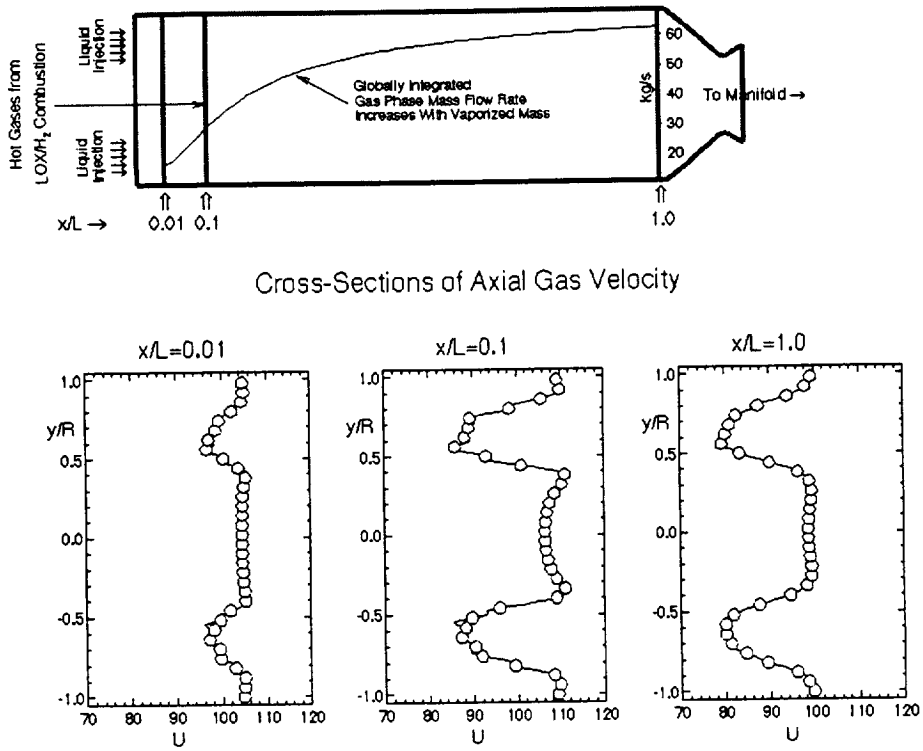


**Fig. 3.8.3. Axial velocity for LOX rich preburner (axial injection geometry).**

temperature gases are then subsequently expanded into the main dilution chamber and mixed with the injected LOX. Numerous test computations such as those presented above have shown that purely axial injection results in rather poor vaporization and mixing. For this reason, the LOX is injected at a small canted angle to enhance the mixing between the spray and the high-temperature gas stream. In addition, the recirculation region behind the recessed chamber into which the spray is injected should also provide some improvement in mixing and some additional uniformity in the flow at the exit.

The axial injection chamber is 12 inches in length, which corresponds to the 15-inch length used above, with injection starting 3 inches downstream. Because multiple recessed combustor elements would be used in a full-scale engine, the diameter of this section is only two inches. The diameter of the recessed core combustion region is one inch. The near-stoichiometric core combustion is again at an O/F ratio of 10, producing inlet gases at 3365 K with an initial velocity of 80 m/s, which corresponds to an inlet gas phase mass flow rate of 0.04 kg/sec. The chamber pressure is 13.6 atm. The drop field is injected as a three-dimensional fan with a spread angle of 20 degrees. The initial spray distribution is determined randomly by sampling from a pdf with a mean axial velocity of 30 m/s. The spray is canted radially inward at

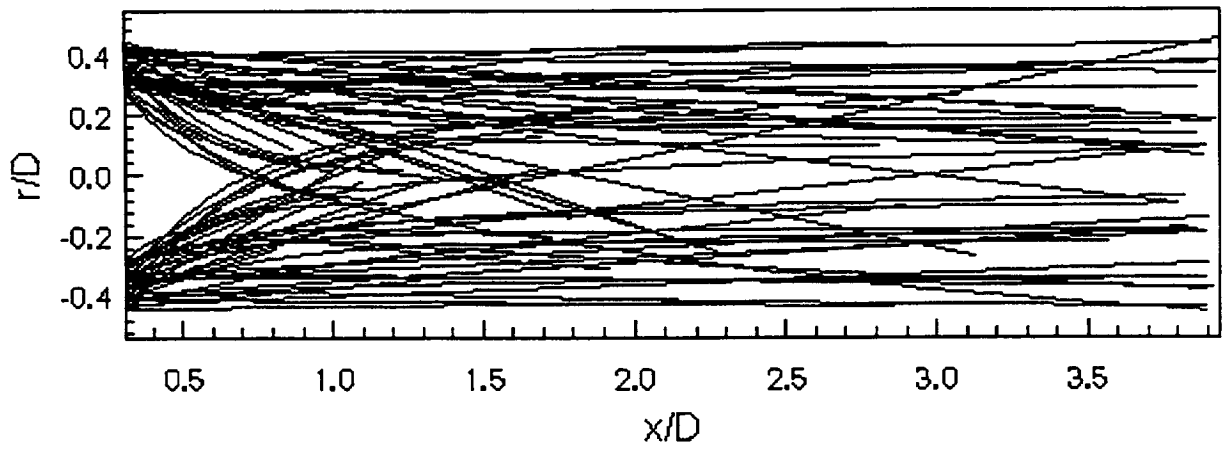


**Fig. 3.8.4. Representative drop trajectories for experimental near-stoichiometric core/downstream dilution experimental geometry (axial LOX injection).**

an angle of 15 degrees. (Note that the initial drop velocity is slower than the gas velocity here.) The initial Sauter mean drop diameter for the baseline case is again 150 μm with an upper-limit distribution function. The mass of injected LOX drops is chosen to increase the overall O/F ratio to 150 after all the LOX has been vaporized. A sketch of the configuration with a representative set of drop trajectories is shown in Fig. 3.8.4.

The results for the baseline conditions defined above are presented in Figs. 3.8.5 (a) and (b). As before, Fig. 3.8.5 (a) shows the temperature contours inside the dilution chamber, while Fig. 3.8.5 (b) shows the oxidizer mass fraction contour plots. The temperature contours for this axial injection case show the high-temperature gas entering from the recessed combustor area and expanding around the back step region into which the drops are injected. The LOX injection again has a dramatic effect on the temperature field within the dilution chamber. The vaporizing drops lower the static temperature from the 3300 K inlet to about 900 K near the centerline and around 500 K in the near-wall regions extending beyond the recirculation zones. The sharp gradients in the flow immediately downstream of the core entrance in Fig. 3.8.5 (a) result from the offsetting tendency for the high-temperature combustion products to expand into the relatively stagnant near-wall region, and the radially inward motion of the liquid spray. Because the vaporization rate associated with the liquid spray in this area is so large, the liquid phase impedes the expansion of the gases into the base region and redirects it inward. These high gradients are rapidly dissipated, leaving a relatively uniform temperature field. The corresponding oxygen mass fractions on Fig. 3.8.5 (b) likewise show very strong gradients

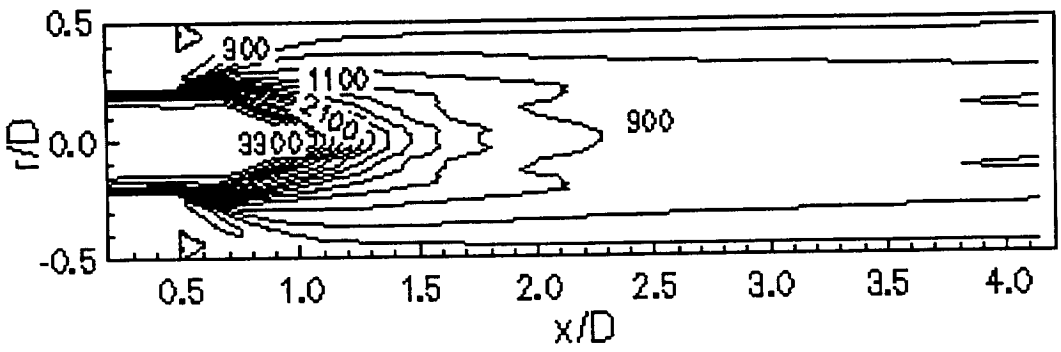


(a)

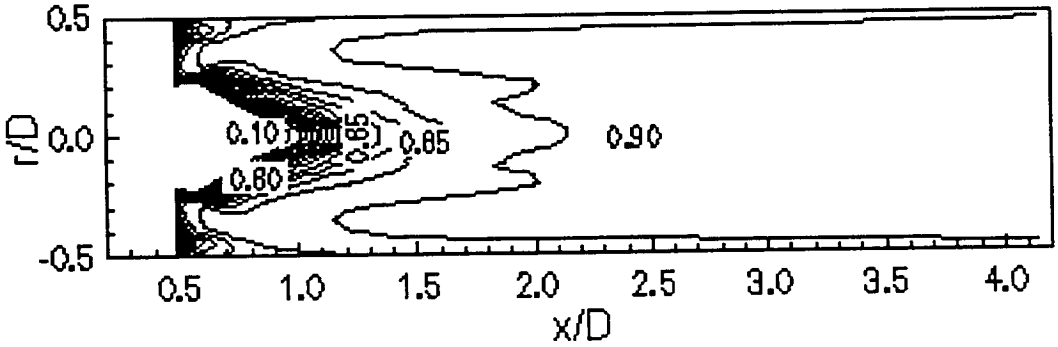


(b)

**Fig. 3.8.5. (a) Gas phase temperature contours and (b) Oxygen mass fraction contours. O/F = 150, $d_{32}$ = 150 μm, $u_{liq}$ = 30 m/s. Axial experiment test geometry.**

near the injection region where the vaporization rate is very high, and approach uniform conditions about halfway down the chamber.

Computational results for spray injection with a smaller mean drop diameter are shown in Figs. 3.8.6 (a) and (b). For this case, the Sauter mean drop diameter was reduced to 75 μm from the nominal 150 μm value shown previously. The drop velocity was kept constant at 30 m/s. These smaller drops are very quickly entrained by the gas phase flow field and convected downstream. The resulting gas phase temperature field in Fig. 3.8.6 (a) indicates significant hot streaks near the centerline due to insufficient penetration by the liquid phase. Because a significantly larger proportion of the liquid phase is located near the chamber walls, the gas phase temperature in the near-wall region is reduced to 300 K. The result is a very strongly distorted temperature field at the downstream exit. This strong distortion is also reflected in the oxygen mass fractions which remain essentially at the upstream value throughout the central region of the preburner, while rising to 0.90 near the walls.

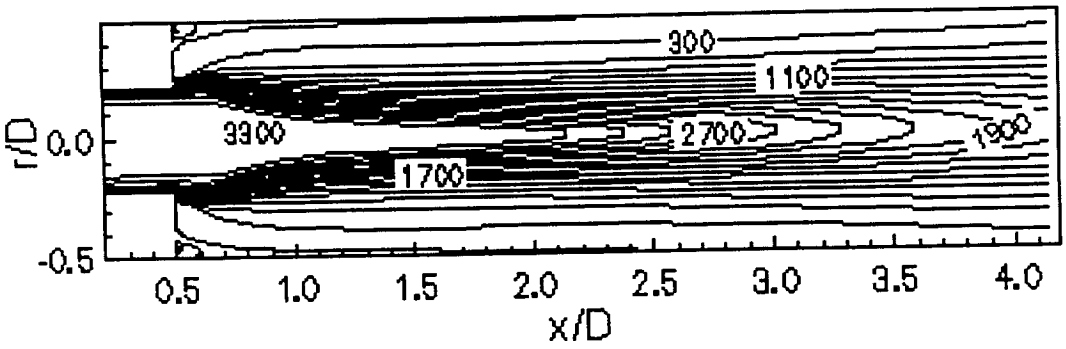


(a)

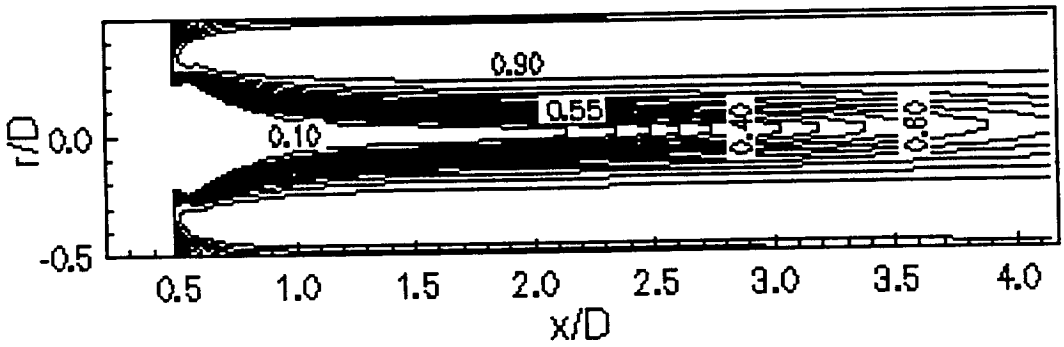


(b)

**Fig. 3.8.6. (a) Gas phase temperature contours and (b) Oxygen mass fraction contours. O/F = 150, $d_{32}$ = 75 μm, $u_{liq}$ = 30 m/s. Axial experiment test geometry.**

To provide a more quantitative measure of the corresponding mixing performance of these two operating conditions, the cross-stream temperature profiles at several axial locations are shown in Fig. 3.8.7. The plots in the figure are presented for only half of the flow domain. Figure 3.8.7 (a) presents the cross-stream temperature distributions in the gas phase for a fixed overall O/F ratio of 150 for the two mean drop diameters. The solid lines are for the larger 150 μm case, while the dashed lines show the smaller 75 μm case. Profiles at three axial locations are given: x/L = 0.25, 0.33, and 1.0. A comparison of the temperatures on the line closest to the injection location, x/L = 0.25, shows that the near-field solutions are quite similar to each other, although the smaller drops lead to somewhat colder flow near the outer wall. The comparison at the two downstream stations, however, demonstrates substantially better mixing and uniformity in the flow field for the larger drop size case. At the exit plane, the 150 μm case ranges between 500 and 800 K, while that for the 75 μm case ranges between 300 and 1800 K. These results are a direct reflection of the contour plots presented in Figs. 3.8.5

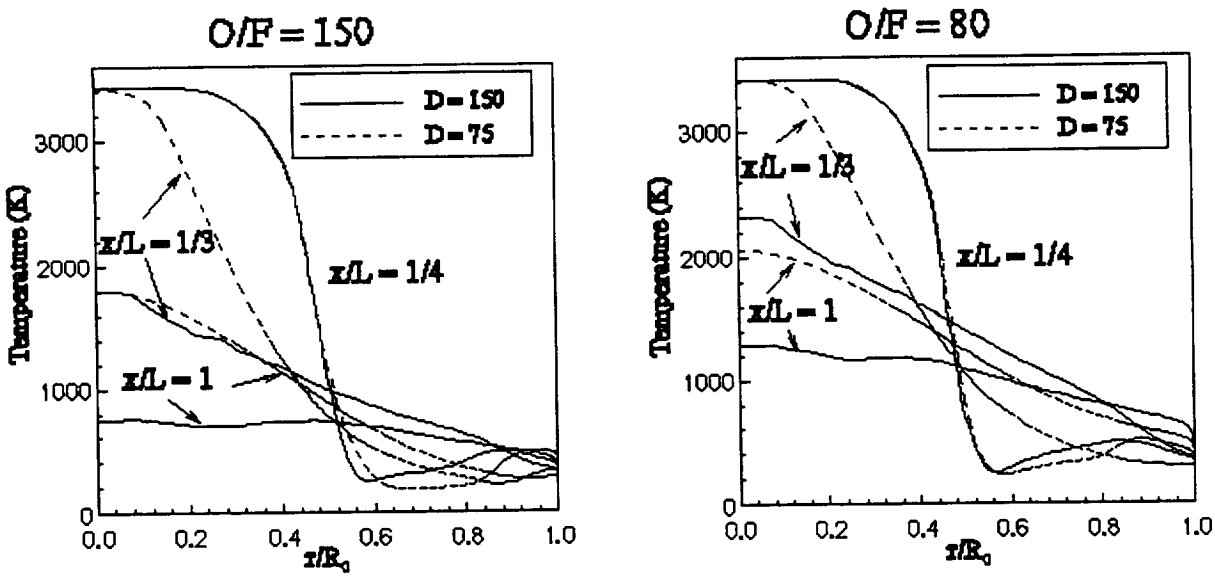


**Fig. 3.8.7. Gas phase temperature cross sections as a function of injected drop size for fixed O/F ratio.**

and 3.8.6. They also suggest that reasonably uniform mixing can be obtained in this axial injection configuration, but that the results are more sensitive to small changes in the inlet conditions than were the radial injection predictions.

Identical results for an O/F ratio of 80 are summarized in Fig. 3.8.7 (b). These predictions were not presented in the earlier figures. The change in the O/F ratio is obtained by reducing the total amount of LOX injected. As for the O/F of 150 case, the larger drop sizes result in better mixing and flow uniformity downstream. Note, however, that the higher O/F ratio in Fig. 3.8.7 (a) resulted in more uniform conditions than does the lower O/F ratio in Fig. 3.8.7 (b).

The final set of results for the axial injection system demonstrates the use of an annular injection geometry. As in the previous case, the liquid drops are entrained in the gas phase flow downstream. As noted from the color contours of Fig. 3.8.8, the gas temperature decreases markedly near the center annulus as the liquid is vaporized, and spreads radially outward in the downstream direction as indicated in the color contours and cross-section diagrams. The gas phase axial velocity is correspondingly decreased in the cool regions due to an increased density, as shown on Fig. 3.8.9. The drop number densities shown on Fig. 3.8.10 indicate the regions

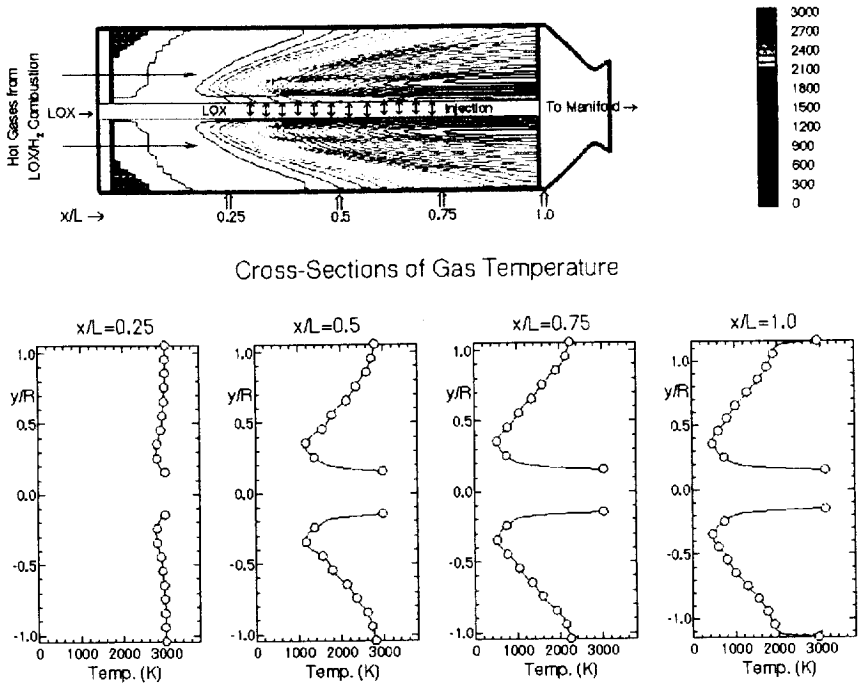


**Fig. 3.8.8. Gas temperature for LOX rich preburner (annular injection geometry).**

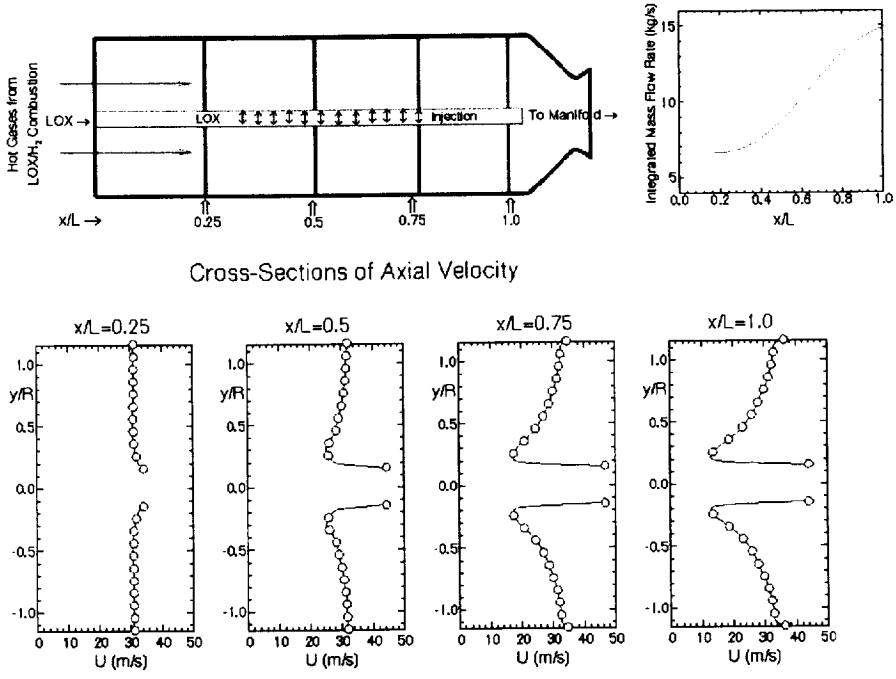


**Fig. 3.8.9. Axial velocity for LOX rich preburner (annular injection geometry).**

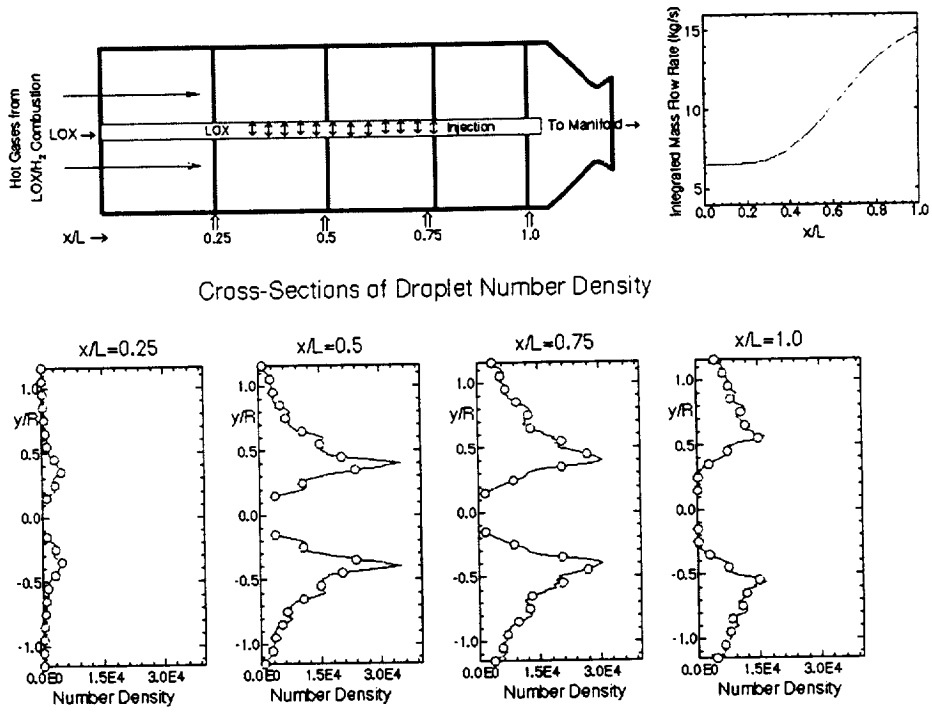


**Fig. 3.8.10. Drop number density for LOX rich preburner (annular injection geometry).**

where vaporization is largest. These correspond nearly exactly with the regions of cool gas temperature, as expected.

### 3.8.2.3. Radial Injection Geometry

The first set of results for the peripheral injection geometry shown on Fig. 3.8.11 corresponds to the case where the LOX is injected radially towards the center of the chamber. Because the liquid is injected nearly perpendicular to the inlet gases, the liquid drops are entrained by drag and follow trajectories similar in shape to the temperature contours. As the liquid drops vaporize, the gas temperature correspondingly decreases, as noted by the contours and cross-section plots shown on Fig. 3.8.11. As in the previous case, the integrated mass flow rate and axial velocity are also given on Fig. 3.8.12. The mixing in this case appears to be improved over that in the axial injection geometry. The locations of the drops in the flowfield are indicated by the cross sectional diagrams of drop number density shown at the bottom of Fig. 3.8.13. Note that the number of liquid drops increases in the downstream direction.

We next consider the radial injection configuration shown in Fig. 3.8.1(b). The dilution chamber diameter is set at 9 inches with a nominal length of 15 inches. For these computations, the drops are injected through a two-inch region of the dilution chamber wall running from

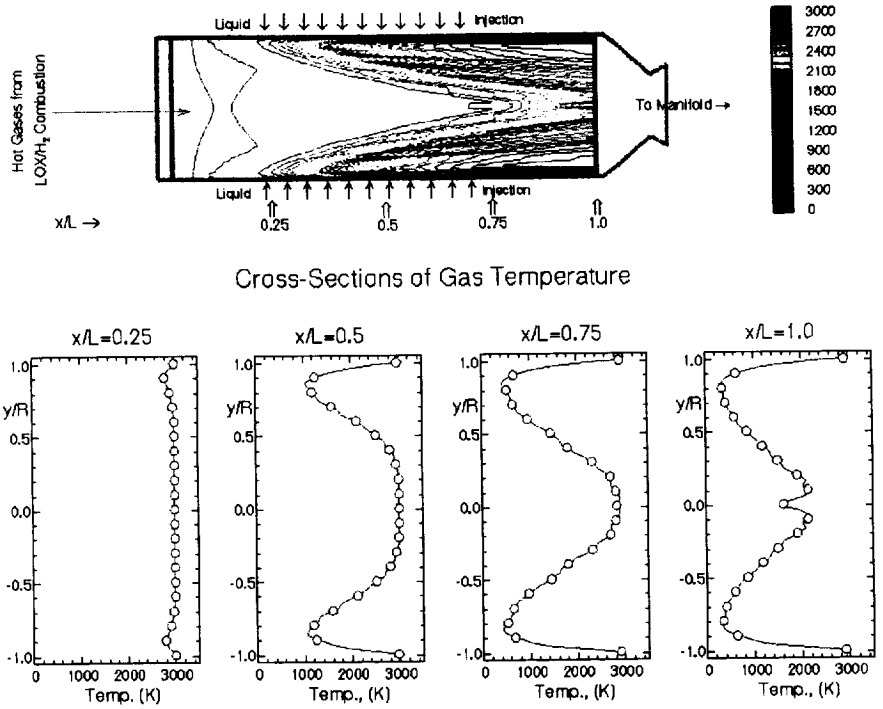


**Fig. 3.8.11. Gas temperature for LOX rich preburner (peripheral injection geometry).**

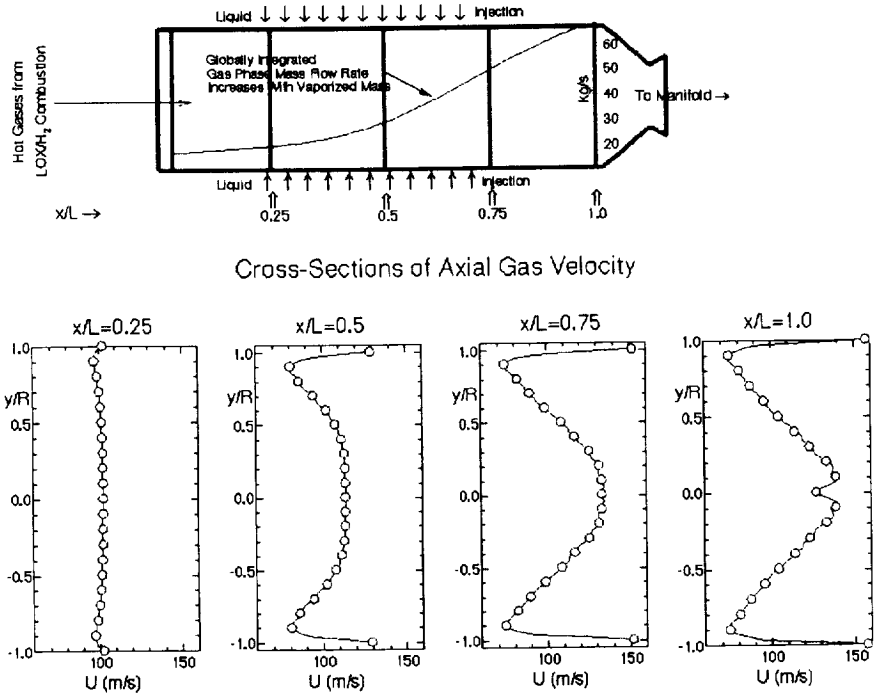


**Fig. 3.8.12. Axial gas velocity for LOX rich preburner (peripheral injection geometry).**

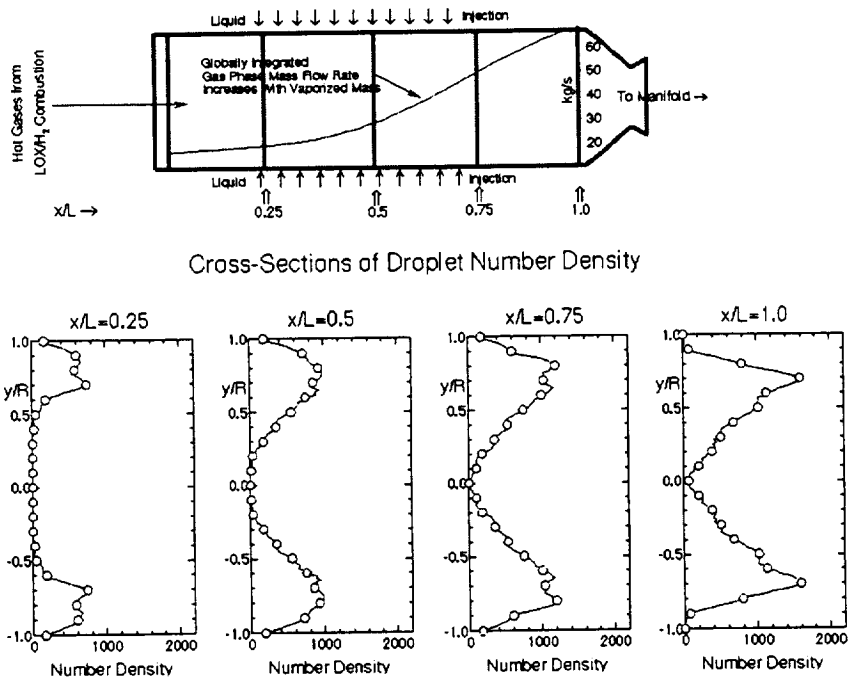


**Fig. 3.8.13. Drop number density for LOX rich preburner (peripheral injection geometry).**

3 inches downstream of the hot gas inlet to 5 inches from the inlet. As a baseline condition, we consider a Sauter mean diameter of 150 μm, a mean radial injection velocity of 100 m/s corresponding to an approximate injector pressure drop of 15% of the mean chamber pressure and a LOX injection rate of 108 kg/s which results in an overall exit O/F ratio of 150 at the downstream end of the chamber.

A sketch of the geometrical configuration along with a representative set of drop trajectories is shown in Fig. 3.8.14. The hot gases enter from the left boundary with an axial velocity, while the LOX drops enter from the outer periphery of the chamber with a predominantly radial velocity. As the drops traverse the chamber, they are turned toward the axial direction and swept downstream by the combustion gases. Because a complete distribution of drop sizes is injected, there is a variation in the radial distance to which the drops penetrate. Results discussed later indicate that effective mixing requires that a controlled fraction of drops cross the center line. The smaller drops in the distribution are entrained in the axial direction more rapidly than larger drops, and the length of the individual trajectories corresponds to the lifetime of the individual drops. This is again a result of the drop size and velocity distributions.

Corresponding contour plots of the temperature and oxygen mass fraction throughout the dilution chamber are given in Figs. 3.8.15 (a) and (b) for this baseline case. Both the axial and

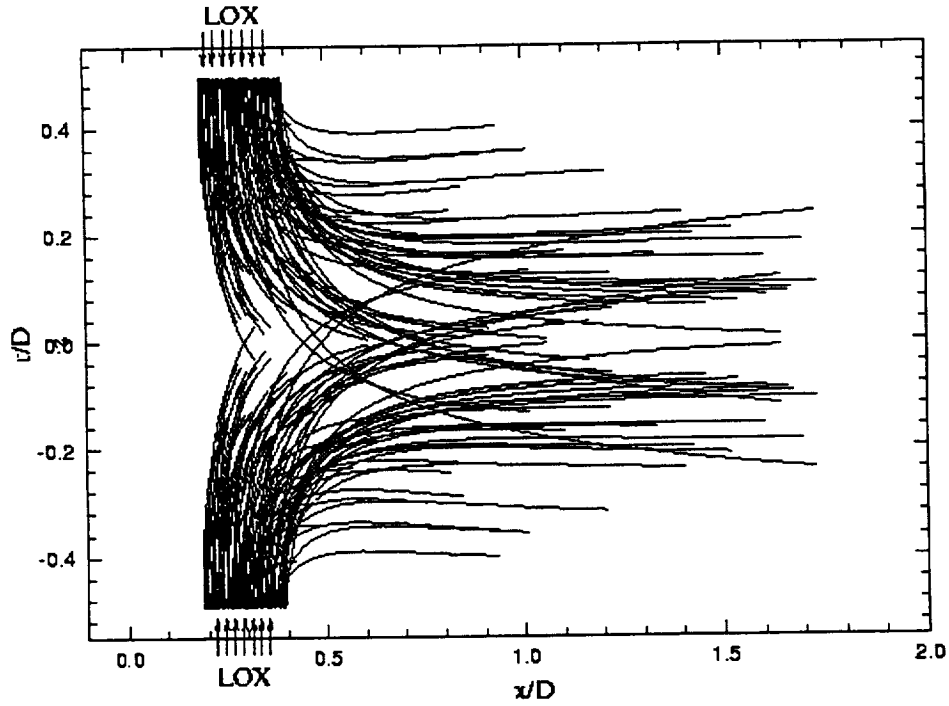


**Fig. 3.8.14 Representative drop trajectories for the radial injection geometry. O/F = 150, $d_{32}$ = 150 μm, $u_{liq}$ = 100 m/s.**

radial coordinates in these and the following figures have been non-dimensionalized with respect to the chamber diameter. The temperature contours in Fig. 3.8.15 (a) start from their maximum value at the left boundary where the upstream combustion gases enter the dilution chamber. Near the LOX injection location, the temperature begins to decrease rapidly as the liquid spray begins evaporating. The curved interface between high and low temperature regions provides a qualitative picture of the nominal trajectory of the spray. For the conditions of the present computation ($d_{32}$ = 150 μm, $u_{liq}$ = 100 m/s), a substantial fraction of the drops penetrate beyond the center of the chamber before they are swept downstream, but the gas temperature remains a maximum there. Essentially all the drops are vaporized by the x/D = 1.25 (x/L = 0.75) station, and beyond this point the temperature contours become axial. The results, however, show a substantial residual temperature profile in the gas. The gas phase temperature at the exit has a maximum value of approximately 1000 K near the centerline of the chamber, and extends to lower, fairly uniform values of 450 K in the near-wall regions.

Fig. 3.8.15 (b) presents companion results for the oxygen mass fraction contours in the gas phase. The combustion gases entering from the left boundary contain an oxygen mass

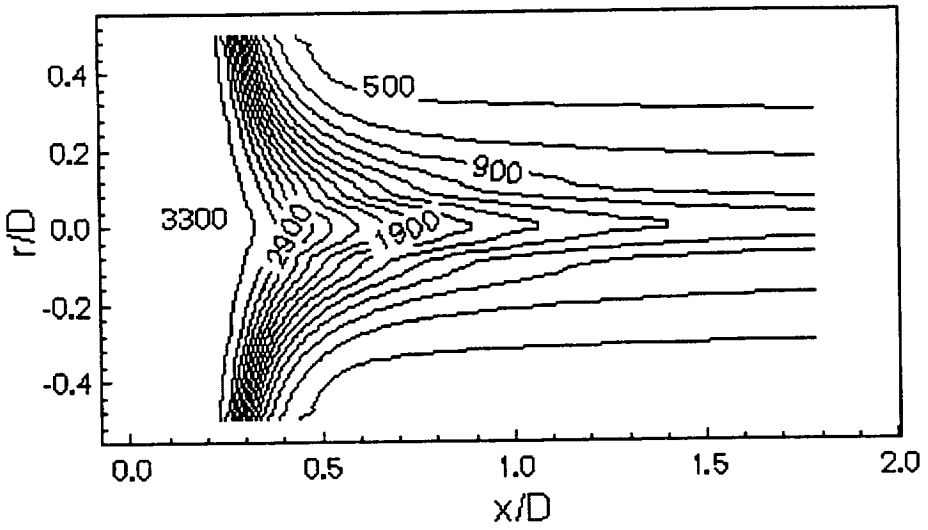


(a)

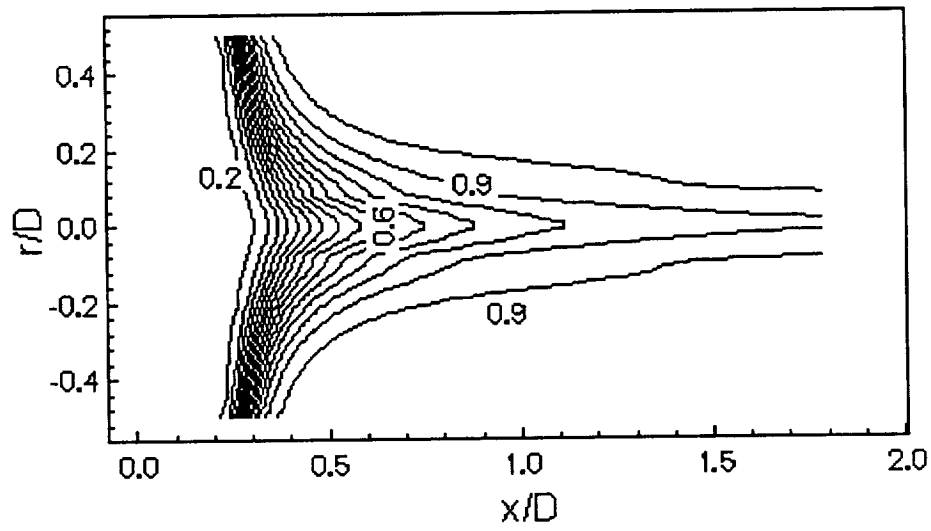


(b)

**Fig. 3.8.15. (a) Gas phase temperature contours and (b) Oxygen mass fraction contours. O/F = 150, $d_{32}$ = 150 μm, $u_{liq}$ = 100 m/s.**

fraction of approximately 0.2, corresponding to slightly oxidizer-rich combustion conditions at an O/F = 10. Thus, at the entry, the gas flow is primarily water vapor. As the gas contacts the liquid spray and begins to vaporize it, the oxygen mass fraction within the flow field increases dramatically, indicating that rapid vaporization takes place. The high local vaporization rates in this region result from the combined effect of high-temperature ambient gases and a high relative velocity between the gas and liquid phases. At the exit of the dilution chamber, the gas

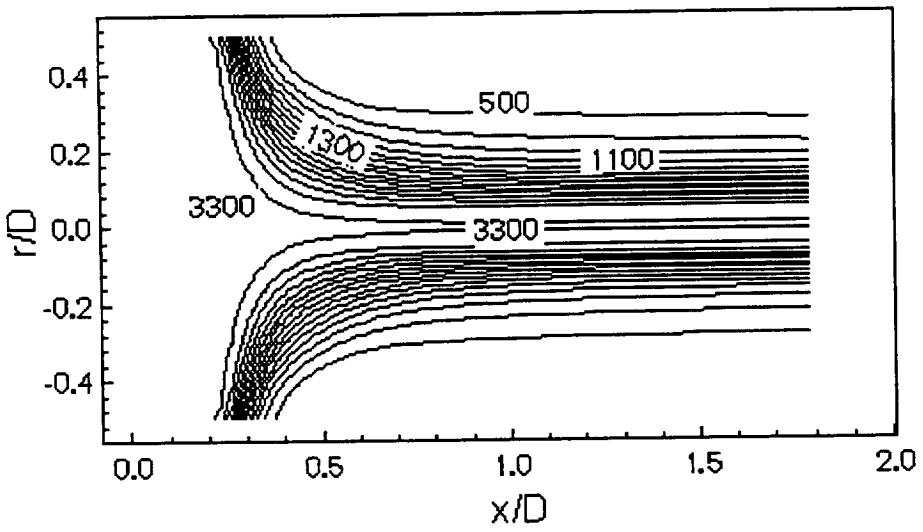


(a)

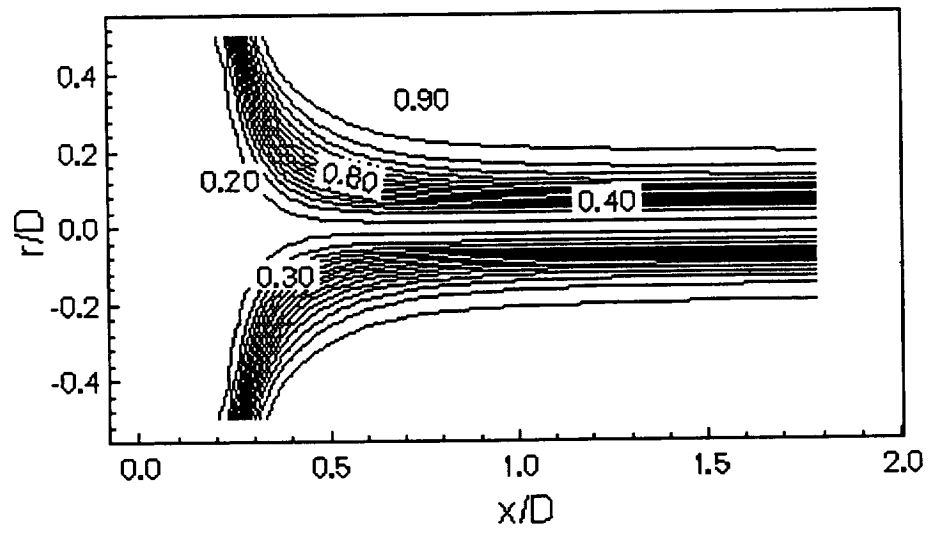


(b)

**Fig. 3.8.16. (a) Gas phase temperature contours and (b) Oxygen mass fraction contours. O/F = 150, $d_{32}$ = 100 μm, $u_{liq}$ = 100 m/s.**

composition adjacent to the walls is more than 90% oxygen, while at the centerline, it is slightly lower. These results are similar to those for the temperature.

The above results show the flow field for one set of input conditions. To provide some understanding of the importance of the various parameters, we present some representative results in Figs. 3.8.16 and 3.8.17. We first look at the effect of changing the injected mean Sauter drop diameter of the injected spray from 150 μm to 100 μm while holding the injection velocity constant. Temperature contours and mass fraction contours for this case are given on

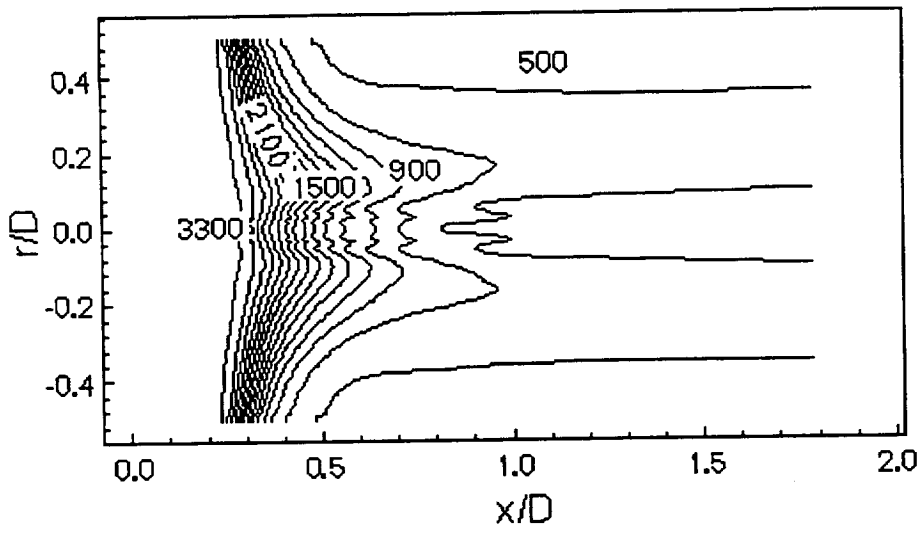


(a)

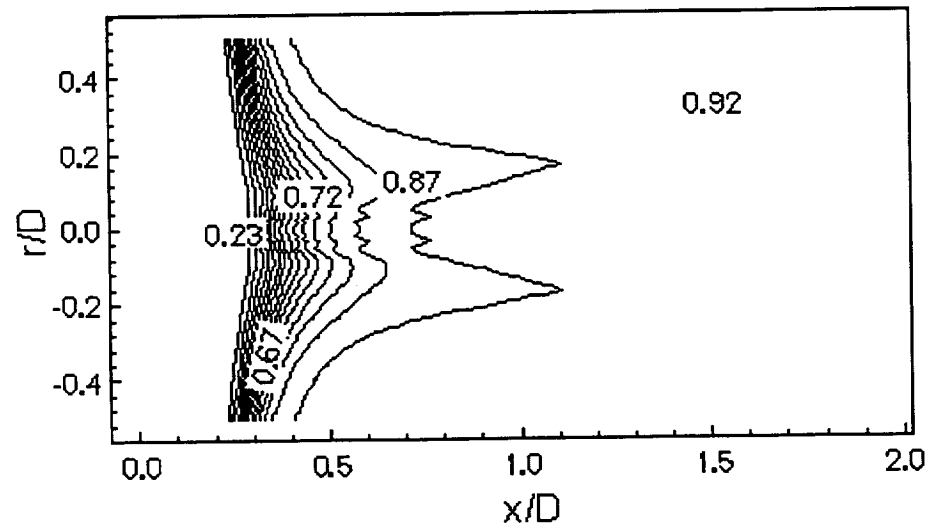


(b)

**Fig. 3.8.17. (a) Gas phase temperature contours and (b) Oxygen mass fraction contours. O/F = 150, $d_{32}$ = 150 μm, $u_{liq}$ = 120 m/s.**

Fig. 3.8.16. To maintain the same overall O/F ratio as before, the total mass flow of LOX is also held constant. The present change in drop size would correspond to an appropriate resizing of the injector (and possibly a change in the injector pressure drop).

The temperature contours in Fig. 3.8.16 (a) show that the change in drop size has a relatively significant effect, as can be seen by comparison with Fig. 3.8.15 (a). The smaller drop sizes are entrained much more rapidly and never penetrate to the center of the dilution chamber. As a result, a hot streak remains on the centerline throughout the chamber length. The peak

temperature at the exit is nearly identical to its 3300 K inlet condition. The flow near the edges remains cold, but the temperature distortion at the exit plane is much larger. This nondiluted region is also readily apparent from the oxygen mass fraction contours shown in Fig. 3.8.16 (b). Clearly, these smaller drop sizes lead to an inferior design.

As a second parametric variation, we consider the effect of changing the initial injection velocity of the liquid spray. For this computation, we again return to the 150 μm drops considered in Fig. 3.8.15, except that here we have increased the mean drop injection velocity from 100 m/s to 120 m/s. Such an adjustment could be made experimentally by changing the pressure drop across the injector face. The results are shown on Fig. 3.8.17. Again, the LOX injection causes the temperature contours on Fig. 3.8.17 (a) to decrease rapidly as the liquid spray begins evaporating, and the curved interface between high and low temperature regions provides a nominal indication of the spray trajectory. Comparison with Fig. 3.8.15 (a) shows that the increased injection velocity causes the mean drop trajectory to penetrate further past the centerline, resulting in a cooler temperature on the centerline, and, as shown by the contours midway through the dilution chamber, a peak that lies slightly off-center. The final downstream temperature profile for this case shows only a small amount of distortion with maximum and minimum temperatures lying between 400 and 600 K. Further, this case, as with the previous cases, shows that additional length in the dilution chamber would have little impact on the temperature contours. The corresponding oxygen mass fraction contours in Fig. 3.8.17 (b) similarly indicate a relatively uniform oxidizer mass fraction at the downstream end. The oxygen mass fraction is approximately 0.92 throughout the last half of the chamber. The results at this condition appear to be reasonably well optimized for a preliminary design.

The results in Figs. 3.8.15-3.8.17 show that the mixing and uniformity obtained from cross-stream injection can vary widely. Nevertheless, it does appear that acceptably uniform conditions can be obtained without the use of mechanical mixing devices which would increase the pressure drop and might raise concerns about erosion and safety. Clearly, the initial momentum of the drops is an important parameter that must be matched with the dilution chamber diameter to ensure that the drops penetrate far enough beyond the center of the chamber to minimize the distortion in the exit temperature and mass fraction contours. The combination of drop size and velocity variations gives an indication of the type of tuning that must be made to

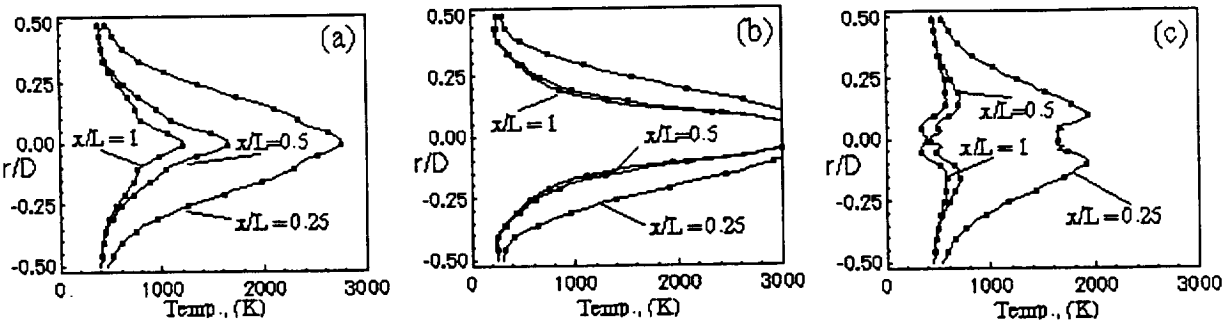


**Fig. 3.8.18. Temperature cross-sections for various axial locations.**

obtain an acceptable design. The computational results provide a good preliminary understanding of a preferred design, but final design would, of course, require verification.

To provide a more quantitative measure of the corresponding mixing performance at each operating condition, the cross-stream temperature profiles for each case are shown in Fig. 3.8.18 at several axial locations. Figure 3.8.18 (a) shows temperature cross-sections at three axial location, x/L = 0.25, 0.5 and 1.0, for the baseline operating condition given in Fig. 3.8.15. The initially high-temperature upstream combustion products are gradually diluted to a maximum temperature of 1000 K for this case, although the flow remains fairly nonuniform in temperature. This does not represent a particularly attractive condition for the turbomachinery, but better profiles can be obtained with an appropriate set of operating conditions, as demonstrated shortly.

The cross-stream temperature profiles for the smaller drop diameter case are shown in Fig. 3.8.18 (b). These results indicate very strong temperature striations in the flow, and significantly poorer mixing than for the conditions in Fig. 3.8.17 (a). The results for the higher drop injection velocity shown in Fig. 3.8.17 (c) clearly indicate an improved temperature field. The peak temperature decreases rapidly with increasing axial distance, indicating the substantial penetration of the liquid phase into the gas phase. As noted earlier, these results show that the length of the dilution chamber is no longer much of an issue. Once the penetration characteristics of the drops have been matched with the chamber radius, the solution becomes quite insensitive to the length of the chamber.

Finally, we note that the chamber diameter (which is here fixed at 9 inches) is an important variable in the radial injection configuration. For very small engines or laboratory-sized tests, the diameter of the dilution chambers would be so small that radial injection would

not be practical, despite its practicality for typical launch-sized engines. For purposes of code validation therefore, only axial injection configurations can be considered. Instead, laboratory-sized testing of LOX dilution must resort to experiments in axial injection configurations. These axial dilution experiments can, however, be used to validate the computational model, which can then be used for investigating radial designs such as the present ones.

## 3.9. COMPARISON OF SWIRLING AND NON-SWIRLING GAS/GAS INJECTORS

Shear coaxial injectors have a long successful history of application in LOX/hydrogen rockets. Their success is probably a result of their effectiveness in atomizing the incoming liquid oxygen. It is well known that their velocity (momentum) ratio must be carefully selected to ensure acceptable atomization. The results presented above show that they provide relative slow mixing, but nevertheless give good performance in rocket engines. In the case of gas-gas injectors, the mixing process becomes more critical since one can no longer rely on dispersing the liquid droplets throughout the gas phase prior to vaporization. In the gas-gas engine, the mixing must be completely accommodated by the injector. For this reason, swirl injectors (which are also attractive for gas-liquid engines) become even more desirable. In the present section, we compare computational solutions of shear coaxial injector flowfields with those of swirl coaxial injector flowfields. The overall conclusions of this study indicate a very substantial increase in mixing for swirl injectors, even when only small amounts of swirl are added.

The computational model used for the comparison is the same as described in previous sections, and the computational domain and grid are likewise similar. The set of results presented here is for an O/F of 4. Other parameters are similar to those in problems described earlier. To provide a more sensitive indicator of mixing effectiveness, we show contour results in the cross-plane at three different axial stations as opposed to contour plots in the azimuthal (r-z) plane.

Back-to-back computational predictions for the shear coaxial case and the swirl case are shown in Figs. 3.9.1-3.9.3. Fig. 3.9.1 shows the temperature contours at each of three downstream axial station, x=1 inch, 2 inches, and 5 inches for both injector configurations. The shear coaxial results are on the left while the swirl results are on the right. As can be seen, the two results are qualitatively similar at the first axial station. The annular high temperature region clearly shows the location of the narrow annular flame. The swirl case is slightly more "out of focus" than the shear case indicating the mixing might be slightly faster, but otherwise they are quite similar. The differences between the two mixing processes, however, becomes very visible at the x = 2-inch station and even more so at the x = 5-inch station as the lower two sets of plots in Fig. 3.9.1 shows. The 2-inch location clearly shows a broader high temperature

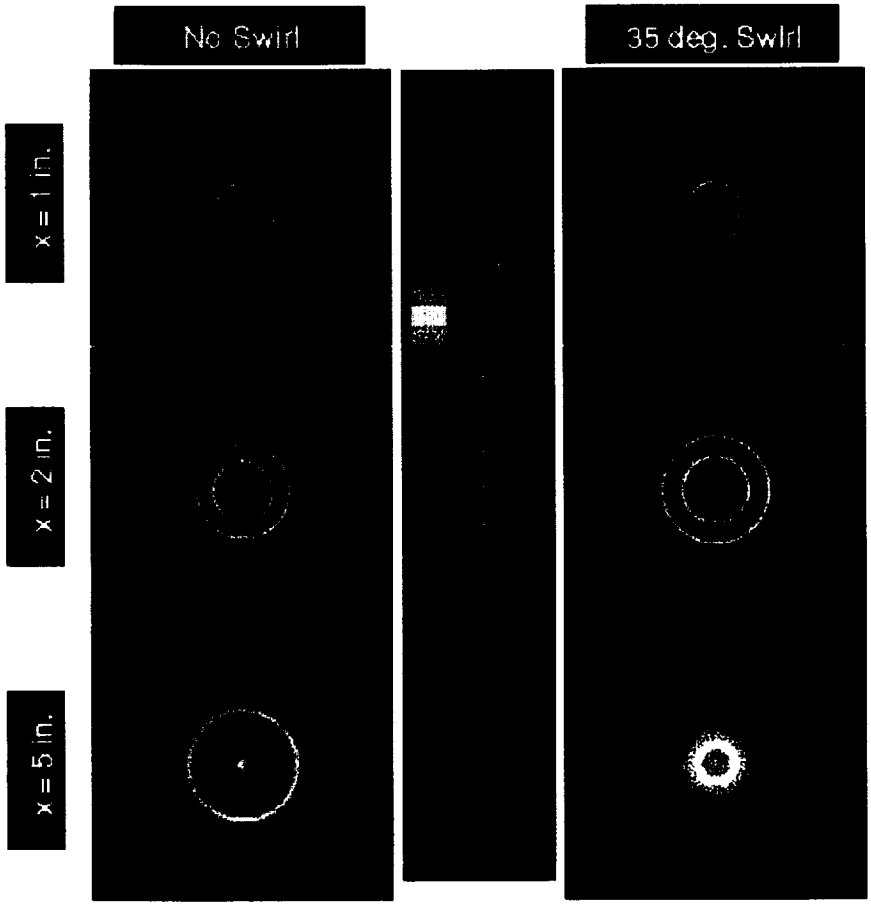


**Fig. 3.9.1. Comparison of shear (left) and swirl (right) injectors. Temperature contours are shown at three axial locations for O/F=4 case.**

region, indicating a wider flame, and again the high temperature region is not as crisply separated from the cold outer hydrogen, also indicating faster mixing.

The comparison at the 5-inch location is the most striking. The shear coaxial injector still shows a sharp high temperature region of finite thickness with a cooler region in the middle. The swirl injector, however, shows a much more faint profile that appears to be much better mixed. In the swirl injector case, the maximum temperature is on the axis and the peak temperature is considerably below the peak temperature exhibited at the earlier stations. The presence of the maximum temperature on the axis is a clear indication of superior mixing for the swirl injector.

Companion results for the oxygen mass fraction are given on Fig. 3.9.2. Again, at the x = 2-inch station, both injectors show a crisp inner circle showing a uniform region with a mass fraction of unity inside the flame region. The shear injector produces a slightly crisper boundary

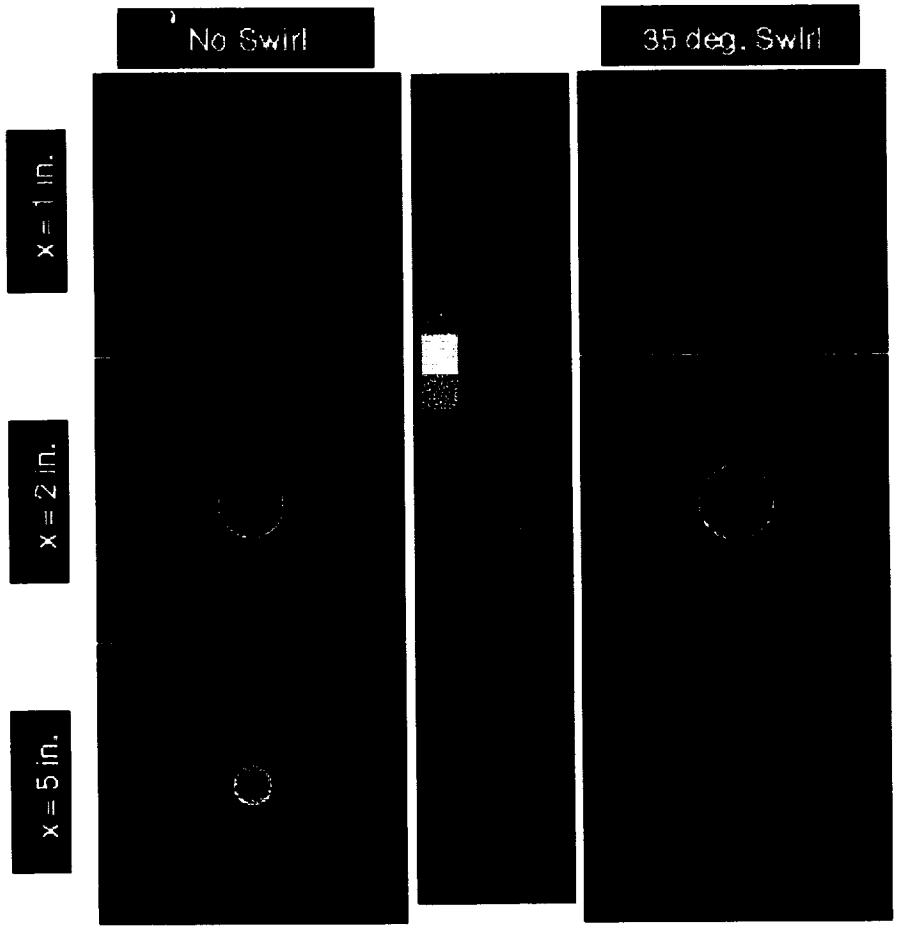


**Fig. 3.9.2. Comparison of shear (left) and swirl (right) injectors. Oxygen mass fraction contours are shown at three axial locations for O/F=4 case.**

between the oxygen and its surroundings, but both are similar. At the 2-inch station, the faster mixing of the swirl injector is beginning to assert its effects clearly, and at the 5-inch station, the swirl injector calculation indicates there is no notable amount of oxygen left anywhere in the field, while the shear injector still exhibits a significant amount of unburned oxygen.

The final comparison for this case is the water mass fraction profiles in Fig. 3.9.3. Again, the swirl injector shows a larger region of water mass fraction (indicating the combustion has progressed further, and that the mixing is more complete). Again at the downstream station, the amount of water mass fraction is much larger in the swirl case. The radial extent of the water has extended farther, and the peak water mass fraction concentration has reached the center of the axisymmetric system. Thus, as noted in the oxygen mass fraction contours and the temperature contours, the flame behind the swirl injector has burned to the centerline by the x = 5-inch

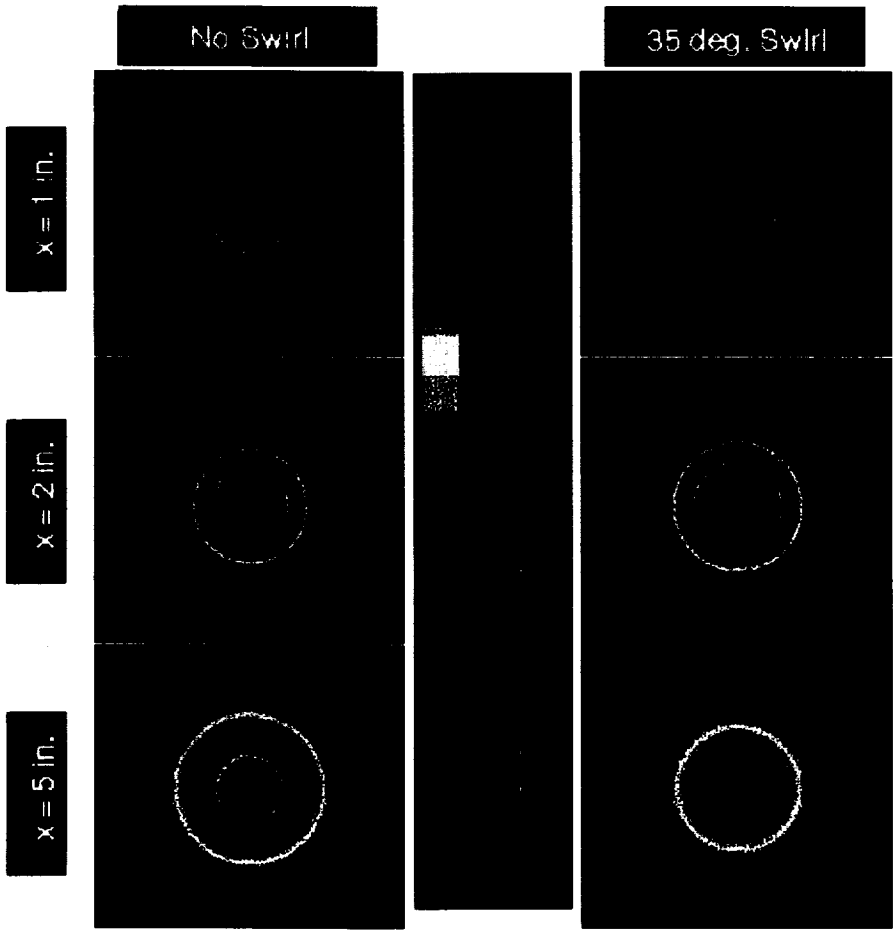


**Fig. 3.9.3. Comparison of shear (left) and swirl (right) injectors. Water mass fraction contours are shown at three axial locations for O/F=4 case.**

location, indicating that the entire amount of oxygen has been consumed. These results clearly indicate the advantages of using swirl in gas-gas injectors.

## 3.10. FLAME HOLDING RESULTS FOR GAS/GAS INJECTORS

The design of gas/gas injectors requires a general knowledge of the heat release zone, an assurance that the flame is stable, and some estimate of the heat feedback to the injector face. All of these phenomena are affected by the flame holding mechanisms that determine where flame initiation begins. CFD solutions allow the study of flame holding in detail, whereas the small scale and harsh environment limit experimental investigations to qualitative observations.

Close inspection of CFD solutions clearly show that the tip of the oxidizer post acts as a flame holder for the gas/gas reaction. This observation is consistent with experimental observations made here and elsewhere. To provide more understanding, a parametric study of the effect of O/F ratio was conducted. The temperature contours in the near-field vicinity of the oxygen post for O/F ratios ranging from 4 to 100 are presented to highlight the flame holding characteristics.

Solutions for four different O/F ratios (4, 8, 16 and 100) were obtained by fixing the oxygen flow rate and varying the hydrogen flow rate for the injector/rocket chamber geometry and chamber pressure discussed earlier. The corresponding hydrogen to oxygen velocity ratios ($U_F/U_O$) are 3.47, 1.74, 0.87 and 0.14. In all cases, the results show that the flame is firmly anchored to the oxygen post tip by the viscous flow around it as shown in Fig. 3.10.1. At an O/F ratio of 4.0 (where the hydrogen velocity is somewhat greater than the oxygen velocity), the hydrogen and oxygen mix reasonably uniformly in the base region surrounding the oxygen post tip. This results in a flame that is anchored uniformly across the width of the post as Fig. 3.10.1 (a) (O/F=4.0, $U_F/U_O$=3.47) shows.

At the higher O/F ratios, where the hydrogen flow rate is smaller, the oxygen issues straight downstream as a jet and the slower hydrogen fills the base region. Accordingly, mixing starts near the inside corner (oxygen side) of the post tip and the flame is anchored on this corner of the post. This effect is clearly seen in Fig. 3.10.1 (b) (O/F=8.0, $U_F/U_O$=1.74), 10 (c) (O/F=16, $U_F/U_O$=0.87) and (d) (O/F=50, $U_F/U_O$=0.14)

The CFD results thus verify that the tip of the oxygen post acts as a flame holder for oxygen/hydrogen combustion. Depending on the relative velocities of the two propellants, the flame may be anchored near the oxygen side (very low hydrogen velocities), in the middle (approximately equal oxygen and hydrogen velocities) or near the hydrogen side of the post (low

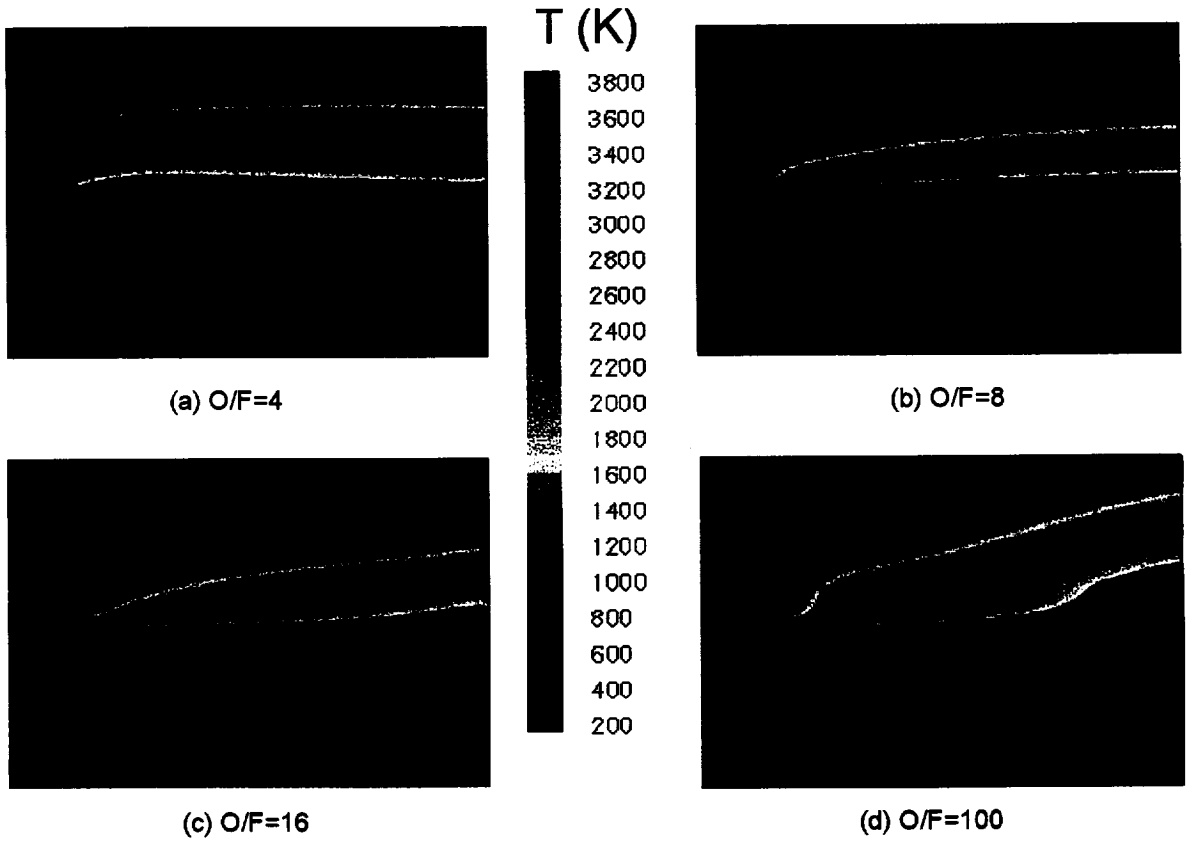


**Fig. 3.10.1. CFD results of the temperature field in the vicinity of the $GO_2$ post tip for increasing O/F ratios. For the calculations, O/F is changed by varying the $GH_2$ flow rate for fixed geometry and $GO_2$ flow rate.**

oxygen velocities). The former case is not shown here but has been observed in the computations. In all cases, the CFD solutions indicate this flame holding mechanism is steady and firm, and there is little tendency for the flame origin to "wander" causing possible flame stability issues. The results further suggest that gas/gas main engines should provide relatively stable combustion over a wide range of O/F ratios. Similar findings have also been reported experimentally.

# IV. REFERENCES


[1] Anon., Liquid Rocket Engine Injectors, NASA SP-8089, March 1976.

[2] Liquid Propellant Rocket Instability, D. T. Harrje and F. H. Reardon (eds.), NASA SP-194, 1972.

[3] Kumakawa, A., Ono, F. and Yatsuyanagi, N., "Combustion and Heat Transfer of $LO_2$/HC/Hydrogen Tripropellant," AIAA-95-2501, 31st AIAA/ASME/SAE/ASEE Joint Propulsion Conference and Exhibit, San Diego, CA, July 10-12, 1995.

[4] Yatsuyanagi, N., Sato, K., Sakamoto, H. and Ono, F., "Improvement of LOX-Kerosene Combustion Efficiency with Hydrogen Injection," Proceeding of the Eighteenth International Symposium on Space Technology and Science, AGNE Pub. Inc., 1992, pp. 61-66.

[5] Ono, F., Tamura, H., Kumakawa, A., Sakamoto, H., Sato, K., Sasaki and Yatsuyanagi, N., Effect of Hydrogen Addition on Combustion Performance of a LOX/Kerosene Rocket, NAL TR-1177 (in Japanese), 1992.

[6] Yatsuyanagi, N., Sato, K., Sakamoto, H., Ono, F. and Tamura, H., "Stabilizing Effect of Hydrogen Injection on LOX/Kerosene Unstable Combustion," Proceeding of the Seventeenth International Symposium on Space Technology and Science, AGNE Pub. Inc., 1990, pp. 309-315.

[7] Carroll, R. G., Bunting, A. K. and Lecuyer, R. P., "Tripropellant Thrust Chamber Technology Program," Air Force Report AL-TR-90-073, 1991.

[8] Green, G. J., Takahashi, F., Walsh, D. E., Dryer, F. L. (1988), "Aerodynamic Device for Generating Mono-Disperse Fuel Droplets," Review of Scientific Insruments, Vol. 60, No. 4, American Institute of Physics, Lancaster, PA, pp. 649-652.

[9] O'Brien, C. J., Advanced Oxygen-Hydrocarbon Rocket Engine Study, NASA CR-161748, 1981.

[10] Beichel, R. and Grey, J., "An Engine for the Next-Generation Launcher," Aerospace America, May 1995, pp. 34-39.

[11] Beichel, R., "A Unique Propulsion System Design for Single-State-To-Orbit. The Key to Assured Affordable Access to Space," Presented at the University of Arizona/NASA/SERC Symposium, The University of Arizona, March 24-25, 1994.

[12] Santangelo, P. J. and Sojka, P. E., "A Holographic Investigation of the Near-Nozzle Structure of an Effervescent Spray," Atomization and Sprays, vol. 5, 1995, pp. 137-155.

[13] Lund, M. T., Sojka, P. E., Lefebvre, A. H. and Gosselin, "Effervescent Atomization at Low Mass Flow Rates. Part 1: The Influence of Surface Tension," Atomization and Sprays, Vol. 3, 1993, pp. 77-89.

[14] Wallis, G. B., One-Dimensional Two-Phase Flow, McGraw-Hill, New York, 1969.

[15] Todreas, N. E., Nuclear Systems, Hemisphere Publishing Corporation, New York, 1990.

[16] Mandhane, J. M., Gregory, G. A., and Aziz, K., "A Flow Pattern Map for Gas-Liquid Flow in Horizontal Pipes," Int. J. Multiphase Flow, Vol. 1, 1974, p. 537.

[17] Liebert, C. H., "Measurement of Local High-Level Transient Surface Heat Flux," NASA Technical Paper 2840, 1988.

[18] Bachalo, W. D. and Houser, M. J., "Phase/Doppler Spray Analyzer for Simultaneous Measurements of Drop Size and Velocity Distribution," Optical Engineering, Vol. 23, 1984, pp. 583-590.

[19] Liquid Particle Size Measurement Techniques, 2nd volume, E. D. Hirleman, W. D. Bachalo and P. G. Felton (eds.), ASTM, Philadelphia, 1990.

[20] M. M. Zaller and M. D. Klem, Coaxial Injector Spray Characterization using Water/Air as Simulants, NASA-TM-105322, November, 1991.

[21] Y. Hardalupas, H. McDonald and J. H. Whitelaw, Two Fluid Mixing, Advanced Earth-to-Orbit Propulsion Technology, NASA Conference Publication 3174, Vol. II, 1992.

[22] Pal, S. Moser, M. D., Ryan, H, M, Foust, M. J. and Santoro, R. J., "Shear Coaxial Injector Atomization Phenomena for Combusting and Non-Combusting Conditions," Atomization and Sprays, Vol. 6, 1996, pp. 227-244.

[23] Rhys, N. O. and Hawk, C. W., "Tripropellant Combustion: Chemical Kinetics and Combustion Instability," AIAA-95-3151, 31st AIAA/ASME/SAE/ASEE Joint Propulsion Conference and Exhibit, San Diego, CA, July 10-12, 1995.

[24] Haidn, O. J., Vogel, A., Mayer, W., Pal, S., Gökalp, I. and Chauveau, C., "Experimental Investigation of Liquid Propellant Spray Combustion," Liquid Rocket Combustion Devices: Proceedings of the Second International Symposium on Liquid Rocket Propulsion, ONERA-Chatillon, France, June 19-21, 1995.

[25] Beisler, M., Pal, S. Moser, M. D. and Santoro, R. J., "Shear Coaxial Injector Atomization in a LOX/$GH_2$ Propellant Rocket," AIAA-94-2775, AIAA/SAE/ASME/ASEE 30th Joint Propulsion Conference and Exhibit, Indianapolis, IN, June 27-29, 1994.

[26] SSME, Program Manager's Handbook, Rocketdyne, North American Rockwell.

[27] Mayer, W. and Tamura, H., "Flow Visualization of Supercritical Propellant Injection in a Firing LOX/$GH_2$ Rocket Engine," AIAA-95-2433, 31st AIAA/ASME/SAE/ASEE Joint Propulsion Conference and Exhibit, San Diego. CA, July 10-12, 1995.

[28] Mayer, W., Schik, A., Schweitzer, C., Schaffler, M., " Injection and Mixing Processes in High Pressure LOX/$GH_2$ Rocket Combustors," AIAA-96-2620, 32nd AIAA/ASME/SAE/ASEE Joint Propulsion Conference, Lake Buena Vista, FL, July 1-3, 1996.

[29] Rahman, S. A., Pal, S. and R. J. Santoro, "Swirl Coaxial Atomization; Cold Flow and Hot-Fire Experiments," AIAA-95-0381, 33rd AIAA Aerospace Sciences Meeting, Reno, NV, January 9-12, 1995.

[30] Lefebvre, A. H., Atomization and Sprays, Hemisphere Publishing, New York, 1989.

[31] Yule, A. J., and Chinn, J. J., "Swirl Atomizer Flow: Classical Inviscid Theory Revisited," International Conference on Liquid Atomization and Spray Systems, Rouen, France, July 1994.

[32] Giffen, E., and Muraszew, A., The Atomisation of Liquid Fuels, Chapman & Hall, 1953.

[33] Oppenheim, A. V., and Schafer, R. W., Discrete-Time Signal Processing, Prentice-Hall, NJ, 1989.

[34] Press, W. H., Teukolsky, S. A., Vetterling, W. T., and Flannery, B. P., Numerical Recipes in Fortran: The Art of Scientific Computing, Cambridge University Press, 1992.

[35] Dombrowski, N., and Hasson, D., "The Flow Characteristics of Swirl (Centrifugal) Spray Pressure Nozzles with Low Viscosity Liquids," AIChe J. Vol. 15, 1969.

[36] Hutt, J. J., McDaniels, D. M., and Smith, A. W., "Internal Flow Environment of Swirl Injectors," AIAA-94-3262, 30th AIAA/ASME/SAE/ASEE Joint Propulsion Conference, Indianapolis, IN, June 27-29, 1994.

[37] Bailey, C. R., "A Preliminary Investigation of Oxidizer-Rich Hydrogen-Oxygen Combustion Characteristics," NASA TN D-3729, NASA Marshall Space Flight Center, December 1966.

[38] Farhangi, S., Hunt, K., Tuegel, L., Matthews, D., and Fisher, S., "Oxidizer-Rich Preburner for Advanced Rocket Engine Application," AIAA-94-3260, AIAA/SAE/ASME/ASEE 30th Joint Propulsion Conference & Exhibit, Indianapolis, IN., June 27-29, 1994.

[39] Hulka, J., Schneider, J. A., and Dexter, C. E., "Performance and Stability of a Booster Class LOX/$GH_2$ Swirl Coaxial Element Injector," AIAA-91-1877, AIAA/SAE/ASME 27th Joint Propulsion Conference, Sacramento, CA., June 24-26, 1991.

[40] Petersen, E. L., Rozelle, R., and Borgel, P. J., "Characterization and Wall Compatibility Testing of a 40K Pound Thrust Class Swirl-Coaxial Injector and Calorimeter Combustion Chamber," AIAA-91-1873, 27th Joint Propulsion Conference, Sacramento, CA, June 24-26, 1991.

[41] Gilroy, R. G. and Sackheim, R. L., "The Lunar Module Descent Engine - A Historical Summary," AIAA-89-2385, 25th AIAA/ASME/SAE/ASEE Joint Propulsion Conference, Monterey, CA, July 10-13, 1989.

[42] Klem, M. D. and Stoddard, F. J., "Results of 178 kN(40,000 lbf) Thrust LOX/$LH_2$ Pintle Injector Engine Tests," JANNAF CS/PSH/EPTS/SPIRITS Joint Meeting, Huntsville, AL, October 23-27, 1995.

[43] Klem, M. D., Janjovsky, A. L. and Stoddard, F. J., "Results of LOX/RP-1 Pintle Injector Engine Tests,"_JANNAF CS/PSH/EPTS/SPIRITS Joint Meeting, Huntsville, AL, October 23-27, 1995.

[44] Communications with Dressler, G., TRW Space & Technology Group.

[45] Riebling, R. W., "Criteria for Optimum Propellant Mixing in Impinging-Jet Injection Elements," Journal of Spacecraft Rockets, vol. 4., no. 6. June 1967, pp. 817-819.

[46] Eckbreth, A. C., Laser Diagnostics for Combustion Temperature and Species. Energy and Engineering Sciences Series, eds. A. K. Gupta and D. G. Lilley, Vol. 7, Abacus Press. Cambridge, Massachusetts, 1988.

[47] Barlow, R. S. and Cater, C. D, "Raman/Rayleigh/LIF Measurements of Nitric Oxide Formation in Turbulent Hydrogen Jet Flames," Combustion and Flame, Vol. 97, 1994, pp. 261-280.

[48] Cheng, T. S., Wehrmeyer, J. A. and Pitz, R. W., "Simultaneous Temperature and Multispecies Measurements in Lifted Hydrogen Diffusion Flame," Combustion and Flame, Vol. 91, 1992, pp. 323-345.

[49] Drake, M. C., Lapp, M. and Penney, C. M., "Use of Vibrational Raman Effect for Gas Temperature Measurements," In Temperature: Its measurements and control in science and industry, ed. J. F. Schooley, Vo. 5. New York: American Institute of Physics, 1982, pp. 631-638.

[50] Eckbreth, A. C., Bonczyk, P. A. and Verdieck, J. F., "Combustion Diagnostics by Laser Raman and Fluorescence Techniques," Progress in Energy and Combustion Science Vol. 5, 1979, pp. 253-323.

[51] Foust, M. J., Deshpande, M., Pal, S., Ni, T., Merkle, C. L. and Santoro, R. J., "Experimental and Analytical Characterization of Shear Coaxial Combusting $GO_2/GH_2$ Flowfield," AIAA-96-0646, 34th AIAA Aerospace Sciences Meeting, Reno, NV, Jan. 15-18, 1996.

[52] Foust, M. J., Pal, S. and Santoro, R. J., "Gaseous Propellant Rocket Studies using Raman Spectroscopy," AIAA-96-2766, 32nd AIAA Joint Propulsion Conference, Lake Buena Vista, FL, July 1-3, 1996.

[53] Farhangi, S., Gylys, V. T. and Jensen, R. J., "Gas Composition and Temperature Measurements in a Rocket Engine Combustor using Raman Technique," AIAA-94-0225, 32nd AIAA Aerospace Sciences Meeting, Reno, NV, January 10-13, 1994.

[54] DeGroot, W. A., "Species and Temperature an $H_2/O_2$ Rocket Flow Fields by Means of Raman Scattering Diagnostics," AIAA-92-3353, 28th AIAA Joint Propulsion Conference, Nashville, TN, July 6-8, 1992.

[55] Williams, D. R., Mckeown, D., Porte, F. M., Baker, C. A., Astill, A. G. and Rawley, K. M., "Coherent Anti-Stokes Raman Spectroscopy (CARS) and Laser-Induced Fluorescence (LIF) Measurements in a Rocket Engine Plume," Combustion and Flame, Vol. 94, 1994, pp. 77-90.

[56] Moser, M. D., Merenich, J. J., Pal, S. and Santoro, R. J., "OH-Radical Imaging and Velocity Field Measurements in a Gaseous Hydrogen/Oxygen Rocket," AIAA-93-2036, 29th AIAA Joint Propulsion Conference, Monterey, CA, June 28-30, 1993.

[57] Wehrmeyer, J.A., Cramer, J. M., Eskridge, R. H. and Dobson, C. C., "UV Raman Diagnostics for Rocket Engine Injector Development," AIAA-97-2843, 33rd AIAA Joint Propulsion Conference, Seattle, WA, July 6-9, 1997.

[58] Krupa, R. J., Culberth, T. F., Smith, B. W. and Winefordner, J. D., "A Flashback-Resistant Burner for Combustion Diagnostics and Analytical Spectrometry," Applied Spectroscopy Vol. 40, No. 6, 1986, pp. 729-733.

[59] Moffat, R. J., "Describing the Uncertainties in Experimental Results," Experimental and Thermal Fluid Science Vol. 1, 1988, pp. 3-17.

[60] Calhoon, D., Ito, J. and Kors, D., "Investigation of Gaseous Propellant Combustion and Associated Injector-Chamber Design Guidelines," Aerojet Liquid Rocket Company, NASA CR-121234, Contract NAS3-13379, July 1973.

[61] Anon., Rocketdyne Interim Report "Advanced Engine Aerospike Experimental Program," Rockwell International, Rocketdyne Division, NASA Contract NAS8-20349, 1968.

[62] Anon., Rocketdyne Final Report, "$O_2/H_2$ Advanced Manuevering Propulsion Technology Program," Rockwell International, Rocketdyne Division, Report No. AFRPL-TR-76-05, 1976.

[63] Anon., Rocketdyne Final Report "Hydrogen/Oxygen APS Engines Program," Rockwell International, Rocketdyne Division, NASA CR-120805, 1973.

[64] Moser, M. D., Pal, S., and Santoro, R. J., "Laser Light Scattering Measurements in $GO_2/GH_2$ Uni-Element Rocket Chamber," AIAA-95-0137, 33rd Aerospace Sciences Meeting and Exhibit, Reno, NV, January 9-13, 1995.

[65] Venkateswaran, S., Deshpande, M. and Merkle, C. L., "The Application of Preconditioning to Reacting Flow Computations," 12th AIAA Computational Fluid Dynamics Conference, San Diego, CA, June 1995.

[66] Choi, Y.-H. and Merkle, C. L., "The Application of Preconditioning in Viscous Flows", Journal of Computational Physics, Vol. 105, no. 2, April 1993, pp. 207-223.

[67] Venkateswaran, S., Weiss, J. M., Merkle, C. L. and Choi, Y.-H., "Propulsion-Related Flowfield Using the Preconditioned Navier-Stokes Equations," AIAA Paper 92-3437, July 1992.

[68] Buelow, P. E. O., Venkateswaran, S. and Merkle, C. L., "Effect of Grid Aspect Ratio on Convergence," AIAA Journal, Vol. 32, No. 12, December 1994, pp. 2401-2408.

[69] Westbrook, C. K. and Dryer, F. L., "Simplified Reaction Mechanisms for the Oxidation of Hydrocarbon Fuels in Flames," Combustion Science and Technology, Vol. 27, 1981, pp. 31-43.

[70] Wang, T. S., Farmer, R. C., and Edelman, R. B., "Turbulent Combustion Kinetics for Complex Hydrocarbon Fuels," AIAA-88-0733, 26th Aerospace Sciences Meeting, Reno, NV, January 11-14, 1988.

[71] Wang, T., R. Farmer, and K. Tucker, "Turbulent Hydrocarbon Combustion Kinetics Stochastic Modeling and Verification," AIAA-89-0486, AIAA 27th Aerospace Sciences Meeting, Reno, NV, January 9-12, 1989.

[72] Kundu, K., NASA Lewis Research Center, personal communication, November 1994.

[73] Yungster, S. and Rabinowitz, M. J., "Computation of Shock-Induced Combustion using a Detailed Methane-Air Mechanism," Journal of Propulsion and Power, Vol. 10, No. 5, September-October 1994, pp. 609-617.

[74] Hunter, T. B., Wang H., Litzinger, T. A. and Frenklach, M., "The Oxidation of Methane at Elevated Pressures: Experiments and Modeling," Combustion and Flame, Vol. 97, 1994, pp. 201-224.

[75] Hoffman, J. S., Lee, W., Litzinger, T. A., Santavicca, D. A. and Pitz, W. J., "Oxidation of Propane at Elevated Pressures: Experiments and Modelling," Combust. Sci. and Tech., Vol. 77, 1991, pp. 95-125.

[76] Westbrook, C. K., "Chemical Kinetic Modeling of Higher Hydrocarbon Fuels," AIAA Journal, Vol. 24, No. 12, December 1986, pp. 2002-2009.

[77] Merkle, C. L., Computational Fluid Dynamics of Inviscid and High Reynolds Number Flows, Penn State University, Lecture Notes, Department of Mechanical Engineering, 1995.

[78] Chien, K.,"Predictions of Channel and Boundary Layer Flows with a Low-Reynolds Number Turbulence Model," AIAA Journal, Vol. 20, No. 1, 1982, pp. 33-38.

[79] Shuen, J.S., "A Theoretical and Experimental Investigation of Turbulent Sprays," Ph.D. Thesis, Department of Mechanical Engineering, Penn State University, 1984.

[80] Sabnis, J.S., DeJong, F., "Calculation of Two-Phase Flow in an Evaporating Spray Using an Eulerian-Lagrangian Analysis," AIAA Paper 90-0447, January 1990.

[81] Priem, R.J., "Propellant Vaporization as a Design Criterion for Rocket-Engine Combustion Chambers," NASA TR R-67, 1960.

# V. PUBLISHED PAPERS


[1] Yeralan, S., Pal, S. and Santoro, R. J., "Major Species and temperature Profiles of LOX/$GH_2$ Combustion, " 33rd AIAA/SAE/ASME/ASEE Joint Propulsion Conference and Exhibit, Paper No. AIAA 97-2940, Seattle, WA, July 6-9, 1997.

[2] Rahman, S., Pal, S. and Santoro, R. J., "Critical Issues for Making Droplet Measurements in Liquid Oxygen/Hydrogen Combusting Sprays, " 33rd AIAA/SAE/ASME/ASEE Joint Propulsion Conference and Exhibit, Paper No. AIAA 97-3238, Seattle, WA, July 6-9, 1997.

[3] Foust, M. J., Pal, S. and Santoro, R. J., "Gaseous Propellant Rocket Studies using Raman Spectroscopy, " 32nd AIAA/SAE/ASME/ASEE Joint Propulsion Conference and Exhibit, Paper No. AIAA 96-2766, Lake Buena Vista FL, July 1-3, 1996.

[4] Deshpande, M., Grenda, J. M. and Merkle, C. L., "CFD Modeling of LOX/$H_2$ Coaxial Combustor Flowfields," Paper No. AIAA-96-2855, 32nd AIAA/SAE/ASME/ASEE Joint Propulsion Conference and Exhibit, Lake Buena Vista FL, July 1-3, 1996.

[5] Deshpande, M., and Merkle, C. L., "Characterization of Unsteady Effects in $GH_2/GO_2$ Combustor Modeling," Paper No. AIAA-96-3128, 32nd AIAA/SAE/ASME/ASEE Joint Propulsion Conference and Exhibit, Lake Buena Vista FL, July 1-3, 1996.

[6] Grenda, J.M., Deshpande, M., Frohman, A. and Merkle, C. L., "Downstream Dilution of Oxygen-Rich Preburners by LOX Injection," Paper No. AIAA-96-2952, 32nd AIAA/SAE/ASME/ASEE Joint Propulsion Conference and Exhibit, Lake Buena Vista FL, July 1-3, 1996.

[7] Grenda, J. M., Merkle, C. L., and Tsuei, H.-H., "Computational Procedure for Three-Dimensional Combustor Flowfield Analysis in Gas-Gas Rocket Engines," JANNAF CS/PSH/EPTS/SPIRITS Joint Meeting, Huntsville, AL, October 23-27, 1995.

[8] Deshpande, M., Grenda, J. M., Frohman, A. and Merkle, C. L., "CFD Analyses of Oxygen-Rich Preburner Concepts," JANNAF CS/PSH/EPTS/SPIRITS Joint Meeting, Huntsville, AL, October 23-27, 1995.

[9] Pal, S., Foust, M. J., Ni, T. and Santoro, R. J., "Uni-Element Studies of Gas/Gas Injectors for Rocket Combustors," JANNAF CS/PSH/EPTS/SPIRITS Joint Meeting, Huntsville, AL, October 23-27, 1995.

[10] Rahman, S., Cramer, J., Pal, S. and Santoro, R. J., "Coaxial Swirl Injector Studies at High O/F Ratios," JANNAF CS/PSH/EPTS/SPIRITS Joint Meeting, Huntsville, AL, October 23-27, 1995.

[11] Pal, S., Foust, M. J., Ni, T. and Santoro, R. J., "Uni-Element Studies of Gas/Gas Injectors for Rocket Combustors," JANNAF CS/PSH/EPTS/SPIRITS Joint Meeting, Huntsville, AL, October 23-27, 1995.

[12] Clemons, K., Schmidt, M., Mouis, A. G. F., Ni, T., Pal, S. and Santoro, R. J., "Tripropellant Combustion using RP-1/$GO_2$/$GH_2$: Droplet and Injector Studies," JANNAF CS/PSH/EPTS/SPIRITS Joint Meeting, Huntsville, AL, October 23-27, 1995.

[13] Rahman, S. A., Pal, S. and Santoro, R. J., "Swirl Coaxial Atomization; Cold Flow and Hot-Fire Experiments," 33rd AIAA AeroSpace Sciences Meeting, Paper No. AIAA 95-0381, Reno, NV, January 9-12, 1995.

# VI. MEETINGS


[1] Yeralan, S., Pal, S. and Santoro, R. J., "Experimental Investigation of LOX/$GH_2$ Rocket Combustion," Eastern States Combustion Institute Fall Technical Meeting, Hartford, CT, October 27-29, 1997.

[2] Yeralan, S., Pal, S. and Santoro, R. J., "Raman Spectroscopy Experiments for $LO_2/GH_2$ Rocket Combustion at Fuel- and Oxidizer-Rich Conditions," Propulsion Engineering Research Center, Penn State, Ninth Annual Symposium, The Pennsylvania State University, Cleveland, OH, October 1-2, 1997.

[3] Tucker, P. K., Pal, S., Foust, M. J., Lehman, M. K. and Santoro, R. J., "An Integrated Injector Design Methodology: Experimental and Analytical Developments," Propulsion Engineering Research Center, Penn State, Ninth Annual Symposium, The Pennsylvania State University, Cleveland, OH, October 1-2, 1997.

[4] Tucker, P. A., Klem, M. D., Smith, T. D., Farhangi, S., Fisher, S. C., and Santoro, R. J., "Design of Efficient $GO_2/GH_2$ Injectors: A NASA, Industry and University Cooperative Effort," 33rd AIAA/ASME/SAE/ASEE Joint Propulsion Conference and Exhibit, Seattle, WA, July 6-9, 1997.

[5] Yeralan, S., Pal, S. and Santoro, R. J., "Major Species and Temperature Profiles of LOX/$GH_2$ Combustion," 33rd AIAA/SAE/ASME/ASEE Joint Propulsion Conference and Exhibit, Seattle, WA, July 6-9, 1997.

[6] Rahman, S., Pal, S. and Santoro, R. J., "Critical Issues for Making Droplet Measurements in Liquid Oxygen/Hydrogen Combusting Sprays," 33rd AIAA/SAE/ASME/ASEE Joint Propulsion Conference and Exhibit, Seattle, WA, July 6-9, 1997.

[7] Escher, D., Pal, S. and Santoro, R. J., "Cold-Flow and Hot-Fire Studies of Pintle Injectors," Propulsion Engineering Research Center, Penn State, Eight Annual Symposium, The Pennsylvania State University, University Park, PA, October 30-31, 1996.

[8] Rahman, S., Pal, S. and Santoro, R. J., "Similitude Features of Swirl Coaxial Rocket Injector Sprays," Propulsion Engineering Research Center, Penn State, Eight Annual Symposium, The Pennsylvania State University, University Park, PA, October 30-31, 1996.

[9] Foust, M., Deshpande, M., Pal, S., Merkle, C. L. and Santoro, R. J., "Experimental and Analytical Characterization of Gas/Gas Injectors," Propulsion Engineering Research Center, Penn State, Eight Annual Symposium, The Pennsylvania State University, University Park, PA, October 30-31, 1996.

[10] Mouis, A., Pal, S. and Santoro, R. J., Tripropellant Rocket Combustion Studies Using a Mixed RP-1/$GH_2$ Injector," Propulsion Engineering Research Center, Penn State, Eight Annual Symposium, The Pennsylvania State University, University Park, PA, October 30-31, 1996.

[11] Ciasullo, A. F., Grenda, J. M., Deshpande, M. and Merkle, C. L., "Modeling of Full-Flow Preburners Utilizing LOX Dilution," Propulsion Engineering Research Center, Penn State, Eight Annual Symposium, The Pennsylvania State University, University Park, PA, October 30-31, 1996.

[12] Ahuja, V., Deshpande, M., Buelow, P. and Merkle, C. L., "CFD Modeling of Swirl Coaxial Injectors," Propulsion Engineering Research Center, Penn State, Eight Annual Symposium, The Pennsylvania State University, University Park, PA, October 30-31, 1996.

[13] Schwer, D., Deshpande, M. and Merkle, C. L., "Unsteady Characterization of Gas/Gas Coaxial Injectors," Propulsion Engineering Research Center, Penn State, Eight Annual Symposium, The Pennsylvania State University, University Park, PA, October 30-31, 1996.

[14] Foust, M. J., Pal, S. and Santoro, R. J., "Gaseous Propellant Rocket Studies using Raman Spectroscopy, " 32nd AIAA/SAE/ASME/ASEE Joint Propulsion Conference and Exhibit, Lake Buena Vista FL, July 1-3, 1996.

[15] Deshpande, M., Grenda, J. M. and Merkle, C. L., "CFD Modeling of LOX/$H_2$ Coaxial Combustor Flowfields," 32nd AIAA/SAE/ASME/ASEE Joint Propulsion Conference and Exhibit, Lake Buena Vista FL, July 1-3, 1996.

[16] Deshpande, M., and Merkle, C. L., "Characterization of Unsteady Effects in $GH_2/GO_2$ Combustor Modeling," 32nd AIAA/SAE/ASME/ASEE Joint Propulsion Conference and Exhibit, Lake Buena Vista FL, July 1-3, 1996.

[17] Grenda, J.M., Deshpande, M., Frohman, A. and Merkle, C. L., "Downstream Dilution of Oxygen-Rich Preburners by LOX Injection," 32nd AIAA/SAE/ASME/ASEE Joint Propulsion Conference and Exhibit, Lake Buena Vista FL, July 1-3, 1996.

[18] Rahman, S. A., Pal, S. and Santoro, R. J., "Atomization Study of Swirl Coaxial Rocket Injectors," 9th Annual Conference on Liquid Atomization and Spray Systems, ILASS AMERICAS 96, San Francisco, CA, May 19-22, 1996.

[19] Rahman, S. A., Pal, S. and Santoro, R. J., "Cold Flow Studies of Swirl Coaxial Injector Sprays," Workshop for Fluid Dynamic Applications in Rocket Propulsion and Launch Vehicle Technology, Marshall Space Flight Center, Huntsville, AL, April 23-25, 1996.

[20] Grenda, J., Clemons, K., Pal, S., Santoro, R. J. and Merkle, C. L. "A Companion Analytical/Experimental Investigation of RP-1 Drop Combustion in $GO_2$ and $GO_2/GH_2$ Environments, " Workshop for Fluid Dynamic Applications in Rocket Propulsion and Launch Vehicle Technology, Marshall Space Flight Center, Huntsville, AL, April 23-25, 1996.

[21] Grenda, J. M., Tsuei, H.-H. and Merkle, C. L., "Three-Dimensional Analyses of Gas-Gas Rocket Engine Combustor Flowfields," Workshop for Fluid Dynamic Applications in Rocket Propulsion and Launch Vehicle Technology, Marshall Space Flight Center, Huntsville, AL, April 23-25, 1996.

[22] Rahman, S., Cramer, J., Pal, S. and Santoro, R. J., "Coaxial Swirl Injector Studies at High O/F Ratios," JANNAF CS/PSH/EPTS/SPIRITS Joint Meeting, Huntsville, AL, October 23-27, 1995.

[23] Pal, S., Foust, M. J., Ni, T. and Santoro, R. J., "Uni-Element Studies of Gas/Gas Injectors for Rocket Combustors," JANNAF CS/PSH/EPTS/SPIRITS Joint Meeting, Huntsville, AL, October 23-27, 1995.

[24] Clemons, K., Schmidt, M., Mouis, A. G. F., Ni, T., Pal, S. and Santoro, R. J., "Tripropellant Combustion using RP-1/$GO_2$/$GH_2$: Droplet and Injector Studies," JANNAF CS/PSH/EPTS/SPIRITS Joint Meeting, Huntsville, AL, October 23-27, 1995.

[25] Grenda, J. M., Merkle, C. L., and Tsuei, H.-H., "Computational Procedure for Three-Dimensional Combustor Flowfield Analysis in Gas-Gas Rocket Engines," JANNAF CS/PSH/EPTS/SPIRITS Joint Meeting, Huntsville, AL, October 23-27, 1995.

[26] Deshpande, M., Grenda, J. M., Frohman, A. and Merkle, C. L., "CFD Analyses of Oxygen-Rich Preburner Concepts," JANNAF CS/PSH/EPTS/SPIRITS Joint Meeting, Huntsville, AL, October 23-27, 1995.

[27] Rahman, S. A., Ryan, H. M., Pal, S. and Santoro, R. J., "Oxygen-rich Combustion Experiments in a LOX/$GH_2$ Uni-Element Rocket," Thirteenth Workshop for Computational Fluid Dynamic Applications in Rocket Propulsion, Marshall Space Flight Center, Huntsville, AL, April 25-27, 1995.

[28] Grenda, J., and Merkle, C. L., "Computational Fluid Dynamic Analyses of Oxygen-Rich Preburners Utilizing Secondary Dilution," Thirteenth Workshop for Computational Fluid Dynamic Applications in Rocket Propulsion, Marshall Space Flight Center, Huntsville, AL, April 25-27, 1995.

[29] Rahman, S. A., Pal, S. and Santoro, R. J., "Swirl Coaxial Atomization; Cold Flow and Hot-Fire Experiments," 33rd AIAA AeroSpace Sciences Meeting, Reno, NV, January 9-12, 1995.

# VII. PERSONNEL

Robert J. Santoro, Professor of Mechanical Engineering, co-Principal Investigator

Charles L. Merkle, Professor of Mechanical Engineering, co-Principal Investigator

Sibtosh Pal, Senior Research Associate, Department of Mechanical Engineering

Sankaran Venkateswaran, Research Associate, Department of Mechanical Engineering

Jeff Grenda, Post-Doctoral Investigator, Department of Mechanical Engineering

Manish Deshpande, Post-Doctoral Investigator, Department of Mechanical Engineering

Vineet Ahuja, Post-Doctoral Investigator, Department of Mechanical Engineering

Serdar Yeralan, Post-Doctoral Investigator, Department of Mechanical Engineering

Michael Foust, Ph.D. 1997, Department of Mechanical Engineering

Shamim Rahman, Ph.D. 1997, Department of Mechanical Engineering

Geraldine Mouis, Ph.D. Degree Student, Department of Mechanical Engineering

Andrea Frohman Ciasullo, Ph.D. Degree Student, Department of Mechanical Engineering

Mark Schmidt, Ph.D. Degree Student, Department of Mechanical Engineering

Kimberly Clemons, M.S. 1996, Department of Mechanical Engineering

Larry Schaaf, Senior Research Technician, Department of Mechanical Engineering

# VIII. AWARDS

**Prof. Robert J. Santoro**

Group Achievement Award, Gas-Gas Injector Characterization Program Team, from National Aeronautics and Space Administration, July 8, 1996.

**Dr. Sibtosh Pal**

Group Achievement Award, Gas-Gas Injector Characterization Program Team, from National Aeronautics and Space Administration, July 8, 1996.

**Dr. Michael Foust**

Group Achievement Award, Gas-Gas Injector Characterization Program Team, from National Aeronautics and Space Administration, July 8, 1996.

**Mr. Larry Schaaf**

Group Achievement Award, Gas-Gas Injector Characterization Program Team, from National Aeronautics and Space Administration, July 8, 1996.